University of California
Santa Barbara

Polymorph selection in continuous, reactive, rate-based, precipitation systems

A dissertation submitted in partial satisfaction
of the requirements for the degree

Doctor of Philosophy
in
Chemical Engineering

by

Thomas Charles Farmer

Committee in charge:

Professor Michael F. Doherty, Co-Chair
Professor Bradley F. Chmelka, Co-Chair
Professor Todd Squires
Professor Trevor Hayton

June 2018

The Dissertation of Thomas Charles Farmer is approved.

Professor Trevor Hayton

Professor Todd Squires

Professor Bradley F. Chmelka, Committee Co-Chair

Professor Michael F. Doherty, Committee Co-Chair

June 2018

Polymorph selection in continuous, reactive, rate-based, precipitation systems

Acknowledgements

I would like to thank both the National Science Foundation and Shell for funding the work described herein. To this day, it is hard for me to believe that I have been paid to think, research, and learn for the last five years. I will always appreciate both organizations for providing the resources that made the experience possible.

I would also like to thank both of my advisers: Mike and Brad. I have learned so much from both of you, and I am grateful for all of the time you spent training, teaching, counseling, and mentoring me. There is no doubt in my mind that I have become a better writer, technical speaker, critical thinker, and scientist over the last 5 years. I hope you know how deeply appreciative I am of all of the time we have spent together and of everything you have taught me.

I would also like to thank the rest of my thesis committee, the past and present members of the Doherty and Chmelka groups, and all four of the visiting master's students I had the pleasure of working with: Philipp, Maria, Arul, and especially Sina, whose data appears in Chapter 4. I have been surrounded by wonderful people my entire time at UCSB, and I hope each and every one of you knows that I appreciate everything you have done for me and every experience we have shared.

To my parents, I cherish your constant guidance and support. Thank you for always pushing me to be the best version of myself that I can be.

To Maci, thank you for moving across the country with me, for never holding the long hours against me, for listening, for always believing that I can do anything I set out to accomplish, and most of all, for being my best friend.

Curriculum Vitæ

Thomas Charles Farmer

Education

2018	Ph.D., Chemical Engineering University of California, Santa Barbara
2013	B.S., Chemical Engineering University of Florida Summa Cum Laude

Publications

Thomas C. Farmer, Corinne L. Carpenter, and Michael F. Doherty, "Polymorph Selection by Continuous Crystallization," *AIChE J.*, **2016**, *62*, 3505-3514.
DOI: 10.1002/aic.15343

Thomas C. Farmer, Sina Schiebel, Bradley F. Chmelka, and Michael F. Doherty, "Polymorph Selection by Continuous Precipitation," *Cryst. Growth Des.*, **2018**
DOI: 10.1021/acs.cgd.8b00116.

External Conference Presentations

Thomas C. Farmer, Sina Schiebel, Bradley F. Chmelka, and Michael F. Doherty, "Polymorph Selection by Continuous Precipitation," American Institute of Chemical Engineers, Annual Meeting, Minneapolis MN, November 2017.

Thomas C. Farmer and Michael F. Doherty, "Polymorph Selection by Continuous Crystallization," American Institute of Chemical Engineers, Annual Meeting, San Francisco CA, November 2016.

Thomas C. Farmer, Bradley F. Chmelka, and Michael F. Doherty, "New conceptual design models for carbon capture and utilization via carbonate-based construction materials," American Institute of Chemical Engineers, Annual Meeting, San Francisco CA, November 2016.

Internships

Research and Development Intern, Frito-Lay North America **2012**

Process and Safety Engineering Intern, Ascend Performance Materials **2011**

Awards and Honors

Best Poster Award at UCSB Graduate Student Symposium **2015**

Heslin Fellowship **2013**

Best Poster Award at UF Senior Poster Competition **2013**

Wheat Engineering Scholarship **2012**

Progress Energy Scholar **2012**

Biery Award **2011**

Chemical Engineering Departmental Scholarship **2011**

College of Engineering Scholarship **2011**

Florida Academic Top Scholar Award **2009**

Abstract

Polymorph selection in continuous, reactive, rate-based, precipitation systems

by

Thomas Charles Farmer

Many materials are capable of organizing into multiple distinct solid phases, each exhibiting a unique set of material properties (e.g., mechanical, optical, electronic, catalytic, etc.). This material property diversity implies that a specific solid form or structure is typically preferred for a specific application. Thus, directing and controlling solid form during crystallization processes is a fundamental solid state engineering challenge. Here, for the first time, a general procedure is presented for designing continuous crystallizers that produce polymorphically pure crystal distributions of a preferred polymorph regardless of that polymorph's relative thermodynamic stability. The design rules were generated by developing and analyzing a multi-polymorph mixed suspension mixed product removal precipitator model, and they have been corroborated both by experimental data generated in our lab and by all of the applicable data in the published literature. These rules were developed to build understanding and aid in the process design of two sustainable energy technologies: carbon capture and utilization as structural materials (CCUSM) and methane pyrolysis (MP). Studying these processes also required the development of new models for calculating interphase mass transport in concentrated, electrolytic, reacting solutions and for describing the reactive transport that occurs in methane pyrolysis membrane reactors. The development and analysis of these models and a thermodynamic minimum energetic cost assessment of a wider set of sustainable energy technologies are also included in the dissertation.

Contents

Chapter 1

Introduction and Background

1.1 Motivation for solid form selection

Solid form diversity is a ubiquitous feature of nature. Identical sets of molecules and atoms can form unique phases by combining in distinct orientations with different atomic positions, bond lengths, and bond angles. Even with identical molecular/atomic stoichiometries, these structural differences lead to observable changes in macroscopic material properties. Solubility, mechanical, catalytic, electrical, and optical properties all vary among distinct solid forms built from identical component molecules or atoms. A specific set of material properties associated with a specific solid structure will always be preferred for a given technological application, and this preferred structure is not necessarily the one that exists more abundantly in nature or that happens to be most thermodynamically stable. Directing crystallization towards preferred solid forms has been an important branch of solid-phase engineering since the first reported observation of polymorphism in 1832. [1] Solid form diversity is observed across all types of solid materials, as evidenced by the elemental allotropes of carbon, the various crystalline and amorphous phases of inorganic materials like $CaCO_3$, and the diversity of solid

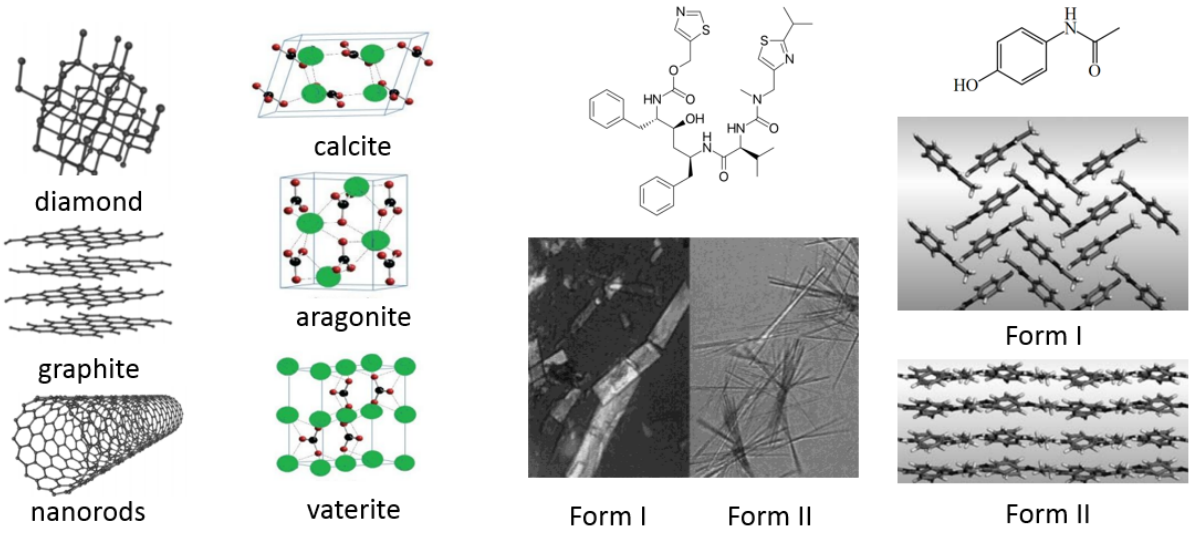

Figure 1.1: (a,b): schematic structures of solid carbon and $CaCO_3$. (c): schematic representation of a ritonavir molecule and SEM images of the two most technologically relevant solid forms. (d) a schematic representation of a paracetamol molecule and a schematic diagram of the crystal structure/packing of the two most technologically relevant polymorphs. Images taken from [2–4]

phases exhibited by small organic molecules such as the pharmaceuticals ritonavir and paracetamol (all illustrated in Figure 1.1).[1]

For many technolgical applications, the solid form produced by a process is critical to the success of the process as a whole, and yet until now no general theory or systematic procedure to selectively produce a desired form existed in the literature. The solvent mediated phase transformation that occurs in batch crystallizers [5] can be intentionally manipulated to yield prefered solid forms in some specific cases, but historically, each of these cases has been approached as a one-off engineering challenge, with widely varying techniques and approaches. [6–12] Unfortunately, this vast literature has not yet generated an algorithmic approach for other investigators to apply to new systems.

The importance of solid form selection across many industries and the elusivity of

[1]Unique crystalline solid forms constructed of the same component chemical entities are called polymorphs. The term "solid form" is more general in that it encompasses crystalline polymorphs and amorphous solid forms.

a general solution to this recurring engineering challenge backdrops the specific systems addressed in this dissertation. The work presented here was specifically motivated by a desire to understand and optimize two sustainable energy technologies, both of which involve solid form selection as a pivotal economic driver. Both specific systems are introduced next, although it will eventual become evident that the work presented here was executed and is presented in general terms to facilitate application of the conclusions to other systems for which the general, recurring challenge of solid form selection can now be solved.

1.2 Specific processes of interest

1.2.1 Carbon capture and utilization as structural materials

Carbon capture and utilization refers to the class of processes that capture CO_2 at point sources and utilize that CO_2 for some industrial purpose, concurrently mitigating anthropogenic CO_2 emissions. The patent literature suggests that thermodynamically metastable solid forms of $CaCO_3$ (vaterite and amorphous calcium carbonate, also called ACC) can be formulated into structural materials that could replace or augment conventional Portland cements. [13, 14] Carbon capture and utilization as structural materials (CCUSM) is the process that attempts to manufacture these solid carbonates from brine solutions and point source CO_2 emissions by the combined chemistry shown in Equation 1.1 (more complete chemistry described in Chapters 4 and 5).

$$CaCl_{2,(aq)} + CO_{2,(g)} + H_2O_{(l)} \rightleftharpoons CaCO_{3,(s)} + 2HCl_{(aq)} \qquad \Delta G^{o}_{rxn} = 56 \text{ KJ/mole} \quad (1.1)$$

In the absence of an input alkalinity source, this process co-produces two moles of acid (aqueous) with each mole of solid calcium carbonate. The large quantities of acid that

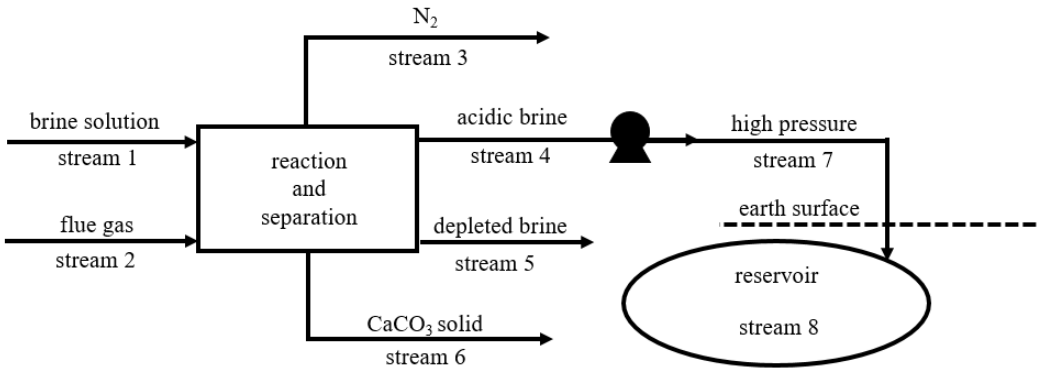

Figure 1.2: A schematic representation of the carbon capture and utilization (CCUSM) process. CCUSM generates solid calcium carbonate for utilization as structural materials from point source CO_2 emissions and brine solutions. The aqueous acid waste that is produced could be geologically sequestered.

would be produced by the application of this technology at any scale comparable to point source CO_2 emissions would be unlikely to find an industrial use. The aqueous acid waste would need to be deposited in geologic reservoirs similar to the ones that are proposed for storing sequestered CO_2. Figure 1.2 is a schematic representation of the overall process.

Attempting to optimize or design this process forces one to confront several generally interesting scientific challenges. First and foremost, the most thermodynamically stable solid form of $CaCO_3$ is calcite. Calcite is naturally abundant (≈ 4 % of the earth's crust), but both vaterite and ACC seem to make better cements. [13, 14] Ironically, limestone, which is largely composed of calcite, is a primary feed material to conventional Portland cement production processes. These processes first convert the limestone to lime through Reaction 1.2

$$CaCO_{3,(s)} \leftrightharpoons CaO_{(s)} + CO_{2,(g)} \qquad \Delta G^{o}_{rxn} = 131 \text{ KJ/mole} \tag{1.2}$$

The heat required by Reaction 1.2 is typically supplied by fossil fuel combustion. The fossil fuel combustion, the stoichiometric emissions from reaction 1.2, and emissions related

to power consumption and product transportation combine to generate $\approx$ 886 Kg CO_2 per ton of conventional cement produced. [15] Therefore, every ton of CO_2 that displaces a ton of traditional cement avoids a ton of emissions at the capture site, and potentially avoids up to another 0.886 tons by reducing the amount of cement produced conventionally. The displacement hinges on the produced $CaCO_3$ being utilized as a cement, which requires the produced $CaCO_3$ to be a thermodynamically metastable solid form. Therefore, the technoeconomic assessment of CCUSM hinges on the ability to selectively produce the higher value, thermodynamically metastable solid forms of $CaCO_3$.

Another interesting aspect of the CCUSM process is the Ca^{2+} source. Natural geologic brines, desalination wastewater, or fracking wastewaters could be utilized by such a process. All of these solutions share a common characteristic: they are concentrated in other electrolytes besides calcium. Concentrated electrolyte solutions exhibit interesting and sometimes counter-intuitive mass transport properties that could render traditional process models ineffective. Mass transport models that accurately account for these effects but remain robust and user-friendly are required for accurate simulation and design of the reactive absorption of CO_2 required by this process.

Furthermore, the process scheme is inherently three phase. The CO_2 is fed as a dilute gas. The Ca^{2+} brine is aqueous, and the product is solid. One can imagine two classes of processes to carry out this transformation. The processing could be done serially by first reactively absorbing CO_2 and then reactively precipitating $CaCO_3$ as in Reactions 1.3 and 1.4.

$$CO_{2,(g)} + H_2O_{(l)} \leftrightharpoons H_2CO_{3,(aq)} \qquad \Delta G^o_{rxn} = 104 \text{ KJ/mole} \tag{1.3}$$

$$CaCl_{2,(aq)} + H_2CO_{3,(aq)} \leftrightharpoons CaCO_{3,(s)} + 2HCl_{(aq)} \qquad \Delta G^o_{rxn} = -48 \text{ KJ/mole} \tag{1.4}$$

In this case, CO_2 is first reactively absorbed into an aqueous solution. Then the aqueous

solution is contacted with a Ca^{2+} rich brine solution, instigating a precipitation reaction. Alternatively, one could intensify the process by combining absorption and precipitation into a single device. A reactive absorber and preciptitator might be able to harness the free energy reduction from Ca^{2+} and CO_3^{2-} in solution to $CaCO_{3,(s)}$ in order to drive more efficient absorption of the CO_2 from the dilute gas phase. Historically, process intensification has driven substantial efficiency gains in processes for which thermodynamic driving forces for one rate process can be utilized to drive slower rates elsewhere in the conventional process flow sheet or for which combining unit operations allows one to sidestep a difficult separation or a reaction equilibirum limitation. For example, Eastman Chemical was able to reduce both initial capital expenditures and continuing energy requirements by a factor of 5 by employing reactive distillation instead of conventional processing during methyl-acetate production. [16, 17] CCUSM may be another candidate for successful process intensification, but tools do not exist in the literature for designing solid form selective reactive absorber/precipitators, and even if they did, it is unlikely that they would be applicable to the concentrated, electrolytic solutions that are required as inputs to this process.

1.2.2 Methane Pyrolysis

The CCUSM process as well as the more studied carbon capture and sequestration processes (CCS) are both motivated by a desire to reduce anthropogenic carbon emissions at point sources, but a large class of carbon emissions cannot be ameliorated by point source mitigation techniques. Most transportation is fueled by fossil fuel combustion, and so the emissions generated by cars, boats, and planes are typically dilute and distributed. A carbon emission neutral future likely requires some transportation energy system that does not emit CO_2 in such a dilute and distributed fashion. Hydrogen fuel is one possible

path towards de-carbonizing transportation because hydrogen releases only water and heat upon combustion.

Hydrogen is conventionally produced by steam methane reforming followed by the water gas shift reaction (SMR). The combined chemistry is summarized in Equation 1.5.

$$CH_{4,(g)} + 2H_2O_{(l)} \leftrightharpoons CO_{2,(g)} + 4H_{2,(g)} \qquad \Delta G^{o}_{rxn} = 131 \text{ KJ/mole} \tag{1.5}$$

Hydrogen produced by SMR generates point source emissions at the production site, and so it is possible that point source emission mitigation techniques could be coupled to conventional hydrogen production to reduce anthropogenic transportation emissions. Unfortunately, hydrogen produced by SMR typically costs 2-3 times as much as the feed methane on a dollar/energy basis, [18] and is expected to cost more if CCS or CCUSM were added.

One potential alternative is to produce hydrogen by the thermal decomposition of methane, also known as methane pyrolysis (MP).

$$CH_{4,(g)} \leftrightharpoons C_{(s)} + 2H_{2,(g)} \qquad \Delta G^{o}_{rxn} = 50.8 \text{ KJ/mole} \tag{1.6}$$

Reaction 1.6 produces solid carbon instead of CO_2. Unfortunately, the solid carbon deposits and accumulates on the reactor walls and on any heterogeneous catalysts present within the reactor. Removing the carbon and reactivating the catalyst requires oxidation with air, generating CO_2 emissions.

Alternatively, one could utilize a catayltic molten metal solvent to drive Reaction 1.6 in a bubble column. Recent reports of molten metal methane pyrolysis in bubble column type reactors indicate that the solid carbon tends to separate from the gas-liquid interface as formed (likely due to convective transport away from the bubble/melt surface due to

the bubble rising through the melt). Once suspended in the melt phase, the carbon tends to float to the top of the reactor, apparently due to bouyancy. [19, 20] Continuous, mechanical collection of the carbon from the top of the reactor may be possible, rendering molten metal catalyzed methane pyrolysis CO_2 emission free. Furthermore, hydrogen and carbon are more soluble in many metals than methane, so it should be possible to utilize reactive separation to deliver conversions in excess of the equilibrium conversion implied by a set of feed conditions.

The primary problem with molten metal catalyzed methane pyrolysis is the stoichiometry of Reaction 1.6 relative to Reaction 1.5. SMR produces four moles of hydrogen per mole of methane fed and MP produces only two. The difference is a bit smaller when the thermodynamically defined minimum energetic costs of each process are considered (See Chapter 2), but even then, there is a high energetic cost of MP relative to SMR. The problem is inherent and unavoidable because the "lost" energy is intentionally trapped within the carbon-carbon bonds in the solid carbon phase. In SMR, energy is released during the oxidation of carbon to CO_2, and avoiding that exothermic reaction increases the energetic costs of the methane pyrolysis process.

For hydrogen produced from MP to compete with hydrogen produced from SMR (or even better, for hydrogen from MP to compete with other potential transportation fuels like gasoline) the solid carbon needs to be a product instead of a waste. If the carbon could be directed towards whichever solid form the market values highest at a given time (e.g., carbon fibers, carbon black, graphite, etc.), then the market price of hydrogen would be driven down, thereby making it an economical (cheap) fuel. Therefore, designing an MP process is yet another exercise in solid form selection and process intensification.

1.3 Research Objectives

The primary objectives of the work reported in this dissertation include developing an algorithmic methodology for directing and controlling solid form during crystallization and precipitation (especially when thermodynamically metastable forms are preferred), developing deeper understanding of mass transport in regimes of process space in which classical descriptions are inadequate, and analyzing and utilizing process intensification to drive more efficient processes. These objectives arise naturally from the motivating systems previously discussed: CCUSM and MP.

The superior cementitious properties associated with the less thermodynamically stable solid forms of calcium carbonate transforms CCUSM process design into a solid form selection and control challenge. The successful realization of an MP process also hinges on the ability to produce high value polymorphs of carbon on demand. Solid form selection is also important for many other industries and processes not specifically considered here. For example, the pharmaceutical industry sometimes prefers a thermodynamically metastable form for its its higher bioavailability (e.g., ritonavir [3]) or for its supperior compression properties that enable simpler and less costly tabletting (e.g., paracetamol [21]). The recurring need across many fields to control and direct crystallization and precipitation towards specific solid forms motivates a general approach built upon first principles, such that the methodology can be utilized for as many of these systems as possible.

The concentrated, electrolytic nature of the absorbing brine solutions in the CCUSM process enables non-Fickian, uphill diffusion that is qualitatively unpredictable from classic constitutive models. Understanding the interplay between electrolyte non-idealities, concentrated, multicomponent mass transport, and the diffusion of charged species may become critical to designing unit operations that utilize brine solutions as starting ma-

terials, and so understanding and modeling these effects is another important objective of this dissertation.

The multi-phase nature of any process that inputs liquids and gases while generating solid products invites process intensification, especially when the final processing step is thermodynamcially spontaneous (CCUSM) or when a required separation might be utilized to drive conversion past reaction equilibrium (MP). Both CCUSM and MP are prime candidates for reactive separation and precipitation. This dissertation aims to develop understanding and build upon past knowledge in all of these fields to attempt to aid in the technoeconomic assessment of both CCUSM and MP processes, while building fundamental, general knowledge that can also be applied to other systems.

1.4 Dissertation Outline

The over-arching technical challenges that motivate the work presented here are selecting and controlling solid form, understanding and manipulating concentrated electrolytic mass transport, and harnessing the power of process intensification. It is hypothesized throughout this dissertation that there are predictable synergies available from intensification of the CCUSM process, and yet the combined, solid form selective, reactive absorber/precipitator process is much more difficult to model, analyze, and characterize experimentally than each of the component unit operations taken separately. Here, these components unit operations are analyzed first to facilitate analysis of the intensified system. The dissertation is organized as follows: First, CCUSM and MP are placed in context among other sustainable energy technologies through a thermodynamic minimum free energy assessment and comparison. Then, a new algorithmic approach for solid form selection using continuous crystallization and precipitation is introduced and specifically applied to the motivating CCUSM system (reactive precipitation of $CaCO_3$). Then, mass

transport models are developed for describing the interphase transport that occurs during the reactive absorption of CO_2 into concentrated brine solutions. Finally, a gas/liquid membrane reactor model is developed and validated against available experimental data from the published literature. It is then utilized to illustrate that reactive separation principles can be utilized to overcome a significant design challenge currently limiting the methane pyrolysis research effort. The same reactor model can be utilized in the future for more systematic conceptual design studies of the MP process. Furthermore, the same bubble column model can be utilized for future reactive absorption (CCUSM) studies by setting $\zeta = 0$ (ζ is the dimensionless group that quantifies the rate of transport through the membranes to the rate of diffusion along the axial direction of the reactor) and replacing the Sievert's law based interphase mass transport kinetic expression with the interphase transport model developed in Chapter 5 for the CCUSM system. The final chapter draws conclusions based on the entire body of work presented here, highlights the next steps one could follow to continue the technoeconomic assessment of CCUSM or MP processes, and proposes several otherwise unrelated technical challenges that might be addressed or explored as an extension of the work presented here.

Bibliography

[1] J. Thun, L. Seyfarth, C. Butterhof, J. Senker, R. E. Dinnebier, and J. Breu. Wohler and liebig revisted: 176 years of polymorphism in benzamide-and the story still continues! *Cryst. Growth Des.*, 9(5):2435–2441, 2009.

[2] J. Brog, C. Chanez, A. Crochet, and K. Fromm. Polymorphism, what it is and how to identify it: a systematic review. *RSC Advances*, 3(38):16905–16931, 2013.

[3] J. Bauer, S. Spanton, R. Henry, J. Quick, W. Dziki, W. Porter, and J. Morris. Ritonavir: An extraordinary example of conformational polymorphism. *Pharm. Res.*, 18(6):859–866, 2001.

[4] S. M. Dizaj, M. Barzegar-Jalali, M. H. Zarrintan, K. Adibkia, and F. Lotfipour. Cal-

cium carbonate nanoparticles; potential in bone and tooth disorders. *Pharmaceutical Sciences*, 20:175–182, 2015.

[5] P. T. Cardew and R. J. Davey. The kinetics of solvent-mediated phase transformations. *Proc. R. Soc. Lond.*, 398:415–428, 1985.

[6] C. Cashell, D. Corcoran, and B. K. Hodnett. Control of polymorphism and crystal size of l-glutamic acid in the absence of additives. *J. Cryst. Growth*, 273(1-2):258–265, 2004.

[7] N. C. Kee, R. B. Tan, and D. Braatz, Richard. Selective crystallizationof the metastable α-form of l-glutamic acid using concentration feedback control. *Crys. Growth Des.*, 9(7):3044–3051, 2009.

[8] R. P. Sangodkar, B. J. Smith, D. Gajan, A. Rossini, L. R. R., G. P. Funkhouser, A. Lesage, L. Emsley, and B. F. Chmelka. Influences of dilute organic adsorbates on the hydration of low-surface-area silicates. *Journal of American Chemical Society*, 137:8096–8112, 2015.

[9] M. W. Hermanto, M. Chiu, and R. D. Braatz. Nonlinear model predictive control for the polymorphic transformation of l-glutamic acid crystals. *AIChE J.*, 54.12:3248–3259, 2009.

[10] X. Yang, B. Sarma, and A. S. Myerson. Polymorph control of micro/nano-sized mefenamic acid crystals on patterned self-assembled monolayer islands. *Cryst. Growth Des.*, 12:5221–5228, 2012.

[11] I. S. Lee, A. Y. Lee, and A. S. Myerson. Concomitant polymorphism in confined environment: Implication to crystal form screening. *Pharm. Res.*, 25:960–968, 2008.

[12] E. Simone, A. N. Saleemi, N. Tonnon, and Z. K. Nagy. Active polymorphic feedback control of crystallization processes using a combined raman and atr-uv/vis spectroscopy approach. *Cryst. Growth Des.*, 14:1839–1850, 2014.

[13] B. R. Constantz, A. Youngs, and T. Holland. Reduced-carbon footprint concrete compositions. U.S. patent 7,815,880, 2010.

[14] B. R. Constantz, K. Farsad, C. Camire, and I. Chen. Methods and compositions using calcium carbonate. U.S. patent 7,922,809, 2011.

[15] WBCSD. Cement industry energy and CO_2 performance: Getting the numbers right. online, 2014.

[16] M. F. Malone and M. F. Doherty. Reactive distillation. *Ind. Eng. Chem. Res.*, 2000.

[17] V. H. Agreda and L. R. Partin. Reactive distillation process for the production of methyl acetate, 1982.

[18] B. Parkinson, J. W. Matthews, T. B. McConnaughy, D. C. Upham, and E. W. McFarland. Techno-economic analysis of methanepyrolysis in molten metals: Decarbonizing natural gas. *Chemical Engineering & Technology*, 2017.

[19] T. Geiβler, M. Plevan, A. Abanades, A. Heinzel, K. Mehravaran, R. Rathnam, C. Rubbia, D. Salmieri, L. S. ad S. Stuckrad, A. Weisenburger, H. Wenninger, and T. Wetzel. Experimental investigation and thermo-chemical modeling of methane pyrolysis in a liquid metal bubble column reactor with a packed bed. *International Journal of Hydrogen Energy*, 40:14134–14146, 2015.

[20] D. C. Upham, V. Agarwal, A. Khechfe, Z. R. Snodgrass, M. J. Gordon, H. Metiu, and E. W. McFarland. Catalytic molten metals for the direct conversion of methane to hydrogen and separable carbon. *Science*, 358:917–921, 2017.

[21] P. Di Martino, A. M. Guyot-Hermann, P. Conflant, M. Drache, and J. C. Guyot. A new pure paracetamol for direct compression: the orthorhombic form. *International Journal of pharmaceutics*, 128(1-2):1–8, 1996.

Chapter 2

Thermodynamic assessment of sustainable energy technologies

2.1 Introduction

Thermodynamic calculations and back of the envelope analyses are often under-rated and under-utilized in the scientific literature. Nonetheless, quick, simple calculations can often provide invaluable context and can even offer practically relevant technological bounds that inform decision making. In the context of ever increasing specialization, it is easy to unintentionally misrepresent the potential impact of a body of research to journal editors, to the public, to policy makers, and even to oneself. As Richard Feynman once said, "The first principle is that you must not fool yourself and you are the easiest person to fool." [1] Forcing oneself to slow down and make time for systems level thinking at the beginning of a research endeavor may help one avoid fooling oneself, or perhaps more importantly, fooling the public and the institutions that fund and support one's work.

Here, some simple methods for framing a research program, its goals, and its potential impact are emphasized through the discussion and comparison of several sustainable

energy technologies: (1) carbon capture and sequestration from point sources (CCS), (2) carbon capture and sequestration from air (CCSA), (3) carbon capture and utilization as structural materials (CCUSM), (4) zero CO_2 emission hydrogen production via steam methane reforming plus CCS (SMR+CCS), and (5) zero CO_2 emission hydrogen production via molten metal methane pyrolysis (MP).[1] New technology improvements and ideas are not presented here for any of these process schemes, but simple material balances and back of the envelope thermodynamic calculations are presented to give each of these technologies some context that the published literature may lack. For some of these processes, theoretical limits for process efficiencies can be estimated *a priori* from classical thermodynamics. These limits can be utilized to answer big-picture, systems-level questions about what is and is not possible in the limit of "perfect" engineering (i.e., reversible processes that generate minimal entropy). These sorts of bounds and their utility can be compared to the classic carnot cycle efficiency for heat to work conversions or to the more recently developed framework for determining upper bounds on reaction selectivities. [2, 3] In both cases, there is value in defining the ultimate limits of clever engineering before substantial resources and effort are deployed towards improving any specific process.

A back of the envelope analysis can only provide weak evidence in support of the pursuit of some research objective, but in some cases, it can provide excellent justification for rejecting one. More practically, it can serve as an estimate of a best case scenario for a given technology. If the best case scenario is unlikely to be "good enough," then the idea can be rejected without further study. The free energy change associated with several common state changes is repeatedly required throughout this chapter, and so it makes sense to begin the analysis by describing and defining these state changes in the

[1] Some related discussion of corn ethanol based biofuel, synthetic CO_2 fixation to fuel, biofuels from bio-wastes, and zero CO_2 emission hydrogen production via the electrolysis of water are availabile in Appendices 2.C and 2.D.

next section.

2.2 Preliminary definitions and calculations

Throughout this chapter, both the maximum work extractable from a state change and the minimum work required to drive a state change are given by the change in Gibbs free energy associated with that state change. In this section, several mathematical expressions are presented for calculating the change in Gibbs free energy associated with several common state changes. Each of the following expressions is described in more detail in Appendix 2.A.

The molar Gibbs free energy change associated with compressing a stream at a molar flow rate of F from state 1 at P_1 and $\hat{v}_1$ to P_2 and $\hat{v}_2$ is

$$\frac{G_2 - G_1}{F} = \mu_2 - \mu_1 = -\int_{\hat{v}_1}^{\hat{v}_2} P(T, \hat{v}, \mathbf{y}) d\hat{v} \tag{2.1}$$

where $\hat{v}_1$ is the molar volume. Imagine a separation process in which component i_r is concentrated into stream k_r. Assuming the mixing enthalpy is negligible, the Gibbs free energy change of separation per mole of component i_r concentrated into stream k_r is given by Equation 2.3 (See Figure 2.6 in Appendix 2.A for a schematic representation).

$$\frac{G_3 + G_2 - G_1}{F_{k_r,i_r}} = RT\left[\frac{F_{3,T}}{F_{k_r,i_r}} \sum_i \left[y_{3,i} \ln(y_{3,i})\right]\right. \tag{2.2}$$

$$\left. + \frac{F_{2,T}}{F_{k_r,i_r}} \sum_i \left[y_{2,i} \ln(y_{2,i})\right] - \frac{F_{1,T}}{F_{k_r,i_r}} \sum_i \left[y_{1,i} \ln(y_{1,i})\right]\right] \tag{2.3}$$

where $y_{k,i}$ denotes the mole fraction of component i in stream k, $F_{k,i}$ denotes the molar flow rate of component i in stream k, and $F_{k,T}$ denotes the total molar flow in stream k.

The minimum work rate (power) required to pump a fluid into a reservoir is just the

PV work required to displace the existing fluid.

$$W_{min} = F_T\left(P_{well}\hat{v}_{well} - P_a\hat{v}_{atm}\right) \tag{2.4}$$

where F_T is the total molar flow rate pumped to the reservoir.

When a process is driven by a heat to work conversion in which heat is supplied by the combustion of a fuel, the enthalpy of combustion is taken as the primary energy available upon combustion. Alternatively, when an endergonic or endothermic reaction is required by a process, the more positive of the change in Gibbs free energy or enthalpy of reaction ($\Delta g^o_{rxn}(T)$ or $\Delta h^o_{rxn}(T)$) is taken as the energetic cost. This is consistent with the second law of thermodynamics, as described in Appendix 2.A. The pressure and mixing free energy changes that occur during reaction are included via equations 2.1-2.3.

2.3 Carbon capture and sequestration/utilization technologies

In 2017, 1.2 Gigatons of CO_2 were emited during the generation of 1210 Terawatt hours of coal-based electricty in the United States. Another 0.5 Gigatons were released during the generation of an additional 1270 Terawatt hours of electricity from natural gas. [4] The massive amount of capital and infrastructure devoted to power generation from fossil fuel combustion makes a large-scale, instantaneous, technological pivot exceedingly unlikely, and so a transition to power generation that involves exclusively renewable, non-CO_2 emitting technologies will take time. For emissions to rapidly decrease in the near term (i.e., more than a few percent per year), it is likely neccessary for some emmision reduction technology to be retrofitted to the existing power plant fleet. Carbon capture and sequestration (CCS) is one possible solution. CCS consists of concentrating CO_2 from

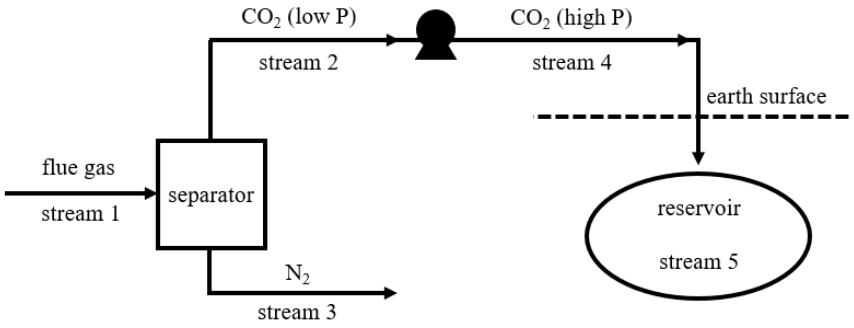

Figure 2.1: A CCS process takes a flue gas (stream 1) as input and ouputs a N_2 stream to the atmosphere and a concenrtated, compressed CO_2 stream to a geologic reservoir below ground. The primary state changes involved include speparation (stream 1 goes to streams 2 and 3), compression (stream 2 goes to stream 4) and pumping to reservoir (stream 4 goes to stream 5).

point sources (such as flue gases), compressing the CO_2 rich stream to $\approx$ 100 atm, and pumping the CO_2 underground. [5] Another process that could be retrofitted to existing power plants and other point source emission sites is carbon capture and utilization as structural materials (CCUSM). [6, 7] A CCUSM process captures CO_2 from flue gases and converts it to carbonate solids suitable for utilization as structural materials. A third mechanism by which point source emmisions could be reduced is the direct capture and sequestration of carbon from air (CCSA). [8] The Gibbs free energy changes associated with (i.e., minimum work/energy input required by) these processes are calculated and contrasted in this section.

2.3.1 Carbon Capture and Sequestration from Point Sources

There are 3 important state changes to consider.

- Stream 1 (flue gas) is separated into streams 2 (CO_2) and 3 (N_2).
- Stream 2 is compressed to stream 4.
- Stream 4 is pumped into the reservoir, becoming stream 5 .

The change in free energy due to separation per mole of CO_2 captured can be calculated from Equation 2.3. After specifying the flue gas CO_2 mole fraction to be 0.10, only $2c-2=2$ degrees of freedom remain. If one further specifies the fraction of CO_2 removed from the flue gas and the concentration of CO_2 in stream 2, all degrees of freedom are specified. When the removal rate is 90 mole % and the concentration of CO_2 in stream 2 is 95 mole %, the free energy change of separation is 9 KJ/mole of CO_2 captured.

The change in Gibbs free energy per mole of CO_2 that occurs between states 2 and 4 is given by Equation 2.1. For an ideal gas that is compressed from atmospheric pressure to 100 atm this quantity is approximately 16 KJ/mole.[2] Another study estimated the integral in Equation 2.1 with real pressure/volume data and estimated this quantity to be 13 KJ/mole of CO_2. [10]

The Gibbs free energy change per mole of CO_2 that occurs between states 4 and 5 is the minimum work required to displace the fluid originally in the reservoir. This state change represents 0.5-1 KJ/mole of CO_2. Throughout this chapter, the compression and pumping steps together are estimated to require a thermodynamic minimum free energy change of 14 KJ/mole CO_2. Thus, the overall minimum free energy change between streams 1 and 5 is 9+14=23 KJ/mole of CO_2 sequestered.

Relating the Minimum Free Energy Change to the Required Work

The free energy change is related to the primary energy required (i.e., higher heating value (HHV) of fuel used by power plant) to drive the transformation through an efficiency. If we define the primary energy necessary to drive the transformation from

[2]The 2010 CCS roadmap published by the DOE estimated the neccessary compression pressure to be 1500-2200 psia or 100-150 atm. [9]

stream 2 to stream 5 as $E_{2,5}$, then

$$E_{2,5} = \frac{14}{\eta_{pp}\eta_{com}} \tag{2.5}$$

where η_{pp} is fraction of inlet primary energy to the power plant that is converted to electricity (without CCS) and η_{com} is the % of the electrical energy delivered to the compressor/pump that is converted to actual compression/pumping.[3] Data from 2017 power outputs and emissions data imply that the US fleet of coal power plants exhibited an average η_{pp} of 0.32 in 2017, while the natural gas fleet exhibited an average efficiency of $\eta_{pp} = 0.455$. [4] Compressors have been reported with η_{com}=0.66-0.73, with the higher values typically associated with prototype compressors not currently available at industrial scale. [10, 11] Therefore, when discussing retrofitting CCS to the existing PC fleet, η_{pp} is unlikely to be improved beyond 0.32 and η_{com} should vary from 0.66-1 (depending on one's expectations of future compressor innovation).

The separation (change from stream 1 to streams 2 and 3) is not necessarily driven by electricity, and so a η_{pp} adjustment is unnecessary. Still, there is a limiting Carnot efficiency for heat to work conversions defined by the highest and lowest temperatures in any cycle. Therefore, one can define the primary energy necessary to drive the separation as shown in equation 2.6.

$$E_{1,2} = \frac{9}{\eta_{car}\eta_{sep}} \tag{2.6}$$

where η_{car} is the Carnot efficiency of the separation and η_{sep} represents ones ability to approach a "perfect" (i.e., reversible) separation. For a traditional temperature swing absorption process with ethanolamines, $\eta_{car} \approx 0.20 - 0.25$. [12] One could imagine new

[3] See Appendix 2.B for definitions of η_{pp} and η_{com}

solvents with larger temperature swings driving this number higher towards 0.3 or 0.4, but then one would have to supply heat at (more costly) higher temperatures, somewhat negating the benefit.

The energy penalty construct is a convenient context within which to consider the energetic costs of a carbon capture process. The energy penalty is defined as the primary energy needed to drive the CCS of a mole of CO_2 divided by the primary energy available during the combustion of the quantity of fuel that generates a mole of CO_2. It therefore signifies the percent of the primary energy of a power generation fuel that must be devoted to the CCS process. The EPA emissions factor for the coal used in the US electric power sector is 95.52 Kg of CO_2 per million BTU of generated heat. This emission factor implies 486 KJ of available energy/mole of CO_2 released ($\Delta H_{combustion}$/mole of CO_2 generated). Therefore, the US coal power plant CCS retrofit energy penalty can be written as Equation 2.7.

$$EP_{CCS} = \left(\frac{9}{\eta_{car}\eta_{sep}} + \frac{14}{\eta_{pp}\eta_{com}} \right) /486 \tag{2.7}$$

The following table gives the energy penalty as a function of the previously defined efficiency parameters.

Scenario	η_c	η_{sep}	η_{com}	Energy Penalty
Absolute minimum	0.3	1	1	15.2 %
Optimistic Goal 1	0.3	0.85	0.95	16.7 %
Optimistic Goal 2	0.2	0.75	0.8	23.6 %
Probable technology 2018	0.2	0.5	0.66	32.2 %

Table 2.1: Energy penalty scenarios for retrofitting CCS to US fleet of coal power plants under a variety of processing efficiency assumptions from "perfect" reversible engineering (15 %) to a more realizable yet still optimistic case (32 %). The optimistic case still requires $\approx$ 1 out of 3 units of fuel/power to be devoted to CCS.

The energy penalties discussed here only account for the energy drain associated with

separation, compression and pumping from the ground to the reservoir and are therefore best described as lower bounds on the energy costs associated with CCS. For context, the 2010 DOE CCS Roadmap estimated that retrofitting the existing coal fired US fleet with existing technologies would increase electricity production costs by $> 300\%$ and add additional costs comparable to about 80 % of the cost of residential electricity or 150 % the cost of industrial electricity (2017 prices [4]). [9] Also, it is worth noting that there are two accepted definitions of the energy penalty. The one discussed here is the fraction of available fuel that would be required to power a CCS process. These energy penalties hold fuel consumption constant during the calculations. If instead, one holds power output constant, the values in the table change to 18%, 20%, 31%, and 47%. These energy penalties represent an estimate of the *additional* fuel needed to maintain power output and perform CCS. It is also worth noting that $\approx 5\%$ more power was produced in the US in 2017 from natural gas than from coal. These power plants are (on average) newer, and their efficiencies are (on average) higher ($\eta_{pp} = 0.445$). [4] Furthermore, natural gas combustion emits $\approx$ 45 % less CO_2 per unit of primary energy. Both of these factors reduce the limiting energy penalties for the natural gas powered plants, and so a CCS retrofit of these plants would be less expensive than retrofitting the PC fleet.

Scenario	η_c	η_{sep}	η_{com}	Energy Penalty
Absolute minimum	0.3	1	1	6.8 %
Optimistic Goal 1	0.3	0.85	0.95	7.6 %
Optimistic Goal 2	0.2	0.75	0.8	11.1 %
Probable technology 2018	0.2	0.5	0.66	15.4 %

Table 2.2: Energy penalty scenarios for retrofitting CCS to US fleet of natural gas fueled power plants under a variety of processing efficiency assumptions from "perfect" reversible engineering (7 %) to a more realizable yet still optimistic case (15 %). The optimistic case still requires $\approx$ 1 out of 7 units of fuel/power to be devoted to CCS.

Assumptions

- The average US coal power plant has a thermal efficiency of 0.32 and is incapable of further heat integration.
- The flue gas has 10 mole % CO_2 and the rest can be considered N_2.
- The carbon capture step will capture 90 mole % of the CO_2 in the flue gas and concentrate it to 95 mole %.
- The pressurized CO_2 is pumped underground at 25 ^{o}C.
- The free energy changes of separation and of compression are calculated as if they occur at a constant 130 and 25 ^{o}C, respectively.[2]

2.3.2 Carbon Capture and Sequestration from Air

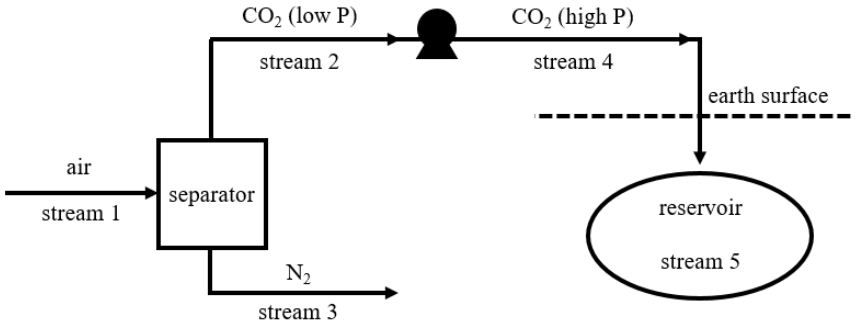

Figure 2.2: A carbon capture and sequestration from air (CCSA) process captures CO_2 from ambient air (stream 1), compresses the CO_2, and pumps the concentrated, compressed CO_2 (stream 4) to) a geologic reservoir below ground. The primary state changes involved include speparation (stream 1 goes to streams 2 and 3), compression (stream 2 goes to stream 4) and pumping to the reservoir (stream 4 goes to stream 5)

[2]Flue gases are often used to pre-heat the air headed to combustion. This step cools the flue gas to 120-150 ^{o}C, and since costs associated with further cooling would need to be included in any calculation, we assume this "cool" stream is fed to the CCS system at 130 ^{o}C.

As illustrated in Figure 2.2, two simple changes to the calculations presented in section 2.3.1 allow one to calculate the free energy change necessary to remove CO_2 from air. First, the CO_2 mole fraction in state 1 should be changed from $y_{1,CO_2} = 0.10$ to $y_{1,CO_2} = 0.0004$ (i.e., 400 ppm). Second, focusing attention on a single capture plant, one assumes that the capture rate is some value $\delta << 0.9$ such that the ambient CO_2 concentration in state 3 is essentially unperturbed because the capture rate is necessarily small relative to the size of the ambient reservoir. Therefore, the relevant free energy change is the change that occurs in the limit $\delta \to 0$. In this limit, the change in free energy per mole of CO_2 removed from ambient air is 16 KJ/mole of CO_2, which is a little less than double the free energy change of separation associated with traditional CCS from point sources. The other free energy consuming processes are identical. For the efficiencies in the CCS section ($\eta_c = 0.3, \eta_{sep} = 1.0, \eta_{com} = 1.0, \eta_{pp} = 0.32$), this process would require 97 KJ/mole CO_2 sequestered (16/.3+14/.32=97). To make a more direct comparison to the energy penalties in Table 2.1, the "Absolute minimum" scenario (i.e., $\eta_{pp} = 0.32$, $\eta_{car} = 0.3$, $\eta_{sep} = 1$, and $\eta_{com} = 1$) is 20.0 %, and the "Probable technology 2018" estimate (i.e., $\eta_{pp} = 0.32$, $\eta_{car} = 0.2$, $\eta_{sep} = 0.5$, and $\eta_{com} = 0.66$) is 46.6 % of fuel consumed (25 and 87 % additional fuel necessary).

To facilitate comparison with the DOE report that estimated a 80-150 % price increase upon CCS retrofitting (and a >300 % increase in cost of production), one can heuristically generate a cost estimate of air capture and sequestration from a Sherwood plot. A 2011 *PNAS* paper looked at traditional Sherwood plots and separation efficiencies for other dilute acid gas separations. [13] The authors noticed that acid gas separations tend to be cheaper than the classic Sherwood plot suggests, so they generated a Sherwood plot for acid gas absorption specifically. Using this new tool, they estimated that air capture and sequestration should have costs on the order of $1000 per ton of CO_2 sequestered. The 2017 average US cost of residential elctricity (0.129 $/kWh) and the 2017 US PC

power plant fleet efficiency ($\eta_{pp} = 0.32$) implies that a ton of CO_2 is generated from about 128 dollars worth of residential PC power in the US. [4] Therefore, if the burden of funding air capture was distributed on a power used basis, the effective cost of residential power would likely increase by a factor of 7.8.[4] Regardless of the specific cost estimate, air capture should be expected to be more expensive than traditional CCS since the component processes are similar, but the free energy change that must be overcome is larger. The same DOE report that estimated PC retrofit levelized cost increases projected that greenfield integrated gasification combined cycle plants with CCS could be built with levelized costs of electricity of only 0.15 \$/kWh. Costs and prices shouldn't be directly compared because of taxes and allowances for mark-ups and profits. Still, electricity could be sold for 4 or 5 times the cost of production from a new IGCC+CCS plant and still be cheaper than a reaslistic estimate of the cost of air capture. In the context of these quick back of the envelope estimates, it seems likely that the sunk cost capital investment in the PC infrastructure might be abandoned before a 7.8 $\times$ increase in power prices were realistically considered.

Assumptions

- The average US coal fired power plant has a thermal efficiency of 32% and is incapable of further heat integration.
- The air has 400 ppm CO_2 and the rest is considered N_2
- The carbon capture step will capture a fraction ($\delta \approx 0\%$) of the CO_2 in ambient air and concentrate it to 90 mole %.
- The free energy changes of separation and of compression are calculated as if they

[4]The average price of industrial power was 46.4% lower, implying that air capture might raise industrial electricity costs by a factor of 14.6

occur at a constant 25 ^{o}C.

2.3.3 Carbon Capture and Utilization as Structural Materials

Carbon capture and utilization as structural materials (CCUSM) involves converting point source CO_2 emissions to carbonate solids that can be utilized as structural materials (e.g., amorphous calcium carbonate, vaterite, etc.). For the purposes of this chapter CCUSM involves the three primary state changes shown schematically in Figure 2.3. The relevant material streams and state changes are summarized below:

- Stream 1 (brine solution) and stream 2 (flue gas) are fed to the process in which reaction and separation occur.
- Stream 3 exits the process as a gas stream that contains mostly N_2 with a small amount of uncaptured CO_2.
- Stream 4 exits the process as a Ca^{2+} depleted, acidic, brine stream.
- Stream 5 exits the process as a Ca^{2+} depleted, pH neutral, brine stream.
- Stream 6 exits the process as solid $CaCO_3$.
- Stream 5 is pressurized to stream 7.
- Stream 7 is pumped into a geologic reservoir, storing the acid waste stream in stream/state 8.

The overall reaction chemistry for a CCUSM process is given in Equation 2.8 (See Chapter 1, Appendix 4.A, and Chapter 5 for a more detailed description of the overall process and chemistry.)

$$CaCl_{2(aq)} + CO_{2(g)} + H_2O_{(l)} \rightleftharpoons CaCO_{3,(s)} + 2HCl_{(aq)} \qquad \Delta g^{o}_{rxn} = 56 \text{ KJ/mole} \qquad (2.8)$$

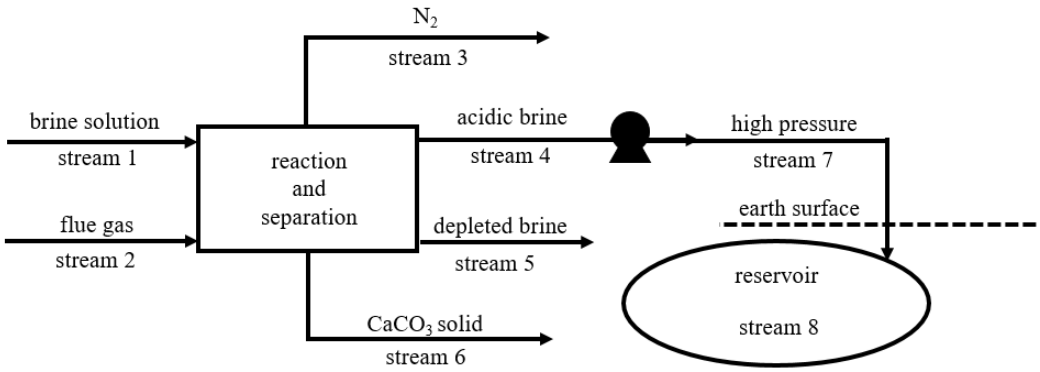

Figure 2.3: A CCUSM process converts a flue gas and a $Ca^{2+}_{(aq)}$ rich brine solution into solid carbonates to utilize as structural materials. The primary state change is the reactive absorption and precipitation of $CaCO_{3(s)}$.. When an alkaline source is not available, the process generates waste acid, which must then be disposed of (likely be pumping to a geologic reservoir, similar to CCS). More details on the CCUSM process and the chemistry are available in Chapter 1, Appendix 4.A, and Chapter 5.

The free energy change of separation calculated from Equation 2.3 varies depending on the concentrations chosen for states 1, 4, and 5. For many reasonable choices, the free energy change of separation varies between 1 and -1 KJ/mole of CO_2 captured. For the concentrations listed in the assumptions below, the total free energy change of mixing/separation is 0.8 KJ/ mole.

The free energy change of associated with pressurizing stream 4 calculated from Equation 2.1 and of pumping calculated from Equation 2.4 totals 6.1 KJ/mole of CO_2 captured. Therefore the total free energy change per mole of CO_2 sequestered is 62.9 KJ/mole.

Relating the free energy change to the required energy input

The same compression and pumping efficiencies apply to this process that applied to CCS.

$$E_{4,8} = \frac{6.1}{\eta_{pp}\eta_{com}} \tag{2.9}$$

The free energy change of reaction is the minimum energy needed to power the reaction. η_{rxn} is defined as the ratio of the minimum energy required for reaction and separation divided by the total primary energy required to power these coupled processes in a real process. Therefore, the total primary energy required per mole of CO_2 captured is

$$E_{CCUSM} = \frac{6.1}{\eta_{pp}\eta_{com}} + \frac{56 + 0.8}{\eta_{rxn}} \tag{2.10}$$

One of the benefits of CCUSM is the indirect emissions reduction associated with traditional cement production displacement. For every Kg of traditional cement produced, $\approx$ 0.9 Kg of CO_2 is emitted. [14] Therefore, if a CCUSM process produced solids that displace traditional cement on a Kg for Kg basis, then 1.9 moles of CO_2 would be avoided by the CCUSM system for each mole of CO_2 captured and utilized in the CCUSM process.[5] Therefore, the free energy change that must be overcome per mole of CO_2 emissions avoided could be as little as 1/1.9 times the free energy per mole of CO_2 captured from the flue gas. If one defines f_{cement} as the amount of CO_2 emissions avoided per unit of CO_2 captured, then the energy penalty for CCUSM can be written as

$$EP_{CCUSM} = \left(\frac{6.1}{\eta_{pp}\eta_{com}} + \frac{56 + 0.8}{\eta_{rxn}\eta_{car}}\right)/486/f_{\text{cement}} \tag{2.11}$$

where f_{cement} varies from 1 to 1.9 depending on the amount of conventional cement emissions avoided per unit of CO_2 utilized. If the CO_2 is captured and utilized as cement and if the pumping is powered with electricity from a plant with the US coal fired power plant average thermal efficiency of 0.32, then the limiting energy penalty per mole of CO_2 emissions avoided is (56.8+6.1/.32)/1.9/486=0.082 which corresponds to a minimum

[5]This estimate is probably a bit generous because some CO_2 is likely absorbed into the traditional cement that may not be absorbed into a CO_2 cement. Counting the maximum possible credit here is consistent with the search for an upper bound best-case scenario limit.

energetic cost of CCU of 39.9 KJ/mole of CO_2 emissions avoided. The energetic cost is up to 1.9 times higher if the credit is not applicable from the cement industry (i.e., $EP_{CCUSM} \approx 0.156$).

Of course, a real process will require more than the minimum thermodynamicly required 56 KJ/mole of reaction to drive the endergonic reaction. Still, these energetic comparisons are favorable to CCS and imply that a best case scenario outcome for CCUSM is comparable to or perhaps better than a best case scenario for CCS. Also, if the produced carbonates are utilized as structural materials, some economic credit may make the comparison even more favorable to CCUSM.

Assumptions

- The concentration of $CaCl_2$ in the brine solution in state 1 is 0.5 molar.
- The flue gas contains 10 % CO_2, 90 % of which is captured by the process.
- All nitrogen gas that enters in stream 2 leaves in state 3.
- There are 55 moles of brine solution in stream 1 ($\approx$ 1 Liter) for each mole of flue gas entering in stream 2.
- The generated HCl can be concentrated into stream 5 such that stream 4 has a pH of $\approx$ 7.
- Stream 5 is concentrated such that only 3.3 % of the moles that entered in stream 1 leave in stream 5 (arbitrary choice that somewhat affects the result +/- several KJ/mole).

Key takeaways from section 2.3

- Retrofitting CCS to the coal-fired US power generation fleet requires an absolute minimum energy penalty of 15.1 %. A more realistic estimate to aim for is 32 %. The DOE recently estimated that the levelized cost of producing electricity would increase by $\approx$ 300 % if currently available technologies were implemented.

- The thermodynamic minimum energy penalty associated with capture from air (relative to power produced from an average US coal fired power plant) is at least 30 % higher than CCS from point sources. Sherwood plot based empirical correlations suggest the cost difference is likely to be greater than the % difference in free energy barrier because the optimal trade-off of increasing capital vs operating costs has historically tended towards intentional design of less thermally efficient processes as feed concentrations decrease. If an air capture process is utilized to render US coal power carbon neutral, the cost of electricity would likely rise by a factor of $\approx 7-8$. [13, 15]

- Carbon capture and utilization as structural materials compares favorably to point source CCS on a best case scenario energy penalty basis (15.8 % vs 15.1 %). If a credit is allowed for the emissions avoided from displacing traditional cement manufacture, then the limiting energy penalty is reduced from 15.8 % to 8.3 %. Any economic value associated with the produced solids may also serve to increase the relative attractiveness of CCUSM. Furthermore, CCUSM is thermodynamically spontaneous if waste alkalinity is available for utilization by the process.

2.4 The Hydrogen Economy

Hydrogen combusts in oxygen to release 286/KJ of heat/mole of hydrogen (Δh_{comb}). Alternatively, the same reaction can generate up to 237 KJ of electricity/mole of hydrogen when utilized in a fuel cell. Regardless of the mechanism of fuel consumption (i.e., in a combustion engine or in a fuel cell), Reaction 2.12 is inherently CO_2 emission free.

$$H_2 + \frac{1}{2}O_2 \leftrightharpoons H_2O \qquad \Delta g^{o}_{rxn} = -237 \text{ KJ/mole} \quad \Delta h^{o}_{rxn} = -286 \text{ KJ/mole} \tag{2.12}$$

The hydrogen economy is the name typically bestowed upon the group of technologies that seek to utilize these two properties of hydrogen to reduce total anthropogenic carbon emissions. The most common industrial process for producing hydrogen is steam reforming of methane (SMR, discussed in section 2.4.1), and so the price of industrial hydrogen has historically correlated to natural gas prices. When natural gas can be purchased for 3 \$/MMBTU (2.84\$/GJ), hydrogen can be produced by SMR for 1.1 \$/Kg (7.75 \$/GJ). [16] Pressurization is neccessary for transportation and consumption, so the cost of hydrogen generated off site must be adjusted higher to account for the compression costs (adding an additional $\approx$ 29 \$/GJ for a total production cost of 37 \$/GJ). [17, 18] The high price relative to gasoline ($\approx$ 16.8 \$/GJ in US in 2017)[6] explains why most hydrogen produced from SMR is utilized as a chemical intermediate instead of as a fuel. [4]

Pressurization and transportation make hydrogen a relatively expensive energy source, but hydrogen does have several advantageous properties that might make the cost difference tolerable. For one, hydrogen can be converted to electricity in a fuel cell, and fuel cell efficiencies are not limited by the same carnot efficiencies that limit combustion engines. Therefore, the gap in price per heat of combustion may be larger than the gap in price per work extracted for some applications. Second, carbon emissions associated

[6] Taxes have been subtracted from these prices to facilitate comparisons.

with utilization of hydrogen as a transportation fuel are concentrated at the plant that generated the hydrogen, whereas the emissions associated with fossil fuel combustion are distributed. Therefore, it is likely cheaper to de-carbonize a hydrogen fuel than a fossil fuel. For example, SMR plants could be retrofitted with CCS relatively cheaply since hydrogen is usually sold at high purity from conventional SMR plants. Compressing and sequestering the already separated CO_2 stream would render hydrogen transportation fuels emission neutral (SMR+CCS). Furthermore, it is even possible that hydrogen production from methane could become cheaper with process innovation, or that some new process that produces hydrogen without emitting CO_2 could be cheaper once an economic penalty is applied to conventional fossil fuels due to the dispersed, difficult to capture, emissions at tailpipes (Methane Pyrolysis, MP). Each of these situation are considered and contrasted in this section.

2.4.1 Steam Methane Reforming with CCS

Industrial hydrogen is typically produced from natural gas via steam methane reforming (SMR) followed by the water-gas shift reaction. The combined chemical reaction is

$$CH_{4(g)} + 2H_2O_{(l)} \leftrightharpoons CO_{2(g)} + 4H_{2(g)} \qquad \Delta g^{o}_{rxn} = 131 \text{ KJ/mole} \quad \Delta h^{o}_{rxn} = 253 \text{ KJ/mole} \tag{2.13}$$

For SMR to be carbon emission neutral, the produced CO_2 must be capture and sequestered. An SMR+CCS process is shown schematically in Figure 2.4 The relevant material streams and state changes are summarized below:

- Stream 1 (water) and stream 2 (methane) are fed to the process that includes generation of steam, SMR, water-gas shift, and separation of the effluent gases.
- Stream 3 exits the process as a gas stream that contains mostly H_2 with a small

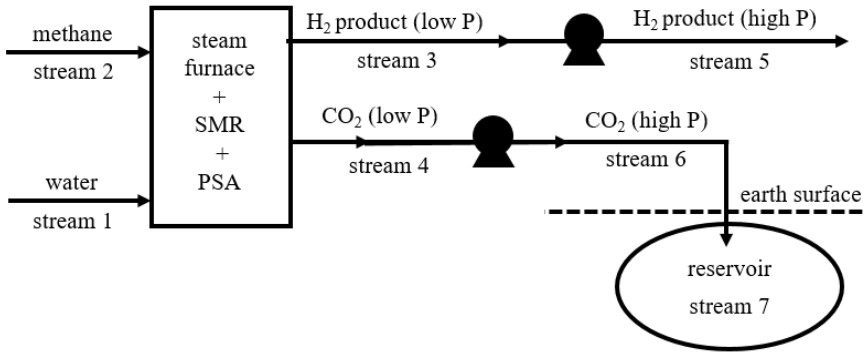

Figure 2.4: Steam methane reforming takes methane and water as inputs and generates CO_2 and H_2 gas. SMR +CCS requires the additional step of compressing the CO_2 stream and pumping it to a reservoir. With or without CCS, the H_2 product must be compressed before it can be transported.

amount of uncaptured CO_2.

- Stream 4 exits the process as a gas stream that contains mostly CO_2 with a small amount of H_2.
- Stream 5 is a compressed version of stream 3, ready for pipeline.
- Stream 6 is a compressed version of stream 4, ready for pumping to the reservoir.
- Stream 7 contains the same material as stream 6, but placed in a reservoir.

The enthalpy of reaction at standard conditions (ΔH_{rxn}) is 253 KJ/mole. Natural gas is typically received from and hydrogen is typically delivered to pipelines at elevated pressures. Here, it is assumed that these pressures are both 735 psia (50 atm). Negligible errors are introduced by assuming both streams follow the ideal gas law, and so Equation 2.3 gives the free energy change associated with expansion of the natural gas to standard conditions, and compression of the hydrogen to pipeline pressure. The free energy costs of this expansion and compression per mole of reaction are -9.7 and 38.8 KJ/mole of reaction, respectively. The cost is higher than the credit, primarily due to more moles of hydrogen being produced than moles of methane consumed. The net free energy

change associated with the mixing across the reactor is -1.3 KJ/mole and the minimum work required for separation of the CO_2 from the hydrogen product is 8.3 KJ/mole of reaction (From Equation 2.3). So the absolute minimum energetic cost of the SMR process (without CCS) is 253-9.7+38.8-1.3+8.3=289.1 KJ/mole of reaction. The actual energy required to drive the transformation is

$$E_{SMR} = \frac{253 - 9.7 + 38.8 - 1.3}{\eta_{rxn}} + \frac{8.3}{\eta_{sep}\eta_{car}} \tag{2.14}$$

Assuming optimistic numbers for the limiting efficiencies ($\eta_{rxn} = 1$, $\eta_{car}\eta_{sep} = 0.3$), the total energy required becomes 308.5 KJ/mole of reaction. This energy could be provided via the combustion of additional methane or by the combustion of product hydrogen. Either way, the net effect is that only $\approx$ 3 moles of hydrogen gas can be produced per mole of methane consumed. This represents a limiting energy penalty of ≈ 0.064, calculated from Equation 2.15.

$$EP_{SMR} = 1 - \left(4\Delta h_{c,H_2} + E_{SMR}\right)/\Delta h_{c,CH_4} \tag{2.15}$$

where $\Delta h_{c,i}$ denotes the enthalpy of combustion of component i. SMR can be made carbon emission free by adding a compression and sequestration step to the end of the process, similar to CCS. In this case, the compression and pumping steps are identical to the compression and pumping steps in the CCS section, and so the associated free energy changes associated are also identical. Therefore, SMR+CCS requires an additional free energy change of 14 KJ/mole of reaction. The primary energy required to drive the overall process is given by Equation 2.16

$$E_{SMR+CCS} = E_{SMR} + \frac{14}{\eta_{pp}\eta_{com}} \tag{2.16}$$

For optimistic estimates of newly installed power plant and compressor efficiencies (η_{pp} η_{com} =0.7), the limiting energetic cost for SMR+CCS is 328.5 KJ/mole of reaction. This number assumes that hydrogen is combusted to provide the energy of reaction and separation. In the limit of perfect reversible engineering, SMR+CCS can be utilized to convert a mole of methane into 2.85 moles of carbon free hydrogen. This represents a limiting energy penalty of ≈ 0.086, calculated from Equation 2.17.

$$EP_{SMR+CCS} = 1 - \left(4\Delta h_{c,H_2} + E_{SMR+CCS}\right)/\Delta h_{c,CH_4} \tag{2.17}$$

In practice, hydrogen from SMR (without CCS) usually costs 2-3 times as much as the feed methane on a \$/ energy basis, and so one can deduce that the capital costs, operating costs, and the process efficiencies (e.g., η_{rxn},η_{sep}, etc.) add significant additional costs above the thermodynamically required energy losses.

Assumptions

- Methane is received at 50 atm and hydrogen is delivered at 50 atm.
- The effluent of the SMR process is a 1:4 CO_2 to H_2 mixture, reflecting a stoichiometric feed composition and full conversion.
- Hydrogen purity of 99.95 % in outlet stream (Praxair compressed H_2 spec).
- The free energy change of separation is calculated as if it occurs at a constant 130 ^{o}C.

2.4.2 Methane Pyrolysis

The term methane pyrolysis is used here to encompass the class of processes that generate hydrogen from methane without emitting CO_2 via the chemical transformation

$$CH_{4(g)} \leftrightharpoons C_s + 2H_{2(g)} \qquad \Delta g^{o}_{rxn} = 51 \text{ KJ/mole} \quad \Delta h^{o}_{rxn} = 75/\text{KJ/mole} \tag{2.18}$$

Historically, methane pyrolysis (MP) processes have emitted CO_2 because they required periodic de-coking of the reactor wall and catalyst particles. If methane pyrolysis is instead implemented in a manner such that de-coking is not required, then the process becomes inherently CO_2 emission neutral because no oxygen is ever introduced into the process. Recent studies have renewed interest in methane pyrolysis from molten metals and salts. [19,20] When pyrolysis is carried out in a molten solvent, the carbon precipitates as it forms and disengages from the gas. It may be possible to mechanically remove the suspended carbon after it rises to the top of the molten metal reactor due to buoyancy. The process is represented schematically in Figure 2.5. The relevant material streams

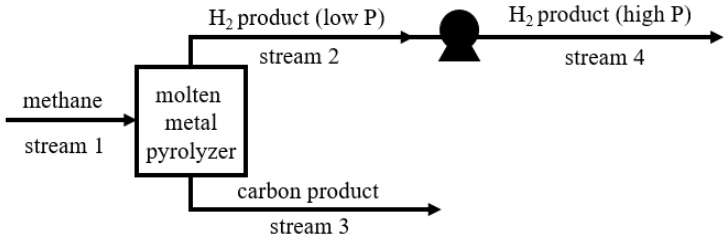

Figure 2.5: Methane pyrolysis converts methane into hydrogen and solid carbon. The hydrogen must be compressed prior to transportation.

and state changes are summarized below:

- Stream 1 (methane) is fed to the molten metal pyrolyzer.
- Stream 2 exits the reactor as low pressure hydrogen.

- Stream 3 leaves the reactor as solid carbon .
- Stream 4 is identical to stream 2, except the pressure has been upgraded for pipeline distribution.

Reaction 2.18 has a free energy change of reaction of 74.9 KJ/mole of reaction at standard conditions. Natural gas is typically received from and hydrogen is typically delivered to pipelines at elevated pressures. Here, it is assumed that these pressures are both 50 atm. Similar to the SMR+CCS discussion above, negligble errors are introduced by assuming that both methane and hydrogen gases follow the ideal gas law at these pressures, so Equation 2.3 gives the Gibbs free energy change associated with expansion of the natural gas to standard conditions, and compression of the hydrogen to pipeline pressure. The free energy costs per mole of reaction are -8.9 and 17.8 KJ/mole of reaction, respectively. For this process, no adjustment is necessary for the mixing terms because both reactant and product streams are essentially pure. Therefore, the total free energy change of the MP process is 74.9-8.9+17.8=83.8 KJ/mole of reaction.

$$E_{MP} = \frac{83.8}{\eta_{rxn}} \tag{2.19}$$

This expression could be further refined if the reactor pressure were specified and therefore compressor duties were more clearly defined. The above expression assumes that the inlet and outlet pressure are equal and no additional compression or expansion is required. The thermodynamic minimum energy cost of a mole of reaction of MP is lower than the limiting value for SMR+CCS (83.8 vs 328.5 KJ/mole of reaction), but MP only produces 2 moles of hydrogen per mole of reaction while SMR produces 4. The difference in energy is trapped in the carbon-carbon bonds for MP, and this relatively high energy "waste" product leads to significantly higher energy penalties. The thermodynamic

limiting energy penalty across a MP process is calculated using equation 2.20.

$$EP_{MP} = 1 - \left(2\Delta h_{c,H_2} + E_{MP}\right)/\Delta h_{c,CH_4} \tag{2.20}$$

If $\eta_{rxn} = 1$, EP_{MP}=0.45. Most of the "lost" energy is trapped in the carbon-carbon bonds within the solid carbon this process co-produces. In fact, if one could swap the carbon for methane on an equivalent energy basis, the energy penalty would drop to 0.017. The relative attractiveness of MP to SMR and SMR+CCS likely depends on the efficiencies of both processes (i.e., η_{rxn}, η_{sep}, etc.), the value of the solid carbon produced, and the cost of the methane feed.

Assumptions

- Natural gas is received at 50 atm and hydrogen is delivered at 50 atm.
- The effluent of the methane pyrolyzer is primarily hydrogen and no further separation is necessary.

Key takeaways

- SMR+CCS has a limiting energy penalty of 0.083.
- MP has a limiting energy penalty of 0.45 if the solid carbon is a waste product.
- Even though MP has a significantly higher limiting energy penalty, it is not obvious that hydrogen produced by MP would be more *expensive* than hydrogen produced by SMR. The relative costs depend on the specific processes that carry our either chemistry, the value of the solid carbon produced, and the availability/cost of wells for placement of pressurized CO_2.

- It was recently estimated that a new SMR facility might have a cost of production of $\approx$ 1.1\$/kg which translates to 7.7 \$/GJ. With a 24 % energy penalty, a "perfect" MP process might produce hydrogen at 3.2/(1-0.24)=4.2 \$/GJ.[7] This implies that it is at least possible that a process with significantly reduced non-fuel costs with respect to SMR might be able to compete on price even without an economic credit for the solid carbon.

2.5 Conclusions

There are many possible technologies society could implement in an attempt to reduce the anthropogenic emissions generated during energy production and consumption. Here, simple energy balances and thermodynamic minimum work calculations have been utilized to compare and contrast several of the possible choices. The results are summarized in Table 2.3. For each technology in the left column, the absolute thermodynamic minimum energy penalty is calculated for retrofitting/coordination with the US coal fired power fleet (middle column). The right column includes a more "realistic" or realizable estimate of the energy penalty that takes into account estimated energy conversion efficiencies. Several concluding observations and implications are included below.

- Retrofitting CCS to the existing fleet of power plants is likely to increase production costs by at least 50 % based on energy costs alone.

- Direct air capture is very likely to be much more expensive than CCS. It could not be reasonably considered unless point source emissions were already "fixed."

[7] 3.2 \$/GJ was the average cost of methane in the US in 2017 and the 1.1 \$/kg came from Parkinson et. al. [4,16]

Process	Absolute Minimum EP	"Realistic" η_j EP
CCS	15.2 %	32.2 %
CCSA	20.0 %	46.6 %
CCUSM	8.2 %	9.3 %
SMR+CCS	11.2 %	20.0 %
MP	45.0 %	45.0 %

Table 2.3: Absolute thermodynamic minimum and "realistic" (efficiency-adjusted) assessments of the energy penalties (EP) associated with each of the sustainable energy technologies discussed here. For energy penalties in the table, the average US coal fired power plant efficiency and the EPA coal emissions factor were used ($\eta_{pp} = 0.324$, 486 KJ/mole of CO_2). For the absolute minimum energy column, all efficiencies were set to $\eta_j = 1$ except for $\eta_{pp} = 0.32$ and $\eta_{car} = 0.3$ For the "realistic" estimates, all efficiencies were set to $\eta_{car} = 0.2$, $\eta_{sep} = 0.5$, $\eta_{com} = 0.66$, $\eta_{rxn} = 1$. It is assumed in both CCUSM columns that f_{cement}=1.9.

- The relatively undeveloped CCUSM technology requires less energy input than point source CCS, but it is not clear without further research if anything close to $\eta_{rxn} = 1$ could be achieved.

- SMR+CCS has a lower thermodynamic minimum energetic cost than MP (8 % vs 45 %).

- Therefore, the solids a MP process produces likely need to be profitably sold for MP hydrogen to be compete economically with SMR or even SMR+CCS.

Appendices

2.A Gibbs free energy change of several common state changes

The Gibbs free energy is the thermodynamic potential that is minimized at equilibrium under constant temperature and pressure conditions. The total Gibbs free energy

of a stream containing the molar flows, F_i, is given by Equation 2.21.

$$G = \sum_{i=1}^{c} F_i \mu_i \tag{2.21}$$

where c is the number of unique molecular components in the mixture stream and μ_i is the chemical potential of component i. The gas-phase chemical potential of component i (μ_i) can be written as a function of the temperature, pressure, and composition as shown below in Equation 2.22

$$\mu_i(T, P, y_i) = \mu_i^o(T) + RT \ln \frac{f_i}{P_s} \tag{2.22}$$

where $\mu_i^o(T)$, the standard chemical potential, signifies the chemical potential of a pure component i at the reference pressure (P_s) as a function of temperature (T) and f_i is the component i fugacity. The temperature dependence of μ_i^o can be written in terms of the constant pressure heat capacity and the standard chemical potential at the standard temperature:

$$\mu_i^o(T) = \mu_i^o(T_s) + \int_{T_s}^{T} C_{p,i} dT - T \int_{T_s}^{T} \frac{C_{p,i}}{T} dT \tag{2.23}$$

where $\mu_i^o(T_s)$ is the standard chemical potential at the standard state, T_s is the standard state reference temperature, P_s is the standard state reference pressure, and $C_{p,i}$ is the constant pressure heat capacity of component i. The Gibbs free energy is a state function, so changes in free energy per mole of gas associated with reversible changes in the temperature or pressure can be can be calculated from equations 2.22-2.23. For the calculations presented here, minimal errors are typically introduced by assuming an ideal gas equation of state, in which case the fugacity can be replaced with the partial pressure P_i.

The liquid phase chemical potential is similarly defined except the fugacity is replaced by the activity, and the standard chemical potential ($\mu_i^o(T)$) is replaced by the pure component chemical potential ($\mu^*(T,P)$)

$$\mu_i(T,P,x_i) = \mu_i^*(T,P) + RT\ln a_i \tag{2.24}$$

For an ideal solution, the activity is equal to the mole fraction such that $\mu_i = \mu_i^* + RT\ln x_i$.

Change in Free Energy Due to Compression/Expansion

Consider a single component fluid stream (gas, liquid, or supercritical fluid) at a temperature (T) and pressure (P_1) named stream 1. Now consider an arbitrary process that converts stream 1 to stream 2, in which the material stream pressure has been reversibly altered to P_2. The reversible work of compression per mole of mixture is given in Equation 2.25.

$$\frac{G_2 - G_1}{F} = \mu_2 - \mu_1 = \int_{\hat{v}_1}^{\hat{v}_2} P(T,\hat{v},\mathbf{y})d\hat{v} \tag{2.25}$$

where F is the molar flow rate into the compression process. If the ideal gas law applies across the entire compression/expansion, and if the compression is done isothermally, then Equation 2.25 becomes

$$\frac{G_2 - G_1}{F} = \mu_2 - \mu_1 = RT\ln\frac{P_2}{P_1} \tag{2.26}$$

This is identical to the result one would calculate from Equation 2.22 with $f_i = P_i$.

Change in Free Energy Due to Separation

Consider a fluid stream made up of c components at a temperature (T), and a pressure (P) named state 1. Now consider an arbitrary process that takes state 1 and converts it into two streams at the same temperature and pressure but with new molar compositions named state 2 and state 3. See Figure 2.6 for a schematic depiction of this reversible, isothermal, isobaric separation. The change in total free energy due to this state change

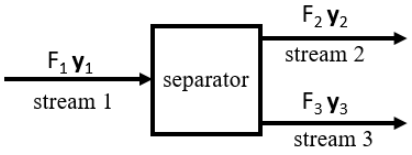

Figure 2.6: Schematic representation of a separation process that takes stream 1 with composition $\boldsymbol{y}_1$ and converts it to streams 2 and 3 with new compositions $\boldsymbol{y}_2$ and $\boldsymbol{y}_3$.

(free energy of separation) is $G_3 + G_2 - G_1$. The total Gibbs free energy of an ideal gas mixture stream named stream k can be written in terms of the component chemical potentials

$$G_k = \sum_i F_{k,i}\mu_i = F_{k,T}\sum_i y_i\mu_i \tag{2.27}$$

where $F_{k,i}$ signifies the molar flow of component i at state k and $F_{k,T}$ is the total molar flow in stream k. For both liquids and gases, the temperature and pressure dependent terms cancel out of equation 2.27 ($\mu_i^o(T) + \ln\frac{P}{P_s}$ for gases and $\mu_i^*(T,P)$ for liquids) leaving just the mixing free energies shown in equation 2.29.

$$G_3 + G_2 - G_1 = RT\Bigg[F_{T,3}\sum_i \big[y_{3,i}\ln(y_{3,i})\big] \tag{2.28}$$

$$+F_{T,2}\sum_i \big[y_{2,i}\ln(y_{2,i})\big] - F_{T,1}\sum_i \big[y_{1,i}\ln(y_{1,i})\big]\Bigg] \tag{2.29}$$

where $y_{k,i}$ is the mole fraction of component i at state k. For this unit operation, there are $3c$ molar flows ($F_{k,i}$), where c is the number of total components. c material balances reduce the number of degrees of freedom to $3c - c = 2c$. The free energy change per molar flow of a specific component in a specific stream (e.g., component i_r in stream k_r) is calculated by dividing both sides by that molar flow (F_{k_r,i_r}). This molar free energy has one less degree of freedom (the $2c$ independent $F_{k,i}$ become $2c$-1 independent $F_{k,i}/F_{k_r,i_r}$).

$$\frac{G_3 + G_2 - G_1}{F_{k_r,i_r}} = RT\left[\frac{F_{3,T}}{F_{k_r,i_r}}\sum_i \left[y_{3,i}\ln(y_{3,i})\right]\right. \tag{2.30}$$

$$\left. + \frac{F_{2,T}}{F_{k_r,i_r}}\sum_i \left[y_{2,i}\ln(y_{2,i})\right] - \frac{F_{1,T}}{F_{k_r,i_r}}\sum_i \left[y_{1,i}\ln(y_{1,i})\right]\right] \tag{2.31}$$

A mixing operation is the exact opposite state change, so the associated free energy change is the negative of expression 2.31.

Change in Free Energy During Chemical Reaction

When a single chemical reaction occurs at constant temperature and pressure, the thermodynamic potential that is minimized is the Gibbs free energy, and the reaction equilibrium condition is

$$\sum_i \nu_i \mu_i = 0 \tag{2.32}$$

where ν_i is the stoichiometric coefficient associated with component i defined such that reactant coefficients are negative, product coefficients are positive, and the largest (least negative) reactant coefficient is -1.[8] The chemical potential of each component i (μ_i) is a function of the fluid composition, which is a function of the extent of reaction (ξ) and the feed conditions. The extent of reaction (ξ) that meets the equality in Equation 2.32

[8]the last condition is not required, but for clarity, the convention used here is explicitly stated.

is the equilibrium extent of reaction the system evolves towards.

For the purposes of back of the envelope minimum energy requirement calculations, the relevant quantity is the energetic change associated with a full extent of reaction ($\xi = F_{LR}$, where F_{LR} is the inlet molar flow rate of the limiting reactant). If both reactants and products form an ideal gas, then the free energy change of reaction per molar flow of limiting reactant fed is

$$\frac{G_p - G_r}{F_{LR}} = \sum_i \nu_i \mu_i = \sum_i \nu_i \left[\mu_i^o(T) + RT\ln\frac{P_i}{P_s}\right] \tag{2.33}$$

Typically, the free energy change per mole of reaction due to changes in the intramolecular interactions within the molecular species is named $\Delta g_{rxn}^o(T)$ [21], simplifying Equation 2.33 to

$$\frac{G_p - G_r}{F_{LR}} = \Delta g_{rxn}^o(T) + \sum_i \nu_i RT\ln\frac{P_i}{P_s} \tag{2.34}$$

$\Delta g_{rxn}^o(T_s)$ can be calculated from tabulated values of the reactants and products Gibbs energies of formation at (T_s). At standard state conditions, the pressure terms are zero and all that is left is the mixing terms discussed in Equation 2.31. Since chemical potential is a state function, a simple way to calculate the free energy change of reaction at nonstandard conditions is to imagine a reversible thermodynamic path that takes the reactants from reactor inlet conditions to standard conditions, converts the reactants to products at standard conditions, and then returns the products to reactor outlet conditions. This thermodynamic path will give an identical free energy change to the one calculated from Equation 2.23 and Equation 2.33 directly at the nonstandard conditions.

For some endothermic reactions, Δg_{rxn}^o is smaller than Δh_{rxn}^o. In these cases, Δh_{rxn} is chosen here as the minimum energy required to power the reaction. This choice will now

be justified with energy and entropy balances. [22] First, consider a reversible, constant temperature process in which a stoichiometric mixture of reactants are fed and reacted to completion. Assuming that kinetic and potential energy changes are minimal, the steady-state energy balance for this process is Equation 2.35.

$$F\Delta h_{rxn} = \dot{Q} + \dot{W} \tag{2.35}$$

If the process is reversible, the entropy balance is Equation 2.36.

$$F\Delta s_{rxn} = \frac{\dot{Q}}{T_e} \tag{2.36}$$

Combining these two expressions, one finds that

$$F\big(\Delta h_{rxn} - T_e\Delta s_{rxn}\big) = \dot{W} \tag{2.37}$$

The temperature in Equations 2.36-2.37 (T_e) is the temperature of the heat reservoir from which the heat ($\dot{Q}$) was delivered to the process. For a reversible process, $T_e \approx T_s$, where T_s is the constant temperature of the system. In this case,

$$\Delta h_{rxn} - T_e\Delta s_{rxn} \approx \Delta h_{rxn} - T_s\Delta s_{rxn} = \Delta g_{rxn} \tag{2.38}$$

These balances demonstrate that for any state change with a negative ΔG, ΔG represents the maximum work extractable from that state change. Furthermore, for a state change that generates a positive ΔG, ΔG represents the minimum work required to drive the same state change.

For the case in which an endothermic reaction exhibits $\Delta g_{rxn} > \Delta h_{rxn}$, $\Delta s_{rxn} < 0$. This implies that some heat must be expelled to the environment during the process.

The heat that must be expelled to the environment must first be supplied to the process, and so the minimum work required to power the state change is larger than the enthalpy change of reaction (i.e., $\Delta g_{rxn} > \Delta h_{rxn}$). More work must be input to the process than is reflected in the enthalpy change of the material flowing through the process precisely because some heat must be ejected to the environment. For this class of reactions, the true energetic cost is Δg_{rxn}, even though the product stream enthalpy only increases by Δh_{rxn}.

For the case in which an endothermic reaction exhibits $\Delta h_{rxn} > \Delta g_{rxn}$, $\Delta s_{rxn} > 0$. This implies that some heat must be supplied to the reversible process. For a minimum energy balance calculation, this minimum heat (in excess of the minimum work) must be considered. In other words, if less energy than the enthalpy of reaction is supplied to the process, then the energy balance (Equation 2.35) is violated. Including the entropy balance allows one to notice when the second law of thermodynamics demands a heat ejection to the environment, increasing the total amount of work required to drive the transformation above the change in enthalpy of the material streams entering and leaving the process. But regardless of the entropy balance, the energy balance may not be violated. Regardless of the type of energy supplied, at least the enthalpy of reaction must be supplied (via heat or work) to balance Equation 2.35. For endothermic reactions, choosing the more positive of Δh_{rxn} and Δg_{rxn} implicitly enforces both the first and second laws of thermodynamics.

2.B Definition of thermodynamic efficiencies

Thermal efficiencies are utilized throughout this chapter to mathematically express the relationship between the energy input to a process and the energetic output of the same process. For example, the thermal efficiency of the US coal fired power plant fleet

was $\eta_{pp} = 0.32$ in 2017. This number was calculated by taking the total amount of electricity generated from coal in 2017 (1,207,901 million kWh) and dividing it by the total enthalpy of combustion available within the coal that was consumed for electricity generation (663,479 thousand short tons containing $\approx$ 3,740,002 million kWh of primary energy).. [4, 23][9] Throughout this chapter, efficiencies are used to calcualte the amount of energy required to drive some transformation. The defintion of η_{pp} is given mathematically in equation 2.39.

$$\eta_{pp} = \frac{\text{electric energy output}}{\text{primary energy input}} \tag{2.39}$$

The total primary energy required to produce a given amount of electricity can be equivalently written as Equation 2.40

$$\text{primary energy input} = \frac{\text{electric energy output}}{\eta_{pp}} \tag{2.40}$$

All of the efficiencies are defined and used in this way.

2.C Bio and synthetic carbon to fuels

Both biofuel and CO_2 to fuel technologies are often promoted as emission-free alternatives to fossil fuels for transportation and/or power generation. Simple balances and thought experiments are presented here and used to generate some reasonable expectations for these technologies.

Any process that converts CO_2 to fuel, either synthetically or biologically, can be schematically represented by the diagrams in Figure 2.7 and 2.8. Figure 2.7 is an overall schematic around a process that produces a fuel from a CO_2 source stream and an

[9]Here, the heating value of 9,617 BTU per pound of coal was used for the mass to primary energy conversion. This number was reported for 2016. The 2017 number has not yet been reported, but one expects the 2017 value to be similar to the 2016 value

emissionless energy source, whereas Figure 2.8 is an overall schematic around the total system that first creates the same fuel and then utilizes the fuel for some purpose. The energy source in stream 2 must be emissionless for the process in Figure 2.8 to be emission-neutral. Any energy source can be made emisionless with carbon capture and sequestration or utilization (CCS/CCUSM), but this class of processes is not considered here because these processes are expected to be more costly than simple utilization (combustion) of the energy source in stream 2 for the purposes of the generated fuel in stream 4 and CCS or CCUSM of the CO_2 in stream 1. If the power source at state 2 emits CO_2, then combustion of the fuel available at state 2 for the purpose at state 4 has an identical emissions profile to the process in Figure 2.8 without the capital, energetic, or operating costs associated with the conversion of CO_2 to fuel. If an available hydrocarbon is to be consumed by the system, it is likely cheapest to utilize the fuel for whatever purpose the carbon based fuel is intended at state 4. Any abundant, emissionless energy source

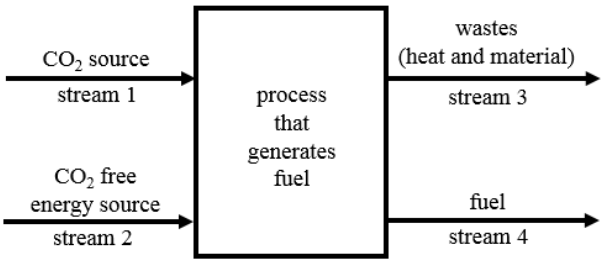

Figure 2.7: A schematic of a process that converts a CO_2 stream and an emissionless energy source to a fuel molecule.

will also be attractive for power and heat generation, implying that the carbon source in state 1 is unlikely to be acquired from a point source associated with power or heat generation. This excludes essentially all of the industrially available point sources, and further implies that a process such as the one outlined in Figure 2.8 must acquire its carbon from either air or from a solid carbon source if the technology is to be deployed at scale.

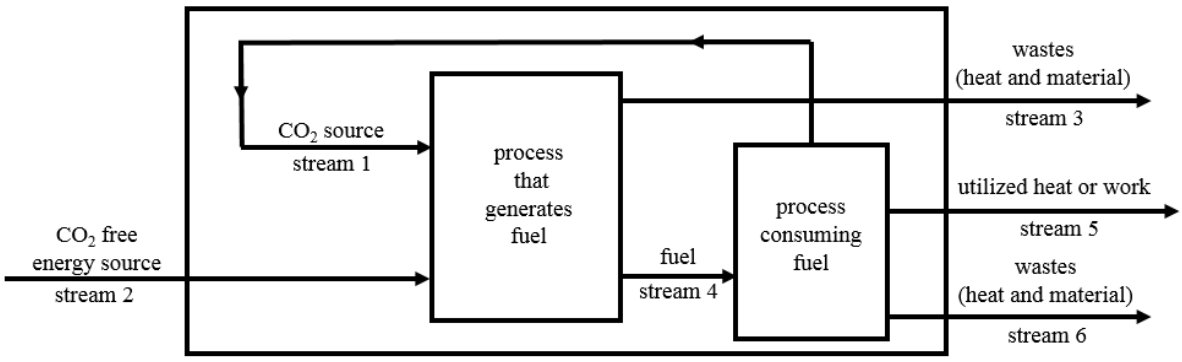

Figure 2.8: A zoomed out picture of the same procses depicted in Figure 2.7 that explicitly includes the conversion of the generated fuel into work, heat, and other wastes.

For any real process, the energy required at state 2 is larger than the energy available in state 4 for two distinct reasons. First, energy is consumed during the separation/pre-processing of CO_2 from the carbon source (state 1). This is true regardless of the carbon source, but first consider the case in which the carbon source is CO_2 in air. The minimum work required to capture the CO_2 (stream 1) is 16 KJ/mole of CO_2.[10] This free energy change can be expressed as an energy penalty with units of KJ of work required to capture/KJ of heat available from the combustion of the product fuel (state 4) by choosing a model fuel compound, multiplying the minimum work required to capture a mole of CO_2 by the number of carbons within the model fuel compound, and then dividing that product by the enthalpy of combustion of the model fuel compound ($\Delta G_{capture} * \nu_{CO_2}/\Delta H_{combustion}$). For example, if one selects ethanol as the model fuel compound,

$$2CO_2 + 3H_2O \leftrightharpoons CH_3CH_2OH + 3O_2 \qquad \Delta H_{rxn} = 1367\ KJ/mol \tag{2.41}$$

the number of moles of CO_2 per mole of ethanol is 2. Therefore, the available heat of combustion at stream 4 per mole of CO_2 is 1367/2=684 KJ/mol. This value is relatively insensitive to choice of reference fuel compound, especially among the medium chain

[10] Calculated from Equation 2.3 as discussed in section 2.3.2).

length hydrocarbons and alcohols. For example, it is 683 KJ/mole for octane and 693 KJ/mole for hexane. Coal and natural gas (486 and 890 KJ/mole) serve as limiting low and high enthalpy values per carbon atom for other carbon-containing fuel compounds. One can further define a separation efficiency to quantify the ratio of the heat available from stream 4 to the total energy input required to drive the change. Altogether, if the separation is "perfect" (η_{sep}=1, $\eta_{car} = 1$), then the fraction of heat of combustion of the fuel at state 4 that must be applied to the separation in state 1 is $16/684 = 0.023$. Any real separation will require a higher fraction of the available energy (e.g., η_{car} ≈0.2-0.3). Furthermore, all carbon-based fuels combust in air to form CO_2. A process that drives the combustion reaction in reverse has an energetic cost of (at least) the heat of reaction. Therefore, the thermodynamic minimum energy requirement for capturing CO_2 from air and then converting the CO_2 to a fuel is $\left(-\Delta h_c/\eta_{rxn}+(16\times 2)/\eta_{car}/\eta_{sep}\right)/(-\Delta h_c)$=107.8 % of the heat that can be released from the the fuel upon eventual combustion (For optimistic estimate of $\eta_{sep} = 1$, $\eta_{car} = 0.3$, $\eta_{rxn} = 1$, $\Delta h_c = -1367$). Any real processes will entail higher energy costs than the minimum required, and so more than 7.8 % of the energy input in stream 2 is unavailable for consumption in stream 4.

Since some energy is lost across the block in Figure 2.8, and since the energy in state 2 has to be emissionless, the fuel generated by this process will be more expensive than the energy source in state 2 with an identical emissions profile. These simple block diagrams imply that a fuel generated from this class of processes cannot compete on a price/energy available or a price/systems-level-emissions-released basis with the energy source at state 2. Therefore, the feasibility of these technologies require that the energy source at state 2 must be incompatible with the end-use application for some reason. Three sets of circumstances are discussed: energy quality or type, energy storage, and transportation fuels.

2.C.1 Energy quality or type

First, there could be a mismatch in energy quality or type. For example, the energy source at state 2 could be a relatively low value energy source such as solar irradiation. Solar irradiation is plentifully available, but it cannot be easily utilized for useful work until it is upgraded to electricity or to energy dense fuel molecules. Synthetic solar to fuel and all biofuel technologies attempt to exploit the natural abundance of this resource in the spirit of Figure 2.8. Discussion of this class of processes is best facilitated by further classification into three distinct groups: waste solar irradiation, waste organic material, and all other sources of organic material and solar irradiation. The distinction becomes clear once one discusses the latter category, and so that category is discussed first.

Biofuels from crops

Consider the situation in which a crop is grown specifically for a bio-fuels application (e.g., corn ethanol in the US). In this case, the energy source cannot be considered emmissionless in the same way that the solar irradiation on a roof or desert may be because the very act of utilizing farmland to grow fuel has indirect effects on other systems that potentially generate/reduce carbon emissions. [24] In fact, more detailed analyses that take into account indirect effects of the process on related systems across the life cycle of the process and these related systems conclude that only *additional* carbon fixation that would not have occured without the biofuels system can count as a carbon emission offset relative to combusting conventinoal fossil fuels. [25] When farm land is allocated to growing fuel, the food production industry may only respond by building new farmland, increasing the yield on existing farmland, or producing less food. New farmland typically displaces grasslands and forests, and so this land use change (LUC) tends to net generate carbon emmissions (natural forests and grasslands are typically larger carbon sinks than

the farmland that replaces them). Alternatively, increases in yield and reductions in total food produced and consumed tend to net reduce carbon emissions. One expects the real response to be some combination of these possible responses, and the net effect on systems level carbon emmisions depends on the relative distribution. Regulators and policy-makers use published global agriculture and land-use models to predict the systems-level impact of shifting the use of farmlands towards biofuels. A recent study analyzed and compared the predicted implications of replacing gasoline with corn based ethanol fuels using 7 of these models. [26] 5 of the models predicted systems level net carbon emission reductions between 4 and 17 %, and the two remaining models predicted net carbon emission *increases* due to extensive land use change. None of the models predicted the ethanol biofuels to be emission neutral. All seven models predict that net carbon emissions associated with corn ethanol combustion are higher than the net emissions from gasoline combustion if one does not accept the proportion of the emission reduction due to reducing overall food consumption. Two important conclusions of this study may be broadly under-appreciated. First, there is not a literature consensus on the net effect of replacing gasoline with ethanol produced from corn. These policies may reduce emissions relative to gasoline combustion by as much as 17 %, or increase emissions by as much as 25 %. Unfortunately, precise quantification is difficult because one has to make substantial qualitative judgments and assumptions to build one of these models. However, all of the models discussed in the referenced study agree that indirect effects cause corn ethanol biofuel processes to net emit carbon, and so these processes are not carbon emission neutral. Second, all of these models predict carbon emission increases if total food production does not decline.

All things considered, Figure 2.8 is not an accurate representation of a corn to biofuels process because it implies that the energy source is emissionless by ignoring the effect of land use change and the impact on the food supply. A more accurate representation is

given in Figure 2.9. When the indirect effects of land use change and food consumption

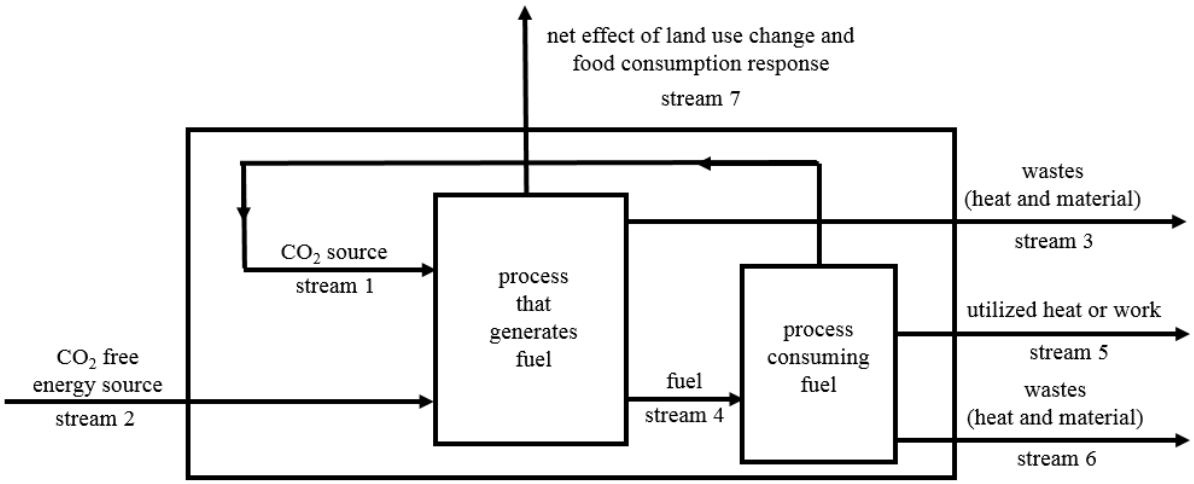

Figure 2.9: When a crop is utilized to produce a biofuel, indirect emissions due to land use change need to be included in the analysis. Stream 7 is added here as an update to Figure 2.8 to explicitly account for these indirect effects.

responses are considered, corn ethanol biofuels are may marginally reduce emissions, but not enough to claim carbon emission neutrality. The situation is fundamentally different if the solar irradiation would be otherwise wasted or if the bio-material that is upgraded to fuel would have eventually respired into the atmosphere anyway. These situations are discussed next.

Waste solar irradiation to fuel

The term "waste solar irradiation" is used here to signify solar irradiation that does not serve as a natural carbon sink. In other words, "waste solar irradiation" is irradiation that might be utilized by a process without significant indirect emissions related to land use change. The most abundant "waste solar irradiation" resources are probably the roofs of homes and businesses and deserts. Devices/plants that can be located/grown on the roofs of buildings or on land that does not otherwise serve as a carbon sink (e.g., a desert) are more accurately described by Figures 2.7 and 2.8. If fuel can be created

from waste irradiation, it will look good on a back of the envelope calculation basis/ free energy balance basis. Ultimately, the feasibility will be determined by the cost of building, installing, and maintaining such a system over its lifetime in relation to other technologies that reduce emissions for similar end-use applications.[11]

biowastes to fuel

Another class of biofuel systems that merits discussion is the class of processes that takes some biological waste and converts it to fuel. For these processes, stream 1 in Figure 2.7 represents some organic bio-waste, and stream 3 may include some carbon emissions associated with collection, production, and transportation of the biofuel from the bio-waste. For these processes, the net effect on emissions is dependent on just two factors, ϕ_r and ϕ_p. ϕ_r is the fraction of the carbon in the bio-waste that would have respired into the atmosphere as CO_2 absent the biofuel process. ϕ_p is the fraction of the carbon in the bio-waste that is released during collection, transportation, and processing into fuel. In other words $(1-\phi_p)$ is the fraction of the carbon in the bio-waste that eventually gets converted into fuel (or permanently sequestered in a more stable carbon waste). If analysis of the life-cycle of the waste bio-material and of the biofuel production process suggests that all of the waste carbon would have eventually respired to the atmosphere as CO_2 ($\phi_r = 1$) and that none of the waste carbon is emitted during collection, transportation, and production of the biofuel ($\phi_p = 0$), then the production/utilization system could be accurately described as net emission neutral. As long as the fraction emitted during collection, transportation, and production is lower than the fraction that would have been emitted "naturally" in the absence of the biofuels process (i.e., $\phi_p < \phi_r$), then the

[11] should I include a back of the envelope estimate of what the cost of the system needs to be for the system to have a price of XX \$/kWh? Prof. McFarland did this in his course by starting at irradiation per m2 and choosing conversion efficiencies etc. Especially assuming free storage, it would be easy to give a $\$/W_{peak}$ estimate.

bio-waste to fuel system reduces emissions relative to burning traditional fossil fuels. ϕ_p and ϕ_r are the pivotal factors that should be prominently featured and discussed in any proposed bio-waste to fuel process scheme.

Alternatively, one might imagine some processing (e.g., bio-charring) of the bio-waste designed to decrease the fraction of the carbon eventually respired and emitted to the atmosphere without producing a fuel. This process could involve producing and burying a biochar, or combusting the bio-waste to generate energy coupled to point source CCS. This class of processes is described by Figure 2.10. Consider that Figure 2.10 is

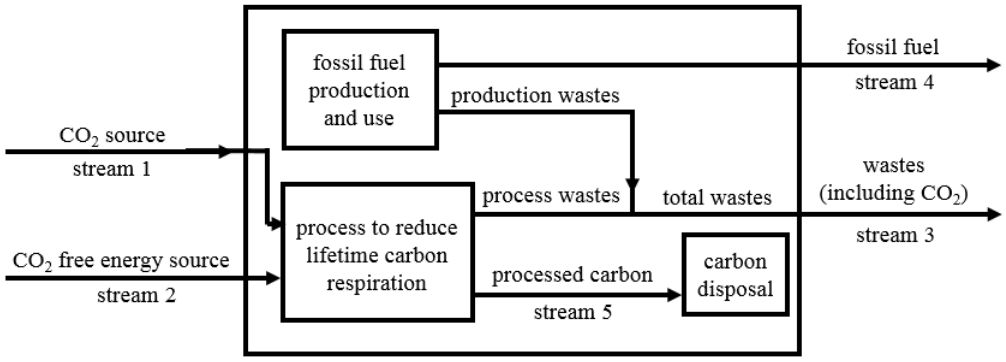

Figure 2.10: A schematic diagram illustrating the similarities between biofuel and biocharr processes. Biochar processes reduce carbon emissions without generating fuels. The process specifics must be known before one can say if a biochar plus fossil fuels or a conventional biofuels process leads to less life cycle carbon emissions.

equivalent to Figure 2.7 from an input/output perspective on both an energy and fuel basis. The relative performance between the processes in Figures 2.7 and 2.10 on a price per energy and on a price per emissions avoided basis depends only on the relative processing/production costs and the relative amounts of CO_2 emitted at stream 3. On an absolute basis, the only factor that matters for either process is the relative decrease in emissions at stream 3 relative to the amount of respiration that would have naturally occurred from the wastes in stream 1 in the absence of any processing (ϕ_p relative to ϕ_r where ϕ_p now includes the emissions associated with the production of the fossil fuel

and any emissions associated with the eventual degradation of the processed carbon). The unconventional approach of burning fossil fuels while applying some treatment to available waste organic material cannot be discarded as obviously inferior to bio-waste to fuel conversions. In fact, it is expected to be technically easier and less disruptive to the existing energy infrastructure, and thus it may deserve more attention.

2.C.2 Large-scale stationary storage

The energy source in stream 2 could be abundantly available but temporally inconvenient. This could result from intermitency of the source in stream 2 or from intermitency of the demand/draw from stream 4. In this scenario, a CO_2 to fuel technology might find utility as a large-scale, stationary energy storage system, but it would have to be competitive with other stationary energy storage solutions. The most appropriate comparison technology depends on the type of energy input in stream 2 and the type required from stream 4. For example, if the energy is to be stored and delivered as heat (i.e., solar thermal or potentially nuclear input from stream 1 and heat extracted from stream 4), then the technology would have to compete with conventional thermal energy storage solutions. A pair of technical reports from the NREL and the DOE [27] [28] estimated the capital cost of a new molten salt storage facility at 26.22 $ /kWh-th, proposed a future capital cost target of 15 $/kWh-th, and reported 99 % round-trip efficiencies. If one defines a CO_2 to fuels efficiency of η_{rxn} where heat input at state 1 $\times$ η_{rxn} is the heat available from combustion of the fuel at state 4 (similar to CCUSM section), then the total energy "cost" ($E_{2,4}$) as a multiple of the energy delivered at state 4 (i.e., the energy penalty associated with storage) is

$$E_{2,4} = \frac{1}{\eta_{rxn}} + \frac{0.023}{\eta_{sep}\eta_{car}} - 1 \tag{2.42}$$

where the units are energy required divided by energy delivered (at stream 4). Even an unrealistically perfect separator and CO_2 to fuels conversion process ($\eta_{sep}, \eta_{rxn} = 1, \eta_{car} = 0.3$) would experience at least 7.8 $\times$ higher operating costs relative to the molten salt system from the free energy change of separation alone (0.023/0.3/0.01=7.8). Comparisons among capital costs are not possible without specifying much more detail about the separation and conversions processes, but suffice to say, 15-26 \$/kWh-th of capital costs seems like a difficult hurdle to overcome, especially when the low capacity factor associated with this type of application is considered.

If the energy is supplied as electricity in stream 2 and required as electricity from stream 4, then an additional efficiency is needed in Equation 2.42 to account for the final chemical fuel to electricity conversion between streams 4, 5, and 6.

$$E_{2,4} = \frac{1}{\eta_{C2F}\eta_{pp}} + \frac{0.023}{\eta_{sep}\eta_{car}} - 1 \tag{2.43}$$

In Equation 2.43, η_{pp} is the efficiency of conversion of the primary energy in the fuel to electricity. The US fleet of PC and natural gas power plants had average thermal (η_{pp}) efficiencies of 0.32 and 0.445 in 2017, respectively, but there are reports of new combined-cycle power plants with efficiencies as high as 0.6222. [4, 29] For a quick comparison, one can optimistically estimate future power plant efficiencies as $\eta_{pp} = 0.70$. An optimistic estimate of the energy fraction lost across the storage system is then $\frac{1}{1\times0.70} + \frac{0.023}{0.3} - 1 = 0.51$.

Two reasonable incumbent technology comparisons for electricty storage are pumped hydro-electric and Li-ion batteries. Roundtrip electricity storage effiiciencies are reported between 70 and 85 % for pumped hydro-electric [30] and 80-95 % for batteries. [31, 32] Assuming that pumped-hydro is deployed where it is cheaper, the more broadly applicable comparison is batteries. Even assuming essentialy reversible CO_2 capture and CO_2 to fuel

conversion processes, the energy loss associated with an optimistic projection of future CO_2 to fuel electricity storage processes is larger than the loss currently achievable in both batteries and hydro-electric storage systems. GM expects to provide lithium ion batteries at a cost of 100 \$/kWh as soon as 2021, and BYD reports that their batteries maintain at least 80 % capacity after 5000 charge cycles. A normalized capital cost of the battery can be estimated by dividing the capital cost by the expected number of uses before replacement: 100/5000= 0.02 / kWh. The EIA published a report on levelized electricty cost expectations by year 2022 based on different electricity generation technologies [33]. This report estimated that a conventional combined-cycle power generation facility will require approximately 0.014 \$/kWh if the capacity factor is 87 %. The capacity factor is expected to be lower for a power plant that exists to intermittenly upgrade fuels to electricity, and the levelized capital cost per kWh scales inversely with the capacity factor. A CO_2 to fuels technology would also require capital investment for the capture and conversion steps, and so one can conclude with confidence that a best-case scenario CO_2 to fuels process would be more expensive than batteries on a capital cost basis as well. Taken in totality, these comparisons indicate that CO_2 to fuels processes are unlikely to become an economical, large-scale storage technology.

2.C.3 Transportation (i.e., small scale storage)

It is also possible for the energy source at state 2 to be abundantly available but inconveniently spatially distributed. A combination of spatial and temporal inconvenience corresponds to the most popular proposed use case for both bio-fuel and CO_2 to fuel technologies: transportation fuels. The combustion of fossil fuel for transportation accounted for 37% of the US carbon emissions in 2017, and the distributed nature of transportation emissions excludes point source emission mitigation strategies. [4] If the

energy is available as electricity, transportation energy storage is likely best served by batteries (See section 2.C.2). If the energy source is otherwise utilized solar irradiation, then the transportation fuel system likely does not impact emissions by the magnitude or mechanism that is commonly assumed (See section 2.C.1). If the energy source would be otherwise wasted (solar irradiation on buildings or on a desert, or the chemical energy trapped in bio-waste chemical bonds that would otherwise respire to the atmosphere), then the technology may be suitable, although one should be careful to ensure that a simpler bio-waste treatment process may not be a cheaper way to get an identical or better net emissions impact. In conclusion, simple balances and some literature references (in which cases the authors perform more complicated material balances in the general spirit of the other analyses presented here) lead to several guidelines for CO_2 to fuel and biofuel technology research.

Key takeaways

- For any (synthetic or biological) CO_2 to fuel technology to be both economically feasible and emission neutral, the energy source powering the process must be emission neutral.
- Growing corn to convert to fuel is not emission neutral. An optimistic estimate of the emissions impact relative to gasoline combustion is a reduction of 17 %.
- The net emission effect of biofuel processes are imprecisely defined due to the difficulty and subjectivity inherent in estimating and modeling the relevant indirect effects. Nonetheless, the models used by government regulators all agree that corn ethanol to fuel technologies increase net emissions if one does not count carbon emissions due to reduced food production.
- Optimistic estimates of future CO_2 to fuel technologies are not cost competitive

with alternative emissionless large-scale energy storage systems.

- Bio-wastes to fuel processes could reduce emissions relative to discarding the bio-wastes and burning fossil fuels if $\phi_p < \phi_r$.

- Utilization of "waste" solar irradiation to fix CO_2 (without an accompanying release of CO_2 from land use change) reduces net emissions.

- Any system that permanently fixes carbon that would have otherwise reached the atmosphere reduces net CO_2 emissions, even if the captured carbon is not converted to a fuel.

2.D Hydrogen economy from electrolysis

A water electrolysis process produces hydrogen from electricity and water by

$$H_2O \rightleftharpoons \frac{1}{2}O_2 + H_2 \tag{2.44}$$

This reaction requires an energy input of at least 285.5 KJ/mole of hydrogen produced. Not much can be learned from a back of the envelope assessment of this idea, except that more electricity is required to power the process than can be eventually extracted from the hydrogen. Therefore, one expects hydrogen from electrolysis to be most useful as utilization of otherwise wasted energy, as a transportation fuel, or as general large scale energy storage.

Electricity is an expensive, relatively valuable form of energy, and so it does not tend to be wasted. However, intermittency of some renewable energy sources has led to negative instantaneous electricity prices in Germany and in California. [34,35] Unfortunately, one would likely need structurally wasted, rather than instantaneously wasted electricity

for the capital costs of an electrolyzer to be justified. The feasibility of water electrolysis as energy storage or as a means to utilize electricity as a transportation fuel depends on four variables: the price of emissionless electricity, the electrolysis efficiency, the average efficiency of the set of devices that consume the product hydrogen, and the price of the competing energy storage or transportation fuel. Hydrogen is an expensive energy source when produced by SMR, and the DOE target cost for hydrogen from electrolysis in 2020 is $\approx 4\times$ higher than the target cost for SMR. [15] These cost estimates do not include the cost of CCS if the electricity source is not emissionless, so emissionless hydrogen would likely be more expensive still.

Key takeaways

- Electrolysis likely requires abundant, emissionless, structurally (as opposed to instantaneously) cheap electricity to be viable.

Bibliography

[1] R. P. Feynman. *Surely You're Joking, Mr. Feynman!* W W Norton, 1985.

[2] M. Feinberg and P. Ellison. General kinetic bounds on productivity and selectivity in reactor - separator systems of arbitrary design: Principles. *Ind. & Eng. Chem.*, 40(14):3181–3194, 2001.

[3] J. A. Frumkin and M. F. Doherty. Target bounds on the reaction selectivity via feinberg's cfstr equivalence principle. *AIChE J.*, 64(3):926–939, 2018.

[4] EIA. March 2018 monthly energy review. Technical report, Energy Information Adminsitration, 2018.

[5] B. Metz, O. Davidson, H. de Conninck, M. Loos, and L. A. Meyer. Ipcc special report on carbon dioxide capture and storage. Technical report, Cambridge University Press, 2005.

[6] B. R. Constantz, A. Youngs, and T. Holland. Reduced-carbon footprint concrete compositions. U.S. patent 7,815,880, 2010.

[7] B. R. Constantz, K. Farsad, C. Camire, and I. Chen. Methods and compositions using calcium carbonate. U.S. patent 7,922,809, 2011.

[8] D. W. Keith. Why capture co2 from the atmosphere? *Science*, 325(5948):1654–1655, 2009.

[9] J. Ciferno, J. Litynski, S. Plasynski, J. Murphy, G. Vaux, R. Munson, and J. Marano. DOE/NETL carbon dioxide capture and storage RD&D roadmap. *US DOE National Energy Technology Laboratory, Pittsburgh*, 2010.

[10] K. Z. House, C. F. Harvey, M. J. Aziz, and D. P. Schrag. The energy penalty of post-combustion CO_2 capture & storage and its implications for retrofitting the US installed base. *Energy & Environmental Science*, 2(2):193–205, 2009.

[11] F. J. Cogswell. High-efficiency low-gwp compressor. Technical report, US DOE United Technologies Research Center, 2017.

[12] G. T. Rochelle. Amine scrubbing for co_2 capture. *Science*, 325:1652–1654, 2009.

[13] K. Z. House, A. C. Baclig, M. Ranjan, E. A. van Nierop, J. Wilcox, and H. J. Herzog. Economic and energetic analysis of capturing CO_2 from ambient air. (51), 2011.

[14] WBCSD. Cement industry energy and CO_2 performance: Getting the numbers right. online, 2014.

[15] Fuel cell technologies office multi-year research, development, and demonstration plan. Technical report, U.S. Department of Energy, 2011.

[16] B. Parkinson, J. W. Matthews, T. B. McConnaughy, D. C. Upham, and E. W. McFarland. Techno-economic analysis of methanepyrolysis in molten metals: Decarbonizing natural gas. *Chemical Engineering & Technology*, 2017.

[17] R. F. Lemus and J. M. M. Duart. Updated hydrogen production costs and parities for conventional and renewable technologies. *International Journal of Hydrogen Energy*, 35:3929–3936, 2010.

[18] B. Parkinson, M. Tabatabaei, D. C. Upham, B. Ballinger, C. Greig, S. Smart, and E. Mcfarland. Hydrogen production using methane: Techno-economics of decarbonizing fuels and chemicals. *International Journal of Hydrogen Energy*, 2018.

[19] T. Geiβler, M. Plevan, A. Abanades, A. Heinzel, K. Mehravaran, R. Rathnam, C. Rubbia, D. Salmieri, L. S. ad S. Stuckrad, A. Weisenburger, H. Wenninger, and T. Wetzel. Experimental investigation and thermo-chemical modeling of methane pyrolysis in a liquid metal bubble column reactor with a packed bed. *International Journal of Hydrogen Energy*, 40:14134–14146, 2015.

[20] D. C. Upham, V. Agarwal, A. Khechfe, Z. R. Snodgrass, M. J. Gordon, H. Metiu, and E. W. McFarland. Catalytic molten metals for the direct conversion of methane to hydrogen and separable carbon. *Science*, 358:917–921, 2017.

[21] M. S. Shell. *Thermodynamics and Statistical Mechanics: An Integrated Approach*. Cambridge University Press, 2015.

[22] S. L. Sandler. *Chemical, Biochemical, and Engineering Thermodynamics*. 4 edition, 2006.

[23] Electric power annual 2016. Technical report, EIA, 2017.

[24] T. Searchinger, R. Heimlich, R. Houghton, F. Dong, A. Elobeid, J. Fabiosa, S. Tokgoz, D. Hayes, and T.-H. Yu. Use of u.s. croplands for biofuels increases greenhouse gases through emissions from land-use change. *Science*, 319:1238–1240, 2008.

[25] T. D. Searchinger. Biofuels and the need for additional carbon. *Environ. Res. Lett.*, 2010.

[26] T. Searchinger, R. Edwards, D. Mulligan, R. Heimlich, and R. Plevin. Do biofuel policies seek to cut emissions by cutting food? *Science*, 347:1420–1422, 2015.

[27] G. Glatzmaier. Developing a cost model and methodology to estimate captial costs for thermal energy storage. Technical report, NREL, 2011.

[28] E. A. DeMeo and J. F. Galdo. Renewable energy technology characterizations. Technical report, EPRI and US DOE, 1997.

[29] T. Kellner. Here‘s why the latest guinness world record will keep france lit up long after soccer fans leave. 2016.

[30] Packing some power. *The Economist*, 2012.

[31] T. Living. Measuring ev charging efficiency. 2014.

[32] H. Chen, T. N. Cong, W. Yang, C. Tan, and Y. L. Y. L. Ding. Progress in elelectric energy storage system: A critical review. *Natural Science*, pages 291–312, 2009.

[33] Levelized cost and levelized avoided cost of new generation resources in the annual energy outlook 2018. Technical report, US EIA, 2018.

[34] S. Reed. Power prices go negative in germany, a positive for energy users. *New York Times*, 2017.

[35] I. Penn. California invested heavily in solar power. now there's so much that other states are sometimes paid to take it. *Los Angeles Times*, 2017.

Chapter 3

Polymorph Selection by Continuous Crystallization

Reproduced in part with permission from:

Thomas C. Farmer, Corinne L. Carpenter, and Michael F. Doherty, "Polymorph Selection by Continuous Crystallization," *AIChE Journal*, **2016**, *62*, 3505-3514.

DOI: 10.1002/aic.15343.

3.1 Introduction

Many solid materials exist in more than one crystal structure. These polymorphic compounds are ubiquitous in both nature and industry and generally exhibit unique mechanical, electrical, and physicochemical properties, as well as unique solubility curves in solution. [1–3] Polymorphism is prevalent in minerals (e.g. vaterite/aragonite/calcite), inorganic oxides (e.g. α- and γ-alumina, α- and γ-ferric oxide, rutile/anatase/brookite, etc.), and especially in pharmaceutical compounds (e.g. ritonavir, erythromycin, paracetamol, clopidogrel, etc.). [4–6]

The kinetics of solvent-mediated phase transformation that govern the growth of the stable polymorph as the metastable one dissolves and the general tendency for the most soluble (least thermodynamically stable) polymorph to nucleate first are understood. [7,8] These ideas are central in all design and control procedures for producing polymorphic materials. It is well known in batch crystallizer design that the polymorph distribution is governed by the induction time of the most stable form. In the limit of very long ($\approx \infty$) batch times, the most stable polymorph is obtained. Producing metastable polymorphs in batch devices takes clever temperature and solute concentration control, choice of solvents, choice of additives, the use of patterned self-assembled monolayers, pH control, or all of the above. [9–15] One expects similar considerations to apply to continuous crystallization devices in which the residence time takes the place of the batch time. However, in batch devices the batch time and the transient (evolution) time from start up conditions are one in the same thing. For continuous devices, they are completely independent concepts. Thus, in a continuous crystallizer, it is possible to evolve the transient from an initial start-up condition for an "infinite" length of time to achieve a dynamically stable steady-state with a finite residence time that corresponds to a metastable polymorph. In the next section, we develop a model and perform a mathematical analysis to formalize this concept.

In this paper, we first define a general bi-polymorph MSMPR population balance model. We then transform the population balance model into a set of nondimensionalized moment equations and characterize the potential steady-states as a function of several dimensionless groups. We then perform a linear stability analysis and produce a simple test that allows one to predict the dominant polymorph for a given set of operating conditions. We then show how this simple test agrees with the L-glutamic acid and p-aminobenzoic acid experimental results that have been reported recently. [16, 17] Experiments on the continuous crystallization of calcium carbonate have also been reported,

but they have been omitted from our analysis because the necessary rate constants were not reported. [18, 19] Finally, we discuss the qualitative implications of several model perturbations in order to illustrate that this effect is general to other physically reasonable models, and to further highlight the advantage of continuous processing for any crystallization process in which polymorph selection is necessary.

3.2 Model Derivation

A classical one-dimensional population balance model has been developed for a MSMPR crystallizer in which the population of each polymorph (α, β) can be written as

$$\frac{\partial n_i}{\partial t} + G_i \frac{\partial n_i}{\partial x} = -\frac{n_i}{\tau} \quad i = \alpha, \beta \tag{3.1}$$

$$n_i(t = 0, x) = n_{i,seed} \qquad n_i(t, x = 0) = \frac{B_i}{G_i} \tag{3.2}$$

where $n_i(t, x)$ is the number density distribution of polymorph i, x indicates crystal size, G is the size-independent linear growth rate, B is the nucleation rate, τ is the crystallizer residence time, and

$$G_i, B_i > 0 \;\; when \;\; C > C_{sat,i} \qquad G_i < 0 \;\; when \;\; C < C_{sat,i} \tag{3.3}$$

$$B_i = 0 \;\; when \;\; C \leq C_{sat,i} \qquad G_i = 0 \;\; when \;\; C = C_{sat,i} \tag{3.4}$$

Nucleation generally occurs via both homogeneous and heterogeneous mechanisms, although the latter often occurs much faster than the former. [20, 21] We will initially restrict our analysis to cases in which homogeneous nucleation is much slower than heterogeneous nucleation mechanisms, as is the case for L-glutamic acid. [22] We will address

the qualitative implications of relaxing this assumption at the end of the article. Equation 3.1 depends on several assumptions: perfect solid/liquid mixing (i.e., a uniformly homogeneous solid-liquid suspension inside the crystallizer), size-independent crystal growth, zero volume change upon crystallization, and suspension properties at the outlet identical to those within the crystallizer. The semi-empirical equations displayed below have been chosen to describe growth and nucleation to facilitate comparisons with the experiments. [16, 17] The implications of different functional forms are discussed later.

$$G_i = k_{g,i}\left(\frac{C}{C_{sat,i}} - 1\right)^{g_i} \qquad B_i = k_{b,i}\left(\frac{C}{C_{sat,i}} - 1\right)^{b_i} m_{2,i} \tag{3.5}$$

where $m_{2,i}$ is the second moment of the polymorph i number density distribution as derived in Appendix 3.A, $k_{g,i}$ and $k_{b,i}$ are temperature-dependent rate constants, and $C_{sat,i}$ is the temperature-dependent polymorph solubility. Both population balance equations are coupled through the total crystallizer mass balance from which the instantaneous value of $C(t)$ determines whether each polymorph is growing or dissolving. The mass deposition rate is calculated from the crystal linear growth rate and the total surface area, which is in turn calculated from the second moment of the particle distribution. Therefore, the time evolution of the solute concentration can be written as

$$\frac{dC}{dt} = \frac{C_o - C}{\tau} - 4\pi \sum_{i=\alpha,\beta} \rho_i G_i \int_0^\infty n_i x^2 dx \tag{3.6}$$

$$C(t=0) = C_o \tag{3.7}$$

where C_o is the inlet concentration, ρ_i is the crystal density of polymorph i, and both

particles are assumed to be spherical.[1] For simplicity of presentation, it is henceforth assumed that both polymorphs have identical crystal density ρ.

The method of moments followed by nondimensionalization (both outlined in Appendix 3.A) transforms the PDE model given by equation 3.1 and 3.6 into the 7-dimensional set of ODEs shown below:

$$\frac{d\omega_{\alpha,0}}{d\xi} = -\omega_{\alpha,0} + Da_\alpha (y+\gamma)^{b_\alpha} \omega_{\alpha,2} \tag{3.8}$$

$$\frac{d\omega_{\alpha,1}}{d\xi} = -\omega_{\alpha,1} + (y+\gamma)^{g_\alpha} \omega_{\alpha,0} \tag{3.9}$$

$$\frac{d\omega_{\alpha,2}}{d\xi} = -\omega_{\alpha,2} + (y+\gamma)^{g_\alpha} \omega_{\alpha,1} \tag{3.10}$$

$$\frac{d\omega_{\beta,0}}{d\xi} = -\omega_{\beta,0} + Da_\beta y^{b_\beta} \omega_{\beta,2} \tag{3.11}$$

$$\frac{d\omega_{\beta,1}}{d\xi} = -\omega_{\beta,1} + y^{g_\beta} \omega_{\beta,0} \tag{3.12}$$

$$\frac{d\omega_{\beta,2}}{d\xi} = -\omega_{\beta,2} + y^{g_\beta} \omega_{\beta,1} \tag{3.13}$$

$$\frac{dy}{d\xi} = (1-y) - \left[(y+\gamma)^{g_\alpha} \omega_{\alpha,2} + y^{g_\beta} \omega_{\beta,2}\right] \tag{3.14}$$

where $\omega_{\alpha,i}$ is moment i of the distribution of α particles, $\omega_{\beta,i}$ is moment i of the distribution of β particles, and y is the dimensionless solute concentration. The system dynamics depend on three dimensionless groups:

$$Da_\alpha = 2\tau k_{b,\alpha} \left(\frac{C_o - C_{sat,\beta}}{C_{sat,\alpha}}\right)^{b_\alpha} \sigma_\alpha^2 > 0 \qquad Da_\beta = 2\tau k_{b,\beta} \left(\frac{C_o - C_{sat,\beta}}{C_{sat,\beta}}\right)^{b_\beta} \sigma_\beta^2 > 0 \tag{3.15}$$

$$\gamma = \frac{C_{sat,\beta} - C_{sat,\alpha}}{C_o - C_{sat,\beta}} < 0 \tag{3.16}$$

The Damköhler numbers (Da_α and Da_β) are ratios of the characteristic process time to the characteristic nucleation time associated with each polymorph; γ is a parameter

[1] Non-spherical particles can be accommodated by altering the shape factor from the 4π used in equation 3.6.

that quantifies the solubility difference between the polymorphs. For our model/process to be distinguishable from the conventional situation of a single polymorph system, the feed must be supersaturated with respect to both polymorphs. Therefore, Da_α and Da_β are strictly positive quantities for any physically interesting operating point. Without loss of generality, we assume phase α is the metastable polymorph and β is the thermodynamically stable polymorph (and thus has the lowest saturation concentration). The dimensionless groups have the signs indicated in equations 3.15-3.16, although the sign of γ changes whenever the relative thermodynamic stabilities change. These seven differential equations and four dimensionless groups now describe the crystallization dynamics in a 2-polymorph MSMPR process such as the L-glutamic acid, p-aminobenzoic acid, and many other bi-polymorphic systems.

3.3 Steady-states

A steady-state is defined at every point in parameter space when all time derivatives vanish. A bi-polymorphic MSMPR crystallizer exhibits four types of steady-states, three of which become uniquely stable in some region of parameter space. We have assigned the names trivial, α, and β to these steady-states to signify that there are no crystals present, only α crystals present, and only β crystals present at each steady-state, respectively. The fourth steady-state is a mixed state containing both α and β crystals. As will be explained in the next section, it can only exist along a line in parameter space and is therefore expected to be difficult to produce experimentally, regardless of its dynamic stability.

3.3.1 Trivial Steady-State: $\omega_\alpha = \mathbf{0}, \omega_\beta = \mathbf{0}$, $y = 1$

This set of state variables satisfies the steady-state algebraic relations for all sets of parameter values, and for a certain range of parameter values, it is in fact the stable steady-state. $y = 1$, $\omega_\alpha = \omega_\beta = \mathbf{0}$ corresponds to zero nucleation and growth resulting in identical supersaturation entering and leaving the crystallizer. This is physically realizable for a crystallizer when the rate at which crystals flow out of the crystallizer is faster than the rate at which they nucleate and grow. This is the expected state of the process as the residence time is taken to zero, and in fact it will be shown in a later section that this is the limit in which the trivial steady-state becomes stable. Clearly, a continuous homogeneous nucleation expression would eliminate this steady-state, but this is actually a technicality that does not affect the qualitative result for a great many systems. This technicality is discussed in more detail in a later section.

3.3.2 α Steady-State: $\omega_\alpha \geq \mathbf{0}$, $\omega_\beta = \mathbf{0}$, $y \leq 1$

The set of equations 3.8-3.10 contains 4 states: $\omega_{\alpha,0}$, $\omega_{\alpha,1}$, $\omega_{\alpha,2}$, and y. Algebraic manipulation leads to the relationship:

$$\omega_{\alpha,2,ss} = Da_\alpha (y_{ss} + \gamma)^{2g_\alpha + b_\alpha} \omega_{\alpha,2,ss} \tag{3.17}$$

which implies a single value of y that is consistent with these 3 equations whenever $\omega_\alpha \neq \mathbf{0}$:

$$y_{ss} = Da_\alpha^{\frac{-1}{2g_\alpha + b_\alpha}} - \gamma \tag{3.18}$$

Now, one can write all the other $\omega_{\alpha,i}$ as simple functions of the parameters and $\omega_{\alpha,2}$:

$$\omega_{\alpha,0,ss} = Da_\alpha(y_{ss}+\gamma)^{b_\alpha}\omega_{\alpha,2,ss} \tag{3.19}$$

$$\omega_{\alpha,1,ss} = Da_\alpha(y_{ss}+\gamma)^{g_\alpha+b_\alpha}\omega_{\alpha,2,ss} \tag{3.20}$$

When y_{ss} is defined by 3.18, the set of steady-state equations 3.11-3.13 becomes full rank and the only general solution is $\omega_\beta = \mathbf{0}$. Therefore, equation 3.14 becomes a function of only $\omega_{\alpha,2,ss}$

$$\omega_{\alpha,2,ss} = \frac{1-y_{ss}}{(y_{ss}+\gamma)^{g_\alpha}} \tag{3.21}$$

Therefore, at the α steady-state all ω_α are explicit functions of only design parameters and $\omega_\beta = 0$.

3.3.3 β Steady-State: $\omega_\alpha = \mathbf{0},\ \omega_\beta \geq \mathbf{0},\ y \leq 1$

Similarly, equations 3.11-3.13 contains 4 states: $\omega_{\beta,0}$, $\omega_{\beta,1}$, $\omega_{\beta,2}$, and y. Again, there is a unique steady-state value of y that is consistent with $\omega_\beta \neq \mathbf{0}$

$$y_{ss} = Da_\beta^{\frac{-1}{2g_\beta+b_\beta}} \tag{3.22}$$

The steady-state β moments similarly become single-valued functions of $\omega_{\beta,2,ss}$

$$\omega_{\beta,0,ss} = Da_\beta y_{ss}^{b_\beta}\omega_{\beta,2,ss} \tag{3.23}$$

$$\omega_{\beta,1,ss} = y_{ss}^{g_\beta}\omega_{\beta,0,ss} = Da_\beta y_{ss}^{g_\beta+b_\beta}\omega_{\beta,2,ss} \tag{3.24}$$

When y_{ss} is defined by 3.22, steady-state equations 3.8-3.10 become full rank with the general solution $\omega_\alpha = 0$. This allows equation 3.14 to be used to calculate $\omega_{\beta,2,ss}$:

$$\omega_{\beta,2,ss} = \frac{1 - y_{ss}}{y_{ss}^{g_\beta}} \tag{3.25}$$

For the particularly fortuitous combination of parameters that leads to the y_{ss} associated with both the pure α and pure β polymorphs being exactly equal, a mixed polymorph steady-state is possible. In this case, equation 3.14 gives a line of potential steady-states. The combination of parameters for which this bifurcation occurs is

$$(Da_\alpha^{\frac{-1}{2g_\alpha + b_\alpha}} - \gamma) = {Da_\beta}^{\frac{-1}{2g_\beta + b_\beta}} \tag{3.26}$$

3.4 Dissolution dynamics at steady-state

In a MSMPR crystallizer fed by a clear supersaturated solution, the functional form of the dissolution rate of the metastable polymorph does not affect the steady-state. At steady-state, a MSMPR crystallizer operates at a single solute concentration and supersaturation inside the vessel. After several residence times, all initial seeds have washed out and the only crystals that remain necessarily nucleated inside the crystallizer. It is not possible for the same supersaturation to (net) generate nuclei, and (net) dissolve crystals of the same polymorph because the driving force for both nucleation and growth are identical. Therefore, at steady-state, each polymorph will either be absent, or nucleating and growing. It is not possible for a metastable polymorph to be constantly present and dissolving at steady-state unless the crystallizer is being continuously fed crystals of that polymorph. The dissolution rate *does* affect the dynamics toward the steady-state, and is therefore important for control of steady-state processes and for modeling any batch

process.

3.5 Stability Analysis

The stability of each steady-state is determined by analyzing the linear system of ordinary differential equations resulting from the Taylor expansion about that steady-state. [23] The Jacobian matrix is given below as a function of the parameters and states (which are known as a function of the parameters for each type of steady-state).

$$\begin{pmatrix} -1 & 0 & Da_\alpha(y_{ss}+\gamma)^{b_\alpha} & 0 & 0 & 0 & b_\alpha Da_\alpha(y_{ss}+\gamma)^{b_\alpha-1}\omega_{\alpha,2,ss} \\ (y_{ss}+\gamma)^{g_\alpha} & -1 & 0 & 0 & 0 & 0 & g_\alpha(y_{ss}+\gamma)^{g_\alpha-1}\omega_{\alpha,0,ss} \\ 0 & (y_{ss}+\gamma)^{g_\alpha} & -1 & 0 & 0 & 0 & g_\alpha(y_{ss}+\gamma)^{g_\alpha-1}\omega_{\alpha,1,ss} \\ 0 & 0 & 0 & y_{ss}^{g_\beta} & -1 & 0 & g_\beta y_{ss}^{g_\beta-1}\omega_{\beta,0,ss} \\ 0 & 0 & 0 & 0 & y_{ss}^{g_\beta} & -1 & g_\beta y_{ss}^{g_\beta-1}\omega_{\beta,1,ss} \\ 0 & 0 & -(y_{ss}+\gamma)^{g_\alpha} & 0 & 0 & -y_{ss}^{g_\beta} & -1-(g_\alpha(y_{ss}+\gamma)^{g_\alpha-1}\omega_{\alpha,2,ss}+g_\beta y_{ss}^{g_\beta-1}\omega_{\beta,2,ss}) \end{pmatrix}$$

This model contains seven states (three α moments, three β moments, and 1 solute concentration) and seven parameters (Da_β, Da_α, γ, g_α, g_β, b_α, and b_β) and is generally applicable to any two-polymorph crystallization process in which the heterogeneous nucleation mechanism dominates. Once a particular solute/solvent system is specified, four of the parameters become fixed (i.e. g_α, g_β, b_α, and b_β). A linear stability analysis has been completed in order to correlate regions of parameter space with the dynamic stability or instability of each steady-state. The results are presented here with details available in Appendix 3.B.

For this model, parameter space can be cleanly subdivided into 3 regions, each corresponding to a separate stable steady-state. Each limit of stability corresponds to a bifurcation in parameter-state space, and along each of these boundaries the determinant of the Jacobian matrix is exactly zero. The trivial steady-state is stable when

$$Da_\beta < 1 \tag{3.27}$$

$$Da_\alpha (1+\gamma)^{2g_\alpha + b_\alpha} < 1 \tag{3.28}$$

The α steady-state is stable when

$$\left[(Da_\alpha^{\frac{-1}{2g_\alpha + b_\alpha}} - \gamma) \right]^{-1} > \left[Da_\beta^{\frac{-1}{2g_\beta + b_\beta}} \right]^{-1} \tag{3.29}$$

$$Da_\alpha (1+\gamma)^{2g_\alpha + b_\alpha} > 1 \tag{3.30}$$

The β steady-state is stable in the remaining region, defined by

$$\left[Da_\beta^{\frac{-1}{2g_\beta + b_\beta}} \right]^{-1} > \left[(Da_\alpha^{\frac{-1}{2g_\alpha + b_\alpha}} - \gamma) \right]^{-1} \tag{3.31}$$

$$Da_\beta > 1 \tag{3.32}$$

These results are presented graphically in Figure 3.1. The three engineering decision variables that remain after choosing a solvent and solute (Da_α, Da_β, and γ) all respond to changes in design variables such as residence time (τ), inlet concentration (C_o), and temperature (T). In most polymorphic systems, one expects to be able to design a MSMPR crystallizer to produce either desired polymorph based on these simple rules. To demonstrate the utility of this design methodology, we have included Figure 3.2. The data points are from the aforementioned reports on the continuous crystallization of polymoprhic L-glutamic acid [16] and p-aminobenzoic acid. [17]

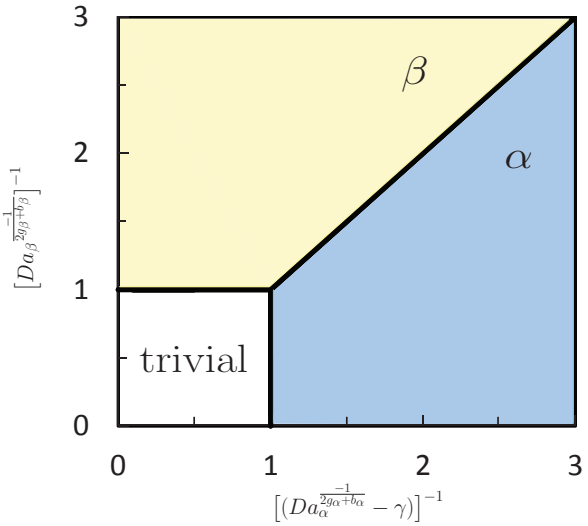

Figure 3.1: There are 3 stability regions. In the upper left region, β is the dominant polymorph. In the lower right region, α is dominant, and in the bottom left corner ($\lim \tau \to 0$) the trivial steady-state is stable.

In [16], Myerson, Trout, and co-workers demonstrated that continuous crystallization of L-glutamic acid spontaneously settles into a steady-state in which only α is produced at 25 °C with a feed concentration of 40 kg/m^3 across 4 different residence times. They also reported a stable pure β steady-state at 45 °C . After non-dimensionalization and recasting their kinetic expressions into the forms presented here, we show that their results are consistent with our stability analysis as shown in Figure 3.2. It is more difficult to compare their 45 °C data with our stability analysis because they did not regress growth and nucleation expressions at that temperature. Fortunately, another paper did determine the growth rates of both α and β L-glutamic acid crystals as a function of temperature. [12] We have used their Arrhenius expressions to estimate the factor by which both growth rates increase when the temperature is increased from 25 °C to 45 °C, and the result is approximately 3 for α and 87 for β. With these multiplicative factors, the data for 45 °C can be plotted on Figure 3.2.

The data from [16] are presented as diamond shapes, and the data from [17] are

presented as squares. Data points are labeled yellow when the β polymorph is observed experimentally, and labeled blue when the α is observed experimentally. The filled points signifiy the thermodynamically stable polymorph, and open points signify the metastable polymorph. Interestingly, the thermodynamically stable form of p-aminobenzoic acid switches from β to α at a temperature of approximately 19 °C such that β is stable for $T < 19^o$C and α is stable for $T > 19^o$C. [17] All polymorph predictions shown in Figure 3.2 match the reported experimental results, although there is some uncertainty in the solubilities associated with point 6.[2]

3.6 Designing a Polymorph Selective Process

Three of the seven stability-relevant parameters can be engineered by design choices. Da_α, Da_β, and γ vary with both the feed solute concentration (C_o) and crystallizer temperature (T). Da_α and Da_β also scale with τ^3. These three design choices allow one to design a process that falls on either side of the α/β bifurcation line on Figures 3.1 and 3.2 in most solute/solvent systems. If a system exists for which this is difficult, changing the solvent (and therefore the solubilities, and the set of parameters g_α, g_β, b_α, and b_β) may significantly expand the feasible region.

Figure 3.3 illustrates a representative steady-state solution branch corresponding to increasing τ from 60 minutes (point A) to 6,000 minutes (point B) at $T = 25$ °C and $C_o = 40$ kg/m^3 in the L-glutamic acid/water system. As expected, the stable polymorph eventually dominates in the limit of large residence time. So far, the concepts have been presented under the convention that one has nondimensionalized so that the thermodynamically metastable polymorph is denoted "α". However, the relative thermodynamic

[2]They were read off of a plot, and the model prediction is sensitive to changes in the second significant digit for this point due to its proximity to the bifurcation. One could definitively move this point to whichever side of the bifurcation one prefers by changing design variables (C_o, T, τ).

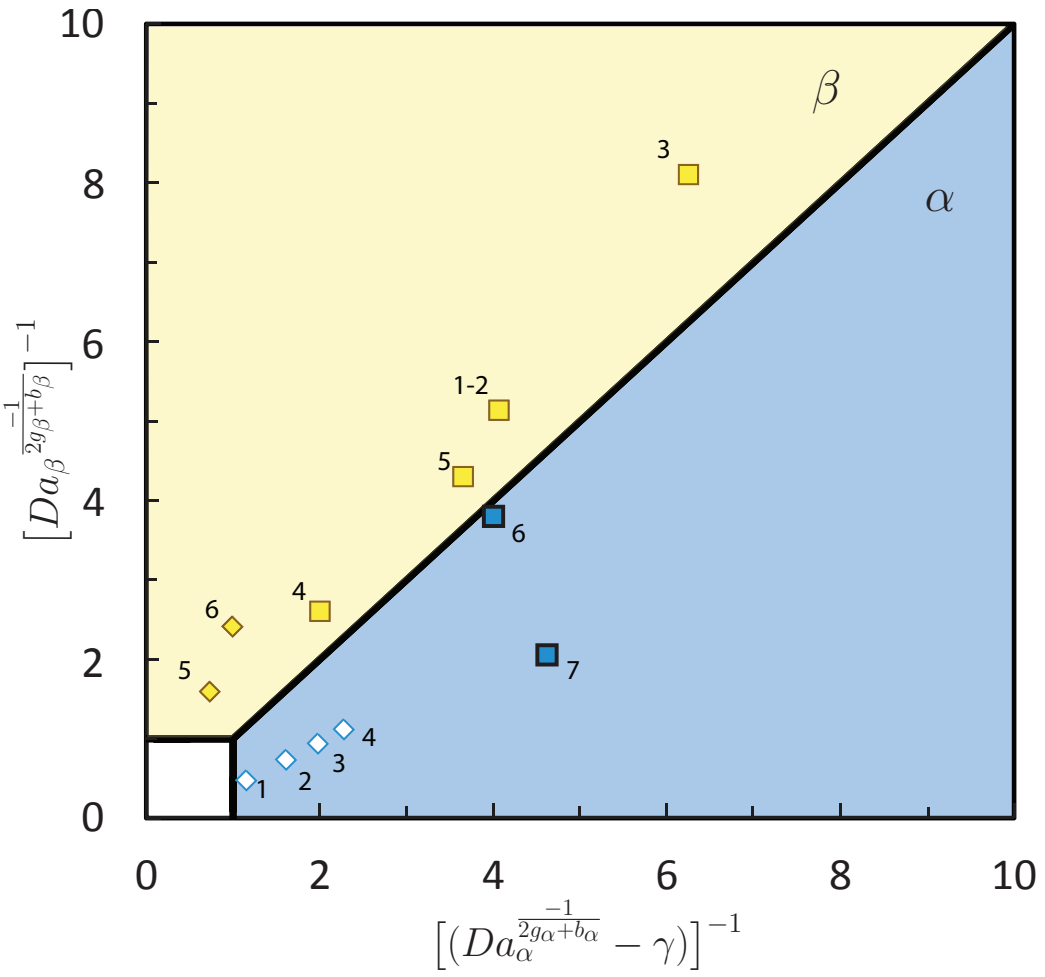

Figure 3.2: The diamond-shaped data points correspond to [16], the square-shaped data points correspond to [17], and both are labeled with the experiment number from their respective publication. Yellow data points correspond to the observation of the β polymorph experimentally and blue data points correspond to the observation of α experimentally. Open markers denote thermodynamic metastability of the solid observed at the temperature corresponding to that experiment, while filled markers denote thermodynamically stable solid forms.

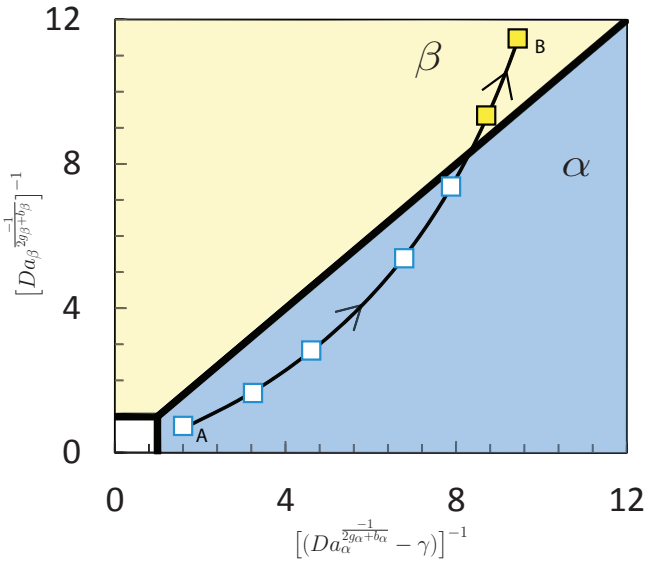

Figure 3.3: The open square labeled A represents $\tau = 60$ minutes, C_o= 40 kg/m^3, and $T = 25$ °C (Experiment 2 in [16]). The filled square labeled B represents $\tau = 6,000$ minutes, C_o= 40 kg/m^3, and $T = 25$ °C. The increasing-τ solution branch moves toward the bifurcation line and eventually crosses as τ increases.

stability of p-aminobenzoic acid changes at a temperature of 19 °C. [17] This is not an issue because the convention was arbitrarily chosen so that the dimensionless concentration would vary from 0 to 1. As long as the concentration inside the crystallizer is above the solubility of both polymorphs, consistent results are produced regardless of the nondimensionalization convention. To illustrate this, we have included Figure 3.4 which shows a steady-state solution branch that again starts from the same location on the stability plot (point A), and follows a path of increasing τ (to point B). Now, the solubility of phase α is less than phase β which causes the parameter γ to become a positive quantity. With this new solubility convention, the branch of steady-states in Figure 3.4 moves away from the bifurcation. This is intuitively pleasing since one expects the thermodynamically stable polymorph to dominate in the limit of large residence time. This general phenomenon (convergence to the thermodynamically stable polymorph in the limit of large τ) has been illustrated mathematically in Appendix 3.C.

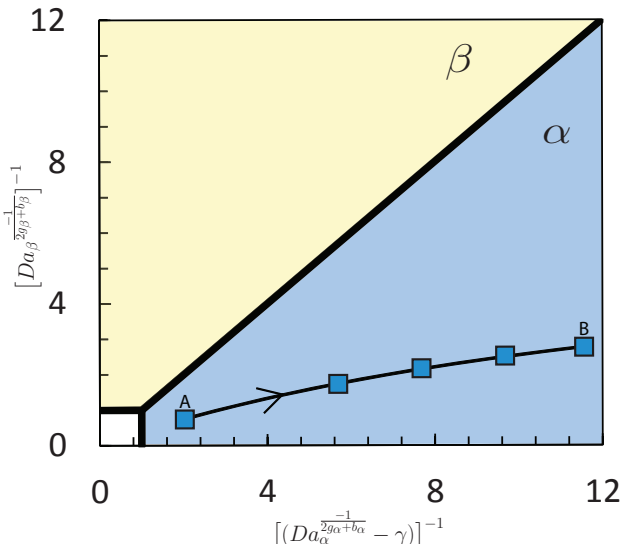

Figure 3.4: The square at point A is placed at the same point in parameter space as the square labeled point A in Figure 3.3. The increasing-τ solution branch moves away from the bifurcation line when "α" is thermodynamically stable.

3.7 Qualitative effect of reasonable model perturbations

To paraphrase Milton Friedman, a theory should not be judged on the realism of its assumptions, but rather on the accuracy of its predictions. [24,25] Continuous steady-state crystallization of L-glutamic acid and p-aminobenzoic acid can be effectively described using the model presented earlier. However, other assumptions and models are possible, and it is therefore fair to ask how the predictions change as the assumptions change. Here, we consider several reasonable model perturbations that might be preferred to describe other crystal systems. This section will illustrate that while some of the quantitative results are peculiar to the model we chose, the qualitative results are general to a broader description or set of assumptions.

First, we have assumed that the heterogeneous nucleation expression scales with m_2 (as assumed by others, for example [26]). In the literature, others have also used $M_T^{2/3}$,

[27] m_3, [12] or ${m_3}^{2/3}$. [28] These choices are clearly correlated. In this work, m_2 was chosen for simplicity of presentation.[3] We have briefly analyzed the resulting model equations, and qualitatively similar steady-states result from any of these choices.

Another reasonable perturbation is in the concentration dependence of the growth and nucleation expressions. If the dimensionless concentration dependence of the growth expression is instead given by $G(y,\gamma)$[4] and the concentration dependence of the nucleation expression is instead given by $B(y,\gamma)$, then the new pure α steady-state is defined by the value of y that solves

$$Da_\alpha B_\alpha(y_{ss},\gamma)G_\alpha^2(y_{ss},\gamma) = 1 \tag{3.33}$$

and the new pure β steady state would be defined by

$$Da_\beta B_\beta(y_{ss},\gamma)G_\beta^2(y_{ss},\gamma) = 1 \tag{3.34}$$

The state-parameter bifurcations now occur along the three lines defined by equations 3.33, 3.34 and 3.35.

$$Da_\beta B_\beta(y_{ss},\gamma)G_\beta^2(y_{ss},\gamma) = Da_\alpha B_\alpha(y_{ss},\gamma)G_\alpha^2(y_{ss},\gamma) \tag{3.35}$$

The analogy to equations 3.18, 3.22, and 3.26 is evident. Thus, our results generalize to a wide variety of growth rate and nucleation rate expressions.

Another significant change could be made by altering the nucleation assumptions. There have been reports of β crystals nucleating from inside and on the surface of α

[3] All the other expressions would have required the third moment of each distribution, unnecessarily complicating the result.

[4] For example, these could be the common Birth and Spread, Burton-Cabrera-Frank, [29] classical nucleation theory, etc.

crystals during L-glutamic acid crystallization. [12, 22, 30–32] This implies B_β should scale with moments of both polymorph distributions. In the general case where the stable polymorph nucleation law scales with the second moment of both polymorph distributions, the "pure α" steady-state becomes a mixed polymorph steady-state whose polymorphic ratio depends on the relative rate of nucleation on each polymorph and the relative rates for growth and nucleation of each polymorph. For example, one could replace the nucleation expressions (equation 3.5) with

$$B_\alpha = k_{b,\alpha}\left(\frac{C}{C_{sat,\alpha}} - 1\right)^{b_\alpha} m_{2,\alpha} \quad B_\beta = k'_{(b,\beta\ on\ \beta)}\left(\frac{C}{C_{sat,\beta}} - 1\right)^{b_\beta}\left(m_{2,\beta} + c\ m_{2,\alpha}\right) \quad (3.36)$$

where c represents $k'_{(b,\beta\ on\ \alpha)}/k'_{(b,\beta\ on\ \beta)}$. If one utilizes this expression in equation 3.1, and then repeats the method of moments and non-dimensionalization outlined in Appendix 3.A, equation 3.11 becomes

$$\frac{d\omega_{\beta,0}}{d\xi} = -\omega_{\beta,0} + Da'_\beta y^{b_\beta}(\omega_{\beta,2} + c\ \omega_{\alpha,2}) \quad (3.37)$$

where $Da'_\beta = Da_\beta\ k'_{(b,\beta\ on\ \beta)}/k_{b,\beta}$. In this case, the ratio of $\omega_{\beta,0}/\omega_{\alpha,0}$ at the "pure α" steady-state becomes

$$\frac{\omega_{\beta,0}}{\omega_{\alpha,0}} = \frac{Da'_\beta}{Da_\alpha}\left[1 + \frac{Da'_\beta\left[Da_\alpha^{-1/(2g_\alpha+b_\alpha)} - \gamma\right]^{b_\beta+2g_\beta}}{1 - Da'_\beta\left[Da_\alpha^{-1/(2g_\alpha+b_\alpha)} - \gamma\right]^{b_\beta+2g_\beta}}\right]\left[Da_\alpha^{-1/(2g_\alpha+b_\alpha)} - \gamma\right]^{b_\beta-b_\alpha}\ c \quad (3.38)$$

The β nucleation expression for L-glutamic acid that was used in [12] can be manipulated into the form of equation 3.36. This gives $c = 0.015$. For L-glutamic acid (and we expect many other systems), including this effect does not appreciably change the result. At the conditions corresponding to the points labeled 1-4 on Figure 3.2, one expects the percent of β crystals to increase from 0% to a maximum of 0.002%. These numbers are necessarily approximate, since we have used data and regressions from multiple studies

to estimate them. Nevertheless, we expect a more detailed analysis to yield results with a similar order of magnitude. Therefore, even when nucleation of the stable form on the metastable form is possible, three types of steady-states remain, one of which is the pure stable polymorph, one of which is dominated by the metastable polymorph (with the specific fractions defined as discussed above), and one corresponding to zero growth and nucleation of either crystal. The structure and absolute values are changed, but the ability to continuously produce an "essentially pure" metastable polymorph is not compromised by accounting for this effect.

The last model perturbation we will address here is the relaxation of the assumption of zero homogeneous nucleation. Industrial crystallizers typically operate at supersaturations, crystal densities, and stirrer speeds that favor heterogeneous nucleation mechanisms over homogeneous ones. Other authors have reported nucleation rates much too fast to be considered homogeneous in the L-glutamic acid system. [12, 22, 33] This is a common feature across many different crystallizer processes and solute/solvent pairs, [26,34,35] although one can imagine a crystallizer in which this is not a reasonable approximation (the case of "infinite" residence time without seeding, for example). In these situations, one could attempt to supplement the nucleation rate through process design. [36] If this is not possible, then homogeneous nucleation will eventually occur. In this case, only one possible mixed-polymorph steady-state remains. Interestingly, the single steady-state that results is qualitatively similar to the stable steady-state predicted by the models presented here (under the assumption of zero homogeneous nucleation). When the heterogeneous-only model predicts a pure α steady-state, α is the dominant polymorph for the combined heterogeneous/homogeneous model and vice versa. Furthermore, predictions from the two types of nucleation models become essentially indistinguishable when the homogeneous nucleation rate is at least 3 orders of magnitude smaller than the heterogeneous rate. Although, when both nucleation mechanisms occur at comparable

rates, the steady-state composition is determined by the relative kinetics of nucleation and growth for each polymorph. In this case, an "almost" pure metastable steady-state can be achieved by increasing the distance in parameter space from the operating point to the α/β bifurcation line in Figure 3.2 regardless of the nucleation mechanism.

3.8 Conclusions

When engineering a crystallization process for a solute that exhibits polymorphism, thermodynamic metastability does not preclude one from producing a desired polymorph in a steady-state continuous process. In fact, we have shown that there is a large domain of parameter space in which production of the thermodynamically metastable α polymorph of L-glutamic acid is the stable steady-state. When designing a polymorphic MSMPR crystallizer, the entirety of the parameter space shown in Figure 1 is experimentally available. γ varies between -1 and 0 as the feed concentration varies from the metastable polymorph solubility ($\gamma = -1$) to ∞ ($\gamma = 0$). Both Damköhler numbers increase with residence time, and their relative ratio changes with both feed concentration and temperature as the nucleation rates, growth rates, and solubilities change. This is true for L-glutamic acid and p-aminobenzoic acid, but will be true generally for many polymorphic systems. When heterogeneous nucleation dominates, all that is required to achieve a pure polymorphic state is tuning the parameters to fall into the region of preference on Figure 3.1 or 3.2. Whenever homogeneous nucleation mechanisms are also occurring, the desired purity can be achieved by tuning the parameters to fall as far as possible from the bifurcation line on the same Figures. The model presented here used power law expressions for crystal growth and nucleation. The heterogeneous nucleation laws were constructed to scale with the second moment of the particle distribution. However, these findings are more general and apply to systems for which other kinetic

descriptions are preferred.

Finally, the model reported here readily extends to mulit-polymorphic systems and to crystallizer cascades. [17] There may be fruitful insights gained by combining the attainable region methodology developed by Vetter et al. [37,38] with the present model, but no attempt has been made to combine these approaches at this time.

Notation

Symbol	Units	Description
n_i	number/volume	particle density of polymorph i
G_i	length/time	growth rate of polymorph i
x	length	crystal length coordinate
τ	time	MSMPR residence time
B_i	number/(volume-time)	nucleation rate of polymorph i
C	mass/volume	solute concentration
$k_{g,i}$	length/time	rate constant in growth rate expression i
$k_{b,i}$	number/length^2/time	rate constant in birth rate expression i
ρ	mass/volume	solid density
$m_{0,i}$	number/volume	zeroth moment of polymorph i population
$m_{1,i}$	length/volume	first moment of polymorph i population
$m_{2,i}$	length^2/volume	second moment of polymorph i population
$\omega_{\alpha,j}$	dimensionless	dimensionless j^{th} moment of α population
$\omega_{\beta,j}$	dimensionless	dimensionless j^{th} moment of β population
y	dimensionless	dimensionless concentration

Appendices

3.A Method of Moments and Nondimensionalization

We define $m_{i,j}$ as the j^{th} moment of $n_i(x,t)$ through the equation

$$m_{i,j} = \int_0^\infty x^j n_i(x,t) dx \tag{3.39}$$

Recasting equations 3.1 and 3.6 in terms of the moments of the population distribution

leads to an infinite set of coupled ordinary differential equations

$$\frac{dm_{i,0}}{dt} = -\frac{m_{i,0}}{\tau} + B_i \qquad \frac{dm_{i,j}}{dt} = -\frac{m_{i,j}}{\tau} + jG_i m_{i,j-1} \tag{3.40}$$

$$\frac{dC}{dt} = \frac{C_o - C}{\tau} - \sum_i 4\pi\rho m_{i,2} G_i \qquad i = \alpha, \beta; \quad j = 1, 2, ... \tag{3.41}$$

The mass balance equation contains moments of order 2 or less, and the moment equations of order 3 or higher do not affect those of lower order. Therefore, the set of equations defined by the mass balance and the first three moment equations is sufficient to characterize the relative stability of each steady-state. Higher moments can be added when more detailed information is needed about the populations. Next, we nondimensionalize the set of equations, resulting in the dimensionless states described below:

$$\xi = \frac{t}{\tau} > 0 \qquad y = \frac{C - C_{sat,\beta}}{C_0 - C_{sat,\beta}} \in [0, 1] \tag{3.42}$$

$$\sigma_\alpha = \tau k_{g,\alpha} \left(\frac{C_o - C_{sat,\beta}}{C_{sat,\alpha}} \right)^{g_\alpha} \qquad \sigma_\beta = \tau k_{g,\beta} \left(\frac{C_o - C_{sat_\beta}}{C_{sat,\beta}} \right)^{g_\beta} \tag{3.43}$$

$$\omega_{\alpha,0} = 8\pi\sigma_\alpha^3 m_{\alpha,0}\Gamma \qquad \omega_{\beta,0} = 8\pi\sigma_\beta^3 m_{\beta,0}\Gamma \tag{3.44}$$

$$\omega_{\alpha,1} = 8\pi\sigma_\alpha^2 m_{\alpha,1}\Gamma \qquad \omega_{\beta,1} = 8\pi\sigma_\beta^2 m_{\beta,1}\Gamma \tag{3.45}$$

$$\omega_{\alpha,2} = 4\pi\sigma_\alpha m_{\alpha,2}\Gamma \qquad \omega_{\beta,2} = 4\pi\sigma_\beta m_{\beta,2}\Gamma \tag{3.46}$$

where $\Gamma = \frac{\rho}{C_o - C_{sat,\beta}} > 0$.

3.B Linear Stability Analysis

The following stability analysis determines which steady-state the system evolves towards as a function of the seven stability-relevant parameters (Da_α, Da_β, γ, g_α, g_β, b_α,

and b_β). The eigenvalues of the Jacobian matrix at each steady-state characterize the stability of and the behavior around that steady-state. A general solution for the roots of the characteristic equation has not been determined at this time, so stability has been analyzed using the Liénard-Chipart test. [39] A necessary but insufficient condition for stability is that all the constants in the characteristic equation (a_1-a_7) must be positive.

$$\lambda^7 + a_1\lambda^6 + a_2\lambda^5 + a_3\lambda^4 + a_4\lambda^3 + a_5\lambda^2 + a_6\lambda + a_7 = 0 \tag{3.47}$$

The Liénard-Chipart test provides 3 additional conditions so that there are 10 conditions that must be met for a steady-state to be stable. The conditions for stability of the trivial steady-state are given below in equations 3.48-3.57. The trivial steady-state has the simplest expressions for the Liénard-Chipart test because the y_{ss} terms go to one and

all the moments go to zero. The analysis gives

$$a_1 = 7 > 0 \tag{3.48}$$

$$a_2 = 21 > 0 \tag{3.49}$$

$$a_3 = 35 - (Da_\beta + Da_\alpha(1+\gamma)^{2g_\alpha+b_\alpha}) > 0 \tag{3.50}$$

$$a_4 = 35 - 4(Da_\beta + Da_\alpha(1+\gamma)^{2g_\alpha+b_\alpha}) > 0 \tag{3.51}$$

$$a_5 = 21 - 6(Da_\beta + Da_\alpha(1+\gamma)^{2g_\alpha+b_\alpha}) > 0 \tag{3.52}$$

$$a_6 = 3(1 - Da_\beta) + (Da_\beta - 4)(Da_\alpha(1+\gamma)^{2g_\alpha+b_\alpha} - 1) > 0 \tag{3.53}$$

$$a_7 = (Da_\beta - 1)(Da_\alpha(1+\gamma)^{2g_\alpha+b_\alpha})) - 1) > 0 \tag{3.54}$$

$$D_2 = 112 + Da_\beta + Da_\alpha(1+\gamma)^{2g_\alpha+b_\alpha} > 0 \tag{3.55}$$

$$\begin{aligned} D_4 = {} & 4(10,752 + Da_\beta(544 + Da_\beta(Da_\beta - 28))) + 2Da_\alpha(1,088 + Da_\beta(224 + 9Da_\beta))+ \\ & (1+\gamma)^{2g_\alpha+b_\alpha} + 2Da_\alpha^2(9Da_\beta - 56)(1+\gamma)^{2(2g_\alpha+b_\alpha)} + 4Da_\alpha^3(1+\gamma)^{3(2g_\alpha+b_\alpha)} > 0 \end{aligned} \tag{3.56}$$

$$\begin{aligned} D_6 = {} & (64 - Da_\beta^2)(Da_\alpha^2(1+\gamma)^{2(2g_\alpha+b_\alpha)} - 64)((Da_\beta - 8)^3 + 3Da_\alpha(64 + Da_\beta(Da_\beta + 56)) \\ & (1+\gamma)^{2g_\alpha+b_\alpha} + 3Da_\alpha^2(Da_\beta - 8)(1+\gamma)^{2(2g_\alpha+b_\alpha)} + Da_\alpha^3(1+\gamma)^{3(2g_\alpha+b_\alpha)}) > 0 \end{aligned} \tag{3.57}$$

Of the 10 expressions above, several prove to be redundant or irrelevant when examined closely. Clearly, a_1, a_2, and D_2 cannot be negative, and a_3 and a_4 cannot be violated before a_5. All of the important information is contained in the a_5, a_6, and a_7 expressions. $a_7 > 0$ when either $Da_\beta < 1$ and $Da_\alpha(1+\gamma)^{2g_\alpha+b_\alpha} < 1$ or $Da_\beta > 1$ and $Da_\alpha(1+\gamma)^{2g_\alpha+b_\alpha} > 1$. However, the latter conditions make $a_6 < 0$ for $1 < Da_\beta < 4$ and $a_5 < 0$ for $Da_\beta > 2.5$. Therefore, equations 3.58 and 3.59 are necessary conditions for stability of the trivial steady-state.

$$Da_\beta < 1 \tag{3.58}$$

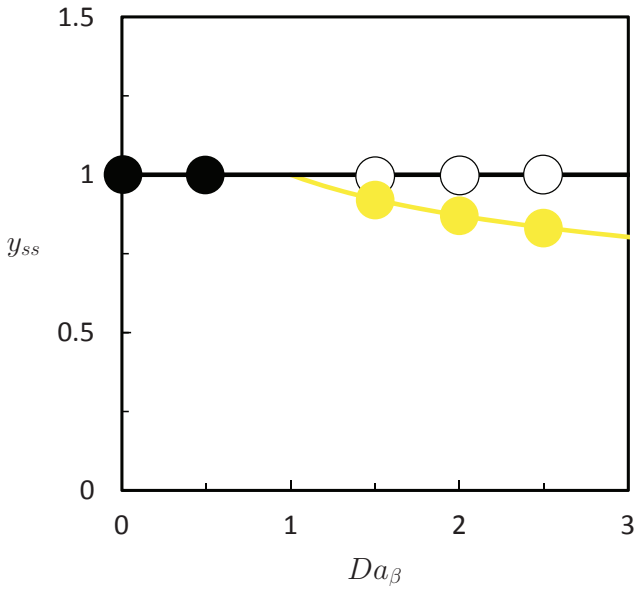

Figure 3.5: When $Da_\beta < 1$, the trivial steady-state is the only possible steady-state. Once Da_β becomes larger than 1, the β steady-state also becomes possible and the trivial steady-state becomes unstable. A bifurcation diagram like this exists for every value of $Da_\alpha(1+\gamma)^{2g_\alpha+b_\alpha} < 1$. Similar diagrams can be constructed for the $y_{ss} - Da_\alpha$ planes.

$$Da_\alpha(1+\gamma)^{2g_\alpha+b_\alpha} < 1 \tag{3.59}$$

If either of these conditions is not met, the Liénard-Chipart test predicts instability. The lines defined by the equality of equation 3.58 and equation 3.59 are bifurcations in the y_{ss}-Da_β and the y_{ss}-Da_α planes respectively. Along the equality of equation 3.58, the pure beta and trivial steady-states coincide, and along the equality of equation 3.59, the pure alpha and trivial steady-states coincide. At lower values of either Damköhler number, the trivial steady-state is the only possible steady-state, but above these critical values, two steady-states become possible. This qualitatively conforms to our expectation that the trivial steady-state becomes dominant as the residence time goes to zero. As expected, the Jacobian matrix is exactly singular along these lines. A representative bifurcation diagram of y_{ss} vs Da_β at a fixed value of $Da_\alpha(1+\gamma)^{2g_\alpha+b_\alpha}$ is shown in Figure 3.5.

We previously presented the specific combination of parameters for which an infinite number of potential steady-states become possible as equation 3.26. All three bifurcation lines in parameter space intersect at exactly one point[5] and therefore cleanly separate the 2-dimensional parameter space parameterized by the left hand side of equations 3.58 and 3.59 into exactly three regions. Knowing that each of these lines is a zero of the determinant of the Jacobian matrix and generally expecting at least three stability transitions in the diagram, we re-parameterize the Liénard-Chipart test for the pure α and β polymorphs in terms of the "distance" from these bifurcation lines.

First, we look at the α polymorph (the thermodynamically metastable polymorph in the L-glutamic acid system). The distance from trivial stability can be further scaled by the growth exponent, as shown below in equation 3.60. This scaled distance will be called ζ and the distance from the α/β bifurcation will be termed ϕ.

$$\zeta = ((1+\gamma)Da_\alpha^{1/(2g_\alpha+b_\alpha)} - 1)g_\alpha \tag{3.60}$$

$$\phi = 1 - Da_\beta(Da_\alpha^{-1/(2g_\alpha+b_\alpha)} - \gamma)^{2g_\beta+b_\beta} \tag{3.61}$$

[5]When each steady-state expression predicts $y_s = 1$

The Liénard-Chipart test for the pure α steady-state now gives

$$a_1 = 7 + \zeta > 0 \tag{3.62}$$

$$a_2 = 7\ (3 + \zeta) > 0 \tag{3.63}$$

$$a_3 = 33 + 21\zeta + \phi > 0 \tag{3.64}$$

$$a_4 = 27 + 4\phi + \zeta\ (32 + \phi + \frac{b_\alpha}{g_\alpha}) > 0 \tag{3.65}$$

$$a_5 = 9 + 4g_\alpha(1 - \phi) + 6\phi + \zeta\ (24 + 3\frac{b_\alpha}{g_\alpha} + 4\phi) > 0 \tag{3.66}$$

$$a_6 = 3\ (2g_\alpha(1 - \phi) + \phi + \zeta\ (2 + \frac{b_\alpha}{g_\alpha} + 2\phi)) > 0 \tag{3.67}$$

$$a_7 = \zeta\ (2 + \frac{b_\alpha}{g_\alpha})\phi > 0 \tag{3.68}$$

$$D_2 = 114 + 7\zeta\ (7 + \zeta) - \phi > 0 \tag{3.69}$$

For the case of L-glutamic acid, the D_4 and D_6 conditions are never violated first, and they result in very long expressions unsuitable for print, so they have been omitted.[6] These expressions show that the pure alpha state becomes unstable whenever either ζ or ϕ become negative. Notice that ϕ is bounded between $-\infty$ and 1 because both Da_α and Da_β are strictly positive quantities. Similarly, ζ is bounded between $-g_a$ and ∞. Therefore, the general expressions for the first 8 stability conditions imply that the α polymorph is the stable steady-state when $\zeta > 0$, $0 < \phi < 1$. This finding is independent of the growth and birth exponents (g_α, b_α, g_β, b_β), the relative polymorph solubility and/or feed concentration (γ), or of the scaling convention.[7] This result justifies the change of variables because $\zeta > 0$, $0 < \phi < 1$ maps exactly onto the rightmost 2-

[6] Failing these last two tests leads to oscillatory solutions around the steady-state predicted to be stable by the preceding 8 tests, so nothing changes qualitatively in the systems in which the last two tests become relevant.

[7] We have scaled the concentrations with respect to the most stable thermodynamic polymorph. This results in y varying from 0 to 1 and $\gamma < 0$. If the opposite convention is adopted, the results do not change, except y now varies between 0 and $1 + \gamma$ and $\gamma > 0$.

dimensional region described by equations 3.27-3.32. The same analysis can be done for the β polymorph to show that it is stable in the region of state space that has already been shown to be unstable to the other 2 steady-states. As previously mentioned, it is generally possible for a steady-state with $\zeta > 0$ and $0 < \phi < 1$ to fail the D_4 and D_6 stability criteria for solutes other than L-glutamic acid. It has already been shown that a stable trivial or pure β steady-state is inconsistent with $\zeta > 0$ and $0 < \phi < 1$, so these instabilities must correspond to orbitally stable oscillations around the pure α unstable steady-state. While these oscillatory solutions do not occur in the L-glutamic acid system, they have been observed elsewhere. [40] Results not included here have shown that they arise at much higher ratios of b_α/g_α (e.g., $b_\alpha/g_\alpha > 10$).

3.C Stability as a function of τ

Here, we give a general proof that the thermodynamically stable polymorph is the stable steady-state in the large τ limit. First, we define a function to represent each axis in Figure 3.1:

$$f = \left[(Da_\alpha^{\frac{-1}{2g_\alpha+b_\alpha}} - \gamma)\right]^{-1} \qquad g = \left[Da_\beta{}^{\frac{-1}{2g_\beta+b_\beta}}\right]^{-1} \tag{3.70}$$

Now we take the derivative of both with respect to τ, holding everything else constant:

$$\frac{\partial f}{\partial \tau} = \frac{3}{(2g_\alpha+b_\alpha)\tau}\frac{Da_\alpha^{\frac{-1}{2g_\alpha+b_\alpha}}}{\left[(Da_\alpha^{\frac{-1}{2g_\alpha+b_\alpha}} - \gamma)\right]^2} \qquad \frac{\partial g}{\partial \tau} = \frac{3}{(2g_\beta+b_\beta)\tau}Da_\beta{}^{\frac{1}{2g_\beta+b_\beta}} \tag{3.71}$$

Therefore, the slope of the solution branch as τ increases is given by:

$$\frac{\partial g}{\partial f} = \frac{(2g_\alpha+b_\alpha)}{(2g_\beta+b_\beta)}\frac{Da_\beta{}^{\frac{1}{2g_\beta+b_\beta}}}{Da_\alpha^{\frac{1}{2g_\alpha+b_\alpha}}}\left[1-\gamma(Da_\alpha^{\frac{1}{2g_\alpha+b_\alpha}})\right]^2 \tag{3.72}$$

Both Da_α and Da_β scale with τ^3, so expression 3.72 can be rewritten:

$$\frac{\partial g}{\partial f} = k_1 \tau^{\left(\frac{3}{2g_\beta + b_\beta} - \frac{3}{2g_\alpha + b_\alpha}\right)} \left[1 - \gamma (k_2 \tau^{\frac{3}{2g_\alpha + b_\alpha}})\right]^2 \tag{3.73}$$

where k_1 and k_2 are positive constants. There are several relevant cases to consider. If α is thermodynamically metastable, then $\gamma < 0$ and the large τ limit becomes

$$\frac{\partial g}{\partial f} \rightarrow k_1 k_2^2 \gamma^2 \tau^{3\left[\frac{1}{2g_\beta + b_\beta} + \frac{1}{2g_\alpha + b_\alpha}\right]} \rightarrow \infty \tag{3.74}$$

Since the slope goes to ∞, then a solution branch that starts in the metastable polymorph stability region will eventually cross the $\alpha - \beta$ bifurcation line and move into the stable polymorph stability region in Figure 3.1.

If instead, we name the thermodynamically stable polymorph α, then $\gamma > 0$ and $\left[1 - \gamma Da_\alpha^{\frac{1}{2g_\alpha + b_\alpha}}\right] = 0$ corresponds to $C = C_{sat,\beta}$. At this point, any increase in τ drives the solute concentration below the metastable polymorph's solubility (now β), and therefore guarantees a pure, thermodynamically stable steady-state. As this bifurcation point is approached on the solution curve,

$$\frac{\partial g}{\partial f} \rightarrow k_1 \tau^{3\left[\frac{1}{2g_\beta + b_\beta} - \frac{1}{2g_\alpha + b_\alpha}\right]} \left[1 - \gamma k_2 \tau^{\frac{3}{2g_\alpha + b_\alpha}}\right] \rightarrow 0 \tag{3.75}$$

A slope of zero means that again, regardless of the starting point, one can always follow the solution branch into the thermodynamically stable (now α) region. Therefore, the thermodynamicly stable polymorph is also the dynamically stable steady-state in the limit of long residence time, and the design rules correctly predict the stable steady state in this limit, regardless of the naming convention.

Bibliography

[1] H. G. Brittain. *Polymorphism in Pharmaceutical Solids*. CRC Press, 2009.

[2] J. Bernstein. *Polymorphism in Molecular Crystals*. Oxford University Press, 2008.

[3] S. R. Byrn. *Solid-state Chemistry of Drugs*. Academic Press, 1982.

[4] A. Y. Lee, D. Erdemir, and A. S. Myerson. Crystal polymorphism in chemical process development. *Annual Review of Chemical and Biomolecular Engineering*, 2:259–280, 2011.

[5] J. Bauer, S. Spanton, R. Henry, J. Quick, W. Dziki, W. Porter, and J. Morris. Ritonavir: An extraordinary example of conformational polymorphism. *Pharm. Res.*, 18(6):859–866, 2001.

[6] A. Nangia and T. N. Guru Row. Polymorphism. *CrystEngComm*, 17:1528, 2015.

[7] P. T. Cardew and R. J. Davey. The kinetics of solvent-mediated phase transformations. *Proc. R. Soc. Lond.*, 398:415–428, 1985.

[8] W. Ostwald. Studien uber die bildung und umwandlung fester korperr. *Zeitschrift fur physikalische Chemie*, 22:289–330, 1897.

[9] C. Cashell, D. Corcoran, and B. K. Hodnett. Control of polymorphism and crystal size of l-glutamic acid in the absence of additives. *J. Cryst. Growth*, 273(1-2):258–265, 2004.

[10] N. C. Kee, R. B. Tan, and D. Braatz, Richard. Selective crystallizationof the metastable α-form of l-glutamic acid using concentration feedback control. *Crys. Growth Des.*, 9(7):3044–3051, 2009.

[11] R. P. Sangodkar, B. J. Smith, D. Gajan, A. Rossini, L. R. R., G. P. Funkhouser, A. Lesage, L. Emsley, and B. F. Chmelka. Influences of dilute organic adsorbates on the hydration of low-surface-area silicates. *Journal of American Chemical Society*, 137:8096–8112, 2015.

[12] M. W. Hermanto, M. Chiu, and R. D. Braatz. Nonlinear model predictive control for the polymorphic transformation of l-glutamic acid crystals. *AIChE J.*, 54.12:3248–3259, 2009.

[13] X. Yang, B. Sarma, and A. S. Myerson. Polymorph control of micro/nano-sized mefenamic acid crystals on patterned self-assembled monolayer islands. *Cryst. Growth Des.*, 12:5221–5228, 2012.

[14] I. S. Lee, A. Y. Lee, and A. S. Myerson. Concomitant polymorphism in confined environment: Implication to crystal form screening. *Pharm. Res.*, 25:960–968, 2008.

[15] E. Simone, A. N. Saleemi, N. Tonnon, and Z. K. Nagy. Active polymorphic feedback control of crystallization processes using a combined raman and atr-uv/vis spectroscopy approach. *Cryst. Growth Des.*, 14:1839–1850, 2014.

[16] T. Lai, S. Ferguson, L. Palmer, B. L. Trout, and A. S. Myerson. Continuous crystallization and polymorph dynamics in the l-gltanic acid system. *Org. Process Res. Dev.*, 18:1382–1390, 2014.

[17] T. C. Lai, J. Cornevin, S. Ferguson, N. Li, B. L. Trout, and A. S. Myerson. Control of polymorphism in continuous crystallization via mixed suspension mixed product removal systems cascade design. *Cryst. Growth Des.*, 15.7:3374–3382, 2015.

[18] J. Hostomsky and A. Jones. Calcium carbonate crystallization, agglomeration and form during continuous precipitation from solution. *J. Phys. D: Appl. Phys.*, 24:165–170, 1991.

[19] H. Nebel and M. Epple. Continuous preparation of calcite, aragonite and vaterite, and of magnesium-substituted amorphous calcium carbonate (mg-acc). *Zeitschrift für anorganische und allgemeine Chemie*, 634(8):1439–1443, 2008.

[20] A. S. Myerson. Concluding remarks. *Faraday Discussions*, 179:543, 2015.

[21] D. Kashchiev and G. van Rosmalen. Nucleation in solutions revisited. *Crystal Research and Technology*, 38:555–574, 2003.

[22] C. Lindenberg and M. Mazzotti. Effect of temperature on the nucleation kinetics of α l-glutamic acid. *Cryst. Growth Des.*, 311(4):1178–1184, 2009.

[23] A. M. Lyapunov. *The general problem of the stability of motion*. Taylor and Francis, 1992.

[24] M. Friedman. The methomethod of positive economics. In *Essays in Positive Economics*, pages 3–16. University of Chicago Press, 1966.

[25] More kirk than spock. 2015.

[26] J. Worlitschek and M. Mazzotti. Model-based optimization of particle size distribution in batch-cooling crstallization of paracetamol. *Cryst. Growth Des.*, 4(5):891–903, 2004.

[27] J. Li, B. L. Trout, and A. S. Myerson. Multistage continuous mixed-suspension, mixed-product removal (msmpr) crystallization with solids recycle. *Org. Process Res. Dev.*, 20:510–516, 2015.

[28] C. Lindenberg, J. Scholl, L. Vicum, M. Mazzotti, and J. Brozio. L-glutamic acid precipitation: Agglomeration effects. *Cryst. Growth Des.*, 8(1):224–237, 2008.

[29] W. K. Burton, N. Cabrera, and F. C. Frank. The growth of crystals and the equilibrium structure of their surfaces. *Philosophical Transactions of the Royal Society A*, 243(866):299–358, 1951.

[30] C. Cashell, D. Corcoran, and B. K. Hodnett. Secondary nucleation of the β-polymorph of l-glutamic acid on the surface of α-form crystals. *Chemical Communications*, 3:374–375, 2003.

[31] J. Cornel, C. Lindenberg, and M. Mazzotti. Experimental characterization and population balance modeling of the polymorph transformation of l-glutamic aci. *Cryst. Growth Des.*, 9(1):243–252, 2009.

[32] T. Ono, H. J. M. Kramer, J. H. ter Horst, and P. J. Jansens. Process modeling of the polymorphic transformation of l-glutamic acid. *Cryst. Growth Des.*, 4(6):1161–1167, 2004.

[33] J. Scholl, L. Bonalumi, D. Vicum, and M. Mazzotti. In situ monitoring and modeling of the solvent-mediated polymorphic transformation of l-glutamic acid. *Cryst. Growth Des.*, 6(5):881–891, 2006.

[34] S. H. Chung, D. L. Ma, and R. D. Braatz. Optima lmodel-based experimental design in batch crystallization. *Chemometrics and Intelligent Laborary Systems*, 50:83–90, 2000.

[35] R. Gunawan, D. L. Ma, M. Fujiwara, and R. D. Braatz. Identification of kinetic pparameter in multidimensional crystallization processes. *International Journal of Modern Physics B*, 2002.

[36] S. Y. Wong, Y. Cui, and A. S. Myerson. Contact secondary nucleation as a means of creating seeds for continuous tubular crystallizers. *Cryst. Growth Des.*, 13:2514–2521, 2013.

[37] T. Vetter, C. L. Burcham, and M. F. Doherty. Regions of attainable particle sizes in continuous and batch crystallization processes. *Chem. Eng. Sci.*, 106:167–180, 2014.

[38] T. Vetter, C. L. Burcham, and M. F. Doherty. Designing robust crystallization processes in the presence of parameter uncertainty using attainable regions. *Ind. Eng. Chem. Res.*, 54(42):10350–10363, 2015.

[39] A. Lienard and M. H. Chipart. Sur le signe de la partie réelle des racines dŠune équation algébrique. *Journal de Mathématiques Pures et Appliquées*, 10.6:291–346, 1914.

[40] G. Jerauld, Y. Vasatis, and M. F. Doherty. Simple conditions for the appearance of sustained oscillations in continuous crystallizers. *Chem. Eng. Sci.*, 38:1675–1681, 1983.

Chapter 4

Polymorph Selection by Continuous Precipitation

Reprinted with permission from:

Thomas C. Farmer, Sina Schiebel, Bradley F. Chmelka, and Michael F. Doherty, "Polymorph Selection by Continuous Precipitation." Crystal Growth & Design (2018).

DOI: 10.1021/acs.cgd.8b00116.

4.1 Introduction

Polymorphism has been prominent in the study of material science and industrial crystallization for over 180 years, [1, 2] and the primary mechanism of polymorphic interconversion, known as solvent-mediated phase transformation, has been postulated, modeled, and experimentally validated over the past 35 years. [3–5] Polymorph selection and control has maintained attention over such long periods of time due to the technological implications of polymorphic variation of a compound's mechanical, electrical, optical, chemical, solubility, bioavailabillity, and bio-activity properties. [6–9] Controlling poly-

morphism in industrial processes has remained difficult and at times elusive, as demonstrated by the extensive literature on concentration control, temperature control, additive selection, templating materials, solvent choice, and combinatoric screening. [10–18] Recently, the ability to produce single polymorph crystal distributions using continuous crystallization has been demonstrated for *L*-glutamic acid and *p*-aminobenzoic acid systems. [19, 20] These observations motivated the development of general design rules for producing pure distributions of any preferred polymorph in a continuous crystallizer dominated by size-independent linear crystal growth and secondary nucleation, regardless of the thermodynamic stability of the desired solid form. [21] This is an unrestrictive set of assumptions that covers many organic crystal systems, including the vast majority of pharmacologically active small molecules. [22, 23]

Still, there are other crystal/crystallizer systems of industrial relevance for which other rate-processes could become important. For example, a process could exhibit (1) homogeneous nucleation, (2) metastable-form nucleation from the surface of a relatively stable form, (3) alternative growth or nucleation rate expressions, (4) agglomeration, (5) breakage, (6) chemical reaction in solution, or (7) a number of possible process permutations (e.g., putting two devices in series, recycling solids, etc.). The first three of these were discussed and classified as qualitatively unimportant for purposes of solid form selection during well-mixed, continuous crystallizations in our previous publication. [21] The last four have not yet been considered and are expected to become important in some crystal systems.

One system of special interest is the reactive precipitation of $CaCO_3$ from Na_2CO_3 and $CaCl_2$. This system exhibits chemical reaction in solution, significant agglomeration, and five unique solid forms near STP: 3 crystalline polymorphs, a crystalline hydrate, and an amorphous form. [24] Furthermore, it is technologically interesting because of efforts to make cementitious materials from flue gases for carbon capture. For this type

of process scheme to work, the solids produced must exhibit suitable material properties for structural materials applications. The patent literature suggests that the thermodynamically stable form of $CaCO_3$ (calcite) is unlikley to make a suitable construction material, while vaterite (highest energy crystalline form) and amorphous calcium carbonnate (ACC, highest energy, amorphous form) seem to work quite well. [25, 26] Therefore, we are presented with the specific challenge of directing solid form during $CaCO_3$ precipitation as a step towards developing carbon capture and utilization processes.

Still, there are many other systems for which solid form selection is a pivotal engineering objective, so here, we address the general challenge of polymorph selection during agglomerative precipitations. Agglomeration events decrease total crystal number density and reduce total crystal surface area. Crystals grow from the surface, so less crystal surface area implies a lower *total* (distribution integrated) growth rate. Therefore, agglomeration changes the relative magnitudes of growth, nucleation, and product removal rates within a crystallizer. Altering the relative rates has a significant effect on the dynamic stability of the various steady-states and therefore on the design rules for solid form selection.

We have characterized the impact of agglomeration on the steady-state multiplicity and relative steady-state dynamic stability by generating and analyzing a bi-polymorph agglomeration-enabled precipitator model. We have demonstrated that adding agglomeration to the model enables the mixed-polymorph steady-states that are often observed during the continuous precipitation of $CaCO_3$, but that were unpredictable with a non-agglomerating, continuous crystallizer model. [21] The insights gained from analyzing the agglomeration-enabled model can be used to direct polymorphism in agglomerative systems such as the technologically, geologically, and biologically important $CaCO_3$ system.

Experimental measurements confirmed the model predictions, yielding pure metastable polymorphs under steady-state process conditions. Polymorph selection can be achieved

through manipulation of the dynamic stability of competing steady-states in a continuous device through this type of process design. Under such circumstances, the resulting process is inherently simple to control. Furthermore, the thermodynamically metastable vaterite crystals generated in this way do not transform to the more stable calcite polymorph over the time scales we have thus far measured and observed (months).

4.2 Theory: Model Equations

The semantic distinction between precipitation and crystallization has different meanings to different investigators. [27, 28] Here, we use the term precipitation to encompass the class of crystallization processes characterized by very high solute supersaturations. These supersaturations are typically generated by chemical reaction of two soluble reactants to form a sparingly soluble product. In these processes, desupersaturation is typically dominated by nucleation, and large crystals form primarily from the agglomeration of many smaller crystals. Crystallization is characterized by lower supersaturations, in which the desupersaturation is dominated by crystal growth. In crystallization, agglomeration tends to have less of an impact on the final distribution of crystal sizes. Often, all three mechanisms need to be taken into account (e.g., $CaCO_3$ precipitation at high supersaturation and paracetamol crystallization at lower supersaturations [29]), and naming the method of crystal formation becomes more a matter of preference and tradition. Some precipitative systems can be described as if the crystal growth rates are exactly zero, [30] but this is not a reasonable approximation for crystallizations.

A multi-polymorph continuous precipitation process can be modeled as the system of partial differential integral equations shown in Equations 4.1-4.3. These equations are generated by applying a population balance and a solute/mass balance to a multi-polymorph, continuous, mixed-suspension, mixed-product-removal (MSMPR) crystal-

lizer. A population balance model is a mathematical expression of conservation of a distributed quantity under the influence of some rate mechanisms described by constitutive rate laws. Therefore, a population balance describes how a distribution changes as a function of time. In this case, that distibution is the crystal size distribution, $n_i(t,x)$, where $n_i(t,x)$ denotes the crystal number density of form i as a function of t (time) and x (crystal length, if spherical then x is crystal radius or diameter). This distribution has units of number per volume per length, such that the integral $\int_{x_a}^{x_b} n_i(t,x)dx$ gives the crystal number density of solid form i between the lengths x_a and x_b as a function of t. For an agglomeration-enabled continuous precipitator, the relevant rate processes that require a constitutive rate law are secondary nucleation (B_i), size-independent linear crystal growth (G_i), and crystal agglomeration. The rate expressions we have chosen for nucleation and growth are given in Equation 4.6. We discussed these rate expression choices in detail in our previous paper and demonstrated that the analysis and results are qualitatively similar for different sets of rate expressions. [21] In fact, the only significant change in the governing system of equations from our previous paper is the notable addition of the two integral terms that describe crystal agglomeration. The first integral term quantifies the combined crystal number density available to form a crystal of length x, as a function of x. The second integral term quantifies the combined crystal number density available for removal from the distribution due to agglomeration events involving a crystal of size x, as a function of x. In both cases, the combined crystal number density is converted to an agglomeration rate through an agglomeration kernel β_i (agglomeration frequency rate coefficient). In general, β_i can be a function of size (x) and supersaturation (S, the ratio of the solute concentration in the device to its saturation concentration), but it will be considered a constant throughout this article. The integral expressions in Equation 4.1 are the simplest expressions possible that conserve volume/mass when the crystal size coordinate has units of length. [31,32] The initial and boundary conditions

are standard and discussed elsewhere. [31, 33] The resulting partial differential integral equation that governs the distribution dynamics of form i is shown in Equations 4.1-4.3

$$\frac{\partial n_i}{\partial t} + G_i \frac{\partial n_i}{\partial x} = -\frac{n_i}{\tau} + \frac{\beta_i x^2}{2} \int_0^x \frac{n_i((x^3-\lambda^3)^{1/3}) n_i(\lambda)}{(x^3-\lambda^3)^{2/3}} d\lambda - \beta_i n_i(x) \int_0^\infty n_i(\lambda) d\lambda \quad (4.1)$$

$$B_i = k_{b,i}\left((\frac{C_1 C_2}{K_{eq/i}})^{1/2} - 1 \right)^{b_i} m_{i,2} \qquad G_i = k_{g,i}\left((\frac{C_1 C_2}{K_{eq/i}})^{1/2} - 1 \right)^{g_i} \quad (4.2)$$

$$i = \alpha, \beta \qquad n_i(t=0,x) = n_{i,seed} \qquad n_i(t,x=0) = \frac{B_i}{G_i} \quad (4.3)$$

where $n_{i,seed}$ is a distribution of seed crystals introduced as a pulse at $t = 0$, $K_{eq,i}$ is the equilibrium solubility constant for form i, C_1 and C_2 are the molar concentrations of Ca^{2+} and CO_3^{2-} ions in solution, and τ is the MSMPR residence time. The 1/2 power that appears in the growth and nucleation driving forces was justified in a previous publication. [34] In general, there are p polymorphs, denoted by the subscript i. Here, the two form case is explicitly considered and analyzed, and the form that is thermodynamically stable at STP (calcite) will be given the subscript $i = \beta$ and the metastable form (vaterite) will be given the subscript $i = \alpha$ (consistent with our previous work). [21] The multi-polymorph case is again considered and discussed in the conclusions.

Another modification to the previous model arises due to the reaction chemistry inherent in this type of reactive precipitation process. The chemistry adds additional mole balance ODEs and additional model parameters and design choices related to the reaction rates and the feed stoichiometry. When the feed is stoichiometric and the pH is relatively high, the mole balance ODEs and the growth and nucleation rate expressions simplify to Equations 4.4 and 4.6, as discussed in detail in the Supplementary Information. These

conditions will be met for the experiments discussed throughout this article.

$$\frac{dC}{dt} = \frac{C_0 - C}{\tau} - \sum_{i=\alpha,\beta...} \rho_i k_{i,v} k_{i,g} \left(\frac{C}{K_{eq,i}^{1/2}} - 1 \right)^{g_i} \int_0^\infty n_i x^2 dx \tag{4.4}$$

$$C(t=0) = C_0 \tag{4.5}$$

$$B_i = k_{i,b} \left(\frac{C}{K_{eq,i}^{1/2}} - 1 \right)^{b_i} \int_0^\infty x^2 n_i(t,x) dx \qquad G_i = k_{i,g} \left(\frac{C}{K_{eq,i}^{1/2}} - 1 \right)^{g_i} \tag{4.6}$$

ρ_i is the molar density of solid form i and $k_{i,v}$ is a shape factor. A derivation of these equations and a discussion of the implication of a non-stoichiometric feed are both available in the Supplementary Information. It is also worth noting that all of the concentrations, equilibrium constants, and densities have been defined on a molar basis here. A mass basis was used in the previous, non-agglomerating model, but a mole basis is more convenient when chemical reactions occur.

Fixed Point Quadrature Method of Moments (F-QMOM)

The method of moments is an integral transformation that allows one to monitor and analyze the moments of a distribution, instead of considering the entire distribution. This transformatoin finds utility in applications for which a more detailed knowledge of a distribution's dynamics is unnecessary. Here, we are concerned with determining process conditions for which a crystal size distribution under the influence of nucleation, growth, agglomeration, and convective flow exhibits one solid form or another. This problem is an ideal candidate for the method of moments because the relative fraction of each form can be determined from the moments of each distribution alone. Typically, application of

the method of moments is restricted to cases in which the moment ODEs close. Closure occurs when the dynamics of some set of moments can be described in terms of only model parameters and moments of order $k \leq N$ (where k is the subscript denoting the moment order, and N is the total number of moments neccessary for closure). Closure is not met when the moment transformation fails to remove all of the $n_i(t,x)$ terms or when lower order moments always depend on higher order moments, neccessitating a solution of the full PDE or of the entire infinite set of moment equations, respectively. Applying the method of moments and a change of variables ($u^3 = x^3 - \lambda^3$) [35] to the agglomeration terms results in Equation 4.7 for the k^{th} moment of the i distribution:

$$\int_0^\infty x^k \left[\frac{\beta_i x^2}{2} \int_0^x \frac{n_i((x^3-\lambda^3)^{1/3}) n_i(\lambda)}{(x^3-\lambda^3)^{2/3}} d\lambda - \beta_i n_i(x) \int_0^\infty n_i(\lambda) d\lambda \right] dx = \frac{\beta_i}{2} \int_0^\infty n_i(\lambda) \int_0^\infty (u^3+\lambda^3)^{k/3} n_i(u) du d\lambda - \beta_i m_{i,k} m_{i,0} \tag{4.7}$$

where $m_{i,k}$ is the k^{th} moment of the i distribution (the method of moments is described in more detail in the Supplmentary Information). Unfortunately, the transformation does not close as defined, though closure can be enforced numerically with a technique termed the quadrature method of moments (QMOM). [36] The QMOM utilizes only the moments of a distribution to estimate integrals over the unknown distribution. The quadrature rule can be defined from the moments using the product-difference algorithm developed by Gordon, [37] by reformulating the model as a system of differential algebraic equations (DAE) using the algebraic definition of the quadrature rule, [38] by tracking the weights and abscissas of the quadrature rule directly through a Jacobian matrix transformation, [39] or by fixing the abscissas at zeros of an orthogonal basis set and directly calculating the weights such that the known moments are recreated exactly. [40] The latter method has been named the Fixed point Quadrature Method of Moments (F-QMOM) and is used here. With the moments defined from the moment ODEs and

the abscissas (L_j) defined as zeros of some orthogonal basis set, the weights (μ_j) can be calculated from Equation 4.8:

$$m_k = \sum_j L_j^k \mu_j \tag{4.8}$$

This can be written in matrix form by defining the matrix $\mathbf{Q}$:

$$Q_{l,j} = L_j^{l-1} \tag{4.9}$$

giving:

$$\mathbf{m} = \mathbf{Q}\mu \tag{4.10}$$

The abscissas or lengths in the quadrature rule can be chosen as the zeros of any orthgonal basis set of polynomials, although the choice of basis set will affect the computation speed and accuracy. [41] Once an orthogonal basis set is chosen, the abscissas are known, and the matrix $\mathbf{Q}$ becomes constant and known. Therefore, one can always define the weights as a known linear combination of the moments as in Equation 4.11:

$$\mu = \mathbf{Q^{-1}m} \tag{4.11}$$

Once the abscissas and weights are known, the remaining integral term in Equation 4.7 can be re-written as the sum in Equation 4.12:

$$\frac{\beta}{2}\int_0^\infty n(\lambda)\int_0^\infty (u^3+\lambda^3)^{k/3} n(u)du d\lambda = \frac{\beta}{2}\sum_l \mu_l \sum_j (L_l^3 + L_j^3)^{k/3}\mu_j \tag{4.12}$$

This can be re-written again as a compact function of only the abscissas and moments by first defining a new three-dimensional matrix $\mathbf{F_k}$:

$$F_k(l,j) = \frac{1}{2}(L_l^3 + L_j^3)^{k/3} \tag{4.13}$$

then Equation 4.12 becomes:

$$\frac{\beta}{2}\int_0^\infty n(\lambda)\int_0^\infty (u^3+\lambda^3)^{k/3} n(u)dud\lambda = \beta\ \mathbf{m'}\ \mathbf{Q^{-1'}}\ \mathbf{F_k}\ \mathbf{Q^{-1}}\ \mathbf{m} \tag{4.14}$$

where $'$ represents a vector or matrix transpose. For every k, this vector-matrix multiplication results in a scalar sum of moment terms up to order $(N-1)$, where N is the number of moments tracked by the model. When written this way, one can increase the accuracy (and computation time) at will by increasing N and adding abscissas from higher order polynomials in the same orthogonal basis set. (Care should also be taken to scale the moments, such that the distribution can be accurately represented by abscissas $\in [0,1]$). After non-dimensionalization (details in Supplementary Information), the resulting model contains $3p+1$ ODEs and $5p-1$ parameters, where p is the number of solid forms included in the model. When considering a metastable polymorph (e.g., vaterite $= \alpha$) and a stable polymorph (e.g., calcite $= \beta$), $p = 2$, and there are $5p-1 = 9$ dimensionless parameters of which $2p$ are exponents in the growth and nucleation rate laws (g_i and b_i). The others are combinations of physical parameters that make up dimensionless groups. For example, $p-1$ of these dimensionless groups are solubility factors that quantify the differences in nucleation and growth driving forces among the various solid forms (γ):

$$\gamma = \frac{K_{eq,\beta}^{1/2} - K_{eq,\alpha}^{1/2}}{C_0 - K_{eq,\beta}^{1/2}} < 0 \tag{4.15}$$

All variables are defined in the notation section, and the non-dimensionalization procedure that leads to these dimensionless groups is detailed in the Supplementary Information. The other $2p$ are relative rates that can be rationally manipulated (or engineered) by the intelligent selection of process variables such as temperature, inlet supersaturation, residence time, and solvent. These are termed Damköhler (Da_i) and Agglomeration

(A_i) numbers:

$$Da_\alpha = 2\tau k_{\alpha,b}\left(\frac{C_0 - K_{eq,\beta}^{1/2}}{K_{eq,\alpha}^{1/2}}\right)^{b_\alpha}\sigma_\alpha^2 > 0 \qquad Da_\beta = 2\tau k_{\beta,b}\left(\frac{C_0 - K_{eq,\beta}^{1/2}}{K_{eq,\beta}^{1/2}}\right)^{b_\beta}\sigma_\beta^2 > 0 \quad (4.16)$$

$$A_\alpha = \frac{\beta_\alpha \tau}{8\pi\sigma_\alpha^3}\frac{\left(C_0 - K_{eq,\alpha}^{1/2}\right)}{\rho_\alpha} > 0 \qquad A_\beta = \frac{\beta_\beta \tau}{8\pi\sigma_\beta^3}\frac{\left(C_0 - K_{eq,\beta}^{1/2}\right)}{\rho_\beta} > 0 \quad (4.17)$$

where σ_i is the characteristic growth length for form i defined as

$$\sigma_\alpha = \tau k_{\alpha,g}\left(\frac{C_0 - K_{eq,\beta}^{1/2}}{K_{eq,\alpha}^{1/2}}\right)^{g_\alpha} \qquad \sigma_\beta = \tau k_{\beta,g}\left(\frac{C_0 - K_{eq,\beta}^{1/2}}{K_{eq,\beta}^{1/2}}\right)^{g_\beta} \quad (4.18)$$

The Damköhler numbers are given this name due to their physicochemical similarity to the Damköhler numbers in reaction engineering. These groups are ratios of the residence time to the crystallization time of each form, such that the rates of nucleation and growth of form i are fast relative to the process residence time when Da_i is large, and slow when Da_i is small. The Damköhler numbers and the solubility correction factor (γ) were discussed in detail in our earlier paper, although the notation is slightly different here due to the reaction chemistry (To translate from one to the other, set $C_{sat,i} = K_{eq,i}^{1/2}$). The Agglomeration numbers are a new feature of the agglomeration-enabled population balance model. Each Agglomeration number is a ratio of the process time (τ) to the agglomeration time associated with that form $(\approx \beta_i^{-1})$. Therefore, agglomeration becomes a more dominant rate process within the precipitator as the Agglomeration numbers increase.

Now, the ODE system can be presented in terms of the vector/matrix operations referenced in Equation 4.14, the dimensionless moments $(\omega_{i,k} \in [0,\infty))$, the dimensionless time $(\xi \in [0,\infty))$, the dimensionless solute concentration $(y \in [0,1])$, and the dimension-

less groups. The $3p + 1 = 7$ resulting ODEs are:

$$\frac{d\omega_{\alpha,0}}{d\xi} = -\omega_{\alpha,0} + Da_\alpha (y+\gamma)^{b_\alpha} \omega_{\alpha,2} - \frac{A_\alpha}{2}\omega_{\alpha,0}^2 \tag{4.19}$$

$$\frac{d\omega_{\alpha,1}}{d\xi} = -\omega_{\alpha,1} + (y+\gamma)^{g_\alpha}\omega_{\alpha,0} + A_\alpha \left({\omega_\alpha}' \, \mathbf{Q^{-1'}} \, \mathbf{F_1} \, \mathbf{Q^{-1}} \, \omega_\alpha - \omega_{\alpha,1}\omega_{\alpha,0}\right) \tag{4.20}$$

$$\frac{d\omega_{\alpha,2}}{d\xi} = -\omega_{\alpha,2} + (y+\gamma)^{g_\alpha}\omega_{\alpha,1} + A_\alpha \left({\omega_\alpha}' \, \mathbf{Q^{-1'}} \, \mathbf{F_2} \, \mathbf{Q^{-1}} \, \omega_\alpha - \omega_{\alpha,2}\omega_{\alpha,0}\right) \tag{4.21}$$

$$\frac{d\omega_{\beta,0}}{d\xi} = -\omega_{\beta,0} + Da_\beta y^{b_\beta} \omega_{\beta,2} - \frac{A_\beta}{2}\omega_{\beta,0}^2 \tag{4.22}$$

$$\frac{d\omega_{\beta,1}}{d\xi} = -\omega_{\beta,1} + y^{g_\beta}\omega_{\beta,0} + A_\beta \left({\omega_\beta}' \, \mathbf{Q^{-1'}} \, \mathbf{F_1} \, \mathbf{Q^{-1}} \, \omega_\beta - \omega_{\beta,1}\omega_{\beta,0}\right) \tag{4.23}$$

$$\frac{d\omega_{\beta,2}}{d\xi} = -\omega_{\beta,2} + y^{g_\beta}\omega_{\beta,1} + A_\beta \left({\omega_\beta}' \, \mathbf{Q^{-1'}} \, \mathbf{F_2} \, \mathbf{Q^{-1}} \, \omega_\beta - \omega_{\beta,2}\omega_{\beta,0}\right) \tag{4.24}$$

$$\frac{dy}{d\xi} = 1 - y - \omega_{2,\beta} y^{g_\beta} - \omega_{2,\alpha}(y+\gamma)^{g_\alpha} \tag{4.25}$$

In the limit $A_\alpha, A_\beta \to 0$, the original, non-agglomerating model is recovered. [21] More details on the derivation and non-dimensionalization of both the stoichiometric (presented here) and non-stoichiometric feed cases are provided in the Supplementary Information.

Parameter continuation of model elucidates steady-state structure

Ideally, process engineers seek to understand how process outputs change as functions of design and operation decision variables. Some systems exhibit steady-state multiplicity, and in these systems, process dynamics play a significant role in process design. Relating decision variables to process outputs requires relating decision variables to the relative dynamic stability of the qualitatively distinct steady-states. With this information, one can make rational design decisions such that a preferred steady-state is obtained and maintains its dynamic stability. When this procedure proves difficult or impossible, one can typically design new degrees of freedom to expand the range of attainable outcomes (for polymorph selection, one could imagine adding a solids recycle,

multiple crystallizers in series, templating additives in the feed, changing the solvent, etc.).

This precipitator model predicts 4 qualitatively distinct steady-states: (1) trivial, (2) pure α polymorph, (3) pure β polymorph, and (4) a mixed-polymorph steady-state. The trivial steady-state occurs for processes exhibiting relatively low Damköhler numbers, when the MSMPR residence time is small relative to the characteristic nucleation and growth times of both forms. In this limit, it is possible for the supersaturated solution to flow in and out of the precipitator without any precipitation occuring. The pure polymorph steady-states are characterized by one of the polymorphs being completely absent from the reactor/crystallizer. The mixed-polymorph steady-state is characterized by non-zero amounts of both polymorphs coexisting in the reactor at steady-state. The first three steady-states were predicted by our previous non-agglomerating model, [21] but the last one is unique to the agglomerating precipitator model. In some regions of parameter space (i.e., for some sets of dimensionless parameters implied by some choice of T, C_0, and τ), only the trivial steady-state is possible. In other regions, two, three, or four of the steady-states described above become possible solutions to the set of steady-state algebraic equations implied by the ODEs in Equations 4.19-4.25. For any set of parameters, only one of these steady-states will be dynamically stable, and that is the one that the system will evolve towards and eventually stabilize at.

The relationship between the parameters and the steady-state multiplicity is presented schematically in Figure 4.1. The axes of Figure 4.1 contain two new dimensionless parameter combinations, Φ_α and Φ_β. In our earlier paper, a linear stability analysis of the non-agglomerating model demonstrated that these two combinations of parameters determine the relative dynamic stability of the available steady-states. All of the bifurcations and steady-state dynamic stability transitions in the non-agglomerating model take on simple functional forms when presented in terms of the stability groups, Φ_α and

Φ_β. This construction allowed us to present all of the potential process design trade-offs, bifurcations, and stability transitions on a single two-dimensional figure, even though the model contained seven dimensionless parameters. The stability groups are defined in terms of the seven dimensionless model parameters from the non-agglomerating model in Equations 4.26-4.27:

$$\Phi_\alpha = [Da_\alpha^{\frac{-1}{2g_\alpha + b_\alpha}} - \gamma]^{-1} \tag{4.26}$$

$$\Phi_\beta = [Da_\beta^{\frac{-1}{2g_\beta + b_\beta}}]^{-1} \tag{4.27}$$

Physically, Φ_i is the inverse of the dimensionless solute concentration (y) at the pure i polymorph steady-state in the absence of agglomeration ($A_i = 0$, see Equations 18 and 22 in our previous paper [21]). Qualitatively, one can think of these stability parameters as modified Damköhler numbers. Both stability groups are proportional to their respective Damköhler numbers, so it is qualitatively correct to equate the two when considering the results presented here. Quantitatively, the distinction remains important during process design.

The stability features of the agglomeration-enabled model are easiest to explain and interpret when presented in terms of the stability groups, because several of the bifurcations and steady-state dynamic stability transitions are independent of the Agglomeration numbers (discussed in detail later). Throughout this article, several figures will have these stability groups as axes, because they represent a simple way to present the stability features of all of the potential processes one could build. When one makes a set of process choices (i.e., solvent, T, C_0, τ), a set of model parameters is implied (i.e., Da_i, g_i, b_i. γ, A_i). This set of parameters implies a value for the stability groups (Φ_α, Φ_β), which defines a point at some position on the stability or steady-state multiplicity diagrams presented here. Therefore, each position on one of these diagrams represents a

potential process, and one can intentionally move around the diagram by making rational design and operation decisions according to the various relationships among the model parameters and the stability groups described in Equations 4.15-4.18 and 4.26-4.27.

For example, Figure 4.1 shows how the steady-state multiplicity changes as one varies the absolute and relative magnitudes of the stability groups (modified Damköhler numbers). Specifically, it indicates that the trivial steady-state is the only possible steady-state when the stability groups are both less than 1. As the stability groups increase, two, three, or four steady-states become possible. The red lines separating the regions of three possible steady-states from the regions of four possible steady-states are the only curves on Figure 4.1 whose positions depend on the Agglomeration numbers. That dependence, and the relationship between the Φ_i, the A_i, and the dynamic stability of the different steady-states will be discussed in detail in the next section.

The non-linearities introduced by the agglomeration terms have prevented the determination of analytic expressions for the states as a function of the parameters at the various steady-states. When a system of algebraic equations does not have an analytic solution such that the states can be written as explicit functions of the parameters, the parameter/solution structure can be elucidated through the use of a number of different numerical analysis techniques. Here, arc-length continuation was utilized to determine the steady-state solution structure as a function of the parameters, Φ_α and Φ_β. [42–44] Figure 4.2 illustrates how the steady-state structure varies as a function of A_α for a fixed value of Da_α, Da_β, γ, g_α, g_β, b_α, and b_β and three select values of A_β ($A_\beta = 0,\ 0.1,\ 1.5$). The remaining parameters (Da_α, Da_β, γ g_α, g_β, b_α, and b_β) were chosen such that the metastable polymorph (α in general or vaterite specifically) is the only form present at steady-state in the absence of agglomeration (i.e., $\Phi_\alpha = 1.4$, $\Phi_\beta = 1.3$, $A_\alpha = A_\beta = 0$). Along the ordinate in Figures 4.2a and 4.2d, both A_α and A_β are zero, corresponding to the non-agglomerating limit discussed in our previous paper. [21] At this point in

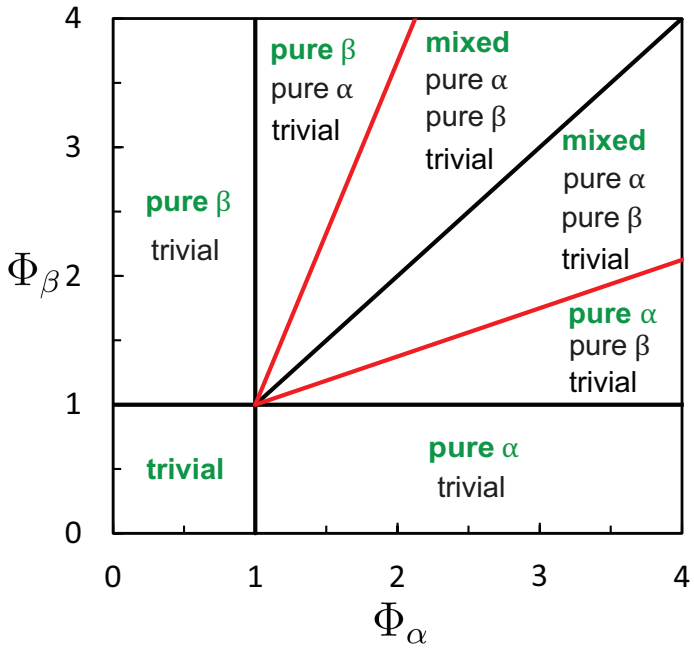

Figure 4.1: Steady-state multiplicity diagram, in which Φ_β is plotted vs Φ_α with parameter regions labeled to indicate the steady-states that are possible in the set of processes implied by each region of parameter space. The steady-state that is dynamically stable in each region is labeled in green, bold face. The black lines represent projections of bifurcation surfaces that are not functions of the Agglomeration numbers. The red bifurcation surfaces collapse to the $\Phi_\alpha = \Phi_\beta$ line in the limit $A_\alpha, A_\beta \to 0$. They collapse to the $\Phi_\alpha = 1$ and Φ_β=1 lines in the limit $A_\alpha, A_\beta \to \infty$. They are shown here schematically for $A_\beta = A_\alpha \neq 0$. The stability parameters (Φ_i on the axes) are defined in Equations 4.26 and 4.27

parameter space, there are three distinct steady-states. At the (dynamically unstable) trivial steady-state, $y = 1$ and $\omega_{0,\alpha} = 0$. By comparison, at the (dynamically stable) pure α steady-state, $y \approx 0.72$ and $\omega_{\alpha,0} \approx 1.3$. At the (dynamically unstable) pure β steady-state, $y \approx 0.78$ and $\omega_{\alpha,0} = 0$ ($\omega_{\beta,0}$ is not shown here, but it is nonzero). Now consider the pure α curves (red). For each value of A_β reported, the value of y at the pure α steady-state increases as A_α increases. This is expected because agglomeration events reduce surface area. As agglomeration becomes more prevalent in the MSMPR precipitator, the average crystal size increases (due to agglomeration) and the total (distribution integrated) surface area decreases. Crystals grow from the surface, so increasing agglomeration tends to lower the total solute deposition rate from solution, thereby pushing C closer to C_0 and increasing the dimensionless reactor supersaturation (y). A bifurcation occurs at a critical value of A_α (designated $A_\alpha^{crit} \approx 0.5$ in this example), at which point a new, mixed-polymorph steady-state becomes possible and dynamically stable for $A_\alpha > A_\alpha^{crit}$. All of our calculations indicate that this bifurcation occurs at the value of A_α for which the steady-state value of y is the same at both the pure α steady-state and the pure β steady-state in the limit $A_\beta = 0$ (i.e., the set of parameters for which $y_{\alpha,A_\alpha \neq 0} = f(Da_\alpha, g_\alpha, b_\alpha, \gamma, A_\alpha) = y_{\beta,A_\beta=0} = g(Da_\beta, g_\beta, b_\beta)$). This observation is consistent with the calculations shown here, and with all similar calculations we have performed while studying this system.

Although A_α^{crit} is the same for all A_β at fixed values of Φ_α and Φ_β, the value of A_β does affect the quantitative values of the states at the mixed-polymorph steady-state when $A_\alpha > A_\alpha^{crit}$. In fact, one can tell from these diagrams that increasing either of the Agglomeration numbers at fixed values of the other parameters tends to direct the quantitative value of each of the states at the mixed-polymorph steady-state towards the value each would have at the opposite form pure steady-state. For example, in Figures 4.2a-c, the values of the mixed-polymorph $\omega_{\alpha,0}$ (blue) approach the pure α curve (red)

as A_β is increased. In other words, the mixed-form distribution approaches a pure α distribution as A_β increases. This is again consistent with the fact that increasing the importance of agglomeration results in a lower *total* growth rate of a given solid form. Similar trends are observed in the y vs A_α curves for both the mixed-polymorph steady-state and the pure α steady-state. The solute concentration at the mixed-polymorph steady-state approaches the quantitative value associated with the pure β steady-state as A_α increases. Similarly, the solute concentration at the pure α steady-state approaches the quantitative value associated with the trivial steady-state as A_α increases. Both trends are again consistent with the fact that higher A_α slows the *total* α growth rate. Lowering the *total* α growth rate at fixed β parameters evolves the mixed-polymorph steady-state towards the pure β steady-state and the pure α steady-state towards the trivial steady-state.

Numerical Stability Analysis

The linear stability analysis performed on the previous model is not possible on the more complicated agglomerating model. Nevertheless, many of the findings from the non-agglomerating model can be applied to the numerical analysis of the agglomerating model. For example, several of the lines in parameter space that served as stability limits and bifurcations in the simpler model can be extended into the agglomeration dimensions, generating stability transition surfaces in higher dimensions. These similarities will be discussed after describing our numerical approach to analyzing the highly nonlinear, agglomerating crystallizer model.

Stability transitions in the full agglomerating model are summarized in Figure 4.3. These figures were generated numerically by solving the full model for many different values of the 9 parameters. Each transient was evolved until the time derivatives of

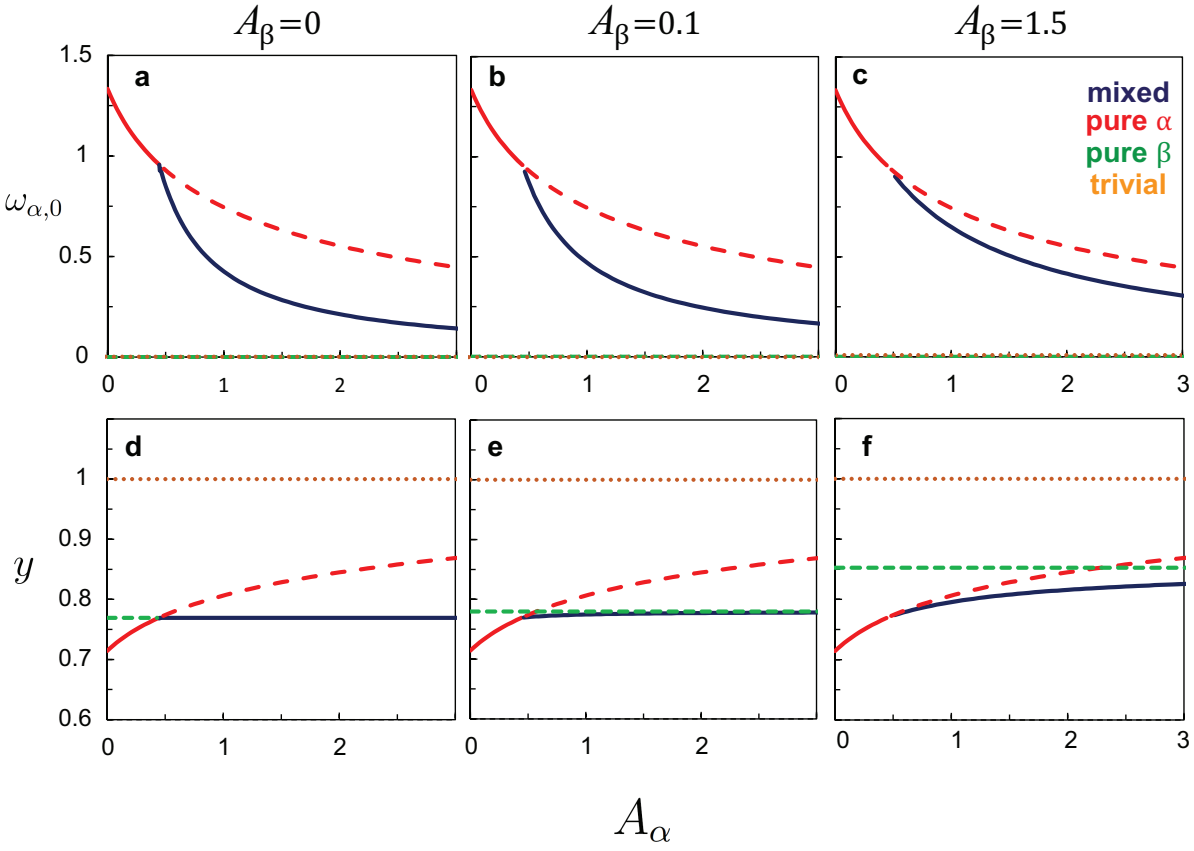

Figure 4.2: Bifurcation diagrams (state variables vs A_α) at fixed values of the stability groups ($\Phi_\alpha = 1.4$ and $\Phi_\beta = 1.3$) for three values of the β form Agglomeration number, A_β; In Figures (a) and (d), $A_\beta = 0$; (b) and (e), $A_\beta = 0.1$; (c) and (f), $A_\beta = 1.5$. $\omega_{\alpha,0}$ is the dimensionless steady-state zeroth moment of the thermodynamically metastable polymorph distribution (dimensionless total α crystal number density). y is the dimensionless steady-state solute concentration. Four qualitatively distinct steady-states are present in the bifurcation diagrams. The mixed-polymorph steady-state becomes possible when $A_\alpha \geq A_\alpha^{crit}$ (≈ 0.5 for this example). Per convention, dynamically stable steady-states are represented as solid curves and unstable ones as dotted or dashed. These figures were generated with $g_i = 1.5$, $b_i = 2.5$, and $\gamma = -0.0042$, which are typical values representative of many systems for g_i and b_i. $\gamma = -0.0042$ is representative of the $CaCO_3$ experiments reported in this paper and is exact for the experiments described in Figure 4.5.

the moment and mass balance ODEs became zero. Then the resulting (stable) state vector was associated with one of the qualitative steady-states (trivial, pure α, pure β, or mixed). The data are presented as projections of the nine-dimensional parameter space onto the two-dimensional stability parameter space defined by Φ_α and Φ_β. This presentation represents all of the stability transitions exactly when $A_\alpha = A_\beta = 0$ (see Figure 4.3a). It remains useful even when $A_i \neq 0$, because many of the general stability transitions can be described in terms of the two stability parameters (Φ_α and Φ_β) alone and even the higher dimensional bifurcation surfaces become weak functions of the other parameters when presented in this way.

For example, the stability transition from the stable, trivial steady-state to the stable pure α or the stable pure β steady-state is not a function of the Agglomeration numbers (see Figures 4.1 and 4.3). The trivial steady-state is linearly stable when:

$$\Phi_\alpha < 1 \tag{4.28}$$

$$\Phi_\beta < 1 \tag{4.29}$$

This is unchanged from the previous, non-agglomerating model. Also similar to the previous non-agglomerating model, both surfaces in parameter space defined by $\Phi_\alpha = 1$, $\Phi_\beta < 1$, $A_\alpha \in [0, \infty)$ and $\Phi_\beta = 1$, $\Phi_\alpha < 1$, $A_\beta \in [0, \infty)$ separate the region of stable trivial steady-states from the regions characterized by the dynamic stability of either the pure α or pure β steady-states, respectively. Independent of Agglomeration numbers, the pure α steady-state is always dynamically stable when:

$$\Phi_\alpha > 1 \tag{4.30}$$

$$\Phi_\beta < 1 \tag{4.31}$$

and the pure β steady-state is always dynamically stable when:

$$\Phi_\alpha < 1 \tag{4.32}$$

$$\Phi_\beta > 1 \tag{4.33}$$

(see Figures 4.1 and 4.3) These relationships would be difficult to establish from the nine-dimensional numerical data without the guidance provided by the analytic results from our earlier study. [21] These past results enabled us to hypothesize that the stability transitions in the Φ_α-Φ_β plane that exist when $A_i = 0$ may remain independent of A_i for the case $A_i \neq 0$. This hypothesis was tested and confirmed for the trivial to pure α and trivial to pure β transitions with the the numerical approach described above. Equations 4.34 and 4.35 define the remaining region of parameter space. This is the only region of parameter space in which the steady-state dynamic stability is affected by the Agglomeration numbers.

$$\Phi_\alpha > 1 \tag{4.34}$$

$$\Phi_\beta > 1 \tag{4.35}$$

In the absence of agglomeration ($A_\alpha = A_\beta = 0$, Figure 4.3a), the dynamic stability of this region is entirely determined by the relative magnitudes of Φ_α and Φ_β. When $\Phi_\alpha > \Phi_\beta$, the pure α steady-state is dynamically stable and when $\Phi_\alpha < \Phi_\beta$, the pure β steady-state is dynamically stable. In the absence of agglomeration, mixed-polymorph steady-states

are only possible along the line $\Phi_\alpha = \Phi_\beta$. A steady-state that is only possible along a line in parameter space cannot be observed experimentally (infinitesimal variations or disturbances in any parameter result in departures from the exact operating conditions necessary to maintain one's position on the line), so we deemed it unworthy of substantial discussion in our previous paper. This transition line becomes a transition region in the presence of agglomeration, enabling the observation of these mixed polymorph steady-states. The region of mixed-polymorph dynamic stability emanates from this line as the Agglomeration numbers increase (see Figures 4.3b, c) and eventually covers the entire region defined by Equations 4.34 and 4.35 in the limit $A_\alpha, A_\beta \to \infty$ (see Figure 4.3d).

For each figure shown, g_α, b_α, g_β, b_β, and γ were fixed, and Da_α and Da_β were manipulated to vary Φ_α and Φ_β. This procedure was repeated for several fixed values of A_α and A_β. Away from the limits of $A_i \approx 0$ and $A_i \approx \infty$, most of the variations in the mixed-polymorph/pure polymorph bifurcation surfaces as functions of the parameters (and all of the variation in the other bifurcation surfaces) can be explained by these four parameters alone. In fact, when the stability results are projected onto this two-dimensional stability plane (as in Figure 4.3), the surface projection characterized by $\Phi_\alpha > \Phi_\beta$ only depends on A_α, γ, g_α, and b_α, while the surface projection characterized by $\Phi_\alpha < \Phi_\beta$ only depends on A_β, g_β, and b_β. Additional discussion of where the bifurcation surfaces generally exist within parameter space and of the (relatively small) movement of the bifurcation surfaces due to changes in the other parameters (γ, g_i, and b_i) is in the Supplementary Information. The two intermediate values of $A_\alpha = A_\beta = 0.1$, 1.5 in Figures 4.3b, c were chosen to represent moderate and high Agglomeration numbers. Figure 4.3d, where $A_i = 150$, is included as a proxy for the limit as $A_i \to \infty$, but its inclusion is not meant to imply that Agglomeration numbers of this magnitude are attainable. Figure 4.3 is intended to be as representative as possible of the $CaCO_3$ experiments presented in this article, but it is difficult to exactly define the bifurcation

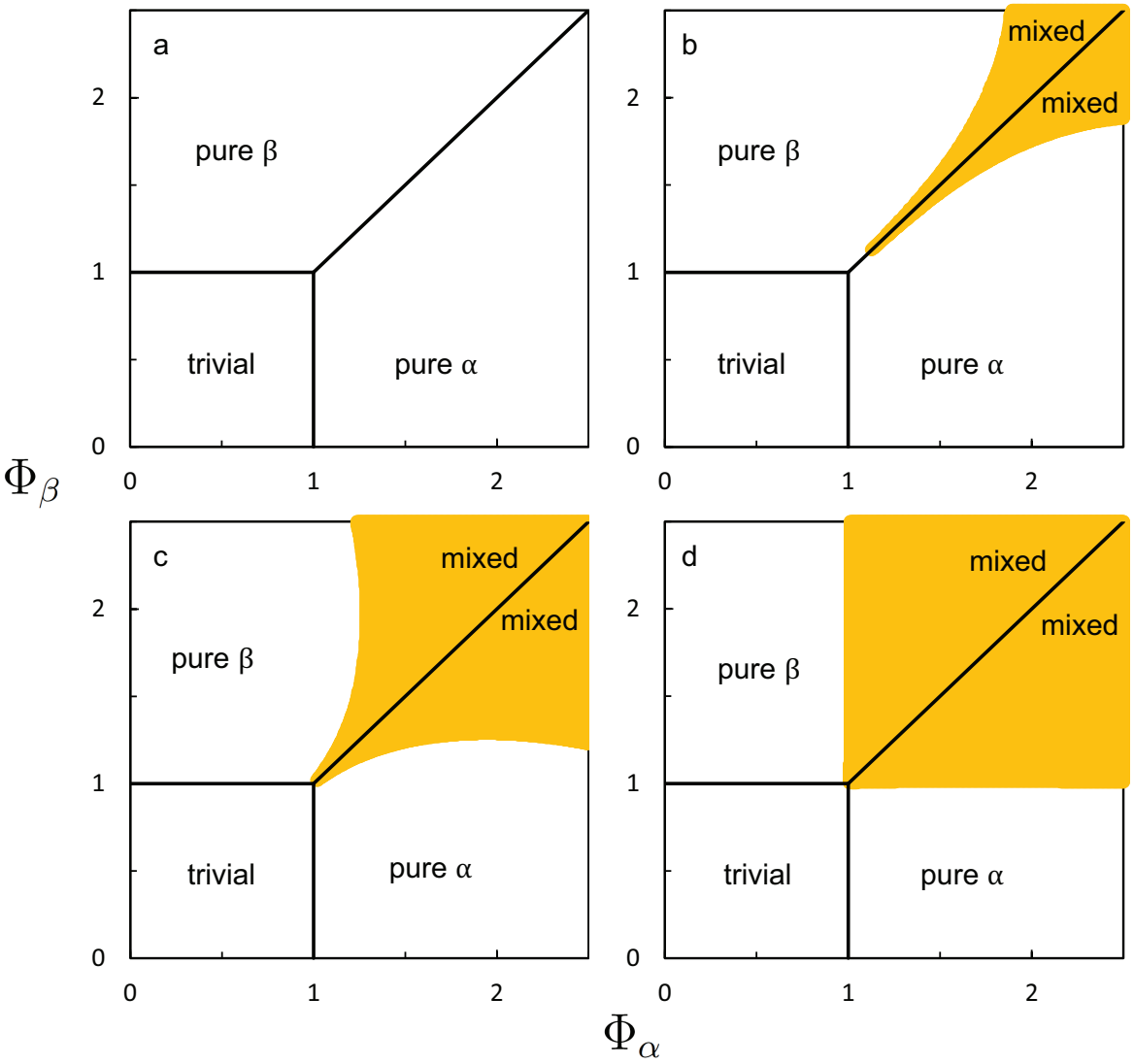

Figure 4.3: Plots of Φ_β versus Φ_α for the Agglomeration numbers, $A_\alpha = A_\beta =$ (a) 0, (b) 0.1, (c) 1.5, and (d) 150. Each point represents a potential process with a set of relative rates defined by the dimensionless groups (Φ_α, Φ_β, A_α, and A_β). These stability diagrams illustrate the relationships among the relative rates (dimensionless groups) and the relative steady-state dynamic stabilities of the four qualitatively distinct steady-states. The region of parameter space characterized by the relative dynamic stability of the mixed-polymorph steady-state is shaded yellow. This region exists only along the $\Phi_\alpha = \Phi_\beta$ line when $A_i = 0$. It emanates from this line in either direction as the Agglomeration numbers increase, and it covers the entire region described by Equations 4.34 and 4.35 in the limit $A_\alpha = A_\beta \to \infty$. Figures 4.3a-d were calculated with γ =-0.0042 (the value associated with the experiments described in Figure 4.5), $g_i = 1.5$, and $b_i = 2.5$ (generally representative of many systems).

surfaces in this system due to the lack of relevant kinetic data. However, the positions of the bifurcation surfaces (with respect to the stability parameters, Φ_i) are weak functions of the unknown parameters and these parameters are physically well-constrained, so these limitations barely reduce the utility of the analysis.

From the above analysis, much can be learned and applied to the production of vaterite. First, outside the mixed-polymorph stability region, the dynamic stability features of this model are remarkably similar to the non-agglomerating model. A region of trivial steady-state dynamic stability remains, characterized by low residence times relative to the nucleation and growth times of both forms. Regions of parameter space also exist in which one expects to observe pure calcite and pure vaterite steady-states. Second, the region in which the mixed-polymorph steady-state is dynamically stable is localized around the original bifurcation line ($\Phi_\alpha = \Phi_\beta$). Third, the mixed-polymorph stability region grows as the Agglomeration numbers increase. These three observations provide enough information to design polymorph selective processes for agglomerating precipitators. Observation 2 implies that holding A_α and A_β constant, one can decrease the relative stability of the mixed-polymorph steady-state by moving orthogonally away from the $\Phi_\alpha = \Phi_\beta$ line. Observation 3 implies that holding Φ_α and Φ_β constant, one can de-stabilize the mixed-polymorph steady-state by decreasing A_α or A_β. Combining these two observations, any design or operation decision that moves the process toward lower Agglomeration numbers or away from the $\Phi_\alpha = \Phi_\beta$ line will tend to de-stabilize the mixed-polymorph steady-states in favor of the pure form steady-states. The pure form steady-state that this change will stabilize will depend on the relative magnitudes of Φ_α to Φ_β, i.e., on which side of the $\Phi_\alpha = \Phi_\beta$ line the operating point falls.

In general, most of the model parameters (dimensionless groups) vary as functions of temperature (T). Therefore, the stability parameters (Φ_α and Φ_β) are also functions of temperature. This implies that changing temperature (while holding all other decision

variables constant) changes the relative values of both the stability parameters (Φ_i) and the Agglomeration numbers (A_i), moving an operating point around Figure 4.3. For some changes in temperature, a different steady-state will become dynamically stable. If one can characterize the growth kinetics, nucleation kinetics, and solubilities of both forms as functions of temperature, then temperature becomes a valuable decision variable to use for polymorph selection.

The inlet concentration (C_0) is another design choice that can be used to select the relative values of the stability groups and the Agglomeration numbers, and accordingly, the steady-state solid form produced. System-specific nucleation and growth rate expressions are required to define the exact relationships between inlet concentration, the stability groups, and the Agglomeration numbers, but scaling arguments can be used to make intentional design decisions in systems for which the kinetics have not yet been characterized. For example, the stability groups increase linearly with increases in the inlet concentration, and the Agglomeration numbers decrease by the nonlinear scaling $A_i \approx C_o^{-(3g_i-1)}$ (see Equations 4.15-4.18 and 4.26-4.27). Since g_i typically varies between 1 and 2, system-specific knowledge is unnecessary to conclude that the Agglomeration numbers decrease at a rate between C_o^{-2} and C_o^{-5}. This nonlinear Agglomeration number decay, coupled with the linear increases of Φ_α and Φ_β, is enough information to accomplish polymorph selection in many systems, even if the exact nucleation and growth kinetics (and therefore the exact functional forms of $\Phi_i = f_\Phi(C_0)$ and $A_i = f_A(C_0)$) are unknown. Increasing C_o has a larger effect on shrinking the region of mixed-polymorph dynamic stability than it does in affecting the relative polymorphic nucleation and growth rates that move an operating point around the [Φ_α, Φ_β] plane. For example, doubling the inlet concentration decreases the Agglomeration numbers by a factor between 4 and 32. Since typical Agglomeration numbers vary between 0 and 1.5, and since Figure 4.3b illustrates how small the mixed-polymorph region becomes for $A_i \leq 0.1$, a small increase in the

inlet concentration will have a relatively large effect on shrinking the mixed-polymorph stability region and a relatively small effect on the relative dynamic stability of the pure polymorph steady-states. Furthermore, if a set of design choices is known to yield a mixed-polymorph steady-state for which the more prevalent form is desired (as in Figure 4.5), one could reasonably conclude that the system is in a position on the stability diagram for which $\Phi_{desired} > \Phi_{undesired}$. Therefore, a hypothesis emerges from these scaling arguments: one can design a polymorph selective process for an agglomerating crystal system by using the design rules from the non-agglomerating model while maintaining a high inlet supersaturation.

Similar scaling arguments also apply to residence time (τ). The Φ_i scale as $\tau^{3/(2g_i+b_i)}$ and the Agglomeration numbers scale as τ^{-2}. The quantity $3/(2g_i + b_i) \in [0, 1]$, so increasing residence time is also a reasonable approach when attempting to de-stabilize a mixed-polymorph steady state. Still, increasing C_0 is likely a better option to try first for two reasons. First, the difference in scaling between the Φ_i and the A_i is typically larger for C_0, indicating that the de-stabilizing effect should be more effective for a smaller change in C_0 (and therefore a smaller displacement in the $[\Phi_\alpha, \Phi_\beta]$ plane). Furthermore, we demonstrated in our earlier study that increasing residence time always increases the relative value of the thermodynamically stable solid form's stability group to the thermodynamically metastable solid form's stability group. Therefore, a large enough increase in residence time is guaranteed to give a pure, thermodynamically stable solid form at steady-state. For some applications, that may be ideal, but for our motivating system of vaterite precipitation, increasing C_0 is a superior design choice. Still, Figure 4.5a, b illustrates that the relative fraction of vaterite increased when the residence time was increased, indicating that both strategies could be effective in this system.

4.3 Experiments

Materials and Apparatus

Experiments were performed in a 1 liter LabMax reactor (Mettler Toledo, see Figure 4.4). The reactor temperature was controlled to 25 °C. Inlet and outlet flows were calibrated to maintain an active reactor volume in the range of 0.2-0.6 liter, so that the residence time could be varied between 6 and 18 min. During each experiment, two separate equimolar (stoichiometric) flows of aqueous Na_2CO_3 and $CaCl_2$ were fed to the MSMPR reactor. The 99%+ purity solid reactants were purchased from Fisher Chemical, and used as-received. The water used to generate the aqueous feed solutions was filtered in a Barsted NANOpure water filtration system with a conductivity of 18 $\mu\Omega$ cm^{-1}. As two separate equimolar streams were fed to the reactor, the inlet concentration as defined in the model (C_0) is one-half the molar concentration in either feed stream (See Supplementary Information for discussion). A set of experimental conditions were repeated to confirm the reproducibility of the experimental procedure (as discussed in the Supplementary Information).

Product Characterization

The pH of the solution inside the reactor was measured every 3 s with a Fisher Scientific accumet AB150. Due to the well-understood pH-sensitive chemistry that occurs during $CaCO_3$ precipitation, pH is a simple and effective way to monitor the crystallization process dynamics (see the Supplementary Information for discussion of the chemistry and justification of this procedure). Solid $CaCO_3$ was continuously removed from the reactor in the exit suspension stream and filtered in a Büchner funnel with a 0.3 μm filter. The solids were then dried in an oven for 24 h at 70 °C before further characterization.

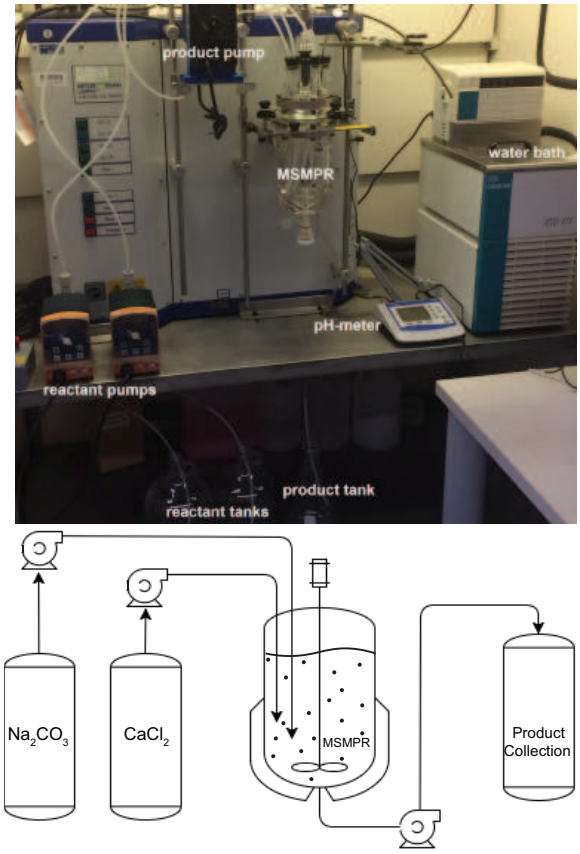

Figure 4.4: Experimental apparatus (top) and schematic (bottom) for continuous precipitation experiments in which Na_2CO_3 and $CaCl_2$ were converted to $CaCO_3$. Temperature was controlled to 25 °C for all experiments. The inlet concentration was varied from 0.0025-0.15 molar. The residence time was varied between 6 and 18 mins.

Complementary powder X-ray diffraction (XRD), solid-state ^{43}Ca nuclear magnetic resonance spectroscopy (NMR), and electron microscopy (SEM) analyses were used to characterize the local and long-range order, compositions, and morphologies of the crystallization products. Powder XRD patterns were acquired under several different drying procedures to confirm that the described drying process did not alter the polymorph distribution (see Supplementary Information for details.) Once dry, XRD patterns of the solid products were acquired on an Empyrean Powder Diffractometer, and phase-fitting of the pattern was completed in Highscore (PANalytical XRD analysis software). Select samples were also characterized with scanning electron microscopy (SEM) on a FEI Nova Nano 650 FEG SEM. Characterization of ^{43}Ca is difficult due to its low gyromagnetic ratio (-1.803 $\times$ 10^7 rad T^{-1} s^{-1}), low natural isotopic abundance ($\approx$ 0.135 %), and the general difficulties associated with quadrupolar nuclei (7/2 spin). These challenges were mitigated with high magnetic fields (19.6 T) and a custom-built 7-mm single-resonance probe specifically designed for low-γ nuclei at the U.S. National High Magnetic Field Laboratory in Tallahassee, Florida. Solid-state, single-pulse ^{43}Ca magic-angle-spinning (MAS) NMR spectra of select samples were acquired on a 19.6 T Bruker DRX NMR spectrometer under magic-angle-spinning (MAS) conditions of 5 kHz, 25 °C, 90° 4 μs pulses, and a 0.5 s recycle delay. The ^{43}Ca shifts were referenced to 1 molar aqueous $CaCl_2$. Additional diffraction patterns and solid-state ^{43}Ca NMR spectra are included in the Supplementary Information, including a ^{43}Ca NMR spectrum of a sample containing calcite, vaterite, and aragonite phases,which shows resolved ^{43}Ca signals from calcite, aragonite, and vaterite. The peaks are centered at 20 ppm, 3 ppm, and -27 ppm, but the exact location of the peaks is sensitive to the reference concentration chosen. [45]

4.4 Results and Discussion

Evidence of Mixed Polymorph Steady-States

Mixed-polymorph steady-states are often observed during the continuous precipitation of $CaCO_3$, but these steady-states are not possible solutions to population balance models for which the dominant rate processes are secondary nucleation and size-independent linear crystal growth alone. [21] We have demonstrated (using arc-length continuation and a numerical stability analysis) that mixed-polymorph steady-states are possible and even dynamically stable for some agglomerative precipitation process models. In this section, we discuss two experiments for which such mixed-polymorph steady-states were observed. These experiments were performed with a stoichiometric feed of Na_2CO_3 and $CaCl_2$ at a concentration (C_0) of 0.0125 molar and a temperature (T) of 25 °C. The residence times (τ) were 6 and 9 minutes for Figure 4.5a and b, respectively. The percentage of the effluent solids that was associated with each polymorph at each time point was determined using powder X-ray diffraction and Rietveld phase fitting. For example, Figure 4.5 illustrates how the effluent crystal polymorph distributionc hanged as a function of time during these two experiments (% polymorph defined as mass of solid form i/total mass of solids $\times$ 100 %). In Figure 4.5a, b, the polymorph distributions vary with time during start-up but eventually plateau, indicating that a steady-state has been reached. In each case, the crystal distribution leaving the precipitator at steady-state contains non-zero amounts of both calcite and vaterite polymorphs (75% vaterite for τ = 6 min and 93% vaterite for τ = 9 min), indicating that some rate process besides size-independent linear crystal growth and secondary nucleation must be important. Figure 4.6 shows typical SEM images of the effluent crystals after filtration and drying. Figure 4.6a is an image of product crystals collected after 30 min of operation for T = 25 °C, C_0 = 0.0125 M, and τ = 9 min (Figure 4.5b) . After 30 min, the process was still ex-

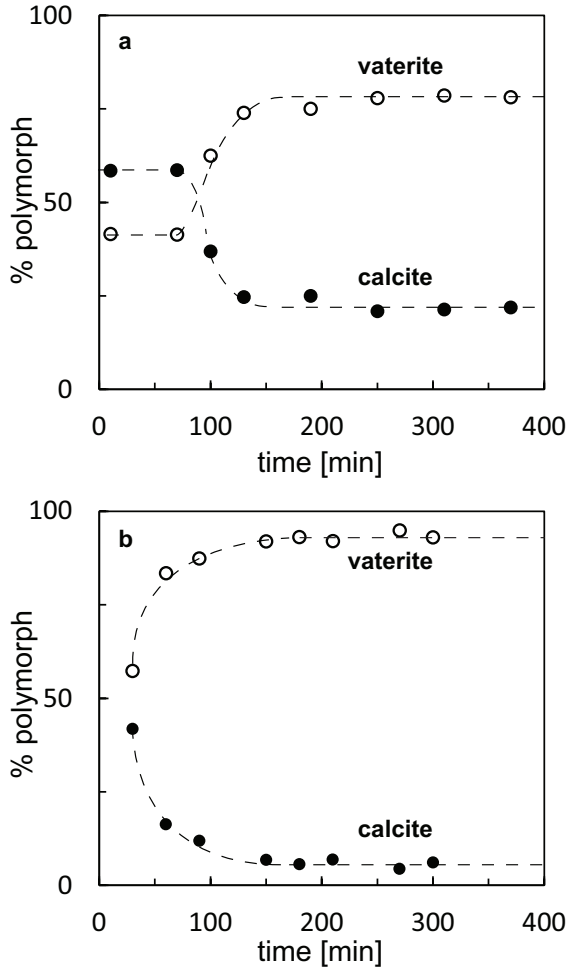

Figure 4.5: The percentages of the different $CaCO_3$ polymorphs plotted as functions of time during continuous precipitation for $T = 25$ °C, $C_0 = 0.0125$ M, and (a) $\tau = 6$ min, or (b) $\tau = 9$ min. Both vaterite (thermodynamically metastable) and calcite (thermodynamically stable) co-exist at steady-state in both experiments. These are typical experiments that exhibit a dynamically stable mixed-polymorph steady-state.

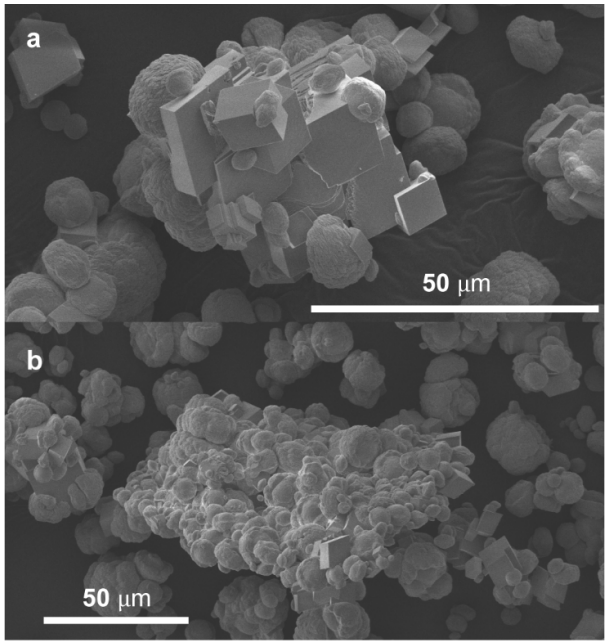

Figure 4.6: Representative SEM images of effluent cube-shaped calcite crystalites and spheroidal vaterite crystalites after (a) 30 min and (b) 60 min of start-up of a continuous $CaCO_3$ precipitation experiment operating at $T = 25$ °C, $C_0 = 0.0125$ M, and $\tau = 9$ min. Both images exhibit mixed-polymorph distributions and significant agglomeration.

hibiting start-up dynamics ($\approx 42\%$ calcite), resulting in a mixture of calcite (cube-like) and vaterite (spheroidal) crystalites. A significant extent of crystal agglomeration is also observed. Figure 4.6b is a representative image collected after 60 min of operation for $T = 25$ °C, $C_0 = 0.0125$ M, and $\tau = 9$ min. This point in the start-up dynamics is closer to the steady-state distribution and therefore exhibits a relatively low calcite fraction (16 %). Again, the image clearly shows that both solid forms are present along with significant agglomeration.

Testing the Hypothesis

The previously discussed analysis indicated that increasing the inlet concentration (C_0), while holding all other decision variables constant with respect to the experiment

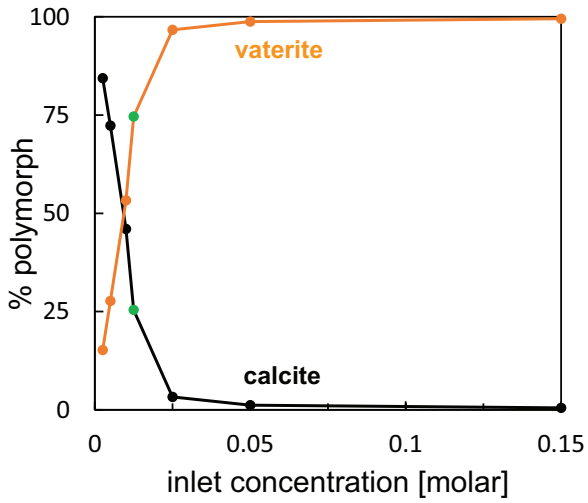

Figure 4.7: Plots of the steady-state percentage of vaterite and calcite polymorphs obtained for various values of C_0 at fixed values of τ (6 min) and T (25 °C). As the inlet concentration is increased, the fraction of effluent crystals identified as vaterite increases and eventually approaches 100%. The green points indicate the steady-state polymorph distribution associated with the experiment described in Figure 4.5a.

described in Figure 4.5a, should have a de-stabilizing effect on the mixed-polymorph steady-state in favor of the pure vaterite steady-state. Figure 4.7 illustrates how the steady-state values of the different polymorph percentages changed as a function of C_0 at the fixed residence time (6 min) and temperature (25°C) corresponding to the conditions used in Figure 4.5a. When $C_0 = 0.0125$ molar, the steady-state distribution contained approximately 75% vaterite and 25% calcite (green points). When C_0 was increased by a factor of 12 to $C_0 = 0.15$ molar, the steady-state percentage of vaterite approached 100%. These $CaCO_3$ data indicate that increasing inlet supersaturation decreases the relative importance of agglomeration inside the continuous MSMPR precipitator, thereby de-stabilizing the mixed-polymorph steady-state in favor of a pure polymorph steady-state. Characterization of the effluent products establishes that for $\tau = 6$ min, $T = 25$ °C, and $C_o = 0.15$ M, the thermodynamically metastable polymorph, vaterite, is almost exlcusively present. Figure 4.8 shows a powder X-ray diffraction pattern (XRD),

a solid-state ^{43}Ca NMR spectrum, and two SEM images of these effluent solids. All of the major reflections in the XRD pattern are indexable to vaterite, although a minor reflection exists that may be indexable to calcite ($< 1\%$). The solid-state ^{43}Ca MAS NMR spectrum in Figure 4.8b shows a broad signal centered at 3 ppm that is assigned to Ca^{2+} ions in a distribution of local vaterite environments. [46,47] An additional ^{43}Ca MAS NMR spectrum acquired on a solid mixture of calcite, vaterite, and aragonite under otherwise identical conditions is included in the Supplementary Information. This additional spectrum shows two additional ^{43}Ca peaks. In Figure 4.8b, there is no observable NMR signal at either 20 ppm (calcite) or -27 ppm (aragonite), indicating that the sample is predominately vaterite. Furthermore, the representative SEM images in Figure 4.8c, d show only spheroidal vaterite crystallites with no cube-shaped calcite crystallites present.

The agglomeration prevalent in the SEM images highlights an important point. Increasing the inlet concentration does not necessarily lower the agglomeration rate. In fact, non-constant agglomeration kernels (β_i) are known to increase as supersaturation increases. [28, 48, 49] The important distinction is that the agglomeration kernel (β_i) is only one component of the Agglomeration number (A_i), and it is this Agglomeration number that affects the steady-state dynamic stability. The Agglomeration number depends on β_i, but it also depends on the crystal growth kinetics and the residence time. In this case, increasing the inlet concentration lowered the Agglomeration number and destabilized the mixed polymorph steady-state, even though the absolute agglomeration frequency likely increased.

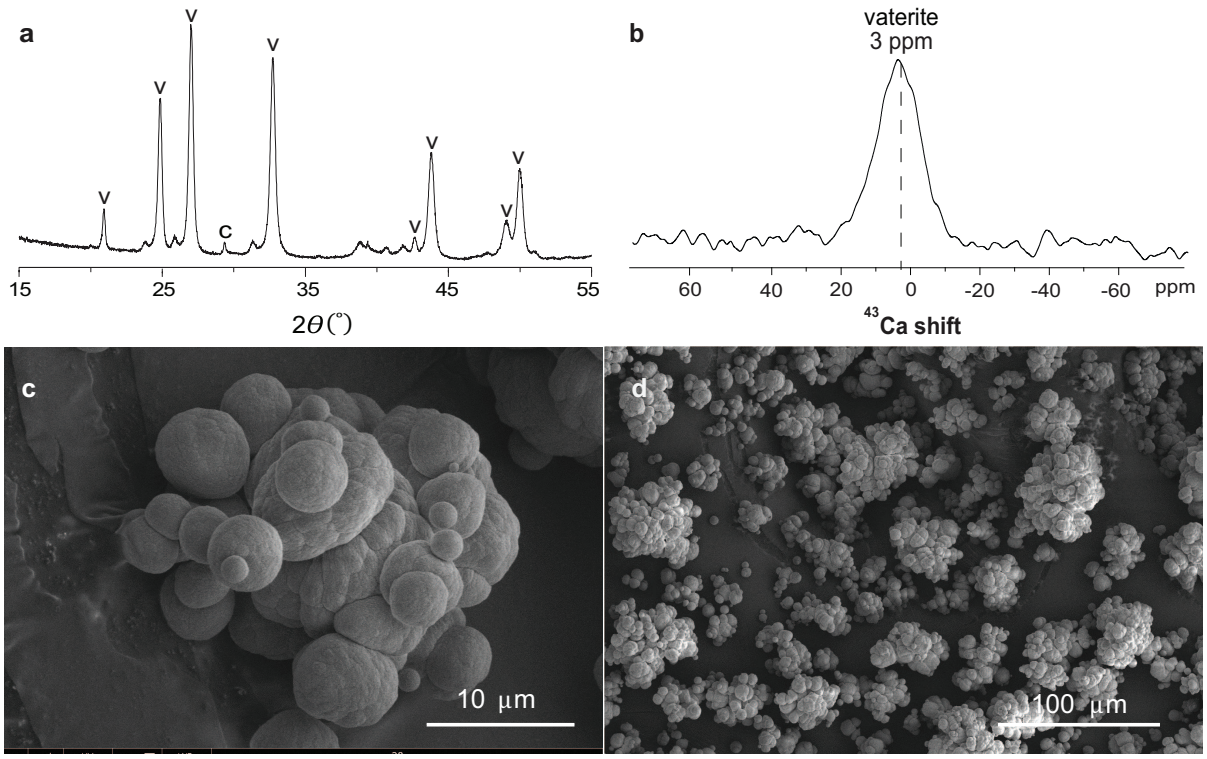

Figure 4.8: (a) Powder X-ray diffraction pattern, (b) solid-state, single-pulse ^{43}Ca MAS NMR spectrum, and (c, d) SEM images. Product collected from a continuous precipitation experiment operating under steady-state conditions, a residence time (τ) of 6 min, a temperature (T) of 25 °C, and an inlet concentration (C_0) of 0.15 molar. All major reflections in the XRD pattern are indexable to vaterite, although a minor reflection may be indexable to calcite ($< 1\%$). The ^{43}Ca MAS NMR spectrum was acquired at 19.6 T, 25 °C, 7 kHz MAS, and required a 47.6 hr acquisition time, yielding a single peak centered around 3 ppm. The spheroidal crystallites in (c) and (d) are consistent with vaterite.

Other polymorphic systems

The previous polymorph selection design rules were constructed to be generally applicable to any bi-polymorphic system in which size-independent linear crystal growth and secondary nucleation are the dominant rate processes. The design rules were tested for specific crystal systems for which relevant experiments had been reported in the literature (e.g., *L*-glutamic acid and p-aminobenzoic acid [21]). These analyses were carried out under the implicit assumption that agglomeration was unimportant in these systems, and the design rules generated in this way were consistent with the reported experimental results. Now that the effect of agglomeration on steady-state dynamic stability during continuous precipitation has been demonstrated to be important in some systems, we revisit the previous assumptions and results, specifically taking into account the agglomeration kinetics in the *L*-glutamic acid system.

Using the expressions from Lindenberg et al., [48] we estimate the size-independent α form agglomeration kernel (β_α) to be in the range of 3.6 $\times 10^{-12}$ - 6.5 $\times 10^{-12}$ m^3/s, depending on the experimental conditions. These are relatively high values for β: for example, β is of the order 10^{-17} for calcium oxalate, [50] 10^{-14} for $CaCO_3$, [51] and general hydrodynamic approximations in the high growth rate and high collision frequency limit are 10^{-18} - 10^{-16}. [52] A relatively high value of β_α suggests that agglomeration could be important in this system, however, the physicochemically important quantity is the dimensionless Agglomeration number (A_α), which is also affected by the growth kinetics and the residence time.

The Agglomeration number can be estimated for the four *L*-glutamic acid experiments that were reported by Lai et al. and discussed in our previous paper by taking the agglomeration kinetics from Lindenberg et al. and the growth kinetics from Lai et al. [19, 21, 48] The relevant experiments were numbered 1-4 and described in Table 1

in Lai et al. [19] During each experiment, *L*-glutamic acid was continuously crystallized to give pure steady-state distributions of the thermodynamically metasatable α polymorph at a temperature of 25 °C and a feed concentration of 40 g/kg. The residence time was varied from 30 min to 120 min in equal increments. Taking the maximum agglomeration frequency rate coefficient from our estimated range ($\beta_\alpha = 6.5 \times 10^{-12}$), the Agglomeration numbers associated with these four experiments are 0.148, 0.028, 0.011, and 0.005, respectively. Figure 4.9 shows the outer envelope of the mixed-polymorph dynamic stability region defined for $A_\alpha = A_\beta = 0.148$. The ordered pairs $\left[\Phi_\alpha,\ \Phi_\beta\right]$ associated with the same experiments are also included on Figure 4.9 to illustrate that these experiments were not near the mixed-polymorph/pure α polymorph dynamic stability boundary. These calculations support the assumptions in the previous analysis and support the simpler theoretical treatment that is typically used in the *L*-glutamic acid system.

While the motivating application for this work was $CaCO_3$ precipitation, the model and the analysis are general and can be expected to apply to other agglomerative precipitations. For other systems with different nucleation, growth, and agglomeration kinetics, one can use Figure 4.3 to interpolate an approximate mixed-polymorph/pure-polymorph bifurcation surface. We expect that most systems will exhibit Agglomeration numbers in the range of 0 - 1.5. As one can see from Figure 4.3c, d, $A_i = 1.5$ is already qualitatively similar to the $A_i \to \infty$ limit, so most interpolations should be possible with just Figure 4.3 alone. To further facilitate this type of interpolation for other systems, we have provided additional numerical results in the Supplementary Information with alternate combinations of γ, g_i and b_i.

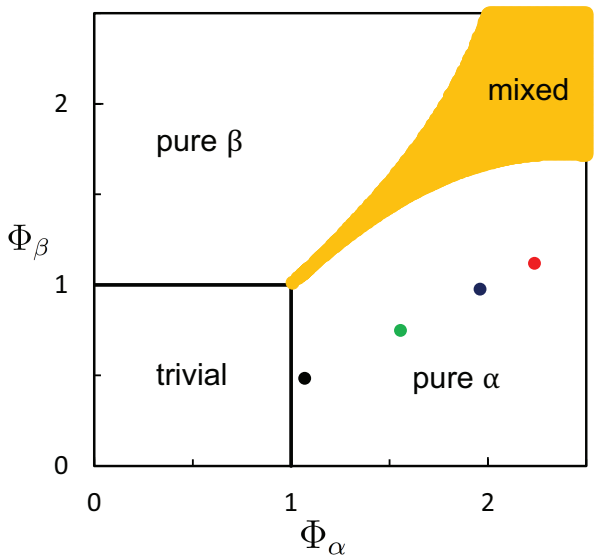

Figure 4.9: Stability diagram for *L*-glutamic acid, in which Φ_β is plotted versus Φ_α with parameter regions labeled to indicate the steady-state that is predicted to be dynamically stable in each region. The mixed-polymorph dynamic stability region is shaded yellow for $A_\alpha = A_\beta = 0.148$. This is the highest Agglomeration number of all of the *L*-glutamic acid experiments considered in our previous publication (Experiments originally reported in Lai et. al.). [19,21] The experiments were performed at 25 °C, $C_0 = 40$ g/kg, and $\tau = 30$ (black), 60 (green), 90 (blue), and 120 min (red). For this figure, $\gamma = -0.07$, $g_\alpha = 1.31$, $b_\alpha = 2.62$, $g_\beta = 1.10$, and $b_\beta = 2.81$, consistent with the calculations discussed in our previous article. [21]

4.5 Conclusion

Atomic-level differences in crystal structure imply and typically correlate to differences in measurable macroscopic properties. These properties often have a significant impact on a material's utility for a given application, and therefore a preferred solid form usually exists when one designs an industrial crystallizer or precipitator. Here, we have shown that agglomeration changes the relative dynamics within the crystallizer/precipitator, thereby affecting the relative dynamic stability of the four competing steady-states. New general design rules have been developed to guide the design and operation of precipitation processes for which a specific solid form is desired, even if the preferred solid form is thermodynamically metastable. A new approach was required to develop polymorph selective precipitators that produce thermodynamically metatable forms of $CaCO_3$ for carbon capture and utilization as structural materials because these crystal systems exhibit significant agglomeration. Pure vaterite crystal distributions have been produced in accordance with the process conditions indicated by the model analysis presented here. The results of this study are expected to be general and applicable to other precipitative systems.

Notation

Symbol	Units	Description
n_i	number/volume/length	particle density of polymorph i
G_i	length/time	growth rate of polymorph i
x	length	crystal length coordinate
β_i	volume/number/time	form i agglomeration frequency rate constant
τ	time	MSMPR residence time
B_i	number/(volume-time)	nucleation rate of polymorph i
C	moles/volume	solute concentration
$k_{g,i}$	length/time	rate constant in growth rate expression
$k_{b,i}$	number/length^2/time	rate constant in birth rate expression
ρ	moles/volume	molar density
$\mu_{i,l}$	number/volume	weight l of form i quadrature rule
L_j	length	length or abscissa in the quadrature rule
$m_{i,0}$	number/volume	zeroth moment of polymorph i population
$m_{i,1}$	length/volume	first moment of polymorph i population
$m_{i,2}$	length^2/volume	second moment of polymorph i population
$\omega_{\alpha,j}$	dimensionless	dimensionless j^{th} moment of α population
$\omega_{\beta,j}$	dimensionless	dimensionless j^{th} moment of β population
y	dimensionless	dimensionless concentration
$K_{eq,i}$	moles^2/volume^2	equilibrium/solubility constant for solid form i

Appendices

4.A Supplementary Information

S1: Summary of $CaCO_3$ chemistry

Precipitator dynamics were monitored continuously via pH and at discrete 30 minute intervals with powder X-Ray diffraction on the effluent solids. Steady-state was declared when both measurements ceased changing in time ($\pm 3\%$ for phase fractions and ± 0.01 for pH). The process dynamics can be monitored with pH because the reaction equilibrium is very pH sensitive. A complete set of linearly independent reactions that occur in the

reactor are summarized below:

$$CO_2 + OH^- \rightleftharpoons HCO_3^- \tag{4.36}$$

$$HCO_3^- + OH^- \rightleftharpoons CO_3^{2-} + H_2O \tag{4.37}$$

$$H_2O \rightleftharpoons H^+ + OH^- \tag{4.38}$$

$$Ca^{2+} + CO_3^{2-} \rightleftharpoons CaCO_{3,(s,i)} \tag{4.39}$$

where $CaCO_{3,(s,i)}$ indicates solid form i. As reaction 4.39 (the precipitation) proceeds, CO_3^{2-} is removed from solution. By Le Chatelier's principle, this tends to drive reactions 4.36 and 4.37 forward, decreasing the pH. The reaction chemistry is coupled to the nucleation and growth rates through the supersaturation. Therefore, the pH will not "line out" until the precipitation process has reached a steady-state, making pH a simple and effective leading steady-state indicator for the $CaCO_3$ system. Once the dynamic start-up phase of the experiment is complete, X-Ray diffraction phase fitting gives identical phase fractions for subsequent measurements spaced several residence times apart.

The equilibrium concentrations of CO_2, HCO_3^-, and CO_3^{2-} change as the pH is changed in a fixed volume of water with a fixed amount of carbon (closed batch system). At "high pH" essentially all of the carbon is in the CO_3^{2-} form. For the experiments discussed in this paper, the lowest steady-state pH value was 10.1 and typical values varied between 10.4 and 10.6. Just one tenth of a millimolar of net back reaction from Equation 4.37 is necessary to move the pH from 7 to 10, so choosing CO_3^{2-} as a carbon source for our experiments (i.e., Na_2CO_3) ensures that the experiment will operate at "high" pH.

S2: Model details

This section provides some of the mathematical details that were omitted from the main text for brevity. The governing partial differential integral equation is not derived here because an excellent, detailed derivaiton already exists in the published literature. [31] The Equation is repeated here for the reader's convenience.

$$\frac{\partial n_i(x)}{\partial t} + G_i \frac{\partial n_i(x)}{\partial x} = -\frac{n_i(x)}{\tau} + \frac{\beta x^2}{2} \int_0^x \frac{n_i((x^3-\lambda^3)^{1/3}) n_i(\lambda)}{(x^3-\lambda^3)^{2/3}} d\lambda - \beta n_i(x) \int_0^\infty n_i(\lambda) d\lambda \tag{4.40}$$

$$B_i = k_{i,b}\left(\frac{C}{K_{eq,i}^{1/2}} - 1\right)^{b_i} m_{i,2} \qquad G_i = k_{i,g}\left(\frac{C}{K_{eq,i}^{1/2}} - 1\right)^{g_i} \tag{4.41}$$

$$i = \alpha, \beta, ... \qquad n_i(t=0,x) = n_{i,seed} \qquad n_i(t,x=0) = \frac{B_i}{G_i} \tag{4.42}$$

where $n_{i,seed}$ represents the size distribution of seeds added to the crystallizer as a pulse at $t = 0$. The agglomeration kernel used here implies that agglomeration events can only occur among particles in the same distribution (of the same solid form). This is empirically false, but one expects that the physical essence and perhaps the important effects of agglomeration can be captured and understood by this description. The simplification is justified by the results obtained. The second governing equation for the model is the solute balance ODE.

$$\frac{dC}{dt} = \frac{C_0 - C}{\tau} - \sum_{i=\alpha,\beta} \rho_i k_{i,g} k_{i,v} \left(\frac{C}{K_{eq,i}^{1/2}} - 1\right)^{g_i} \int_0^\infty n_i x^2 dx \tag{4.43}$$

$$C(t=0) = C_0 \tag{4.44}$$

where C_0 is the inlet concentration. The method of moments changes some distribution function, $f(t,x)$, into an infinite set of moments that are explicitly independent of the variable, x, but that collectively retain much of the information relating the original function to the eliminated variable (x). The method of moments can be used to eliminate the x dependence from some distribution function $f(t,x) \in [0,\infty)$ as shown below

$$m_0(t) = \int_0^\infty f(t,x)dx \tag{4.45}$$

$$m_1(t) = \int_0^\infty x\ f(t,x)dx \tag{4.46}$$

$$m_2(t) = \int_0^\infty x^2\ f(t,x)dx \tag{4.47}$$

$$m_k(t) = \int_0^\infty x^k\ f(t,x)dx \tag{4.48}$$

In the precipitator model, the method of moments was used to transform the partial differential integral equation (Equation 4.40) in t and x into an infinite set of ODEs in just t. When this procedure is followed, the moments take on physical significance; the zeroth moment is the total crystal number density, the first is the total particle length density, the second is related to the total particle surface area density through a shape factor ($k_{i,v}$), and the 3rd is related to the total crystal volume density through a shape factor. The k^{th} moment transformation of each term in Equation 4.40 is given in Equations 4.49-4.55. Note that both populations (n_α and n_β) are generally functions of t and x. In the interest of simplicity of presentation, the time functionality of the $n_i(t,x)$ and $m_i(t)$ is implicit throughout much of this Supplementary Information. The first term

in Equation 4.40 (farthest to the left):

$$\int_0^\infty x^k \frac{\partial n_i}{\partial t} dx = \frac{\partial}{\partial t} \int_0^\infty x^k \, n_i dx = \frac{dm_k}{dt} \tag{4.49}$$

The second term requires integration by parts. When $k = 0$,

$$G_i \int_0^\infty \frac{\partial n_i}{\partial x} dx = B_i \tag{4.50}$$

and the $k \neq 0$ case becomes

$$\int_0^\infty G_i \; x^k \frac{\partial n_i}{\partial x} dx = G_i \left[x^k n(t,x) \Big|_0^\infty - k m_{k-1} \right] = -k G_i m_{k-1} \tag{4.51}$$

The third term:

$$\int_0^\infty -x^k \frac{n_i(t,x)}{\tau} dx = -\frac{m_k}{\tau} \tag{4.52}$$

For the fourth term, it is helpful to first swap the order of integration

$$\int_0^\infty \frac{\beta x^{2+k}}{2} \int_0^x \frac{n_i((x^3-\lambda^3)^{1/3}) n_i(\lambda)}{(x^3-\lambda^3)^{2/3}} d\lambda dx = \frac{\beta}{2} \int_0^\infty \int_\lambda^\infty x^{2+k} \frac{n_i((x^3-\lambda^3)^{1/3}) n_i(\lambda)}{(x^3-\lambda^3)^{2/3}} dx d\lambda \tag{4.53}$$

Then, it is helpful to make the change of variables, $u^3 = (x^3 - \lambda^3)$. (See Ref. 2) [35]

$$\frac{\beta}{2} \int_0^\infty \int_\lambda^\infty x^{2+k} \frac{n_i((x^3-\lambda^3)^{1/3}) n_i(\lambda)}{(x^3-\lambda^3)^{2/3}} d\lambda dx = \frac{\beta}{2} \int_0^\infty n(\lambda) \int_0^\infty (u^3+\lambda^3)^{k/3} n(u) du d\lambda \tag{4.54}$$

The fifth term simplifies to

$$-\int_0^\infty x^k \beta n_i(x) \int_0^\infty n_i(\lambda) d\lambda dx = -\beta m_k m_0 \tag{4.55}$$

And since the i form nucleation expression can be rewritten in terms of the second moment of the i distribution,

$$B_i = k_{i,b}\left(\frac{C}{K_{eq,i}^{1/2}} - 1\right)^{b_i} m_{i,2} \tag{4.56}$$

the infinite set of moment equations describing the populations (n_i) can be written succinctly as Equations 4.57 and 4.58 below. For $k = 0$:

$$\frac{dm_0}{dt} = -\frac{m_0}{\tau} + k_{i,b}\left(\frac{C}{K_{eq,i}^{1/2}} - 1\right)^{b_i} m_{i,2} - \frac{\beta}{2} m_o^2 \tag{4.57}$$

when $k \neq 0$

$$\frac{dm_k}{dt} = -\frac{m_k}{\tau} + kG_i m_{k-1} + \frac{\beta}{2}\int_0^\infty n(\lambda)\int_0^\infty (u^3 + \lambda^3)^{k/3} n(u) du d\lambda - \beta m_k m_0 \tag{4.58}$$

The only piece of the solute balance ODE affected by the transformation is the last term (on the far right of Equation 4.43: $4\pi\rho_i k_{g,i}\left(\frac{C}{K_{eq,i}^{1/2}} - 1\right)^{g_i} \int_0^\infty n_i x^2 dx$). This term represents the moles of solute deposited from the solution into the solid distribution of polymorph i (n_i) per unit volume per unit time. Crystals grow from the surface, so the total solid crystal deposition rate is a product of the linear growth rate and the total amount of surface area that exists in the distribution. The integral term is necessary to determine how much crystal surface area exists in the distribution. In Equation 4.43, $k_{i,v}$ is the shape factor that relates the crystal length coordinate to its surface area and volume. After the method of moments transformation, the solute balance ODE simplifies to

$$\frac{dC}{dt} = \frac{C_0 - C}{\tau} - \sum_{i=\alpha,\beta} \rho_i k_{i,g} k_{i,v}\left(\frac{C}{K_{eq/i}^{1/2}} - 1\right)^{g_i} m_{i,2} \tag{4.59}$$

S3: Non-stoichiometric feed and non-dimensionalization

The experiments reported in this paper took place at relatively high pH conditions. Therefore, we have assumed that the reactant salts were fully dissociated and that all of the aqueous carbon was in the carbonate form (CO_3^{2-}). In this case, the only relevant aqueous species are Ca^{2+} and CO_3^{2-}, and the chemistry can be summarized as:

$$Ca^{2+} + CO_3^{2-} \rightleftharpoons CaCO_{3,(s,\alpha)} \qquad Ca^{2+} + CO_3^{2-} \rightleftharpoons CaCO_{3,(s,\beta)} \tag{4.60}$$

Therefore, there are $C - R = 2$ independent mole balances. Once the power law growth and nucleation kinetic expressions are defined, the solute balances for component 1 (Ca^{2+}) and component 2 (CO_3^{2-}) can be written:

$$\frac{dC_1}{dt} = \frac{C_{1,0} - C_1}{\tau} - 4\pi \sum_{i=\alpha,\beta} \rho_i k_g \left((\frac{C_1 C_2}{K_{eq/i}})^{1/2} - 1 \right)^{g_i} \int_0^\infty n_i x^2 dx \tag{4.61}$$

$$\frac{dC_2}{dt} = \frac{C_{2,0} - C_2}{\tau} - 4\pi \sum_{i=\alpha,\beta} \rho_i k_g \left((\frac{C_1 C_2}{K_{eq/i}})^{1/2} - 1 \right)^{g_i} \int_0^\infty n_i x^2 dx \tag{4.62}$$

$$B_i = k_{b,i} \left((\frac{C_1 C_2}{K_{eq/i}})^{1/2} - 1 \right)^{b_i} m_{i,2} \qquad G_i = k_{g,i} \left((\frac{C_1 C_2}{K_{eq/i}})^{1/2} - 1 \right)^{g_i} \tag{4.63}$$

The 1/2 power that appears in the growth and nucleation driving forces was justified in a previous publication. [34] Subtracting Equation 4.61 from Equation 4.62 (at steady-state) yields the mole balance

$$C_2 = C_{2,0} + C_1 - C_{1,0} \tag{4.64}$$

Only one of the solute balances (4.61 and 4.62) is linearly independent of equation 4.64. Now define $\phi = C_{2,0} - C_{1,0}$ to eliminate C_2 from Equation 4.61 to give a single solute balance in terms of $C_{1,0}$ and ϕ

$$\frac{dC_1}{dt} = \frac{C_{1,0} - C_1}{\tau} - 4\pi \sum_{i=\alpha,\beta} \rho_i k_g \left(\left(\frac{C_1(C_1+\phi)}{K_{eq/i}} \right)^{1/2} - 1 \right)^{g_i} \int_0^\infty n_i x^2 dx \tag{4.65}$$

The model is only meaningful for systems in which the feed is supersaturated, so the lowest possible value of C_1 is the value that gives a saturated solution, given ϕ. If $K_{eq,\beta}$ is the solubility product equilibrium constant of the least soluble form (calcite), then the limiting value of C_1 can be defined as a function of ϕ as shown in Equation 4.66.

$$C_{1,min} = \frac{(\phi^2 + 4K_{eq,\beta})^{1/2} - \phi}{2} \tag{4.66}$$

$C_{1,min}$ is essentially the concentration expected to exist in the reactor after an infinite residence time. Notice that in the limit $\phi \to 0$ (i.e., a stoichiometric feed), $C_{1,min} \to K_{eq,\beta}^{1/2}$. This is the expected result because $K_{eq,\beta}^{1/2}$ is the concentration of $CaCO_{3,aq}$ present in a saturated, stoichiometric solution. Now that the minimum value of C_1 is known, one can non-dimensionalize C_1.

$$y = \frac{C_1 - C_{1,min}}{(C_{1,0}(C_{1,0}+\phi))^{1/2} - C_{1,min}} \tag{4.67}$$

$y \in [0,1]$ when $\phi = 0$. If $\phi > 0$ or < 0, the upper bound for y is lower or higher, respectively. The non-stoichiometric non-dimensionalization generates four new dimensionless groups within the solute balance ODE:

$$y_0 = \frac{C_{1,0} - C_{1,min}}{(C_{1,0}(C_{1,0}+\phi))^{1/2} - C_{1,min}} \tag{4.68}$$

$$\Gamma = \frac{K_{eq,\beta}^{1/2}}{(C_{1,0}(C_{1,0}+\phi))^{1/2} - C_{1,min}} \tag{4.69}$$

$$\gamma = \frac{K_{eq,\beta}^{1/2} - K_{eq,\alpha}^{1/2}}{(C_{1,0}(C_{1,0}+\phi))^{1/2} - C_{1,min}} \tag{4.70}$$

$$Z = \frac{(\phi^2 + 4K_{eq,\beta})^{1/2}}{(C_{1,0}(C_{1,0}+\phi))^{1/2} - C_{1,min}} = \Gamma \frac{(\phi^2 + 4K_{eq,\beta})^{1/2}}{K_{eq,\beta}^{1/2}} \tag{4.71}$$

$$\frac{dy}{d\xi} = y_0 - y - \omega_{2,\beta}\left[(y^2 + Zy + \Gamma^2)^{1/2} - \Gamma\right]^{g_\beta} - \omega_{2,\alpha}\left[(y^2 + Zy + \Gamma^2)^{1/2} - \Gamma + \gamma\right]^{g_\alpha} \tag{4.72}$$

With these definitions, the dimensionless states of both the moment equations and the solute balance can be defined as shown below

$$\xi = \frac{t}{\tau} > 0 \qquad y = \frac{C_1 - C_{1,min}}{(C_{1,0}(C_{1,0}+\phi))^{1/2} - C_{1,min}} \tag{4.73}$$

$$\sigma_\alpha = \tau k_{g,\alpha}\left(\frac{1}{\Gamma - \gamma}\right)^{g_\alpha} \qquad \sigma_\beta = \tau k_{g,\beta}\left(\frac{1}{\Gamma}\right)^{g_\beta} \tag{4.74}$$

$$\omega_{\alpha,0} = 8\pi\sigma_\alpha^3 m_{\alpha,0}\frac{\rho_\alpha}{C_0 - K_{eq,\beta}^{1/2}} \qquad \omega_{\beta,0} = 8\pi\sigma_\beta^3 m_{\beta,0}\frac{\rho_\beta}{C_0 - K_{eq,\beta}^{1/2}} \tag{4.75}$$

$$\omega_{\alpha,1} = 8\pi\sigma_\alpha^2 m_{\alpha,1}\frac{\rho_\alpha}{C_0 - K_{eq,\beta}^{1/2}} \qquad \omega_{\beta,1} = 8\pi\sigma_\beta^2 m_{\beta,1}\frac{\rho_\beta}{C_0 - K_{eq,\beta}^{1/2}} \tag{4.76}$$

$$\omega_{\alpha,2} = 4\pi\sigma_\alpha m_{\alpha,2}\frac{\rho_\alpha}{C_0 - K_{eq,\beta}^{1/2}} \qquad \omega_{\beta,2} = 4\pi\sigma_\beta m_{\beta,2}\frac{\rho_\beta}{C_0 - K_{eq,\beta}^{1/2}} \tag{4.77}$$

In the limit $\phi \to 0$ (i.e., a stoichiometric feed), the following simplifications occur. $y_0 \to 1$,

$Z \to 2\Gamma$, and $C_{1,min} \to K_{eq,\beta}^{1/2}$. After these simplifications, Equation 4.72 becomes

$$\frac{dy}{d\xi} = 1 - y - \omega_{2,\beta} y^{g_\beta} - \omega_{2,\alpha}(y+\gamma)^{g_\alpha} \tag{4.78}$$

Equation 4.78 is equivalent to Equation 24 in the main text of the article.

When $\phi \to 0$, the dimensionless state definitions become:

$$\xi = \frac{t}{\tau} > 0 \qquad y = \frac{C_1 - K_{eq,\beta}^{1/2}}{C_0 - K_{eq,\beta}^{1/2}} \tag{4.79}$$

$$\sigma_\alpha = \tau k_{g,\alpha}\left(\frac{C_0 - K_{eq,\beta}^{1/2}}{K_{eq,\alpha}^{1/2}}\right)^{g_\alpha} \qquad \sigma_\beta = \tau k_{g,\beta}\left(\frac{C_0 - K_{eq,\beta}^{1/2}}{K_{eq,\beta}^{1/2}}\right)^{g_\beta} \tag{4.80}$$

$$\omega_{\alpha,0} = 8\pi\sigma_\alpha^3 m_{\alpha,0}\frac{\rho_\alpha}{C_0 - K_{eq,\beta}^{1/2}} \qquad \omega_{\beta,0} = 8\pi\sigma_\beta^3 m_{\beta,0}\frac{\rho_\beta}{C_0 - K_{eq,\beta}^{1/2}} \tag{4.81}$$

$$\omega_{\alpha,1} = 8\pi\sigma_\alpha^2 m_{\alpha,1}\frac{\rho_\alpha}{C_0 - K_{eq,\beta}^{1/2}} \qquad \omega_{\beta,1} = 8\pi\sigma_\beta^2 m_{\beta,1}\frac{\rho_\beta}{C_0 - K_{eq,\beta}^{1/2}} \tag{4.82}$$

$$\omega_{\alpha,2} = 4\pi\sigma_\alpha m_{\alpha,2}\frac{\rho_\alpha}{C_0 - K_{eq,\beta}^{1/2}} \qquad \omega_{\beta,2} = 4\pi\sigma_\beta m_{\beta,2}\frac{\rho_\beta}{C_0 - K_{eq,\beta}^{1/2}} \tag{4.83}$$

All of the experiments reported here were performed with a stoichiometric feed and at high enough pH such that Equation 4.60 is representative of the chemistry. In this case, $y \in [0,1]$ and Equation 4.78 is the only necessary solute balance ODE.

S4: Crystal drying procedure

The data in Table 4.1 support the claim that polymorph transition does not occur during the drying procedure described in the experimental section. The table reports how the percent polymorph (by mass) of three different samples changed as a function of drying procedure. Each sample was measured without drying, after drying for 1 hour at $70°C$, and after drying for 72 hours at $70°C$. The phase fractions were the same for all

Sample	preparation	% calcite	% vaterite	% aragonite
1	moist	73	27	0
	dried 1 hr	73	27	0
	dried 72 hr	73	27	0
2	moist	70	30	0
	dried 1 hr	70	30	<1
	dried 72 hr	70	30	<1
3	moist	64	36	0
	dried 1 hr	64	35	<1
	dried 72 hr	64	35	<1

Table 4.1: Each sample was collected from experiments performed at $T = 25°C$ with $\tau = 6$ minutes. Samples 1, 2 and 3 were performed with $C_0 = 0.0125$, 0.05, and 0.15 moles/liter, respectively. The samples were taken during startup dynamics to ensure that the initial distribution would contain both vaterite and calcite. The percent polymorph (mass) did not change when the drying procedure was varied.

drying procedures (within experimental error). In all subsequent experiments, solids were dried for 24 hours at $70°C$ before measuring the phase fractions with XRD. A similar procedure was followed in several published articles. [19, 53]

S5: Reproducibility

We duplicated one set of experimental conditions to confirm that our experimental procedure was reproducible. The repeated experiment was performed with a residence time of $\tau = 12$ minutes, a temperature of $T = 25°C$, and an inlet concentration of 0.0125 molar. As in all of the experiments, there is some noise ($\approx 3\%$) in the phase fitting results, but the average of the readings can be compared. The data in Table 4.2 illustrate that the experiment is reproducible within the error of the phase fitting. The average phase fraction measured at steady state in sample 1 and sample 2 was 95 and 94 wt. %, respectively. We therefore declare this experiment reproducible.

Sample	max %	min %	mean %
1	95	93	94
2	96	93	95

Table 4.2: Percent polymorph was characterized with powder XRD phase fitting at 30 minute intervals. The experiments described here were performed at $T = 25°C$, $\tau = 12$ minutes, and $C_0 = 0.0125$ molar. The table reports the maximum, minimum, and average polymorph % calculated from the powder XRD patterns taken after the process reached steady-state. The noise in the measurement is evident in the spread between the maximum and minimum values that were observed. The experimental observation was reproducible within the error of the measurement ($\approx \pm 3\%$).

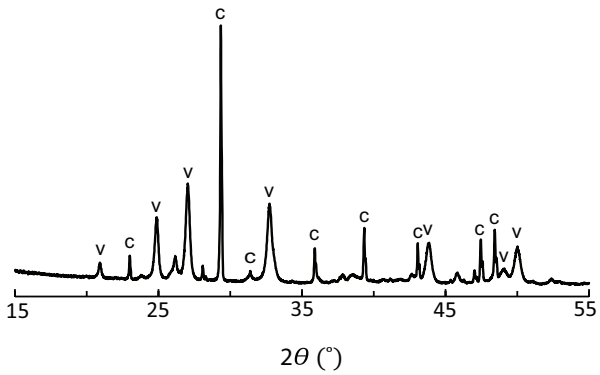

Figure 4.10: Powder X-ray diffraction pattern collected on solids removed from the steady-state precipitation experiment described in Figure 5a of the main text of this publication. The experiment was performed at $T = 25$ °C, τ= 6 min, and C_0=0.0125 M. Rietveld phase fitting indicates that the solids are 75 % vaterite and 25 % calcite.

S6: Additional NMR spectra and XRD patterns

Throughout this paper, the primary technique used to quantify phase fractions was Rietveld phase fitting of powder XRD patterns. This method is quick and accurate whenever the phase domains are large enough to reflect Xrays. Figures 4.10 and 4.11 were acquired on the steady-state effluent crystals from the experiments described in Figures 5a and 5b in the main text of this publication. Rietveld phase fitting of the pattern in Figure 4.10 and 4.11 indicate that the solids are 75 % and 93 % vaterite, respectively. Complementary ^{43}Ca NMR spectra were acquired on two select samples to determine the local 43Ca environments associated with the different $CaCO_3$ phases.

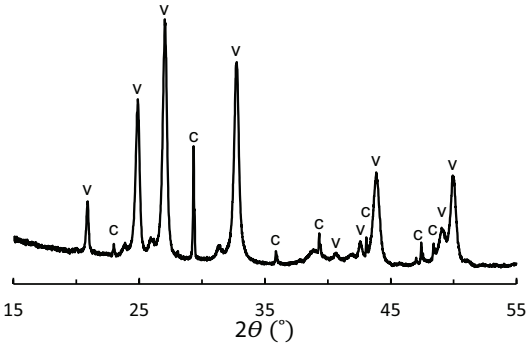

Figure 4.11: Powder X-ray diffraction pattern collected on solids removed from the steady-state precipitation experiment described in Figure 5b of the main text of this publication. The experiment was performed at $T = 25$ °C, $\tau = 9$ min, and C_0=0.0125 M. Rietveld phase fitting indicates that the solids are 93 % vaterite and 7 % calcite.

^{43}Ca is difficult to characterize with NMR due to its low gyromagnetic ratio (-1.803 $\times$ 10^7 rad T^{-1} s^{-1}), low natural isotopic abundance ($\approx$ 0.135 %), and the general difficulties associated with quadrupolar nuclei (7/2 spin). These challenges were overcome with the high magnetic fields (19.6 T) possible at the U.S. National High Magnetic Field Laboratory in Tallahassee, Florida. The spectrum in Figure 4.12 was acquired on a solid sample known to contain aragonite, calcite, and vaterite. This sample was chosen to confirm that each solid form displays unique, resolvable chemical shifts under our experimental conditions. A second spectrum (Figure 8b) was acquired on a sample produced in our precipitator for which XRD indicated that the sample was predominantly vaterite ($<$ 1% calcite). The single peak centered around 3 ppm in Figure 8b indicates that the only form present within the detection of the measurement is vaterite. This corroborates the powder XRD data, and the SEM images presented in the main text (Figure 8a, c, d). Therefore, vaterite is the only detectable solid form in the sample obtained at a residence time of 6 minutes, an inlet concentration of 0.15 molar, and a temperature of 25 °C.

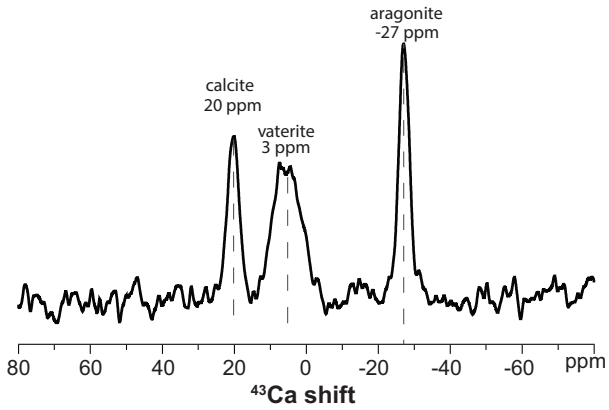

Figure 4.12: Solid-state, single pulse ^{43}Ca NMR spectrum acquired from a solid sample known to contain vaterite, aragonite, and calcite (from XRD phase fitting). The NMR spectrum was acquired at 19.6 T, 25 °C, and 5 kHz MAS with a 0.5 s delay time. The peaks at 20, 3 and -27 ppm can be assigned to calcite, vaterite, and aragonite, respectively. This measurement confirms that all three solid forms have resolvable chemical shifts at these conditions.

The centers of the NMR peaks associated with calcite, vaterite, and aragonite are sensitive to the molar concentration of the aqueous $CaCl_2$ used to reference the spectrum, but the broad vaterite peak is found between the calcite and aragonite peaks for all reference concentrations. [45]

S7: Additional discussion of model analysis

When the stability transitions are projected onto the 2-dimensional Φ_α vs. Φ_β plane as in Figure 3 (main text of this article), the location of the mixed-polymorph/pure-polymorph bifurcation lines are strong functions of the Agglomeration numbers and weak functions of all of the other parameters. The two stability transition boundaries that mark the dynamic stability transition from a pure α or a pure β steady-state to a mixed-polymorph steady-state move away from the $\Phi_\alpha = \Phi_\beta$ line as the Agglomeration numbers increase from zero. In the main text of the article, A_α^{crit} was identified as the lowest value of A_α for which the mixed-polymorph steady-state is possible at a fixed value of the

other 8 parameters such that $\Phi_\alpha > \Phi_\beta$. Our numerical results consistently show that this critical agglomeration number occurs when the steady-state solute concentration at the pure α steady-state is exactly equal to the steady-state concentration at the pure β steady-state in the limit of $A_\beta \to 0$. The mixed-polymorph steady-state also becomes linearly stable when $A_\alpha > A_\alpha^{crit}$.

A similar critical agglomeration number (A_β^{crit}) exists when $\Phi_\beta > \Phi_\alpha$. Qualitatively, this pure β/mixed-polymorph bifurcation surface similarly corresponds to all of the parameter combinations at which the solute concentration (y) is the same at both the pure β steady-state ($A_\beta \neq 0$) and the pure α steady-state when $A_\alpha = 0$ (i.e., $y_{\beta,A_\beta \neq 0} = f(Da_\beta, g_\beta, b_\beta, A_\beta) = y_{\alpha,A_\alpha=0} = g(Da_\alpha, g_\alpha, b_\alpha, \gamma)$). Analogously, the mixed-polymorph steady-state is linearly stable when $A_\beta > A_\beta^{crit}$.

Therefore, the position of each bifurcation surface projection in the Φ_α vs Φ_β plane that separates a region of pure polymorph dynamic stability from a region of mixed-polymorph dynamic stability depends on only one of the Agglomeration numbers. When $\Phi_\alpha > \Phi_\beta$, the important Agglomeration number for relative dynamic stability is A_α. Alternatively, when $\Phi_\alpha < \Phi_\beta$, the important Agglomeration number for relative dynamic stability is A_β. Each of the stability diagrams in this article were calculated with $A_\beta = A_\alpha$. The same information could have been presented with $A_i = 0$, $A_j \neq 0$, and twice as many figures. In other words, each Agglomeration number only affects the stability relationships for 1/2 of the stability diagram ($\Phi_{i=q} > \Phi_{i \neq q}$). Each stability diagram presented at fixed $A_\alpha = A_\beta$ is technically a projection of the four dimensional stability space defined by $[\Phi_\alpha, \Phi_\beta, A_\alpha, A_\beta]$ onto the two dimensional plane defined by $[\Phi_\alpha, \Phi_\beta, A_\alpha = A_\beta = A]$ (where A is some constant). Based on all of our calculations, we believe that no information is lost when the results are presented and discussed in terms of a three dimensional stability space defined by $[\Phi_\alpha, \Phi_\beta, A_\alpha = A_\beta]$. Therefore, we presented and discussed all stability diagrams as two dimensional slices/projections of the three

dimensional stability space defined by $[\Phi_\alpha, \Phi_\beta, A_\alpha = A_\beta = A]$

Figures 4.13-4.15 demonstrate that the projections of the bifurcation surfaces onto the Φ_α and Φ_β plane are relatively insensitive to physically reasonable changes in the remaining parameters (g_α, b_α, g_β, b_β, and γ). In each figure, all but one parameter that affects each bifurcation surface is held constant at the "base case" values defined in Figure 3b of the main text of this paper ($g_i = 1.5$, $b_i = 2.5$, $\gamma = -0.0042$, and $A_i = 0.1$). Then, the mixed-polymorph stability boundary is projected onto the Φ_α, Φ_β plane for several different physically reasonable values of the last parameter. The figure then illustrates how changing that parameter affects the position of the mixed-polymorph stability boundary.

In Figure 4.13, the mixed polymorph stability boundary is shown for g_α and $g_\beta = 1$, 1.5, and 2. Variation in both g_α and g_β is presented on the same figure because each parameter only affects the boundary on one side of the $\Phi_\alpha = \Phi_\beta$ line. Increasing the growth exponent while holding all of the other parameters constant grows the mixed-polymorph stability region, but has very little effect on the overall shape of the boundary.

In Figure 4.14 the mixed-polymorph stability boundary is shown for b_α and $b_\beta = 1.5$, 2.5, and 3.5. Similarly, variation of the bifurcation surface projection's position in the Φ_α vs Φ_β plane with respect to both b_α and b_β is presented on the same figure because each b_i only affects the boundary on one side of the $\Phi_\alpha = \Phi_\beta$ line. The bifurcation surfaces are relatively insensitive to changes in b_i, but the total mixed-polymorph stability region does shrink as the b_i are increased.

In Figure 4.15 the mixed-polymorph stability boundary is shown for $\gamma = -0.0042$, -0.1, and -0.2. The solubility parameter (γ) exhibits no effect on the mixed-polymorph stability bifurcation surface above the $\Phi_\alpha = \Phi_\beta$ line, but it has a substantial effect on the surface below this line. γ quantifies the difference in solubility between the two forms

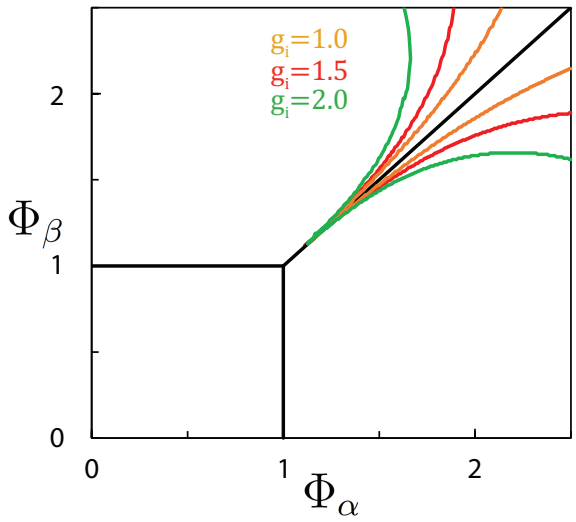

Figure 4.13: The outermost (green), middle (red), and inner (orange) curves are the mixed-polymorph/pure-polymorph stability transition boundaries when $g_i = 2$, 1.5, and 1, respectively. These curves were all calculated with the other 8 dimensionless model parameters fixed at the values associated with Figure 3b in the main text of the article ($b_\alpha = b_\beta = 2.5$, $\gamma = -0.0042$, and $A_\alpha = A_\beta = 0.1$)). The mixed-polymorph stability region is larger when the growth exponent is higher, but changing the growth exponent does not change the qualitative shape of the curve.

relative to the inlet supersaturation of the most stable form. When it is close to zero (such as in the experiments reported here in which $\gamma \approx -0.0042$), the mixed polymorph bifurcation surfaces are almost symmetric around the $\Phi_\alpha = \Phi_\beta$ line. As γ approaches -1, the mixed polymorph-stability region grows below the $\Phi_\alpha = \Phi_\beta$ line, introducing considerable asymmetry.

S8: Vaterite stability data

Table S3 shows how the solid form of two different samples changed during storage. Each data point was determined by phase fitting of a powder X-Ray diffraction pattern. Samples were filtered and dried as previously discussed. Crystals were then stored in a sealed vial for the time listed in the table. Dry vaterite prepared in this way is stable for

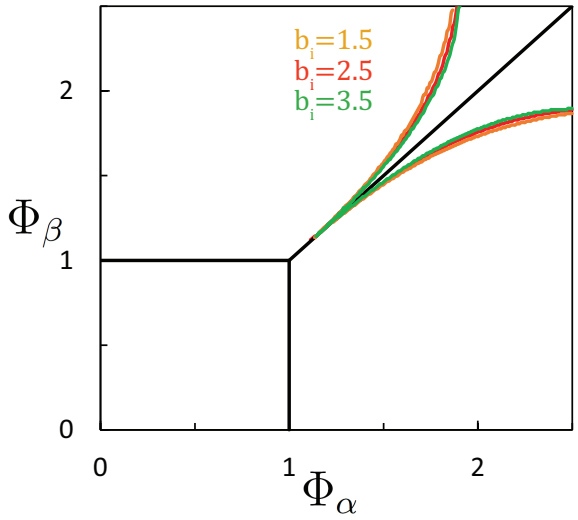

Figure 4.14: The outermost (orange), middle (red), and inner (green) curves are the mixed-polymorph/pure-polymorph stability transition boundaries when $b_i = 1.5$, 2.5, and 3.5, respectively. These curves were all calculated with the other 8 dimensionless model parameters fixed at the values associated with Figure 3b in the main text of the article ($g_\alpha = g_\beta = 1.5$, $\gamma = -0.0042$, and $A_\alpha = A_\beta = 0.1$)). The bifurcation surfaces are relatively insensitive to changes in b_i, but the total mixed-polymorph stability region does shrink as the b_i are increased.

at least 31 days.

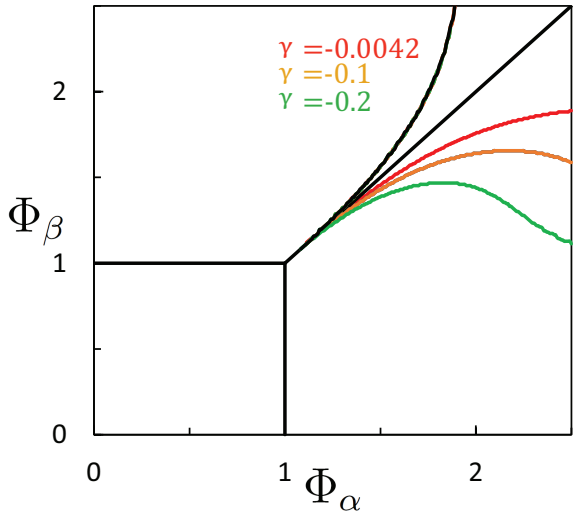

Figure 4.15: The outermost (green), middle (orange), and inner (red) curves are the mixed-polymorph/pure-polymorph stability transition boundaries when $\gamma = -0.2$, -0.1, and -0.0042, respectively. These curves were all calculated with the other 8 dimensionless model parameters fixed at the values associated with Figure 3b in the main text of the article ($g_\alpha = g_\beta = 1.5$, $b_\alpha = b_\beta = 2.5$, and $A_\alpha = A_\beta = 0.1$)). The position of the mixed-polymorph/pure polymorph stability transition surface projection onto the Φ_α vs Φ_β plane above the $\Phi_\alpha = \Phi_\beta$ line is not a function of γ. This is intuitively consistent because γ only affects the metastable form driving forces in the model. The position of the mixed-polymorph/pure polymorph stability transition surface projection onto the Φ_α vs Φ_β plane below the $\Phi_\alpha = \Phi_\beta$ line shows a relatively strong dependence on γ.

Sample	# of days	% calcite	% vaterite
1	0	1.1	98.9
	21	1.7	98.3
	31	1.1	98.9
2	0	0.5	99.5
	8	0.6	99.4

Table 4.3: Two separate samples were monitored that initially contained >98% vaterite (based on X-Ray diffraction phase fitting). Changes in polymorph % that have been observed thus far are smaller than the error of the phase fitting procedure. Dry vaterite can be stable for at least 31 days without any additional additives or treatments.

Bibliography

[1] J. Thun, L. Seyfarth, C. Butterhof, J. Senker, R. E. Dinnebier, and J. Breu. Wohler and liebig revisted: 176 years of polymorphism in benzamide-and the story still continues! *Cryst. Growth Des.*, 9(5):2435–2441, 2009.

[2] W. Ostwald. Studien uber die bildung und umwandlung fester korperr. *Zeitschrift fur physikalische Chemie*, 22:289–330, 1897.

[3] P. T. Cardew and R. J. Davey. The kinetics of solvent-mediated phase transformations. *Proc. R. Soc. Lond.*, 398:415–428, 1985.

[4] J. Scholl, C. Lindenberg, L. Vicum, J. Brozio, and M. Mazzotti. Precipitation of a l-glutamic acid: Determination of growth kinetics. *Faraday discussions*, 136:247–264, 2006.

[5] E. S. Ferrari, R. J. Davey, C. W. I., A. L. Gillon, and C. S. Towler. Crystallization in polymorphic systems: The solution-mediated transformation of β to α glycine. *Cryst. Growth Des.*, 3(1):53–60, 2003.

[6] H. G. Brittain. *Polymorphism in Pharmaceutical Solids.* CRC Press, 2009.

[7] J. Bernstein. *Polymorphism in Molecular Crystals.* Oxford University Press, 2008.

[8] S. R. Byrn. *Solid-state Chemistry of Drugs.* Academic Press, 1982.

[9] A. LLinas and J. M. Goodman. Polymorph control: Past, present and future. *Drug Discovery Today*, 13:198–210, 2008.

[10] C. Cashell, D. Corcoran, and B. K. Hodnett. Control of polymorphism and crystal size of l-glutamic acid in the absence of additives. *J. Cryst. Growth*, 273(1-2):258–265, 2004.

[11] N. C. Kee, R. B. H. Tan, and R. D. Braatz. Selective crystallization of the metastable α-form of l-glutamic acid using concentration feedback control. *Cryst. Growth Des.*, 7:3044–351, 2009.

[12] M. W. Hermanto, M. Chiu, and R. D. Braatz. Nonlinear model predictive control for the polymorphic transformation of l-glutamic acid crystals. *AIChE J.*, 54.12:3248–3259, 2009.

[13] X. Yang, B. Sarma, and A. S. Myerson. Polymorph control of micro/nano-sized mefenamic acid crystals on patterned self-assembled monolayer islands. *Cryst. Growth Des.*, 12:5221–5228, 2012.

[14] I. S. Lee, A. Y. Lee, and A. S. Myerson. Concomitant polymorphism in confined environment: Implication to crystal form screening. *Pharm. Res.*, 25:960–968, 2008.

[15] T. Kato, T. Suzuki, T. Amamiya, T. Irie, and M. Komiyama. Effects of macromolecules on the crystallization of $caco_3$: the formation of organic/inorganic composites. *Supramolecular Science*, 5:411–415, 1998.

[16] C. Gu, K. Chatterjee, V. Young Jr., and D. J. W. Grant. Stabilization of a metastable polymorph of sulfamerazine by structure related additives. *J. Cryst. Growth*, 235(1):471–481, 2002.

[17] E. Simone, A. N. Saleemi, N. Tonnon, and Z. K. Nagy. Active polymorphic feedback control of crystallization processes using a combined raman and atr-uv/vis spectroscopy approach. *Cryst. Growth Des.*, 14:1839–1850, 2014.

[18] S. L. Morissette, S. Soukasene, D. Levinson, M. J. Cima, and O. Almarsson. Elucidation of crystal form diversity of the hiv protease inhibitor ritonavir by high-throughput crystallization. *Proc. Natl. Acad. Sci.*, 100(5):2180–2184, 2003.

[19] T. Lai, S. Ferguson, L. Palmer, B. L. Trout, and A. S. Myerson. Continuous crystallization and polymorph dynamics in the l-gltanic acid system. *Org. Process Res. Dev.*, 18:1382–1390, 2014.

[20] T. C. Lai, J. Cornevin, S. Ferguson, N. Li, B. L. Trout, and A. S. Myerson. Control of polymorphism in continuous crystallization via mixed suspension mixed product removal systems cascade design. *Cryst. Growth Des.*, 15.7:3374–3382, 2015.

[21] T. C. Farmer, C. L. Carpenter, and M. F. Doherty. Polymorph selection by continuous crystallization. *AIChE J.*, 62:3505–3514, 2016.

[22] J. Worlitscek and M. Mazzotti. Model-based optimization of particle size distribution in batch-cooling crystallization of paracetamol. *Cryst. Growth Des.*, 4(5):891–903, 2004.

[23] J. Garside. Industrial crystallization from solution. *Chem. Eng. Sci.*, 40(1):3–26, 1985.

[24] J. Kawano, N. Shimbayashi, A. Miyake, and M. Kitamura. Precipitation diagram of calcium carbonate polymorphs: Its construction and significance. *J. Phys. Condens. Matter*, 21(42):1–6, 2009.

[25] B. R. Constantz, A. Youngs, and T. Holland. Reduced-carbon footprint concrete compositions. U.S. patent 7,815,880, 2010.

[26] B. R. Constantz, K. Farsad, C. Camire, and I. Chen. Methods and compositions using calcium carbonate. U.S. patent 7,922,809, 2011.

[27] A. McNaught and A. Wilkinson. *Compendium of Chemical Terminology*. 1997.

[28] J. W. Mullin. *Crystallization*. Oxford: Butterworth-Heinemann, 1993.

[29] M. Fujiwara, P. S. Chow, D. L. Ma, and R. D. Braatz. Paracetamol crystallization using laser backscattering and atr-ftir spectroscopy: Metastability, agglomeration, and control. *Cryst. Growth Des.*, 2(5):363–370, 2002.

[30] B. K. Padia and S. K. Bhatia. Multiplicity and stability analysis of agglomeration controlled precipitation. *Chem. Eng. Comm.*, 104:227–244, 1991.

[31] D. Ramkrishna. *Population Blances: Theory and Application to Particulate Systems in Engineering.* Academic Press, 2000.

[32] D. L. Marchisio, R. D. Vigil, and R. O. Fox. Quadrature method of moments for aggregation-breakage processes. *J. Colloid Interface Sci.*, 258(2):322–334, 2002.

[33] A. G. Fredrickson, D. Ramkrishna, and H. M. Tsuchiya. Statistics and dynamics of procaryotic cell populations. *Math. Biosci.*, 1:327–374, 1967.

[34] P. Dandekar and M. F. Doherty. A mechanstic growth model for inorganic crystals: Growth mechanism. *AIChE J.*, 60:3720–3731, 2014.

[35] D. L. Marchisio, J. T. Pikturna, R. O. Fox, R. D. Vigil, and A. A. Barresi. Quadature method of moments for population-balance equations. *AIChE J.*, 49(5):1266–1276, 2004.

[36] R. Mcgraw. Description of aerosol dynamics by the quadrature method of moments. *Aerosol Science and Technology*, 27:255–265, 1997.

[37] R. G. Gordon. Error bounds in equilibirum statistical mechanics. *Journal of Mathematical Physics*, 9(5):655–663, 1968.

[38] J. Gimbun, Z. K. Nagy, and C. D. Rielly. Simultaneous quadrature method of moments for the solution of population balance equations, using a differential algebraic equation framework. *Ind. Eng. Chem. Res.*, 48(16):7798–7812, 2009.

[39] R. Mcgraw and D. L. Wright. Chemically resolved aerosol dynamics for internal mixtures by the quadrature method of moments. *Journal of Aerosol Science*, pages 189–209, 2003.

[40] V. Alopaeus, M. Laakonen, and J. Aittamaa. Numerical solution of moment-transformed population balance equation with fixed quadrature points. *Chem. Eng. Sci.*, 61:4919–4929, 2006.

[41] K. J. Sampson and D. Ramkrishna. A new solution to the brownian coagulation equation through the use of root-shifted poroblem-specific polynomials. *J. Colloid Interface Sci.*, 103(1):245–254, 1985.

[42] S. H. Strogatz. *Nonlinear Dynamics and Chaos.* Westview Press, 1994.

[43] R. Seydel. *Practical Bifurcation and Stability Analysis*. Springer Science & Business Media, 2009.

[44] M. Kubicek. Algorithm 502 dependence of solution of nonlinear systems on a parameter. *ACM Transactions on Mathematical Software*, 2(1):98–107, 1976.

[45] D. L. Bryce, E. B. Bultz, and D. Aebi. Calcium-43 chemical shift tensors as probes of calcium binding environments. insights into the structure of the vaterite $CaCO_3$ Polymorph by ^{43}Ca solid-state NMR spectroscopy. *J. Am. Chem. Soc.*, 130(29):9282–9292, 2008.

[46] R. Demichelis, P. Raiteri, J. D. Gale, and J. D. Dovesi. The multiple structures of vaterite. *Cryst. Growth Des.*, 13(6):2247–2251, 2013.

[47] L. Kabalah-Amitai, B. Mayzel, Y. Kaufmann, A. N. Fitch, L. Bloch, P. U. P. A. Gilbert, and B. Pokroy. Vaterite crystals contain two interdispersed structures. *Science*, 340:454–457, 2013.

[48] C. Lindenberg, J. Scholl, L. Vicum, M. Mazzotti, and J. Brozio. L-glutamic acid precipitation: Agglomeration effects. *Cryst. Growth Des.*, 8(1):224–237, 2008.

[49] A. P. Collier and M. J. Hounslow. Growth and aggregation rates for calcite and calcium oxdalate monohydrate. *AIChE J.*, 45(11):2298–2305, 1999.

[50] R. Zauner and A. Jones. Determination of nucleation, growth, agglomeration, and disruption kinetics from experimental precipitation data: the calcium oxalate system. *Chem. Eng. Sci.*, 55:4129–4232, 2000.

[51] J. Hostomsky and A. Jones. Calcium carbonate crystallization, agglomeration and form during continuous precipitation from solution. *J. Phys. D: Appl. Phys.*, 24:165–170, 1991.

[52] R. David, F. Espitalier, A. Cameirao, and L. Rouleau. Developments in the understanding and modeling of the agglomeration of suspended crystals in crystallization from solutions. *KONA Powder and Particle Journal*, (21):40–53, 2003.

[53] D. Kralj, L. Brecevic, and A. E. Nielson. Vaterite growth and dissolution in aqueous solution i. kinetics of crystal growth. *J. Cryst. Growth*, 104:793–800, 1990.

Chapter 5

Rate-based, multi-component, electroclytic mass transport during reactive absorption

5.1 Introduction

Concentrated, multicomponent mixtures of non-charged species are capable of exhibitting osmotic diffusion, diffusion barriers, and even reverse diffusion effects that are qualitatively unpredictable with mass transport descriptions based on Fick's laws. [1] When the diffusing species are charged, these effects are excacerbated by the diffusion potentials set up to maintain macroscopic electroneutrality. [2] Furthermore, the relatively long-range electrostatic interactions aqueous electrolytes impose on each other generate significant solution phase non-idealities at realtively low concentrations. [3] These effects and the challenges they present during process design are entirely nonexistent in binary and in dilute multicomponent, non-charged systems. Each of these effects are individually documented in the literature, but limited tools exist for considering them all simul-

taneously during process synthesis, especially in systems requiring a rate-based (kinetic) description of simultaneous chemical reaction during mass transport. Despite the lack of available tools to accurately describe these systems, multicomponent mass transport effects combine with electrochemical and reaction effects in nonlinear combinations across a wide array of industrially relevant systems and processes. Essentially every process that involves aqueous oxides also involves the coupled heat and mass transport of concentrated charged species, such as hydrothermal zeolite synthesis of aluminates (Al_xO_y) and silicates (Si_xO_y), phosphate (P_xO_y) production for agricultural fertilizers, and the ubiquitous carbon dioxide/bicarbonate/carbonate ($CO_2/HCO_3^-/CO_3^{2-}$) chemistry. The carbonate chemistry buffers the ocean pH and supplies CO_3^{2-} for the biomineralization of calcium carbonate ($CaCO_3$) in coral reefs and in crustacean shells. It also monitors the pH of mammalian blood by absorbing waste CO_2 from cells and tissues throughout the body and dumping it to the atmosphere via the lungs. Some geologic brine and oil reservoirs are encased by $CaCO_3$, generating the same chemistry near mineral surfaces such that the transport properties of these ionic species become integral to brine and/or oil extraction. It even governs the reactive absorption and precipitation of CO_2 during carbon capture and utilization as structural materials (CCUSM).

The CCUSM chemistry involves the complete set of reactions given in Equations 5.1 through 5.4 below.

$$CO_2 + OH^- \leftrightharpoons HCO_3^- \tag{5.1}$$

$$HCO_3^- + OH^- \leftrightharpoons H_2O + CO_3^{2-} \tag{5.2}$$

$$H^+ + OH^- \leftrightharpoons H_2O \tag{5.3}$$

$$Ca^{2+} + CO_3^{2-} \leftrightharpoons CaCO_{3,(s)} \tag{5.4}$$

The reaction rates of reactions 5.2 and 5.3 are fast enough that they are typically modeled

as if they occur infinitely fast (i.e., chemical equilibrium is always maintained). $CaCO_{3,(aq)}$ also forms essentially instantaneously, but the precipitation of $CaCO_3$ into the solid phase requires a kinetic treatment through a population balance model (See Chapter 4). The only single phase reaction that requires a kinetic rate expression is reaction 5.1. It is best described by a rate law that is first order in both $[OH^-_{aq}]$ and $[CO_{2,(aq)}]$.

Naturally concentrated Ca^{2+} sources include hydraulic fracturing waste water, desalination brines, and sub-surface geologic brine reservoirs. Geologic brines have electrolyte concentrations up to 100,000 ppm, with Ca^{2+} concentrations as high as 30,000 ppm. Each of these feedstocks are concentrated in additional electrolytes (besides Ca^{2+}), and so one expects that CCUSM process design likely requires confronting the multicomponent, electrolytic, non-ideal mass transport challenges mentioned above. Here, a procedure is presented for accurately accounting for all of these effects during the gas/liquid interphase reactive transport that occurs during CCUSM, but the approach taken here is presented in such a way that it remains generally applicable to other reactive, electrolytic, multicomponent, mass transport systems.

5.2 Model development and description

5.2.1 Interfacial Diffusion and Film Models

There are two primary aproaches one can take when modeling mass transport across a gas/liquid phase boundary: a stagnant film or surface renewal model. The stagnant film model was the first interphase mass transport description to appear in the literature in 1923. [4] In this description, one imagines a stagnant film of finite thickness δ_l on the liquid side of the interface and a stagnant film of finite thickness δ_g on the gas side. In both films, mass transport occurs via molecular diffusion only, and the two phases

maintain phase equilibrium exactly at the interface.

The other class of models can be broadly characterized as surface renewal or surface penetration models. These models also imagine a stagnant film at the phase boundary, but they further assume that the stagnant film is periodically convectively replaced by solution of the bulk phase composition. The first model of this sort hypothesized a fixed replacement period θ, [5] and later updates eventually included a time indepndent replacement probability s. [6] Each of these three models (film, renewal, penetration) requires a single experimental parameter per phase (δ_l, θ, s) and so each method is equally experimentally expensive to implement for design purposes. Each of these descriptions of the gas/liquid interface can be modified to account for any set of constitutive laws relating composition and state conditions to diffusive molar fluxes, and so any of them might be a reasonable starting point for describing interphase transport in a concentrated, electrolytic, reactive absorber. More complicated descriptions do exist in the literature, but their complication has not been sufficiently justified experimentally and so they are not considered here.[1]

Each of these models gives similar interphase molar fluxes in simple reactive systems for which Fick's law holds and the important reactant species have similar diffusivities. When the reactant diffusivities differ, there is some experimental evidence that the renewal and penetration theories may lead to marginally superior estimates of the absorption rates relative to the stagnant film model. [7] When the diffusivities of all diffusing species are comparable, one can likely use whichever model one prefers or is most convenient without sacrificing significant accuracy. If one knows that the diffusivities of non-negligible components differ, then it might be slightly preferable to describe the interface as a renewed surface. Regardless of the physicochemical description one utilizes to describe the interface, concentrated, electrolytic mass transport must use a more so-

[1]See Appendix 5.E for additional literature review.

phisticated diffusion description than Fick's law. The Maxwell-Stefan description is an ideal starting point for accommodating these effects, and so it is described in the next section.

5.2.2 Multicomponent, electrolytic, mass transport in non-ideal solutions

Fick's first law (i.e. a component's diffusive flux is directly proportional to the negative of its activity gradient) is often stated as a self evident fact with little thought devoted to its applicability or derivation. [8,9] This is true in much of the mass transport literature, and ironically, it is how Fick first presented the idea in 1855. [10] James Clerk Maxwell first derived the diffusion description that takes his name from the kinetic theory of gases in 1865. [11][2] Although, the original derivation was for gas molecules that interact via collision events, the same arguments hold for real gases and condensed phases capable of more complex interactions. [12] This description, in contrast to Fick's law, enables the mathematical consideration of the experimentally observable [13] coupling between solutes such that all activity gradients in a mixture affect all diffusive fluxes in the same mixture. The one-dimensional Maxwell-Stefan relation for multicomponent diffusion in the z-direction is given in Equation 5.5 (See Appendix 5.A for notation and tutorial derivation).

$$\frac{x_i}{RT}\frac{d\mu_i}{dz} = -\sum_{j\neq i}\frac{(x_j N_i - x_i N_j)}{c_T Đ_{i,j}} \tag{5.5}$$

[2]A simple tutorial derivation can be found in Appendix 5.A. The Appendix also illustrates how one can simplify the Maxwell-Stefan relations to the Nernst-Planck equation and then to Fick's law in the limiting case of infinite dilution. It also demonstrates that the Maxwell-Stefan equations can be used to generate the Gibbs-Duhem relation with only kinetic arguments and is thus independently consistent with thermodynamics.

If one is describing an ideal mixture of only two components, equation 5.5 simplifies to

$$\frac{dx_A}{dz} = -\frac{(x_B N_A - x_A N_B)}{c_T Đ_{A,B}} \tag{5.6}$$

If component A is sufficiently dilute such that $x_A \approx 0$ and $x_B \approx 1$, then Equation 5.6 becomes Fick's law.

Equation 5.5 can be presented in a form that more closely resembles Fick's law by recasting the equations in vector-matrix form. Defining $\boldsymbol{B}$ in Equations 5.7 and 5.8 and the thermodynamic factor $\boldsymbol{\Gamma}$ (closely related to the thermodynamic stability matrix) in Equation 5.9 leads to Equation 5.10.

$$B_{i,j} = -x_i \left(\frac{1}{Đ_{i,j}} - \frac{1}{Đ_{i,c}} \right) \tag{5.7}$$

$$B_{i,i} = \frac{x_i}{Đ_{i,c}} + \sum_{k \neq i} \frac{x_k}{Đ_{i,k}} \tag{5.8}$$

$$\Gamma_{i,j} = \delta_{i,j} + x_i \frac{\partial\ ln\gamma_i}{\partial x_j} \equiv \frac{x_i}{RT} \frac{\partial^2 g}{\partial x_i x_j} \tag{5.9}$$

$$\boldsymbol{N} = -c_T \boldsymbol{B}^{-1} \boldsymbol{\Gamma} \frac{d\boldsymbol{x}}{dz} \tag{5.10}$$

where $g(T, P, \boldsymbol{x})$ is the molar Gibbs free energy of the mixture, $\delta_{i,j}$ is the kronecker delta, and γ_i is the activity coefficient associated with component i. $\boldsymbol{\Gamma}$ simplifies to the identity matrix I when the solution is ideal. As can be seen from equations 5.5 through 5.10, each component flux is coupled to all the others in multicomponent diffusion. Osmotic diffusion effects occur when a component diffuses even though its activity gradient is zero. Diffusion barrier effects occur when a component has net zero flux even though

it is experiencing an activity gradient driving force. Even reverse diffusion is possible, whereby a component diffuses *against* its own activity gradient. [12, 13] All of these effects emerge from the interdependence of all the fluxes and the arising friction forces among the component species. When Fick's first law (direct proportionality between the negative of the component i activity gradient and the component i flux) is used, one is implicitly making the assumption that solute-solute interactions are negligible and that none of these effects occur.[3]

Many multicomponent diffusion models are presented as "generalizations of Fick's law" in vector-matrix form like equation 5.10 with $\boldsymbol{B}^{-1}\boldsymbol{\Gamma}$ replaced by $\boldsymbol{D}$, the multicomponent Fick diffusivity matrix. This can be done in a manner consistent with the framework presented here if one recognizes how the generalized Fick diffusion matrix is built, how it should be expected to vary with composition, and that it does not physically represent a proportionality constant between friction forces and a single chemical potential gradient in the same way that the Maxwell-Stefan diffusivities ($Đ$) do. In this way, one is effectively describing the system using the Maxwell-Stefan description but choosing to present it in the more conventional Fickian form. Although, problems can arise when generalizations are made without considering what is hidden inside $\boldsymbol{D}$, especially considering that the multicomponent Fick diffusivity matrices are neither uniquely defined, guaranteed to be symmetric, nor guaranteed to contain positive off-diagonal elements. [12][4] Also, generalized Fick diffusivity matrices are generally strong functions of composition in both the liquid and the gas phase,[5] whereas the Maxwell-Stefan diffusivities are constant with respect to composition in the gas phase and maintain a weak, predictable composition dependence in the liquid phase. [12] Many simplifications in the description and the nu-

[3]Use of the Nernst-Planck equations implicitly assumes that the only solute-solute interaction that is non-zero is the effects a solute exerts on the diffusion potential.

[4]Interestingly, although they are not uniquely defined, all physically consistent representations will have identical eigenvalues. See Appendix 5.A and [12].

[5]Examine the structure of $\boldsymbol{B}$ and Γ.

merical calculation of these effects have been proposed in the literature, and many of them are suffciiently accurate for the types of systems they are specifically designed for. Unfortunately, none of these simplifications apply to the general case of concentrated, reacting, electrolytic, non-ideal mixtures that are considered here. [14]

When some of the diffusing species are electrolytes, an additional term must be added to Equation 5.5 to account for the effect that electric fields have on charged species.

$$\frac{x_i}{RT}\frac{d\mu_i}{dz} + Fz_i x_i \frac{d\phi}{dz} = -\sum_{j\neq i} \frac{(x_j N_i - x_i N_j)}{c_T Đ_{i,j}} \tag{5.11}$$

where F is the Faraday constant, z_i is the charge number of component i, and ϕ is the electric potential. The electric potential gradient term is necessary even in the absence of an applied field because diffusing electrolytes generate electric potentials that alter the relative diffusion rates to maintain macroscopic electroneutrality in solution. [6]

Most common activity models do not include the Coulombic interactions that dominate and complicate the thermodynamics of electrolyte solutions. Here, the OLI Mixed-solvent electrolyte (MSE) activity model is utilized for several reasons. [3] First, in a recent publication that compared electrolyte thermodynamic models to experimental observations, this model compared favorably to the other models that were studied. [15] Second, the company that developed the model (OLI Systems) sells access that can be directly integrated into matlab for direct implementation into a model like the one discussed here. Furthermore, OLI systems also developed a model for estimating self-diffusivities in concentrated, multicomponent, electrolytic solutions, [16] and these estimates are available through the same software. The self-diffusivity estimates are useful because the best methods available for estimating the multicomponent Maxwell-Stefan diffusivities ($Đ$) as functions of concentration require the mole fractions and self-diffusivities of each compo-

[6] This phenomena is discussed in more detail in Appendix 5.A.3.

nent in the mixture as functions of concentration. [17] For all of these reasons, the activity coeficients used here are based on the OLI systems mixed-solvent electrolyte model, [3] and the Maxwell-Stefan diffusivities are based on the OLI self-diffusion model [16] and the predictive Darken equation. [17] Other activity models, self-diffusivity models, and Maxwell-Stefan diffusivity prediction models could have been chosen without changing any of the other features of the model presented here.

After defining the component i activity as $a_i = \gamma_i x_i$, Equation 5.11 can be re-written.

$$\frac{x_i RT}{a_i}\frac{da_i}{dz} + Fz_i x_i \frac{d\phi}{dz} = -\sum_{\substack{j=1 \\ j\neq i}}^{c} RT\frac{(x_j N_i - x_i N_j)}{c_T Đ_{i,j}} \qquad i = 1\ldots c-1 \tag{5.12}$$

Equation 5.12 is true for each component i, but only $c-1$ are independent as written ($\sum_i x_i = 1$). The electric potential can be eliminated by utilizing the no-current relation and the entire set of $(c-1)$ independent Maxwell-Stefan relations to give equation 5.13.[7]

$$\frac{x_i}{a_i}\frac{da_i}{dz} + \frac{\sum_k \frac{z_k}{\sum_{p\neq k}\frac{x_p}{Đ_{k,p}}}[x_k(\sum_{j\neq k}\frac{N_j}{c_T Đ_{k,j}}) - \frac{dx_k}{dz}]}{\sum_h \frac{z_h^2 x_h}{\sum_{m\neq h}\frac{x_m}{Đ_{h,m}}}} = -\sum_{\substack{j=1 \\ j\neq i}}^{c} \frac{(x_j N_i - x_i N_j)}{c_T Đ_{i,j}} \qquad i = 1\ldots c-2 \tag{5.13}$$

This substitution renders one of the remaining $(c-1)$ Maxwell-Stefan relations dependent on the rest (See Appendix 5.A). Even in the ideal limit, these equations are now implicit in dx_k/dz, but after some manipulation, they can be written in explicit compact matrix form as shown in equation 5.14 below.[8]

$$\boldsymbol{x}' = -[\boldsymbol{\Gamma} + \boldsymbol{\Xi}]^{-1}\boldsymbol{\beta}\boldsymbol{J} \qquad i = 1\ldots c-2 \tag{5.14}$$

[7] Discussion of the no-current relation and the derivation of equation 5.12 are available in Appendix 5.A.

[8] See Appendix 5.C

This set of equations describes the diffusion and electrolytic migration of an electrolyte in a concentrated solution. When $Đ$ and γ_i are known functions of concentration (In this case, these functions are known from the OLI systems MSE and self-diffusivity models.), Equation 5.14 quantifies the relationship between component mole fractions, mole fraction gradients, and molar fluxes (N_i). These equations enable the characterization of the molar fluxes given some set of mole fraction gradients or the calculation of the set of mole fraction gradients implied by a set of molar fluxes if no other important physicohcemical effects are present. Here, chemical reactions further complicate the situation.

5.2.3 Reaction effect on interphase transport

Sirozi Hatta first described chemical reaction effects on diffusion in 1928. [18,19] When an absorbed gas is consumed in a reaction (as CO_2 is in equation 5.1), the thermodynamic driving force for diffusion within the stagnant film at the interface is increased, increasing the rate of absorption. Hatta demonstrated that the strength of a non-reversible, first-order reaction's effect on absorption of a dilute, non-charged species is governed by the dimensionless ratio given in equation 5.15 (based on the stagnant film model).

$$\gamma = \delta_l \sqrt{\frac{k}{D}} \tag{5.15}$$

where k is the reaction rate constant in units of s^{-1} and D is the diffusivity of the absorbed component in the relevant solvent.[9] A more intuitive dimensionless group is γ^2 because it then has an easy to understand physical significance as a ratio of the diffusion time to the reaction time. In the decades since Hatta's papers, dimensionless groups that represents a diffusion time divided by a reaction time have been referred to as Hatta

[9]The D in Equations 5.15 and 5.16 could be a Fickian diffusivity, a component in the Maxwell Stefan B^{-1} matrix, or a Maxwell-Stefan diffusivity ($Đ$) depending on the diffusion description chosen and the characteristic dimension used to non-dimensionalize the governing differential equations.

numbers in the gas absorption literature (Ha).

$$Ha = \delta_l^2 \frac{k}{D} \tag{5.16}$$

When the Hatta number is high, reaction occurs too fast for the reacting component to diffuse the thickness δ_l before it is consumed by reaction. When it is low, the reaction effect is relatively small, and the absorption rate approaches that which would be expected from physical absorption. In the absorption literature, this number is referred to as the Hatta number, but the ratio has physical significance in any system in which chemical reaction affects a diffusive process. For example, the same quantity and effect appear in the Thiele modulus that is commonly used to describe mass transport effects inside catalyst particles. Thiele's work was published in 1939, [20] but there was no citation of Hatta's work or reference to the similarities in the two dimensionless groups. Perhaps communication between scientists and engineers in the United States and those in Japan was limited in the 1930s.[10] On the other hand, Hatta praises work done by Whitman in the early 1920s [4] and criticizes work done by Payne and Dodge in the early 1930s. [21] It is possible that his work was unavailable or simply unknown to Thiele, but it is interesting to note that Thiele chose to name his dimensionless group h. For whatever reason, the catalysis community has referred to the quantity as the Thiele modulus and the gas absorption community has referred to it as the Hatta number ever since. They are the same quantity, but to keep with convention, the number will be referred to as the Hatta number here.

Others have extended Hatta and Whitman's original insights and developed methods for designing process equipment for reactive absorption. Most notably, *Gas-Liquid Reactions* [7] champions the use of enhancement factors (E) to account for reaction effects

[10] Thiele worked for Standard Oil Company in Indiana, and Hatta worked at Tohoku University in Japan.

in an absorber. The enhancement factor is defined as the ratio of the absorption rate in the presence of reaction to the physical absorption rate that would result in the absence of reaction. Enhancement factors have been analytically derived for situations simple enough to allow for exact analytic solutions. In many situations, some assumptions have been made about the speed of reaction, diffusion, or both in some system such that analytic solutions could be presented for limiting cases. In other situations, E has been calculated numerically for a range of conditions and assumptions and then fitted to correlations or functions that can be used to estimate E in these intermediate regions. Once an average enhancement factor has been determined for a given reactive absorber, it can be multiplied by the non-reactive mass transport coefficient to give a reaction adjusted mass transfer coefficient. This adjustment allows design calculations to proceed by conventional methodologies based on physical absorption. Unfortunately, these methods all describe diffusion with Ficks' first law, implicitly ignoring multicomponent effects and limiting the method's applicability to the dilute limit.

Chemical reaction consumes or generates reactants or products according to the reaction stoichiometry. Equation 5.13 is true at every point along the diffusion film, but reaction may cause the fluxes to change in time or in space and this must be consistently accounted for. A continuity equation allows the consistent consideration of the effect that chemical reaction imposes on the molar fluxes as functions of time and space.

$$\frac{\partial C_i}{\partial t} = -\frac{\partial N_i}{\partial z} + \sum_{j=1}^{r} v_{i,j} r_j \qquad i = 1 \ldots c \tag{5.17}$$

where C_i is the molar concentration of component i, $\nu_{i,j}$ denotes the stoichiometric coefficient of component i in reaction j, N_i denotes the total molar flux relative to some fixed reference plane, and r_j denotes the volumetric reaction rate of reaction j.[11]

[11] N_i is used here to represent the total molar flux relative to a fixed reference plane. A more conven-

So Equations 5.13 and 5.17 form a set of $2c-2$ independent differential equations with $c-2$ independent mole fractions[12] and c independent molar fluxes for $(2c-2)$ total independent states. Therefore, no degrees of freedom remain once the $2c-2$ boundary values and the the $2c-2$ initial conditions are chosen.

The boundary values and initial conditions depend on the phase interface model one utilizes (stagnant film or surface renewal). For both models, phase equilibrium is assumed at the gas/liquid interface for all species that transport between the phases. Therefore, both models require boundary values to be specified at the interface for any component capable of transporting between phases. The boundary value must be supplied on the opposite edge of the diffusion film (away from the interface) for components that cannot transport between the phases (e.g., aqueous electrolytes during gas/liquid transport). These boundary values away from the gas/liquid interface are set to the bulk phase concentrations or mole fractions. For the stagnant film description of the interface, the non-interface boundary is placed a distance δ_l from the interface, where δ_l is determined from a physical mass transport coefficient for a non-reacting solute, either measured or estimated from some correlation. Alternatively, the non-interface boundary is infinitely far from the interface in the renewal models and the renewal time (θ) is determined from the measured or estimated mass transport coefficient. Infinitely far can be approximated in a simulation by starting with some educated guess (perhaps $5 \times (\mathcal{D}_{i,c}\theta)^{1/2}$) where $D_{i,c}$ is the diffusivity of the primary absorbing component) and then solving the system of

tional presentation might describe the convective and diffusive fluxes separately, and then a convective term would appear explicitly in Equation 5.17. This convention is convenient for describing Fickian diffusion because the Fickian diffusion description only describes the diffusive flux. Alternatively, Equation 5.13 is valid if either total fluxes or diffusive fluxes are used in place of all of the "N_i" terms (the reference flux cancels out). Therefore the convention is less convenient in this context. If one preferred to write all fluxes in terms of diffusive fluxes only, one would need to rewrite Equation 5.17 to include a convective term, or one would need to explicitly mention that the total convective flux is assumed to be zero. See Appendix 5.A and [12]

[12]Electroneutrality and the definition of the mole fraction summation (i.e., $\sum_i x_i = 1$) both reduce the number of independent mole fractions. See Appendix 5.A for more discussion.

equations at increasing values of the diffusion length.[13] Once the solution stops changing as a function of diffusion length, the length is effectively infinitely long with respect to the other physicochemical processes occurring within the diffusion film. The initial conditions should always be the bulk phase compositions for the renewal and penetration models, and initial conditions are not required for the stagnant film model. For the stagnant film model, all of the states are specified as functions of position (z) once one specifies $2c-2$ boundary values. Similarly for the renewal models, all of the states are specified as functions of position (z) and time (t) once one specifies $2c-2$ boundary values and $2c-2$ initial conditions.

The absorption flux predictions from the surface renewal descriptions of the interface can be compared with the stagnant film calculations or with the conventional enhancement factor based methods by averaging the calculated flux over a renewal period (θ). This average flux is the flux that would be observed experimentally at steady-state or predicted by the other models.

$$N_{SR} \neq f(t) = \frac{\int_{t=0}^{t=\theta} N_{SR}(t)dt}{\theta} \tag{5.18}$$

where N_{SR} is the flux of the primary species across the phase boundary predicted from the surface renewal theory with units of moles/area/time. The predicted flux does not change as a function of time because it is averaged over a surface renewal period, θ.

5.2.4 Non-dimensionalization

The nondimensionalization that leads to the most physically meaningful dimensionless groups depends on the gas/liquid interface model one utilizes. When the renewal models

[13]The best diffusivity to use to determine the diffusion length depends on how everything is defined. If the Maxwell-Stefan description of diffusion is utilized then $Đ_{i,c}$ is appropriate where i signifies the absorbing component and c signifies the most concentrated "other" component (often the solvent).

are utilized, the states are non-dimensionalized as follows

$$C_r = C_{T,(0,0)} \tag{5.19}$$

$$t_r = \theta \tag{5.20}$$

$$Đ_r = Đ_{i,c} \tag{5.21}$$

$$z_r = (Đ_r\theta)^{1/2} \tag{5.22}$$

$$N_r = \frac{C_{T,(0,0)} z_r}{\theta} \tag{5.23}$$

where the subscript r indicates a reference value for a given quantity, $C_{T,(0,0)}$ indicates the total molar concentration at $z = 0$ and $t = 0$, $Đ_{i,c}$ is the Maxwell-Stefan diffusivity of the primary component of interest relative to component c,[14] z_r is the characteristic diffusion length, θ is the renewal time, and N_r is a reference molar flux with units of moles/area/time. These definitions can be accommodated in Equation 5.13 by replacing every C_T with $\overline{C_T}$, every $Đ$ with $\overline{Đ}$ and changing the $\frac{d}{dz}$ to $\frac{d}{d\overline{z}}$, where overbars indicate a quantity that has been divided by its reference value, rendering it dimensionless. This produces Equation 5.24.

$$\frac{x_i}{a_i}\frac{da_i}{d\overline{z}} + \frac{\sum_k \frac{z_k}{\sum_{p\neq k}\frac{x_p}{\overline{Đ}_{k,p}}}\left[x_k\left(\sum_{j\neq k}\frac{\overline{N}_j}{\overline{c}_T\overline{Đ}_{k,j}}\right) - \frac{dx_k}{d\overline{z}}\right]}{\sum_h \frac{z_h^2 x_h}{\sum_{m\neq h}\frac{x_m}{\overline{Đ}_{h,m}}}} = -\sum_{\substack{j=1\\ j\neq i}}^{c} \frac{(x_j\overline{N}_i - x_i\overline{N}_j)}{\overline{c}_T\overline{Đ}_{i,j}} \qquad i = 1\ldots c-2 \tag{5.24}$$

Equation 5.17 is transformed to Equation 5.25 upon nondimensionalization.

$$\frac{\partial\overline{C}_i}{\partial\overline{t}} = -\frac{\partial\overline{N}_i}{\partial\overline{z}} + \sum_{j=1}^{r} v_{i,j} Ha_j \overline{r}_j \qquad i = 1\ldots c \tag{5.25}$$

[14] Component c is typically a solvent.

where Ha_j represents the Hatta number for reaction j.

$$Ha_j = \theta k_{f,j} C_{T,(0,0)} \tag{5.26}$$

where $k_{f,j}$ has units of volume/moles/time, consistent with a second order reaction such as Reaction 5.1. For a n^{th} order reaction, $k_{f,j}$ would be replaced by $k_{f,j} C_{T,(0,0)}^{n-1}$ such that Ha_j is nondimensional.

If instead, the gas/liquid interface is described as a stagnant film, then the most physically meaningful nondimensionalization involves the following reference dimensions.

$$C_r = C_{T,(0,0)} \tag{5.27}$$

$$Đ_r = Đ_p \tag{5.28}$$

$$z_r = \delta_l \tag{5.29}$$

$$N_r = \frac{C_{T,(0,0)} Đ_p}{\delta_l} \tag{5.30}$$

$$\tag{5.31}$$

where δ_l signifies the thickness of the stagnant film. Equation 5.24 applies to both gas/liquid interface descriptions, but Equation 5.25 does not. The time derivative is always zero for the stagnant film description and the Hatta number definition is slightly different.

$$\frac{\partial \overline{N}_i}{\partial \bar{z}} = \sum_{j=1}^{r} v_{i,j} Ha_j \bar{r}_j \qquad i = 1 \ldots c \tag{5.32}$$

$$Ha_j = \frac{\delta_l^2 k_{f,j}}{C_{T,(0,0)} Đ_p} \tag{5.33}$$

Both definitions of the Hatta number represent ratios of a reaction rate to a diffusion rate, but the specific dimensions they are composed of look slightly different under the

two different descriptions of the gas/liquid phase boundary. Although, this distinction isn't as physically significant as it seems. Both θ and δ_l must be measured experimentally or determined from correlations based on past experimental data. Since both θ and δ_l are determined from mass transport coefficients in the absence of chemical reaction, both Equation 5.26 and 5.33 can be re-written in terms of the classic mass transport coefficient, $k_L A$ by utilizing their respective functional forms of $\theta = f(k_L A)$ and $\delta_l = g(k_L A)$. [7] When this substitution is made, both Equations 5.26 and 5.33 scale as $k_{f,j}\mathcal{D}_p/k_L^2 A$.[15]

5.3 Comparison to conventional enhancement factor methods

Reaction effects in film model descriptions of gas absorption are well documented for dilute systems with a single chemical reaction. The reacting, concentrated, electrolyte-containing diffusion models presented here converge to these enhancement factor treatments when the diffusing species are dilute, ideal, non-charged, and undergoing reactions with stoichiometries that have been studied and reported in the literature. Even when charged species are present, one expects relatively small deviations from the enhancement factor results if the solutions are sufficiently dilute and effective salt diffusivities are chosen to account for the diffusion potential (Effective salt diffusivities are discussed in Appendix 5.A). For some systems, these simplifications are just not adequate.

The tendency for the conventional methods to diverge from the more complete description presented here in concentrated electrolytic solutions is illustrated with the following example. Imagine a gas/liquid interface in which an alkaline, salty brine absorbs CO_2

[15]Similar to the Thiele modulus, the Hatta number is often defined as the square root of the dimensionless group in Equations 5.26 and 5.33. Here, the number is defined such that it is a ratio of times or rates. The interconversion between the two conventions is simple.

from a dilute gas. The conventional enhancement factor methods depend on the reaction kinetics, the reaction stoichiometry, and the non-absorbing reactant concentrations (e.g., OH^-, HCO_3^-, etc.), but not on any other components that might be present in the absorbing solution (such as concentrated electrolytes). [7] Table 5.1 illustrates how the enhancements predicted by the model presented here can diverge from the enhancements predicted by the conventional methods as the concentrations of non-primary components increase. These comparisons were calculated under the assumption of a stagnant film

[NaCl]	[carbon]	pH	MS Model	Classic E	% difference
0.0	0.0	11.5	1.13	1.16	2.7
1.0	1.0	11.0	1.2	1.87	57
5.0	0.0	12.0	1.3	1.75	30

Table 5.1: The first column signifies the aqueous concentration of NaCl in the bulk solution in units of moles per liter. The second column signifies the total concentration of carbon containing molecules in the bulk solution in units of moles per liter. The column labeled MS Model is the enhancement factor predicted from the equations presented in this chapter. The column labeled "Classic E" signifies the enhancement factor one would predict based on the conventional methods. [7]

model using the Matlab built in boundary value collocation script bvp4c and arc-length continuation (See Appendices 5.B and 5.D). Figure 5.1 illustrates how the model predicts the concentrations to vary over the length of the stagnant film when CO_2 is absorbed into a pH 12, 5 molar NaCl solution (Conditions in the bottom row of Table 5.1). These conditions might be typical of a CCUSM reactive absorber. Even though it is expensive to prepare pH=12 solutions, the absolute hydroxide consumption per mole of CO_2 captured is not changed by the concentration the reactants are contacted in. Higher pH leads to larger reaction rates and smaller equipment sizes, so one expects that higher pH might be preferred for these processes. In terms of the salt concentration, 5 molar is near the upper limit of what one might expect to encounter in the natural calcium

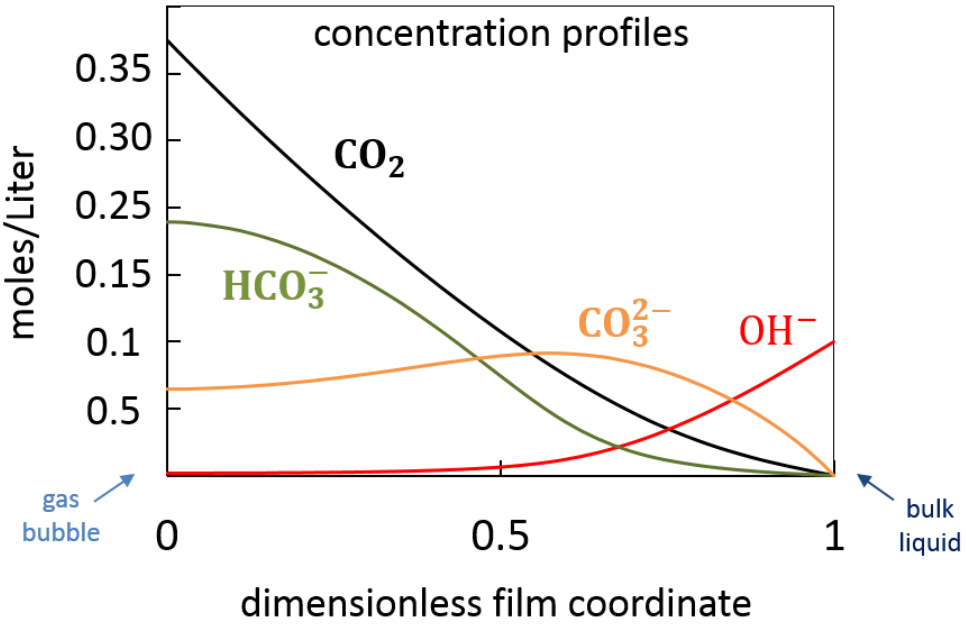

Figure 5.1: The molar concentrations of the various carbon containing molecules vary along the stagnant film thickness. The driving forces for mass transport are coupled among all of these components and the actual molar flux of CO_2 through the interface is predicted to be 30 % lower than one would expect from the conventional reactive absorption models alone.

sources discussed earlier (e.g., geologic brines, desalination waste waters, and hydraulic fracturing wastes), but it is by no means out of the range of possible feed concentrations. The real value of these solution conditions are that they give a clear example of a possible operating point for CCUSM in which the physicochemical effects discussed within this chapter lead to significantly different results from the conventional methods. The off-diagonal terms in the matrix implied by Equation 5.14 ($\left[[\boldsymbol{\Gamma}+\boldsymbol{\Xi}]^{-1}\boldsymbol{\beta}\right]^{-1}$) are as much as 60 times higher than the diagonal terms for these conditions. Therefore, for these conditions, some components are diffusing under a driving force that is almost entirely (i.e., $\approx 60/61$) due to other component activity gradients and electrochemical effects. In this example calculation, the CO_2 flux from the gas phase into the liquid phase predicted by the model equations presented here is 30 % lower than the predicted flux from the conventional enhancement factor methods.

5.4 Conclusions

Fick's law is an inadequate description of diffusion when a mixture is concentrated, electrolytic, and reacting. Here, a model has been described that accounts for all of the complications that arise during the reactive absorption of CO_2 into concentrated, non-ideal, electrolytic, brine solutions. These models also apply to countless other industrially important systems for which concentrated reactive transport can occur. These interphase transport models can be utilized in future studies in conjunction with the gas/liquid bubble column reactor model presented in Chapter 6. Taken together, the interphase transport models presented here, the reactor model presented in Chapter 6, and the reactive precipitator solid form selection design rules presented in Chapter 4 can be utilized to design and optimize the serial CCUSM process in which a polymorph selective, reactive precipitator follows a reactive absorber. Exciting future work that will be discussed in more detail in Chapter 7 includes combining all of these models into the intensified polymorph selective, reactive absorber/precipitator.

Appendices

5.A Maxwell-Stefan Diffusion

5.A.1 Deriving the Maxwell-Stefan Equations

Consider the collision between a molecule of A and a molecule of B in an isolated enclosure with no external forces. In any collision, momentum is conserved.

$$\triangle \boldsymbol{p_A} + \triangle \boldsymbol{p_B} = m_A(\boldsymbol{u_{A,f}} - \boldsymbol{u_{A,o}}) + m_B(\boldsymbol{u_{B,f}} - \boldsymbol{u_{B,o}}) = 0 \tag{5.34}$$

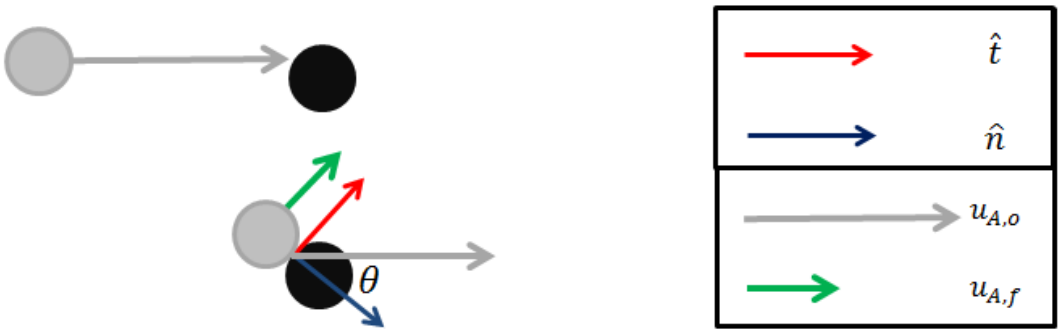

Figure 5.2: When molecule A undergoes an elastic collision with the stationary molecule B at a collision angle θ, its tangential momentum remains unchanged, but all of the A momentum normal to the surface is exchanged to B.

The collision could be elastic, inelastic or somewhere in between. Consider the two limiting cases of perfect elasticity (hard spheres) and perfect inelasticity (upon collision, the particles stick together and thereafter move as a single object). When the collision is perfectly elastic, the kinetic energy is also conserved upon collision leading to equation 5.35.

$$m_A(\boldsymbol{u_{A,f}}^2 - \boldsymbol{u_{A,o}}^2) + m_B(\boldsymbol{u_{B,f}}^2 - \boldsymbol{u_{B,o}}^2) = 0 \tag{5.35}$$

Figure 5.2 shows an elastic collision between two molecules, A and B, at a collision angle θ.

In a one-dimensional collision, the total velocity is entirely normal to the collision surface, but in higher dimensions it is possible for the collision angle, θ to be nonzero[16]. In a 2 (or 3) dimensional collision, each molecule's velocity can always be deconstructed into 2 (or 3) perpendicular components, one normal and the other (2) tangent to the collision surface. Tangential velocities are unaffected by an elastic collision, but momentum is exchanged normal to the collision surface. In the case where the collision angle is nonzero, equations 5.36 and 5.37 describe post collision *normal* velocities. Once the

[16]Here, the collision angle, θ is defined as the angle between molecule A's approach velocity and the vector normal to the collision surface.

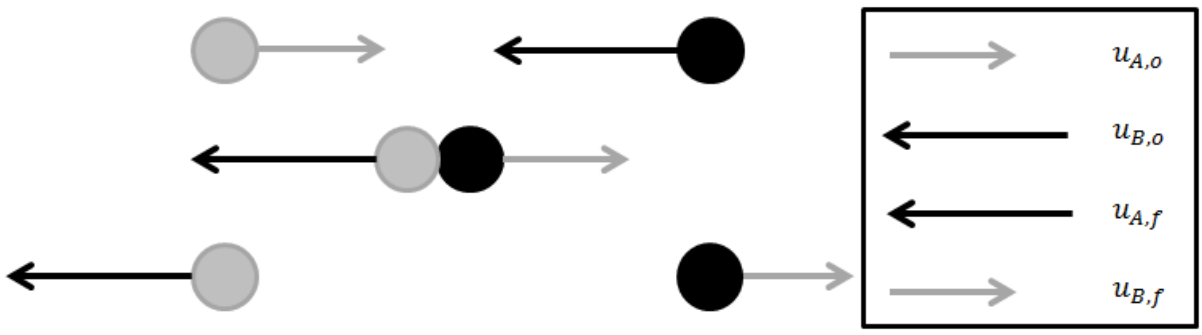

Figure 5.3: A perfectly elastic head-on collision between a molecule of A and B.

post-collision normal velocities are calculated, they can be added to the pre-collision tangential velocities to calculate the final post-collision velocities for both molecules. In the simpler case of one-dimensional or head-on ($\theta = 0$) collisions, both tangential velocities are zero so that $\boldsymbol{u_{A,f}}$ and $\boldsymbol{u_{B,f}}$ are exactly $\boldsymbol{u_{A,f,n}}$ and $\boldsymbol{u_{B,f,n}}$.

$$\boldsymbol{u_{A,f,n}} = \frac{\boldsymbol{u_{A,o,n}}(m_A - m_B) + 2m_B\boldsymbol{u_{B,o,n}}}{m_A + m_B} \tag{5.36}$$

$$\boldsymbol{u_{B,f,n}} = \frac{\boldsymbol{u_{B,o,n}}(m_B - m_A) + 2m_A\boldsymbol{u_{A,o,n}}}{m_A + m_B} \tag{5.37}$$

The following arguments are valid independent of collision angle, so for simplicity of presentation, strictly normal collisions will be considered henceforth. Figure 5.3 depicts a perfectly elastic head-on collision between two molecules of the same mass. As one can see from equations 3 and 4 above, in such a situation the molecules trade velocities.
The post collision velocity vector can then be used to calculate the change in momentum of molecule A upon collision.

$$\triangle\boldsymbol{p_A} = m_A(\boldsymbol{u_{A,f}} - \boldsymbol{u_{A,o}}) = \frac{2m_Am_B(\boldsymbol{u_{B,o}} - \boldsymbol{u_{A,o}})}{m_A + m_B} \tag{5.38}$$

In this case, the change in momentum of molecule B is $-\triangle\boldsymbol{p_A}$ so that the total linear

Figure 5.4: A perfectly inelastic collision between a molecule of A and B.

momentum is conserved.

Alternatively, the collision could be perfectly inelastic. In a perfectly inelastic collision, the kinetic energy of the system is minimized under the constraint of conservation of momentum. The kinetic energy loss is partly interchanged to internal degrees of freedom during the collision and to the generation of heat. This is collectively termed friction. In the perfectly inelastic case, this kinetic energy minimization leads to the two molecules sticking together and both exiting the collision at their combined center of mass velocity prior to the collision. A perfectly inelastic collision between 2 molecules of equal mass is depicted below in Figure 5.4. When the two molecules have the same mass, the combined center of mass velocity is just the average of the two velocity vectors prior to collision. The final velocity after a perfectly inelastic collision is given by equation 5.39.

$$\boldsymbol{u_{A,f}} = \boldsymbol{u_{B,f}} = \frac{m_A \boldsymbol{u_{A,o}} + m_B \boldsymbol{u_{B,o}}}{m_A + m_B} \tag{5.39}$$

The corresponding momentum change after collision is given by equation 5.40.

$$\triangle \boldsymbol{p_A} = m_A(\boldsymbol{u_{A,f}} - \boldsymbol{u_{A,o}}) = \frac{m_A m_B(\boldsymbol{u_{B,o}} - \boldsymbol{u_{A,o}})}{m_A + m_B} \tag{5.40}$$

The momentum change of molecule A in the two limiting cases differ by a factor of 2, but

the expressions are otherwise identical. Both depend linearly on the difference between the two initial velocity vectors, and both depend on a constant factor that is a function of the masses of both molecules and the extent of elasticity of the collision. Therefore, for all types of collisions including those between the two limiting cases already discussed, it is reasonable to write relation 5.41 below.

$$\triangle \boldsymbol{p_A} \propto (\boldsymbol{u_{B,o}} - \boldsymbol{u_{A,o}}) \tag{5.41}$$

Thus, the exchange of momentum between two molecules during a single collision is proportional to the velocity difference between the two molecules prior to the collision.[17] In a mixture of a large number of A and B molecules, a single velocity no longer characterizes the movement and momentum of A or B. In an ensemble of A and B, a distribution of momenta and velocities exists. The cumulative momentum of the collection of molecules of A is determined by summing over the individual molecules as shown below in equation 5.42.

$$\boldsymbol{p_{A,total}} = \sum_{i=1}^{n} m_A \boldsymbol{u_{A,molecule\ i}} \tag{5.42}$$

Equation 5.43 relates the ensemble average molecular velocity to the total momentum by utilizing the definition of the average velocity and equation 5.42 above.

$$\boldsymbol{p_{A,total}} = n m_A \frac{\sum_{i=1}^{n} \boldsymbol{u_{A,molecule\ i}}}{n} = M_A \bar{\boldsymbol{u}}_{\boldsymbol{A}} \tag{5.43}$$

where M_A now represents the total mass of A particles in the ensemble, and $\bar{\boldsymbol{u}}_{\boldsymbol{A}}$ is the average velocity of the ensemble of A molecules. Equation 5.41 shows that the change

[17] If one considers collisions that are not head-on, the momenta and velocities change by factors varying from zero to unity depending on the collision angle, θ. Therefore, the proportionality argument is not weakened by the presence of those collisions.

in momentum for a single collision is proportional to the difference in velocity of the two molecules prior to that collision. In the same way that the total momentum of all A molecules in an ensemble has been shown to depend only on the average velocity and the total mass, the average change in molecule A momentum per collision after many collisions with many B molecules is proportional only to the velocity difference of the two ensemble average velocities of A and B. This is written in equation 5.44 below.

$$\triangle \boldsymbol{p_A} \propto (\bar{\boldsymbol{u}}_{\boldsymbol{B}} - \bar{\boldsymbol{u}}_{\boldsymbol{A}}) \tag{5.44}$$

For simplicity of notation, from here forward $\boldsymbol{u_A}$ will represent the ensemble average velocity of A molecules and $\boldsymbol{u_B}$ will represent the ensemble average velocity of B molecules. The rate of change of momentum per unit time per mole of mixture is proportional to the average momentum exchange per collision and the rate of collisions per mole of mixture. Now $\triangle\, \hat{\boldsymbol{p}}_{\boldsymbol{A}}$ will be the rate of change of A momentum due to collisions with B per mole of mixture per unit time.

$$\triangle \hat{\boldsymbol{p}}_{\boldsymbol{A}} \propto \frac{total\ A,B\ collisions}{(unit\ time)(mole\ of\ mixture)} \triangle\, \boldsymbol{p_A} \tag{5.45}$$

The rate of collisions per mole of mixture is proportional to both the mole fraction of A and the mole fraction of B. Thus,

$$\frac{total\ A,B\ collisions}{(unit\ time)(mole\ of\ mixture)}) \propto x_A x_B \tag{5.46}$$

Equations 5.44, 5.45 and 5.46 lead to equation 5.47.

$$\triangle \hat{\boldsymbol{p}}_{\boldsymbol{A}} \propto x_A x_B (\boldsymbol{u_B} - \boldsymbol{u_A}) \tag{5.47}$$

The above proportionality can be made an equality by including a friction factor $f_{A,B}$

on the right hand side to correct the units, account for the masses of each molecule, the distribution of collision angles, and the relative elasticity of the average collision.

$$\triangle \hat{\boldsymbol{p}}_{\boldsymbol{A}} = f_{A,B} x_A x_B (\boldsymbol{u_B} - \boldsymbol{u_A}) \tag{5.48}$$

where $f_{A,B}$ has units $\frac{\text{energy}}{\text{mole}} / \frac{\text{length}^2}{\text{time}}$. Other forces can simultaneously act on molecules of A and drive changes in the total A momentum. A common force that must be considered during diffusion is the negative of the component A chemical potential gradient, although there can be others[18]. The *total* rate of change of A momentum is the sum of all the forces acting on component A plus the rate of change due to collisions with B. At steady-state, neither A nor B experiences a net acceleration, so the *total* rate of change of A momentum per mole of mixture must be zero. Therefore, the sum of the forces acting on molecules of A must be balanced by the momentum A transfers to B during collisions, which is $\triangle \hat{\boldsymbol{p}}_{\boldsymbol{B}}$, or equivalently $- \triangle \hat{\boldsymbol{p}}_{\boldsymbol{A}}$. Thus we obtain

$$-x_A \boldsymbol{\nabla} \mu_A + f_{A,B} x_A x_B (\boldsymbol{u_B} - \boldsymbol{u_A}) = 0 \tag{5.49}$$

Or, as it is more commonly presented

$$\boldsymbol{d_A} = x_A \boldsymbol{\nabla} \mu_A = f_{A,B} x_A x_B (\boldsymbol{u_B} - \boldsymbol{u_A}) \tag{5.50}$$

A new quantity $\boldsymbol{d_A}$ appears in equation 5.50. This quantity is termed the driving force on A per mole of mixture, and it represents a sum over all forces acting on molecules of component A per mole of mixture. The sum of the forces on A is the negative sum of all potential gradients acting on A. Equation 16 only includes the chemical potential gradient (the chemical potential gradient is multiplied into the component mole fraction

[18] some of which will be discussed later

to make the force per mole of mixture instead of per mole of A), but other types of potential gradients can also affect the momentum of component A and drive diffusive processes. These will be discussed later.

For simplicity, the one dimensional Maxwell-Stefan relations will be discussed for the remainder of this document unless stated otherwise, although the driving forces and velocity differences are in general vector quantities in 3 dimensions. This makes each flux or velocity a scalar with the implied direction of the driving force and gives equation 5.51 below. Equation 5.51 is the Maxwell-Stefan relation in the z-direction for a mixture of A and B only.

$$d_A = x_A \frac{d\mu_A}{dz} = x_A RT \frac{dln(\gamma_A x_A)}{dz} = f_{A,B} x_A x_B (u_{B,z} - u_{A,z}) \tag{5.51}$$

When the activity coefficient is unity the relation simplifies to the traditional representation of the Maxwell-Stefan relation for a 2 component system that forms an ideal mixture. Equation 5.52 was first derived rigorously from the kinetic theory of gases in James C. Maxwell's famous paper *On the Dynamical Theory of Gases*. [11]

$$RT \frac{dx_A}{dz} = f_{A,B} x_A x_B (u_{B,z} - u_{A,z}) \tag{5.52}$$

The quantity $f_{A,B}$ is a type of friction factor. Maxwell's paper uses slightly different notation, but he makes the connection between the friction factor in equation 5.52 and the diffusivities discussed in previous work by Fick [10] and Graham. [22, 23] In 1905, Einstein would more clearly articulate the relationship between the drag exerted on a particle of type A by a sea of particles of type B around it and the diffusivity of particle A with respect to B. [24] Since there is no reason to expect the friction forces to be a strong function of temperature, and since liquid diffusivities typically have temperature dependencies of $T^{1-1.5}$, $f_{A,B}$ can be redefined as $\frac{RT}{D_{A,B}}$. Substituting this expression into

equation 5.51 or 5.52 yields equation 5.53.

$$\frac{dx_A}{dz} = x_A x_B \frac{(u_{B,z} - u_{A,z})}{Đ_{A,B}} \tag{5.53}$$

$Đ_{A,B}$ is the Maxwell-Stefan diffusivity between components A and B. As it is written, the Maxwell-Stefan relation balances the driving forces for diffusion in the z-direction (the left hand side of equations 5.51 and 5.52) with the dissipative friction forces in the mixture in the z-direction (the right hand side of equations 5.51 and 5.52). Maxwell had some interesting insights on the relationship between energy dissipation and entropy. Even as he was contemplating the results of Graham's [22, 23] experiments and offering a theoretically consistent theory to describe and predict them, he was pointing out his inherent dissatisfaction with the terms dissipation, confusion, order and friction.

> "It follows from this that the idea of dissipation of energy depends on the extent of our knowledge. Available energy is energy which we can direct into any desired channel. Dissipated energy is energy which we cannot lay hold of and direct at pleasure, such as the energy of the confused agitation of molecules which we call heat. Now, confusion, like the correlative term order, is not a property of material things in themselves, but only in relation to the mind which perceives them. A memorandum-book does not, provided it is neatly written, appear confused to an illiterate person, or to the owner who understands it thoroughly, but to any other person able to read it appears to be inextricably confused. Similarly the notion of dissipated energy could not occur to a being who could not turn any of the energies of nature to his own account, or to one who could trace the motion of every molecule and seize it at the right moment. It is only to a being in the intermediate stage, who can lay hold of some forms of energy while others elude his grasp, that energy

appears to be passing inevitably from the available to the dissipated state."

James C. Maxwell [25]

In 1871, Stefan first stated that equation 5.51 could be generalized to more than 2 components by accounting for all i, j interactions. [26] He hypothesized that the total diffusional resistance (friction) experienced by species i as it diffuses through a mixture is the simple sum of the individual binary resistances it would experience when diffusing through each individual component (j) at equivalent concentrations and relative velocities. Summing over all i, j interactions gives the full set of (isothermal) Maxwell-Stefan relations as they are typically presented in the literature.

$$\frac{x_i}{RT}\frac{d\mu_i}{dz} = \sum_{\substack{j=1 \\ j\neq i}}^{c} \frac{x_i x_j (u_j - u_i)}{Đ_{i,j}} \qquad i = 1 \ldots c \tag{5.54}$$

This hypothesis has been empirically confirmed in the gaseous phase. [13, 27] The functional form has also been confirmed both empirically and theoretically (utilizing the thermodynamics of irreversible processes) in condensed phases. [28] In order to improve predictions for condensed phases, the binary Maxwell-Stefan diffusivities are allowed to be functions of the mixture properties. [12] Fortunately, thermodynamically consistent functional forms have been proposed and validated that depend only on the infinite dilution diffusivities and the mole fractions. [29]

When there are other driving forces for mass transport like centrifugal forces, pressure gradients, electrostatic potential gradients or any other imaginable body force, more terms appear on the left to account for these forces. The equation can be re-written in terms of the absolute molar fluxes of each species N_i, by noticing that $N_i = c_i u_i = c_T x_i u_i$, where c_i is the molar concentration of component i and c_T is the total molar density of

the mixture.

$$\frac{x_i}{RT}\frac{d\mu_i}{dz} = -\sum_{\substack{j=1 \\ j\neq i}}^{c} \frac{(x_j N_i - x_i N_j)}{c_T Đ_{i,j}} \qquad i = 1 \ldots c \tag{5.55}$$

When all (c) Maxwell-Stefan equations are summed up, the right hand side is exactly zero. This result can be formally written as equation 5.56 below.

$$\sum_{i=1}^{c} x_i \frac{d\mu_i}{dz} = 0 \tag{5.56}$$

This relation is clearly the Gibbs-Duhem relation. No thermodynamic arguments have been made in the presentation of equation 5.56. Thus, the Maxwell-Stefan formulation of multicomponent diffusion is independently consistent with the expected thermodynamic result.[19] This result renders the $(c)^{th}$ Maxwell-Stefan relation linearly dependent on the rest. Since, by definition, the mole fractions must also sum to unity, the system of equations now has $(c-1)$ independent mole fractions and (c) absolute molar fluxes totaling $(2c-1)$ variables. There are $(c-1)$ independent Maxwell-Stefan relations, so the system as described contains (c) degrees of freedom. If the system is an ideal mixture, the Maxwell-Stefan relations take the form of equation 5.57 below.

$$\frac{x_i RT}{a_i}\frac{da_i}{dz} = RT\frac{dx_i}{dz} = -\sum_{\substack{j=1 \\ j\neq i}}^{c} RT\frac{(x_j N_i - x_i N_j)}{c_T Đ_{i,j}} \qquad i = 1 \ldots c \tag{5.57}$$

If the (c) Maxwell-Stefan relations in equation 5.57 are summed, again the right hand side is always exactly zero. Thus, when the system is an ideal mixture, equations 5.57

[19] In fact, it follows that any self-consistent multicomponent diffusion theory must obey this requirement.

lead to.

$$\sum_{i=1}^{c} \frac{dx_i}{dz} = 0 \tag{5.58}$$

This relationship is equivalent to requiring that the mole fractions must sum to a constant. Therefore, only $(c-1)$ Maxwell-Stefan equations are again independent in the ideal case, and there are again (c) degrees of freedom. In either case, after specifying initial conditions for the Maxwell-Stefan relations and setting (c) absolute molar fluxes or mole fractions, the value of all remaining variables are determined everywhere.

An interesting feature of the Maxwell-Stefan relations is that the chemical potential gradients only depend on molar flux or velocity differences. When the absolute velocities or fluxes are not required, there are only $(c-1)$ degrees of freedom. The dependence on flux or velocity differences makes the Maxwell-Stefan relations independent of reference frame, so the fluxes can be defined as diffusive fluxes or total fluxes without changing the equations. Let N_i be the absolute molar flux of species i, and let J_i be the diffusive flux of component i relative to the molar average velocity of the mixture, u_t.

$$N_i = J_i + c_i u_t = J_i + x_i N_t \tag{5.59}$$

where $N_t = \sum_{i=1}^{c} N_i$ and $\sum_{i=1}^{c} J_i = 0$. The resulting set of equations and the number of variables is the same if the $\boldsymbol{J}$ or $\boldsymbol{N}$ are used in the Maxwell-Stefan relations. When the $\boldsymbol{N}$ are used, there are (c) N_i variables (and $(c-1)$ differences). If $\boldsymbol{J}$ are used, there are only $(c-1)$ independent fluxes (and still $(c-1)$ differences), but u_t is a new variable leading to (c) total variables.[20] Once $\boldsymbol{J}$ and u_t have been determined, the $\boldsymbol{N}$ can be calculated or vice versa. Therefore, the choice of formulation is arbitrary; there are

[20] (c) variables $+(c-1)$ x's $= (2c-1)$, as before with $(c-1)$ Maxwell-Stefan equations giving (c) degrees of freedom

always (c) degrees of freedom and it is possible to determine all the remaining variables from the Maxwell-Stefan equations once the degrees of freedom are specified. For the rest of the discussion, it will be assumed that the absolute flux values are of interest (not just their differences).

In practice, one commonly specifies boundary conditions with the intent of calculating the fluxes that result from the Maxwell-Stefan relations. As previously discussed, when absolute flux values are required, the system contains (c) degrees of freedom. Since only ($c-1$) boundary value mole fractions can be specified independently, (1) more relation is needed to calculate absolute flux values from a set of Maxwell-Stefan equations. This last relation is typically termed the "bootstrap relation" or the "determinacy condition." Without the "bootstrap relation," all the calculated velocities or fluxes are relative to each other, and not tied to a reference frame. Common "bootstrap relations" include a single absolute flux being known to have a specific value, a known algebraic relationship between several of the fluxes, or a known total flux through the boundaries. Reaction stoichiometry can give bootstrap relations when diffusion away from a catalyst site is being described. This extra relation is needed to specify the reference frame for the fluxes.

5.A.2 Matrix Generalization and Similarities to other Diffusion Descriptions

The coeficients relating fluxes to driving forces and chemical potentials to mole fractions can be presented in vector/matrix notation as shown below in equations 5.60-5.64.

$$B_{i,j} = -x_i \left(\frac{1}{Đ_{i,j}} - \frac{1}{Đ_{i,c}} \right) \tag{5.60}$$

$$B_{i,i} = \frac{x_i}{Đ_{i,c}} + \sum_{k \neq i} \frac{x_k}{Đ_{i,k}} \tag{5.61}$$

$$\Gamma_{i,j} = \delta_{i,j} + x_i \frac{\partial\ ln\gamma_i}{\partial x_j} \tag{5.62}$$

These matrices can then be combined with the vector of mole fraction derivatives and diffusive fluxes, $\nabla \boldsymbol{x}$ and $\boldsymbol{J}$, respectively, to write the set of $(c-1)\times(c-1)$ Maxwell-Stefan equations in vector/matrix form as shown in equation 5.63.

$$-c_T \boldsymbol{\Gamma} \nabla \boldsymbol{x} = \boldsymbol{B}\boldsymbol{J} \tag{5.63}$$

which can be rewritten as equation 5.64

$$\boldsymbol{J} = -c_T \boldsymbol{B}^{-1} \boldsymbol{\Gamma} \nabla \boldsymbol{x} \tag{5.64}$$

This formulation highlights the similarities between the Maxwell-Stefan description and other multicomponent diffusion descriptions. The most common competing description in the literature is a simple generalization of Fick's law as shown below in equation 5.65.

$$\boldsymbol{J} = -c_T \boldsymbol{D} \nabla \boldsymbol{x} \tag{5.65}$$

In this description, $\boldsymbol{D}$ encompasses all of the multicomponent coupling and thermodynamic information inside the matrix product $\boldsymbol{B}^{-1}\boldsymbol{\Gamma}$. Equation 5.65 is a presentation that looks more like Fick's law for binary component diffusion, but we see that $\boldsymbol{D}$ is a non-sparse matrix with terms accounting for all of the cross coupling between driving forces. $\boldsymbol{D}$ must be either measured experimentally [29–34] or predicted by some deeper theory. When a deeper resolution (other than the Maxwell-Stefan description described herein)

is offered, it is typically presented as an appeal to the thermodynamics of irreversible processes.

The thermodynamics of irreversible processes[21] (TIP) is the application of thermodynamic principles to the *time evolution* of coupled irreversible processes. After making several fundamental postulates, TIP predicts the relationships between fluxes and forces in a system either evolving towards equilibrium or maintaining a stationary-state (non-equilibrium or steady-state) due to thermodynamic constraints. The first postulate is that the rate of increase of entropy plays the role of the potential driving irreversible processes. [28] A second postulate is that close to equilibrium, non-equilibrium systems can be accurately described using thermodynamic relations (e.g. the fundamental equation in the entropy representation). In a system away from equilibrium, fluxes spontaneously arise in response to thermodynamic forces (imposed either externally or internally via a non-equilibrium configuration) such that entropy is generated, consistent with the second law of thermodynamics. General expressions for the rate of entropy production inside a control volume in terms of thermodynamic driving forces and fluxes have been derived. [36, 37] In general, if all force/flux pairings are defined such that each force is a derivative of the entropy with respect to the quantity that is fluxing, the sum over all the products of fluxes and the forces becomes a rate of entropy production. When all force/flux pairings are described in this way, the second law of thermodynamics guarantees that the sum of the products of these pairs is always positive during a spontaneous process. [35] We have

$$J_i = \frac{da_i}{dt} \tag{5.66}$$

$$F_i = \frac{\partial S}{\partial a_i} \tag{5.67}$$

[21] Otherwise known as the thermodynamics of the steady-state or non-equilibrium thermodynamics [35].

$$\frac{dS}{dt} = \sum_i F_i J_i = \sum_i \frac{\partial S}{\partial a_i}\frac{da_i}{dt} \tag{5.68}$$

where a_i is any thermodynamic quantity. For isothermal, isobaric, multicomponent diffusion, J_i is the molar diffusive flux and F_i is $-T^{-1}\nabla\mu_i$ so that the entropy generation rate per unit volume is

$$\frac{dS}{dt} = \sum_i J_i F_i = -\frac{1}{T}\sum_i J_i \nabla\mu_i \tag{5.69}$$

Third, it is postulated that close to equilibrium fluxes become linear functions of *all* the driving forces. A functional form must be imposed so that the entropy generation goes to zero when the driving forces vanish (at equilibrium). Therefore, close enough to equilibrium, this linear law must hold. This linearity postulate enables the prediction of many couplings among simultaneous irreversible processes that have been previously or since observed experimentally (e.g. multicomponent diffusional, thermo-mechanical, thermo-osmosotic, thermo-electrical, and ionic diffusion coupling).

$$J_i = \sum_p L_{i,p} F_p \tag{5.70}$$

The $L_{i,k}$ are termed the phenomenological coefficients. They represent the proportionality between forces and fluxes. The linearity postulate combined with microscopic reversibility/time reversal invariance arguments first presented in Onsager's classic 1931 paper give the Onsager Reciprocal Relations (ORR). [28] These relations state that any conjugate pair of forces and fluxes that combine to give a rate of entropy production must have a symmetric phenomenological coefficient matrix, i.e. $L_{i,k} \equiv L_{k,i}$.

With that background, multicomponent diffusion can be described in terms of TIP. If the fluxes are chosen to be the (c) molar fluxes, $\boldsymbol{J}$, then the driving forces should be chosen as the (c) forces, $-\nabla(\mu_i/T)$. In an isothermal, isobaric system, the gradient of

the chemical potential is the correct driving force for molar diffusion. Since only $(c-1)$ diffusive fluxes (or chemical potential gradients) are independent, the driving force can be re-written as $-\nabla(\mu_i-\mu_c)/T$ without loss of generality.[22][23] In practice, chemical potential models are functions of concentration or mole fraction, so it is preferred to present the quantity $\nabla(\mu_i-\mu_c)$ as a function of $\nabla \boldsymbol{x}$ as is shown below. [39, 40]

$$\nabla(\mu_i-\mu_c)=\sum_j \boldsymbol{G_{i,j}}\nabla x_j \tag{5.71}$$

$$\boldsymbol{G_{i,j}}=\frac{\partial g}{\partial x_i \partial x_j} \tag{5.72}$$

$\boldsymbol{G}$ is a $(c-1)\times(c-1)$ matrix known as the Hessian of the molar Gibbs free energy. It is now possible to use the linearity postulate, equation 5.70, to write the diffusive flux as shown in equation 5.73 below.[24]

$$\boldsymbol{J}=-c_T\boldsymbol{L}\boldsymbol{G}\nabla\boldsymbol{x} \tag{5.73}$$

This formulation is particularly interesting because $\boldsymbol{L}$ is guaranteed to be symmetric by the ORR and positive definite by the second law of thermodynamics. $\boldsymbol{G}$ is also guaranteed to be positive definite in a thermodynamically stable fluid away from the critical point due to stability arguments from classical thermodynamics. Therefore, the eigenvalues of each matrix $\boldsymbol{L}$ and $\boldsymbol{G}$ are real and positive, and each has a complete set of eigenvectors. Moreover, the composite matrix of diffusion coefficients $\boldsymbol{D}=\boldsymbol{L}\boldsymbol{G}$ is non-symmetric, but

[22] For more details on the thermodynamics of irreversible processes in non-isothermal or non-isobaric conditions, see [12, 37, 38].

[23] Also, when isothermal diffusion is being described, it is common to absorb the T^{-1} into the phenomenological coefficient matrix, $\boldsymbol{L}$. Equivalently, one can just consider the potential in equations 5.67 and 5.68 to be TS making the correct driving force $\nabla\mu$.

[24] $\boldsymbol{L}$ has been replaced by $\frac{\boldsymbol{L}}{c_T}$ to highlight the similarity between the three methods.

because of the special properties of $\boldsymbol{L}$ and $\boldsymbol{G}$, it too has real, positive eigenvalues and a complete set of eigenvectors. [41]

The Maxwell-Stefan relations have been generated from TIP, [37, 42] implying that both presentations are theoretically consistent even though they have significant differences. $\boldsymbol{G}$ is not equivalent to $\boldsymbol{\Gamma}$, and $\boldsymbol{L}$ is not equivalent to $\boldsymbol{B}$, but $\boldsymbol{LG}$, $\boldsymbol{B}^{-1}\boldsymbol{\Gamma}$, and $\boldsymbol{D}$ clearly contain the same information.

To illustrate this point, here is an example from Taylor and Krishna's *Multicomponent Mass Transfer* [12] based on measured diffusivity data taken from Cullinan and Toor's 1965 paper. [34] Multicomponent generalized Fick diffusivities were measured for the system acetone (1), benzene (2) carbon tetrachloride (3) at a temperature of 25 C and a composition of $x_1 = 0.70$, $x_2 = 0.15$, and $x_3 = 0.15$. The diffusivity matrix $\boldsymbol{D}$ was found to be

$$\boldsymbol{D} = \begin{pmatrix} 2.354 & -0.471 \\ 0.089 & 2.947 \end{pmatrix} \times 10^{-9} \quad m^2/s \tag{5.74}$$

The Hessian matrix $\boldsymbol{G}$ was then calculated from the NRTL model as

$$\boldsymbol{G} = \begin{pmatrix} 16.995 & 15.441 \\ 15.441 & 33.026 \end{pmatrix} \times 10^{2} \quad J/mol \tag{5.75}$$

Clearly, $\boldsymbol{G}$ is symmetric as expected and $\boldsymbol{D}$ is not, also as expected. The phenomenological matrix $\boldsymbol{L}$ can now be calculated from equations 5.65 and 5.73-5.76

$$\boldsymbol{D} = \boldsymbol{LG} \tag{5.76}$$

$$\boldsymbol{L} = \begin{pmatrix} 2.632 & -1.373 \\ -1.318 & 1.509 \end{pmatrix} \times 10^{-12} \quad \frac{m^2 \cdot mol}{J \cdot s} \tag{5.77}$$

The phenomenological coefficient matrix $\boldsymbol{L}$ is not exactly symmetric due to inaccuracies in experimental measurements of $\boldsymbol{D}$ and in the NRTL parameters used to calculate $\boldsymbol{G}$. The matrix is symmetric to one significant figure and it is clear from this example that $\boldsymbol{LG} = \boldsymbol{D}$ to experimental precision.

The great advantage of the Maxwell-Stefan formulation is that the Maxwell-Stefan matrix, $\boldsymbol{B}$, is simpler to work with than the corresponding $\boldsymbol{L}$ and $\boldsymbol{D}$ matrices. Also, the $Đ_{i,j}$ are symmetric and have physical meanings that are relatively intuitive. Also, the multicomponent $Đ_{i,j}$ are easily defined from only infinite dilution binary diffusivities and composition information in both ideal gases and condensed phases, while the $\boldsymbol{L}_{i,j}$ and $\boldsymbol{D}_{i,j}$ require experimental measurement at every point in composition space for each mixture in which they are required. [29–34] Therefore, even though most tabulated diffusivities are generalized Fick coefficients, and even though the thermodynamics of irreversible processes generates several mathematical conveniences, the Maxwell-Stefan framework is consistent with both the other approaches, is the easiest to conceptualize, and gives the most insight per experimental effort. For all these reasons, the Maxwell-Stefan equations are preferred here.

5.A.3 Diffusion of Electrolytes

In order to extend this discussion into the realm of liquid electrolyte diffusion that is pertinent to this work, the force that the electric potential gradient applies on electrolytes needs to be included in the Maxwell-Stefan relations. First, several terms must be defined. The electric potential (ϕ) is expressed in volts (joule/coulomb). The elementary charge ($e = 1.6 \times 10^{-19}$ coulombs) is the absolute value of the amount of charge on an electron. The faraday constant is the absolute value of the amount of charge on a mole of electrons ($F = eN_a = 9.65 \times 10^4 \ \frac{\text{coulombs}}{\text{gmol}}$); z_i is the charge number or valence of an electrolyte

(units of charge on i per elementary charge). The charge number can be multiplied by the elementary charge to give the total charge on an electrolyte (in coulombs). Together, Fz_ix_i gives the amount of charge on component i per mole of mixture so that the term $-Fz_ix_i\frac{d\phi}{dz}$ is a force on component i in the z direction per mole of mixture (similar to the chemical potential term). Including this new force into the driving force on i per mole of mixture (d_i), the Maxwell-Stefan relation becomes equation 5.78.

$$\frac{x_iRT}{a_i}\frac{da_i}{dz} + Fz_ix_i\frac{d\phi}{dz} = -\sum_{\substack{j=1\\j\neq i}}^{c} RT\frac{(x_jN_i - x_iN_j)}{c_T\text{Đ}_{i,j}} \qquad i = 1\ldots c-1 \tag{5.78}$$

If the mixture is also ideal, equation 5.78 can be further simplified to equation 5.79 below.

$$\frac{dx_i}{dz} + \frac{Fz_ix_i}{RT}\frac{d\phi}{dz} = -\sum_{\substack{j=1\\j\neq i}}^{c} \frac{(x_jN_i - x_iN_j)}{c_T\text{Đ}_{i,j}} \qquad i = 1\ldots c-1 \tag{5.79}$$

The electric potential term complicates things considerably. In the absence of an externally applied electric potential, the electric potential induced by the electrolytes in solution is termed the diffusion potential. Diffusion potentials arise to maintain charge balance in space. The physical mechanism that sets up these diffusion potentials is intrinsically related to electroneutrality. Any infinitesimal charge separation that naturally arises from electrolytes diffusing at different speeds induces a potential gradient that "pulls" the faster ions back towards the slower ions while simultaneously "pulling" the slower ions forward towards the faster ones. This phenomenon leads to relatively simple effective diffusivities for dilute solutions of single salt pairs. The situation is more complicated when there is more than one salt pair or when the system cannot be considered dilute. When there is more than one salt pair, the electroneutrality constraint can be met without both electrolytes in a salt pair being "forced" to diffuse together (at some intermediate effective diffusivity). If multiple electrolytes exist in solution,

the ratio of any pair of components (i to j) can change without necessarily separating charge. It is not difficult to imagine examples where all these phenomena lead to one of the electrolytes diffusing against its concentration gradient. These complications render effective diffusivities inaccurate and generally unuseful in concentrated multicomponent electrolyte systems. [12, 14] Macroscopic charge densities must be vanishingly small in liquids in the absence of an applied field. When one analyzes solutions of Poisson's equation for typical charge distributions in a liquid electrolyte system (equation 5.80 below), one can see that any appreciable charge separation is not physically reasonable.

$$\boldsymbol{\nabla}^2\phi = -\frac{F}{\varepsilon}\sum_{i=1}^{c} c_i z_i \tag{5.80}$$

The ε in Poisson's equation is the permittivity of the material (ε of water at $20°C$ is $7.1 \times 10^{-10} \frac{coulomb^2}{kg\ m^3\ s^2}$). Poisson's equation is generated by applying the divergence theorem to Gauss's law and is exact. It states the relationship between the Laplacian of the electric potential and the charge density ($\sum_{i=1}^{c} c_i z_i$) over a control volume. If one calculates the Laplacian of the electric potential for examples containing realistic numbers (as is done in *Electrochemical Systems* [43]), the large magnitude of F/ε sets charge densities at $\pm$ 1×10^{-11} molar equivalents per liter in liquids[25]. Therefore, assuming the charge density of a liquid to be zero, while technically inexact, is a good approximation of reality that greatly simplifies the mathematics. The full electroneutrality relation is shown below in equation 5.81. This relationship is required to hold at every point in space.

$$\sum_{i}^{c} F c_T z_i x_i = 0 \tag{5.81}$$

Since the faraday and the molar density of the mixture are independent of index i they

[25]Molar equivalents (eq) is a unit of electrical charge. It is the number of moles of elementary charge per mole of an ion, so that a mole of Na^+ is one eq and a mole of Ca^{2+} is 2 eq.

can be factored out. This simplification leads to the most common form of the electroneutrality relation shown below.

$$\sum_{i}^{c} z_i x_i = 0 \tag{5.82}$$

Including electrolytes also adds another feature to the set of equations. Now it is feasible that electric current could be passed through the film by diffusing electrolytes. A mathematical expression of this statement is shown in equation 5.83.

$$\sum_{i}^{c} F z_i N_i = I \tag{5.83}$$

where I is the electric current. Electric charge is a conserved quantity, like mass, energy and linear momentum. Reactions have not been considered yet, but as long as any reactions that are considered are written so that they balance charge, I must be a constant at steady-state. This leads to an interesting conclusion for the physical situations relevant to this work. While non-zero magnitude currents are possible in solution between two charged electrodes, there will be no net current flowing through the liquid phase without some externally applied potential. The electrolyte migration being modeled in this work (and the corresponding electric potential gradient) will result from diffusion potentials set up to maintain electroneutrality, not from externally applied potentials. This means that for this work the net current can be assumed to be zero, simplifying equation 5.83 to equation 5.84.

$$\sum_{i}^{c} z_i N_i = 0 \tag{5.84}$$

By considering the charge of electrolyte species in our model we have added some new variables and equations. Now, there are two more algebraic relations between the mole

fractions and fluxes (equations 5.82 and 5.84). In total there are now $(c-1)$ independent Maxwell-Stefan relations, (1) electroneutrality relation (equation 5.82) and (1) no current relation (equation 5.84). This leaves $(c+1)$ equations between all of the variables. There are still $(c-1)$ mole fractions and (c) fluxes at every point, but now there is also a single unknown electric potential gradient, $\frac{d\phi}{dz}$. Therefore, the number of degrees of freedom has been reduced to $(c-1)$. The loss of a degree of freedom is best reflected in the coupling of the fluxes to disallow the flow of electric current. Another statement of this change, that is consistent with the terminology in the literature, would be that the no current relationship provides a bootstrap relation for the fluxes.

These systems are large, coupled, and non-linear, so numerical methods are necessary to find a solution. Common numerical methods require systems of differential equations to be in the form of a set of first-order ODE's, as in equation 5.85.

$$\frac{d\boldsymbol{y}}{dz} = \boldsymbol{f}(\boldsymbol{y}, z, parameters) \tag{5.85}$$

where $\boldsymbol{y}$ is a column vector of states and $\boldsymbol{f}$ is a vector function, usually assumed to be differentiable. It is thus convenient to write the electric potential, $\frac{d\phi}{dz}$, in terms of the fluxes, mole fractions and their gradients and eliminate it from the Maxwell-Stefan equations, i.e., to decouple the system of equations. The no-current relation and the $(c-1)$ Maxwell-Stefan relations can be used to eliminate the electric potential term. After some algebra, it can be shown that this leads to equation 5.86.

$$\frac{F}{RT}\frac{d\phi}{dz} = \frac{\sum_k \frac{z_k}{\frac{\sum_{p\neq k} x_p}{\mathcal{D}_{k,p}}}\left[x_k\left(\sum_{j\neq k}\frac{N_j}{c_T \mathcal{D}_{k,j}}\right) - \frac{dx_k}{dz}\right]}{\sum_h \frac{z_h^2 x_h}{\sum_{m\neq h}\frac{x_m}{\mathcal{D}_{h,m}}}} \tag{5.86}$$

Eliminating the electric potential term renders one of the Maxwell-Stefan equations linearly dependent on the others. Now, the new set of Maxwell-Stefan relations is reduced

to a set of $(c-2)$ implicit ODE's (i.e., implicit in the derivatives $\frac{dx_i}{dz}$). At this point, it is desired to reformulate the problem as an explicit set of first order ODEs by utilizing all of the available algebraic equations to eliminate as many variables as possible.

The $(c-1)^{st}$ mole fraction and the (c^{th}) flux can be eliminated by utilizing the electroneutrality relation and the no current relation. After some algebraic manipulation, the problem can be reformulated as a set of $(c-2)\times(c-2)$ explicit differential equations. There are still $(c-1)$ degrees of freedom, so if the remaining $(c-2)$ Maxwell-Stefan relations are supplied with an initial value and the $(c-1)$ initial fluxes are set, the entire system is defined.

Some salts disassociate completely enough that an accurate diffusion description need not account for their dissociation chemistry, but this is not generally the case. When appreciable but incomplete reactions occur in the liquid film, molar fluxes are no longer conserved. Now, a continuity equation is needed to define the change of each component flux with position. Equation 5.87 is the general steady-state continuity equation (in the absence of convective flows) for a component undergoing (r) independent reactions with stoichiometric coefficients $v_{i,j}$[26].

$$\frac{dN_i}{dz} = \sum_{j=1}^{r} v_{i,j} r_j \qquad i = 1 \ldots c-1 \tag{5.87}$$

where $v_{i,j}r_j$ is the rate of production of i due to reaction j[27]. In practice, only (r) of the fluxes can change independently[28].

The (r) independent continuity equations are explicit, so the total system can be set

[26]Equation 5.87 results when the time derivative becomes zero (at steady-state) in the general continuity equation describing the transport of moles of component i. This equation describes the molar transport of i in the z direction in the absence of convective motion at steady-state.

[27]By convention, reactant stoichiometric coefficients are negative and product stoichiometric coefficients are positive.

[28]In fact, the actual number of reactions can be greater than the number of independent reactions, but this does not change the number of independent fluxes, which is still (r) [44, 45].

up as a $(c-2+r)$ set of explicit ODE's[29]. This new set is only a function of the $(c-2)$ initial mole fractions and the $(c-1)$ initial fluxes. In other words, one could specify the initial mole fractions and fluxes and integrate forward to calculate all properties at any value of the z-coordinate.

If one of the reactions is known to be fast enough to instantaneously achieve chemical equilibrium throughout the regime of interest, a chemical equilibrium relation can be used instead of one of the continuity equations. The equilibrium relation can also be used to eliminate another mole fraction from the remaining list. Then, the Maxwell-Stefan relation based on the recently eliminated mole fraction can be re-written as an algebraic equation for the extent of interest, since the mole fraction derivative is no longer independent. This new equation can be solved at every step to find the correct magnitude of conversion necessary to maintain equilibrium. If this is done (r_{eq}) times, one is left with $(c-2-r_{eq})$ Maxwell-Stefan relations, $(r-r_{eq})$ independent continuity equations and (r_{eq}) extent algebraic equations for a total of $(c-2+r-r_{eq})$ independent equations. There are still $(c-1)$ initial fluxes and (r) independently varying fluxes, but now there are only $(c-2-r_{eq})$ independent mole fractions. Therefore, after specifying the $(c-2-r_{eq})$ Maxwell-Stefan initial conditions, $(c-1)$ degrees of freedom remain. Therefore, everything is determined when initial mole fractions and fluxes are specified.

5.A.4 Simplification of the Maxwell-Stefan Relations

The Nernst-Planck equation is the most common model in the literature for diffusion under the influence of electric potential gradients. It explicitly defines each flux similar to FickâĂŹs law and accounts for electric forces via an additional $\frac{d\phi}{dz}$ term. It can be derived from the Maxwell-Stefan equations by assuming the electrolyte solution is infinitely dilute

[29]The other $(c-1-r)$ fluxes are trivially related to the r independent fluxes through the stoichiometric matrix $\boldsymbol{\mathcal{V}}$ [44]

in ions and ideal. In this limit, the solvent must be a neutral molecular species (e.g., water molecules), all electrolyte mole fractions go to zero, the solvent mole fraction (component c) goes to unity, and the activity coefficients all become unity.[30] In this limit, friction forces between ions become negligible, and the summation on the right hand side of the Maxwell-Stefan equations simplifies to a single term divided by the Maxwell-Stefan diffusivity between that ionic solute (i) and the solvent (c).

$$\frac{dx_i}{dz} + \frac{Fz_i x_i}{RT}\frac{d\phi}{dz} = -\frac{x_c N_i}{c_T \text{Đ}_{i,c}} \qquad i = 1 \ldots c-1 \tag{5.88}$$

Or it can be re-written in terms of the diffusive flux relative to the solvent velocity u_c (rather than the molar average velcoity of the mixture u_t), to give the traditional Nernst-Planck representation below:

$$J_i = -c_T \text{Đ}_{i,c}\frac{dx_i}{dz} - c_T \text{Đ}_{i,c}\frac{Fz_i x_i}{RT}\frac{d\phi}{dz} + c_i u_c \qquad i = 1 \ldots c-1 \tag{5.89}$$

Each system must be examined on a case by case basis, but a rule of thumb for electrolyte containing systems is that unacceptable errors (on the order of $> 5\%$) begin to appear in the Nernst-Planck description of diffusion when total salt concentration approaches 0.1 molar. [2, 12] The no-current relation can be used to eliminate $\frac{d\phi}{dz}$ from the Nernst-Planck relation similar to the way it was used in equation 5.86 in the general Maxwell-Stefan formalism.

When the Nernst-Planck relations are used (instead of the Maxwell-Stefan relations) to eliminate the electric potential, the resulting expression is

$$\frac{F}{RT}\frac{d\phi}{dz} = -\frac{\sum_p z_p \text{Đ}_{p,c}\frac{dx_p}{dz}}{\sum_k z_k^2 x_k D_{k,c}} \tag{5.90}$$

[30] Here we adopt the activity coefficient convention in which solute activity coefficients go to unity in the dilute limit and solvent activity coefficients go to unity in the pure limit [46, 47].

Thus, equation 5.89 becomes

$$J_i = -c_T Đ_{i,c} \frac{dx_i}{dz} + c_T Đ_{i,c} z_i x_i \frac{\sum_p z_p Đ_{p,c} \frac{dx_p}{dz}}{\sum_k z_k^2 x_k D_{k,c}} + c_i u_c \qquad i = 1 \ldots c-1 \tag{5.91}$$

5.A.5 Further Simplification to Fick's First Law

When there are no charged species, the $\frac{d\phi}{dz}$ term is exactly zero and equation 5.89 becomes

$$J_i = -c_T Đ_{i,c} \frac{dx_i}{dz} + c_i u_c \qquad i = 1 \ldots c-1 \tag{5.92}$$

Without solvent motion, the convective $c_i u_c$ term is zero. After these simplifications, all that is left is FickâĂŹs law.

$$J_i = -c_T Đ_{i,c} \frac{dx_i}{dz} = -Đ_{i,c} \frac{dc_i}{dz} \tag{5.93}$$

Fick's first law is valid in the infinitely dilute, ideal solution limit in the absence of body forces. In this limit, the Maxwell-Stefan and Fick diffusivities are the same, thus $D_i \equiv Đ_{i,c}$.

The Fick's law formalism can be extended to multicomponent mixtures by including another term in each Fick's law expression for each chemical potential gradient in the system. While this *can* be done formally and correctly, the Maxwell-Stefan description is superior. The main reason is that in the Maxwell-Stefan formalism, diffusivities represent proportionalities between friction dissipation in a mixture and the potential gradients in that mixture. Fickian diffusivities must account for non-idealities and composition effects as well as friction effects, so there is no simple physical interpretation of their meaning.

Surprisingly, multicomponent Fick diffusion coefficients are not uniquely defined or even guaranteed to be positive in multicomponent mixtures, as they depend on the arbitrary choice of reference component (solvent or c^{th} component) and are strong functions of composition. [12] The Maxwell-Stefan relations are intended to be used with an activity model, and their composition dependence is built into the structure of the equations more generally. In this way, the Maxwell-Stefan description is more intuitive and fundamental.

5.A.6 Effective Diffusivities

It is common in the literature to lump multicomponent effects into a single effective diffusivity to use in the place of a Fick diffusion coefficient. These methods can be quite useful in dilute limits where multicomponent effects can be considered negligible. Unfortunately, most of the treatments of this type are simply referred to as effective diffusivity methods in the literature, oftentimes leaving the reader unsure what the writer has assumed. More importantly, there are many systems (with and without electrolytes) where effective diffusivities simply cannot capture all of the relevant physics. Several effects that can arise in these systems include osmotic diffusion (diffusing in the absence of an activity gradient), diffusion barriers (absence of diffusion in the presence of an activity gradient), and even reverse diffusion (where a component diffuses *against* its own activity gradient). It is in these situations that the use of effective diffusivities should be particularly questioned.

Sometimes, the diffusion of highly soluble salts is described by FickâĂŹs law with an effective diffusivity chosen to correct the conventional FickâĂŹs formulation for the electric forces that arise from the diffusion of electrolytes. The effective diffusivity is calculated by using the no-current relation to eliminate the gradient of the electric potential from the Nernst-Planck equation and lumping all the terms in front of the mole

fraction gradient into one "constant". This can work well in dilute systems, but can be inaccurate at higher concentrations of electrolytes or when there are more than 3 components.[31] In a three component system (one solvent and one salt pair), equation 5.91 can be manipulated so that it looks like equation 5.92 with an effective diffusivity. The effective diffusivity is then defined as

$$Đ_{1,eff} = Đ_{2,eff} = Đ_{1,c}\left[1 - z_1 x_1 \frac{\left(z_1 Đ_{1,c}\frac{dx_1}{dz} + z_2 Đ_{2,c}\frac{dx_2}{dz}\right)/\frac{dx_1}{dz}}{z_1^2 x_1 Đ_{1,c} + z_2^2 x_2 Đ_{2,c}}\right] \tag{5.94}$$

When the electroneutrality relation is utilized to eliminate one of the mole fractions and one of the mole fraction gradients, all of these terms cancel out leaving the much simplified form

$$Đ_{eff} = \frac{Đ_{1,c} Đ_{2,c}(z_1 - z_2)}{z_1 Đ_{1,c} - z_2 Đ_{2,c}} \tag{5.95}$$

When $z_1 = -z_2$, this expression simplifies to the common expression for D_{eff} below [7].

$$Đ_{eff} = \frac{2Đ_{1,c} Đ_{2,c}}{Đ_{1,c} + Đ_{2,c}} \tag{5.96}$$

This is clearly a useful expression (when applicable) because the complicated electric potential term has been eliminated, and the two electrolytes can now be described as a single component. Trouble can arise in concentrated mixtures and/or when more components are present. Depending on the way the effective diffusivity is derived and applied it either ignores or linearizes the solute/solute interactions in multicomponent solutions. When electrolytes are present, it often gives the electric potential gradient a similar treatment. Although the use of effective diffusivities abounds in the literature, some have labeled this method almost useless for describing multicomponent systems

[31] The multicomponent effects are implicitly ignored when starting from the Nernst-Planck relation.

away from the dilute limit, as the humorous quote below aptly describes:

> "To use these formulas, knowingly or unknowingly, in situations such that these limiting cases do not apply would stand about as much chance of successfully predicting the fluxes as the throw of a dice to predict the magnitude and the toss of a coin to predict the sign."
>
> Lawrence W. Smith and Ross Taylor [14]

This quote is specifically referring to the use of effective diffusivities to describe multi-component diffusion in the absence of electrolytes. The additional complexity introduced by diffusing electrolytes clearly does nothing to increase the accuracy of these methods. The concentrated electrolytic nature of our systems makes the use of effective diffusivities especially likely to be inappropriate for our models.

5.B Numerical solution to model equations

Coupled, non-linear, boundary-valued systems often occur in nature, and thus many possible solution schemes have been developed. [48] A set of solution algorithms commonly used for solving boundary-valued problems are the shooting or multiple shooting methods [49] in which one guesses initial conditions, interior conditions, or both and then integrates an initial value problem to the boundary. One can then calculate boundary value residuals and uses the vector of residuals as an objective function to be minimized by varying the initial guesses. These methods work very well in some systems, but they are known to require very accurate initial guesses. [50] Other methods include collocation methods, [51] finite difference methods, [52] and finite element methods. [53]

Typically, boundary-value methods are sensitive to the initial guesses supplied, so much work has been done on developing reasonable schemes for making initial guesses.

One clever class of methods is termed parameter continuation. In simple parameter continuations, one starts with a solution that is known, usually in a simplifying limit where the equations become trivial or some physical intuition can be used to formulate initial guesses. The system of equations can then be systematically stepped toward the system of interest by changing a parameter (or multiple parameters) in small steps. [54] If the steps are small enough, the solution from the previous step (or some gradient based approximation) can become an excellent initial guess for the next step. Simple parameter continuation works well in systems of linear boundary-valued equations that are sensitive to initial guesses, but it often fails in non-linear systems. In non-linear systems, multiple solutions are generally possible and solution features such as branching points, turning points, and other bifurcations can disrupt a simple parameter continuation. In these systems, arc-length continuation is superior. [55] Arc-length continuation methods reparameterize the initial guesses and all parameters with respect to a new parameter, the arc-length in the parameter-solution space. Then, one steps in the new arc-length (instead of the parameter) to trace out solution paths, even around turning points. One can concurrently monitor the modified Jacobian matrix for singularities to flag potential branching points for later tracing.[32] Arc-length continuation based solution algorithms were used here for determining initial guesses for the highly nonlinear film model equations. These methods are ideal for the class of problems presented here because the case of $Ha = 0$ (physical absorption) and the case of $B(i,j) << B(i,i)$ (dilute limit) are both well characterized. An initial point on the solution-parameter arc is relatively easy to estimate, and then solutions can be progressively traced toward parameter regions of interest.

Matlab has a built in boundary value problem sollocation solver named bvp4c that has been used to solve the stagnant film boundary value problems described in this

[32]See Appendix 5.D for more detail on bifurcation points and arc-length continuation.

chapter. The built in pdepe function can be used to solve the renewal and penetration models also discussed here. Both can be integrated with the OLI MSE model directly through a developer edition license. The developer edition license allows one to send a set of solution conditions to the OLI engine and retrieve activity coefficients, activity coefficient gradients, and self-diffusiviteis back into the matlab script. These parameters can then be integrated into the solution algorithm for either the stagnant film (bvp4c) or surface renewal (pdepe) models. The governing PDEs are identical for the renewal and penetration theories. The only difference is how one calculates the average molar flux from $N(t,z)$.

5.C Construction of the concentated, electrolytic diffusion matrix

The term, $[\boldsymbol{I}+\boldsymbol{\Xi}]^{-1}\boldsymbol{\beta}$, was written without derivation or detail in the chapter and in Appendix 5.A. It is defined and discussed here. Several component matrices have been defined to simplify the presentation (named $\boldsymbol{E}-\boldsymbol{G}$).

First, one constructs the $\boldsymbol{B}$ matrix described in Chapter 5. In general, it is a $(c-2)\times(c-1)$ dimensional matrix. In the CO_2 capture example, it is actually only $(c-4)\times(c-1)$ because two less mole fractions are linearly independent due to the two chemical equilibrium relationships, but for simplicity of presentation, the equations are displayed here in general terms. If other relationships between the mole fractions exist, the expressions must be modified to maintain consistency.

$$E=\sum_{k=1}^{c}\frac{z_k^2 x_k}{\sum_{m\neq k}\frac{x_m}{D_{k,m}}} \tag{5.97}$$

$$\boldsymbol{F}(i,j) = \frac{z_i x_i z_j x_j}{E \sum_{t \neq j} \frac{x_t}{Đ_{j,t}}} \tag{5.98}$$

$$\boldsymbol{G}(i,i) = \frac{-1}{Đ_{i,c}} \tag{5.99}$$

$$\boldsymbol{G}(i,j) = \frac{1}{Đ_{i,j}} - \frac{1}{Đ_{i,c}} \tag{5.100}$$

With these definitions, $\boldsymbol{\beta}$ can be defined.

$$\boldsymbol{\beta} = \boldsymbol{B} + \boldsymbol{F}\boldsymbol{G} \tag{5.101}$$

and $\boldsymbol{\Xi}$

$$\boldsymbol{\Xi}(i,j) = \frac{z_i x_i z_j}{G} \left[\frac{1}{\sum_{t \neq j} \frac{x_t}{Đ_{t,j}}} - \frac{1}{\sum_{t \neq j} \frac{x_t}{Đ_{t,c-1}}} \right] \tag{5.102}$$

$\boldsymbol{\Xi}$ is $(c-2) \times (c-2)$. The liquid film equations can now be written as

$$[\boldsymbol{I} + \boldsymbol{\Xi}]\boldsymbol{\Gamma}\boldsymbol{x}' = -\boldsymbol{\beta}\boldsymbol{J} \tag{5.103}$$

Then, when $[\boldsymbol{I} + \boldsymbol{\Xi}]$ has an inverse,

$$\boldsymbol{x}' = -[\boldsymbol{\Gamma} + \boldsymbol{\Xi}]^{-1}\boldsymbol{\beta}\boldsymbol{J} \tag{5.104}$$

5.D Nonlinear Systems and Arc-Length Continuation

This section will discuss some of the peculiarities and solution strategies of nonlinear equations of either form 5.105 or 5.106 below.

$$\boldsymbol{f}(\boldsymbol{y}, \lambda) = 0 \tag{5.105}$$

or

$$\dot{\boldsymbol{y}} = \boldsymbol{f}(\boldsymbol{y}, \lambda) \quad \boldsymbol{g}(\boldsymbol{y}(\boldsymbol{t_{bv}}, \boldsymbol{\lambda}), \lambda) = 0 \tag{5.106}$$

where λ is some parameter and t_{bv} is the point where the boundary condition $\boldsymbol{g} = 0$ is specified. The ideas and general procedures are similar for both types of systems, so the simpler algebraic system will be discussed here. Before proceeding, we also need to define the Jacobian matrix, $\boldsymbol{J}$, and the modified Jacobian, $\boldsymbol{J}_m$.

$$\boldsymbol{J}(i,j) = \frac{df_i}{dy_j} \tag{5.107}$$

$$\boldsymbol{f}_\lambda = \frac{df_i}{d\lambda} \tag{5.108}$$

$$\boldsymbol{J}_m = \left[\boldsymbol{J}, \boldsymbol{f}_\lambda\right] \tag{5.109}$$

Solutions to systems of nonlinear equations (of the form 5.105) usually require numerical solvers. These are well documented and don't require more discussion here. [56,57][33] These numerical solvers generally require highly accurate initial guesses for convergence. One common method for finding initial guesses, and thus solutions, for these types of

[33]Systems of the form 5.106 require similar solvers. The objective function becomes a residual value calculated at some internal or boundary points from $\boldsymbol{g}$.

systems is parameter continuation. This method is based on the implicit function theorem, which states that when a solution of equation 5.105 is known at some point $(\boldsymbol{y}^*, \lambda^*)$, $\boldsymbol{f}$ is continuously differentiable on its domain, and $\boldsymbol{J}$ is non-singular, then

$$\boldsymbol{y} = \boldsymbol{F}(\lambda) \tag{5.110}$$

and

$$\boldsymbol{J}\frac{d\boldsymbol{y}}{d\lambda} + \boldsymbol{f}_\lambda = 0 \tag{5.111}$$

$\boldsymbol{F}$ is also unique and continuously differentiable over some range $\lambda_1 < \lambda < \lambda_2$. [48] In other words, the solution is a unique function of λ in the vicinity of the known solution and simple integration along $\frac{d\boldsymbol{F}}{d\lambda}$ will give solutions of $\boldsymbol{F}$ and therefore $\boldsymbol{f}$ as a function of λ. These methods work well when the implicit function theorem conditions hold, but nonlinear systems are capable of forming multiple solutions that lead to singularities in the Jacobian matrix, $\boldsymbol{J}$. A point at which the number of solutions to equation 5.105 increases as λ passes through λ_o is termed a bifurcation point, as is generally any point where the Jacobian becomes singular. At these points, simple parameter continuation methods fail because there is no longer a unique tangent in the solution-parameter space to integrate along. One clever solution to the problems associated with bifurcation points is to reparameterize the solution and the parameter λ in a new variable s, where s is an arc-length in solution-parameter space.

$$(\frac{dy_1}{ds})^2 + (\frac{dy_2}{ds})^2 + ... (\frac{dy_n}{ds})^2 + (\frac{d\lambda}{ds})^2 = 1 \tag{5.112}$$

This new relationship allows one to specify a step in arc-length and then calculate the resulting $\boldsymbol{y}$ and λ. By stepping forward in s instead of in λ, it is possible to trace out turning points and other bifurcations that might be missed by simple parameter con-

tinuation. [58] These algorithms can be quite robust, often continuing directly through bifurcation points. If all of the solutions are desired, one must monitor the Jacobian in order to catch the possible bifurcation points. Often, test functions are constructed so that bifurcation points can be flagged during continuation. If flagged, an algorithm can return to them at the end of a solution curve and branch switch to the other solution so that all solutions emanating from that point can be found. Since bifurcation points represent singularities in the Jacobian, common test functions include products of successive eigenvalues (which would typically be negative when a bifurcation existed in between two solution points), the maximum eigenvalue (which tends to be continuous and which changes sign at singularities), or simply the determinant of the Jacobian (which is zero at a singularity). There is not a correct method, as each one represents some trade-off between computational effort and accuracy.

It is typically advantageous to have some knowledge of the solution before building a solution algorithm. For example, some systems are much more unstable to shooting methods in one direction relative to the other. [59, 60] This situation arises when a required boundary value is near an unstable node. As one shoots closer and closer to the unstable node, the precision requirement of the initial guess approaches infinite precision. This feature works for you in the other direction, wherein a large range of inital guesses converge to similar solutions on the other side of the domain. Also, discretization of the problem into smaller pieces where the nonlinearities are especially prevalent can improve stability if one knows where these discretizations should be located.

5.E History of the Film Model

The film model description of phase interfaces was a contentious literature topic for 30-40 years after Whitman's paper. [4] Most discussion challenged the assumption

that a stagnant film with exactly zero convective effects could actually exist near a real interface. The first surface renewal theory claimed that a stagnant film initially exists, but is replaced by material of the bulk composition after some time θ. [5] In this film model variant, any extension to account for multicomponent or reaction effects must consistently account for time variations on time-scales $< \theta$ that average out on time-scales $> \theta$. This idea was further pursued by Danckwerts in 1951 by allowing the stagnant films to have some distribution of times before replacement, instead of some constant value θ. [61] Both of these models still require only one fitted parameter per phase, although other methods have been proposed since that require additional parameters or correlations. King proposed a model in 1966 that added an "eddy diffusivity" to the diffusive flux definition that had an increasing role in transport at increasing distances from the interface. [62] Another proposal discussed in 1955 [6] and 1961 [63] suggested that the convective "surface renewal" need not happen in all or nothing bursts. Perhaps a piece of the stagnant film could be replaced by bulk fluid without replacing the entirety of the film, leading to concentration discontinuities and higher instantaneous (but quickly decaying) transfer rates after replacement. In 1962, another paper discussed a similar process, but with a different frequency of displacement. [64] After much study by the authors mentioned above (and many others), it was generally accepted that the one parameter models matched experimental results within the error limits of the physical properties that were used for the calculations. [7] Therefore, the two parameter models do not provide enough additional resolution to justify the additional complexity or need for empirical data. It was also found that the surface renewal models (that only require one parameter) give surprisingly similar results to the easier to generalize stagnant film model when the component diffusivities are the same, but that the surface renewal models are likely more accurate when the component diffusivities differ. [12]

Bibliography

[1] R. Taylor and D. R. Webb. Film models for multicomponent mass transfer; computational methods: The exact solution of the maxwell-stefan equations. *Computers & Chemical Engineering*, 1981.

[2] R. Krishna. Diffusion in multicomponent electrolyte systems. *The Chemical Engineering Journal*, 35:19–24, 1987.

[3] P. Wang, A. Anderko, and R. D. Young. A speciation-based model for mixed-solvent electrolyte systems. *Fluid Phase Equilibria*, 203:141–176, 2002.

[4] W. G. Whitman. *Chem. and Met. Eng.*, 147:23, 1923.

[5] R. Higbie. The rate of absorption of a pure gas into still liquid during short periods of exposure. 1935.

[6] P. Danckwerts. Gas absorption accompanied by chemical reaction. *AIChE J.*, 1955.

[7] P. Danckwerts. *Gas-Liquid Reactions*. McGraw-Hill, 1970.

[8] M. L. McCabe, J. C. Smith, and P. Hrriott. *Unit Operations of Chemical Engineering*. McGraw Hill, 2005.

[9] S. H. Fogler. *Elements of Chemical Reaction Engineering*. Prentice Hall, 2006.

[10] A. Fick. On liquid diffusion. *Philosophical Magazine Series 4*, 10:30–39, 1855.

[11] J. Maxwell. On the dynamical theory of gases. *Philosophical Transactions of the Royal Society of London*, 157:49–88, 1867.

[12] R. Taylor and R. Krishna. *Multicomponent Mass Transfer*. Wiley New York, 1993.

[13] H. L. Toor. Diffusion in three-component gas mixtures. *AIChE J.*, page 198, 1957.

[14] L. Smith and R. Taylor. Film models for multicomponent mass transfer: A statistical comparison. *Industrial & Engineering Chemistry Research*, 22:97–104, 1983.

[15] Y. Lin, A. ten Kate, M. Mooijer, J. Delgado, P. L. Fosbol, and K. Thomsen. Comparison of activity coefficient models for electrolyte systems. *AIchE J.*, 56(5):1334–1351, 2010.

[16] A. Anderko and M. M. Lencka. Modeling self-diffusion in multicomponent aqueous electrolyte systems in wide concentration ranges. *Industrial and Engineering Chemistry Research*, 37(7):2878–2888, 1998.

[17] X. Liu, T. J. Vlug, and A. Bardow. Predictive darken equation for maxwell-stefan diffusivities in multicomponent mixtures. *Industrial & Engineering Chemistry Research*, 50(17):10350–0358, 2011.

[18] S. Hatta. Technical reports. Technical report, Tohoku Imperial University, 1928.

[19] S. Hatta. Technical reports. Technical report, Tohoku University, 1933.

[20] E. Thiele. Relation between catalytic activity and size of particle. *Industrial & Engineering Chemistry Research*, 1939.

[21] Payne and Dodge. Rate of absorption of carbon dioxide in water and in alkaline media. 1932.

[22] T. Graham. On the motion of gases. *Philosophical Transactions of the Royal Society of London*, 136:573–631, 1846.

[23] T. Graham. On the molecular mobility of gases. *Philosophical Transactions of the Royal Society of London*, 153:385–405, 1863.

[24] A. Einstein. *Ann. der Physik*, 17:549, 1905.

[25] J. C. Maxwell. *The Scientific Papers of James Clerk Maxwell*. Dover Publications, 2003.

[26] J. Stefan. Über das gleichgewicht und die bewegung, insbesondere die diffusion von gasgemengen. *Proceedings of the Imperial Academy of Sciences Vienna*, 63:63–124, 1871.

[27] H. L. Toor. Dual diffusion-reaction coupling in first order multicomponent systems. *Chem. Eng. Sci.*, 20:941–951, 1965.

[28] L. Onsager. Reciprocal relations in irreversible processes. i. *Physical Review*, 37:405–426, 1931.

[29] H. A. Kooijman and R. Taylor. Estimation of diffusion coefficients in multicomponent liquid systems. *Industrial & Engineering Chemistry Research*, 30:1217–1222, 1991.

[30] D. Leaist. Ternary diffusion coefficients of 18-crown-6 ether-kcl-water by direct least-squares analysis of taylor dispersion measurements. *J. Chem. Soc. Faraday Trans.*, 74:597–601, 1991.

[31] S. Rehfeldt and J. Stichlmair. Measurement and calculation of multicomponent diffusion coefficients in liquids. *Fluid Phase Equilibria*, 256:99–104, 2007.

[32] A. Leahy-Dios, B.-A. M.M., J. K. Platten, and A. Firoozabadi. Measurements of molecular and thermal diffusion coefficients in ternary mixtures. *The Journal of Chemical Physics*, 122, 2005.

[33] Y. Kim and A. S. Myerson. Diffusivity of protein in aqueous solutions. *Korean J. Of Chem. Eng.*, 13:288–293, 1996.

[34] H. T. J. Cullinan and H. L. Toor. Diffusion in the three-component liquid system acetone-benzene-carbon tetrachloride. *The Journal of Physical Chemistry*, 69:3941–3949, 1965.

[35] J. Wei. Irreversible thermodynamics in engineering. *Industrial and Engineering Chemistry*, 58:55–60, 1966.

[36] S. R. de Groot and P. Mazur. *Non-equilibrium Thermodynamics*. North-Holland Publishing Company, 1962.

[37] R. B. Bird, W. E. Stewart, and E. N. Lightfoot. *Transport Phenomena*. John Wiley and Sons, 2007.

[38] C. Curtiss and R. B. Bird. Multicomponent diffusion. *Industrial & Engineering Chemistry Research*, 38:2515–2522, 1999.

[39] M. F. Doherty and J. D. Perkins. Properties of liquid-vapor composition surfaces at azeotropic points. *Chem. Eng. Sci.*, 32:1112–1114, 1977.

[40] W. E. Stewart and R. Prober. Matrix calculation of multicomponent mass transfer in isothermal systems. *I & EC Fundamentals*, page 224, 1964.

[41] T. Davis. Completeness theorem for a product of self-adjoint matrices. *Chem. Eng. Commun.*, 41:267–270, 1986.

[42] H. J. Merk. *Applied Scientific Research*, A8:73–79, 1959.

[43] J. S. Newman. *Electrochemical Systems*. Prentice Hall, 2 edition, 1991.

[44] S. G. Gadewar, M. F. Doherty, and Malone. A systematic method for reaction invariants and mole balances for complex chemistries. *Computers and Chemical Engineering*, 25:1199–1217, 2001.

[45] S. B. Gadewar, M. F. Doherty, and M. Malone. Reaction invariants and mole balances for plant complexes. *Industrial & Engineering Chemistry Research*, 41:3771–3783, 2002.

[46] K. G. Denbigh. *The Principles of Chemical Equilibirum*. Cambridge University Press, 1981.

[47] M. S. Shell. *Thermodynamics and Statistical Mechanics: An Integrated Approach*. Cambridge University Press, 2015.

[48] R. Seydel. *Practical Bifurcation and Stability Analysis*. Springer Science & Business Media, 2009.

[49] D. D. Morrison. Multiple shooting method for two-point boundary value problems. *Numerical Analysis*, 1963.

[50] L. Graney. The numerical solution of unstable two point boundary value problems. *Journal of Computational and Applied Mathematics,*, 3, 1977.

[51] R. D. Russell and L. F. Shampine. A collocation method for boundary value problems. *Numerische Mathematik*, 19:1–28, 1971.

[52] G. D. Smith. *Numerical Solution of Partial Differential Equations: Finite Difference Methods*. Oxford University Press, 1985.

[53] J. Chaskalovic. *Finite element methods for engineering sciences: theoretical approach and problem solving techniques*. Springer, 2008.

[54] M. Chiplunkar, M. Hong, M. F. Malone, and M. F. DOherty. Experimental study of feasibility in kinetically-controlled reactive distillation. *AIChE J.*, 51, 2003.

[55] H. B. Keller. Numerical solution of bifurcation and nonlinear eigenvalue problems. *Applications of bifurcation theory*, pages 359–384, 1977.

[56] T. Coleman and Y. Li. An interior, trust region approach for nonlinear minimization subject to bounds. *SIAM Journal on Optimization*, 6:418–445, 1996.

[57] J. J. More. *Numerical Analysis*. Springer, 1977.

[58] M. Kubicek. Algorithm 502 dependence of solution of nonlinear systems on a parameter. *ACM Transactions on Mathematical Software*, 2(1):98–107, 1976.

[59] C. A. N. R. Varma, A. Georgakis and R. Aris. Computational methods for te tubular reactor. *Computer Methods in Applied Mechanics and Engineering*, 8:319–330, 1976.

[60] J. Lee and K. D.H. An improved solution method for computation of effectiveness factors in porous catalysts. *Chem. Eng. Sci.*, 2005.

[61] P. Danckwerts. Significance of liquid-film coefficients in gas absorption. *Industrial & Engineering Chemistry Research*, 1951.

[62] C. King. Diffusivities of slightly soluble gases in water. *AIChE J.*, 1964.

[63] S. P. S. Andrew. *Alta Technologia Chimica, Processi di Scambio*. Academia Nazionale dei Lincei, Roma, 1961.

[64] Harriott. A random eddy modification to the penetration theory. *Chem. Eng. Sci.*, 1962.

Chapter 6

Membrane bubble column reactor model for the production of hydrogen by methane pyrolysis

6.1 Introduction

Fossil fuels combust in air to release heat, water, and CO_2. In contrast, hydrogen combustion exclusively emits heat and water. Historically, hydrogen has been produced for and primarily utilized as a chemical intermediate, but it may find new utility as an energy-carrier molecule in the 21st century due to this carbon emission advantage. Most hydrogen is currently produced by steam reforming of methane followed by water gas shift (SMR). The combined chemistry is Reaction 6.1.

$$CH_{4(g)} + 2H_2O_{(l)} \rightleftharpoons 4H_{2(g)} + CO_{2(g)} \qquad \Delta g^{o}_{rxn} = 131 \text{ KJ/mole} \quad \Delta h^{o}_{rxn} = 253 \text{ KJ/mole} \tag{6.1}$$

Stoichiometric conversion generates 1 mole of CO_2 per 4 moles of hydrogen produced. In practice, more CO_2 is emitted per hydrogen produced because some fraction of the feed methane or of the hydrogen product must be combusted to compensate for the endothermic heat of reaction. Industrial hydrogen produced by SMR costs $\approx$ 1.1 \$/kg to produce when natural gas costs 3 \$/MMBTU (a typical cost for 2017). This converts to $\approx$ 7.8 \$/GJ)[1], which is $\approx$ 2-3 times as expensive as the methane it was produced from (2.8 \$/GJ). [1] Including the compression and transportation costs (and ignoring taxes), hydrogen from SMR (37 \$/GJ) is $\approx$ 2.3 times as expensive as the most common transportation fuel in the US, gasoline (16 \$/GJ). [2] These comparisons overstate the effective price differences because hydrogen may be utilized in fuel cells, whereas gasoline must be combusted in an engine. Fuel cells are not limited by the Carnot efficiencies that limit heat to work engines, so fuel cells tend to extract more useful work from a fuel than could be extracted from a heat to work cycle. Therefore, the difference in price per useful work extracted is lower than the difference in price per primary energy available. In fact, the fuel cell electrical efficiency can be as much as twice as high as the hydrocarbon heat to work efficiency associated with a similar application, as evidenced by the high miles per gallon-equivalent (mpg-e) ratings earned by hydrogen fuel cell electric vehicles. For example, the Toyota Mirai's combined city/highway mpg-e is 66.

It is conceivable that the barriers to hydrogen utilization as an energy carrier (price and production emissions) may be ameliorated to some extent by pursuing new methods of hydrogen production. For example, hydrogen gas may also be produced by methane pyrolysis.

$$CH_{4(g)} \rightleftharpoons 2H_{2(g)} + C_{(s)} \qquad \Delta g^{o}_{rxn} = 51 \text{ KJ/mole} \quad \Delta h^{o}_{rxn} = 75/\text{KJ/mole} \tag{6.2}$$

[1] Conversion factors are $\Delta H_c = 285.5$ KJ/mole and $M_w, H_2 = 2.016$g/mole.

The thermal decomposition of methane to form hydrogen is potentially advantageous because oxygen is never required in the reaction zone, guaranteeing that solid carbon forms instead of CO_2. [3] Early methane pyrolysis studies focused on high temperatures (>1000 °C) because increasing temperature increases equilibirum conversions and gas phase reaction rates. [4–7] Later, investigators began promoting the reaction on metal catalysts, enabling appreciable conversions at lower temperatures. [8–10] The catalysts increase reaction rates, but the solid carbon produced by these processes deposits on the catalyst, rapidly deactivating it. The coked catalyst (or in the case of uncatalyzed reactors, the coked reactor wall) requires oxidation for reactivation, emitting CO_2.

The CO_2 emissions associated with the reactor/catalyst de-coking steps might be avoided by designing a molten metal bubble column pryolysis reactor. [3, 11–19] A rising gas bubble generates convective flows near the gas/melt interface, removing solid carbon from the reaction zone as it forms. In fact, it has been reported that the solid carbon suspends in and bouyantly rises up through the melt phase within the reactor, eventually settling on top of the molten metal layer. It may be possible to mechanically separate the carbon from this surface layer as it accumulates, allowing a continuous gas phase flow into and a gas and solid flow out of the reactor. [1, 3, 11–20]

More recently, investigators have begun to use molten metal solvents not only as a carbon separation tool but also as a catalyst. [21, 22] In these molten metal bubble column reactors, catalyic activity is imparted from the molten metal/gas interface and reaction rates are observed in excess of the rates expected from the gas phase chemistry alone. Furthermore, hydrogen is more soluble in many molten metals than methane. This solubility difference may enable reactive separation in which hydrogen is passively transported away from the reaction zone as it is produced, potentially driving reaction conversions past the equilibrium conversion implied by a set of feed compositions, reactor operating parameters, and reaction equilibrium thermodynamics.

Emissionless hydrogen may also be attainable by retrofitting existing SMR plants with CCS, but it seems prudent to simultaneously pursue methane pyrolysis process development for at least two reasons. First, neglecting the compression and transportation costs, hydrogen produced by SMR is $\approx$ 2-3 times as expensive as natural gas, and a CCS retrofit would further increase the cost of hydrogen production. SMR has been practiced industrially for decades, so one can reasonably assume that the technology is unlikely to experience disruptive efficiency gains that drastically change the realtionship between feed and product prices in the future. Alternatively, it is unknown at this time how efficiently a MP process might convert methane to hydrogen, and so it remains possible that it could be competetive with SMR, especially since it is thermodynamically possible that a well designed MP process could produce hydrogen at comparable prices (See Chapter 2). In fact, a recent study that compared the projected costs of greenfield MP to conventional SMR suggested that even an uncatalytic molten metal MP process might produce hydrogen at comparble costs to SMR. [20] Second, methane pyrolysis produces a solid carbon that may or may not have economic value, whereas SMR produces carbon that definitively carries a negative value (CO_2). Even in a worst case scenario for MP, a "zero value" solid carbon might be cheaper to dispose of than high pressure CO_2.

Molten metal methane pyrolysis presents an abundant design problem with many interesting trade-offs. Higher temperatures yield higher equilibrium conversions (by Le Chatelier's principle) and reaction rates, but also increase the costs of materials of construction. Increasing pressure increases reaction rates and reduces equipment sizes, but it simultaneously decreases equilibrium conversions (by Le Chatelier's principle) and increases costs of construction. Lower conversions lead to larger equipment sizes and to a gaseous product mixture that requires downstream purification. When viewed as an optimization problem, there are likely multiple local cost minima corresponding to multiple reasonable early design decisions with respect to these trade-offs. It is difficult to ratio-

nally analyze these trade-offs at this time because some of these choices have unknown impacts on the final cost of production.

For example, one especially challenging yet unresolved process design question relates to removing and cleaning the solid carbon. Molten metals have non-negligible vapor pressures at the temperatures required for methane pyrolysis. This leads to vaporized metal accumulating in the reactor headspace, eventually depositing on the surface of solid carbon particles floating on top of the molten melt. This is problematic because any end use for the solid carbon requires a vanishingly small metal fraction and moreover, any metal lost on the carbon must be replaced in the reactor. Depending on the metal solvent chosen and the rate of metal loss, the replacement cost could be significant. Many molten salts are less dense than molten metals, and molten salts tend to have much lower (effectively zero) vapor pressures. These two properties make molten salt caps an effective tool to reduce the molten metal vapor pressure in the reactor headspace. In fact, collaborators have demonstrated that molten salt caps decrease the amount of metal deposited on the solid carbon. [23] Unfortunately, this seems to ameliorate but not eliminate the problem because vaporized metal is carried through the salt cap inside the gas bubbles. Therefore, the salt cap reduces, but does not eliminate the steady-state, molten metal vapor pressure in the reactor headspace. This presents a design challenge because one expects that metal contaminated carbon must be "cleaned" prior to disposal or sale, and yet this cleaning step has not yet been sufficiently characterized such that a reliable cost estimate (capital, operating, environmental, etc.) can be generated.

So a bifurcation in design space is presented: Can any design solution that mitigates the carbon cleaning issue in an environmentally friendly manner be assumed to be superior to one that leaves the carbon cleaning as an uncharacterized post processing step? At this stage, this question cannot be answered with any confidence. Implicitly ignoring the post-processing challenge leads to the conclusion that MP can compete directly

with SMR under a set of reasonable assumptions and market conditions. [1] Here, a design is considered that explicitly avoids the post-processing complications by utilizing a membrane separation within the reactor. Both approaches (assuming the post-process cleaning is easy and cheap versus assuming it is prohibitively expensive and must be avoided) can be pursued simultaneously until the time at which enough is known about both sets of processes that one can be determined to be definitively superior.

Imagine a reactor constructed from a hydrogen-permeable membrane and operated at elevated pressure. This reactor could be designed to utilize reactive separation to achieve full conversion (even past equilibrium), simultaneously removing all of the generated hydrogen from the reactor before gas bubbles can break through the top of the molten metal phase. If such a reactor were constructed, the molten metal vapor pressure in the headspace above the molten salt cap might be reduced to zero, and the produced carbon might be entirely free of metal contamination after buoyantly rising through the salt cap. Here, a reactor model is described and then utilized to illustrate that this reactor design is possible with conservative estimates of membrane and molten metal properties. This reactor model also applies to non-membrane reactors with minor modification, so it enables future studies that can explore all of the design trade-offs discussed above. When membrane (permeability, selectivity, cost, etc.) and melt properties (catalytic, solubility, density, cost, etc.) are better characterized, this reactor model will further enable a direct comparison of hydrogen production costs from MP to the hydrogen production costs of SMR.

6.2 Molten metal pyrolysis reactor model

Consider the isothermal, molten metal reactor presented schematically in Figure 1. Gaseous bubbles containing methane enter the reactor at $z = 0$ and flow up through the

stagnant molten metal solvent towards the end of the reactor volume at $z = h$. The only important chemical reaction is Reaction 6.2. The reactor is assumed to be radially well-mixed in both the melt and gas phase, but concentration gradients are anticipated in the axial (z) direction. The solid carbon that is formed floats to the top of the reactor, enters the salt cap phase, and is mechanically separated from the molten salt.

In general, each component is capable of fluxing across the phase boundary between gas bubbles and the molten metal phase, but only the hydrogen interphase flux is explicitly considered for several reasons. First, methane typically exhibits a much lower metal solubility than hydrogen, so treating methane solubility as if it were zero simplifies the analysis without introducing significant error. Atomic carbon likely exhibits intermediate melt phase solubility (relative to methane and hydrogen), but the phase distribution of carbon cannot be quantified without explicitly characterizing and modeling the precipitation kinetics. These precipitation kinetics have not yet been characterized experimentally, and so the additional model complexity associated with explicitly modeling the precipitation via a coupled population balance model cannot be justified at this time. Therefore, the carbon is assumed to immediately become a solid particle as it is formed. This must be (net) true at steady-state, because the mechanical removal of solid carbon from the top of the reactor is the only carbon removal mechanism considered in Figure 6.1 and the carbon cannot accumulate at steady-state.

At expected temperatures of operation, mass transport is fast enough inside the gas bubbles that significant intra-bubble gas phase concentration gradients are not expected to persist, and therefore, all of the resistance to inter-phase mass transport is on the melt side. The simplest, thermodnamically consistent functional form for the interphase hydrogen flux is a mass transport coefficient multiplied by the difference between the saturation concentration and the actual melt phase concentration, where the saturation concentration is assumed to be proportional to the square root of the partial pressure of

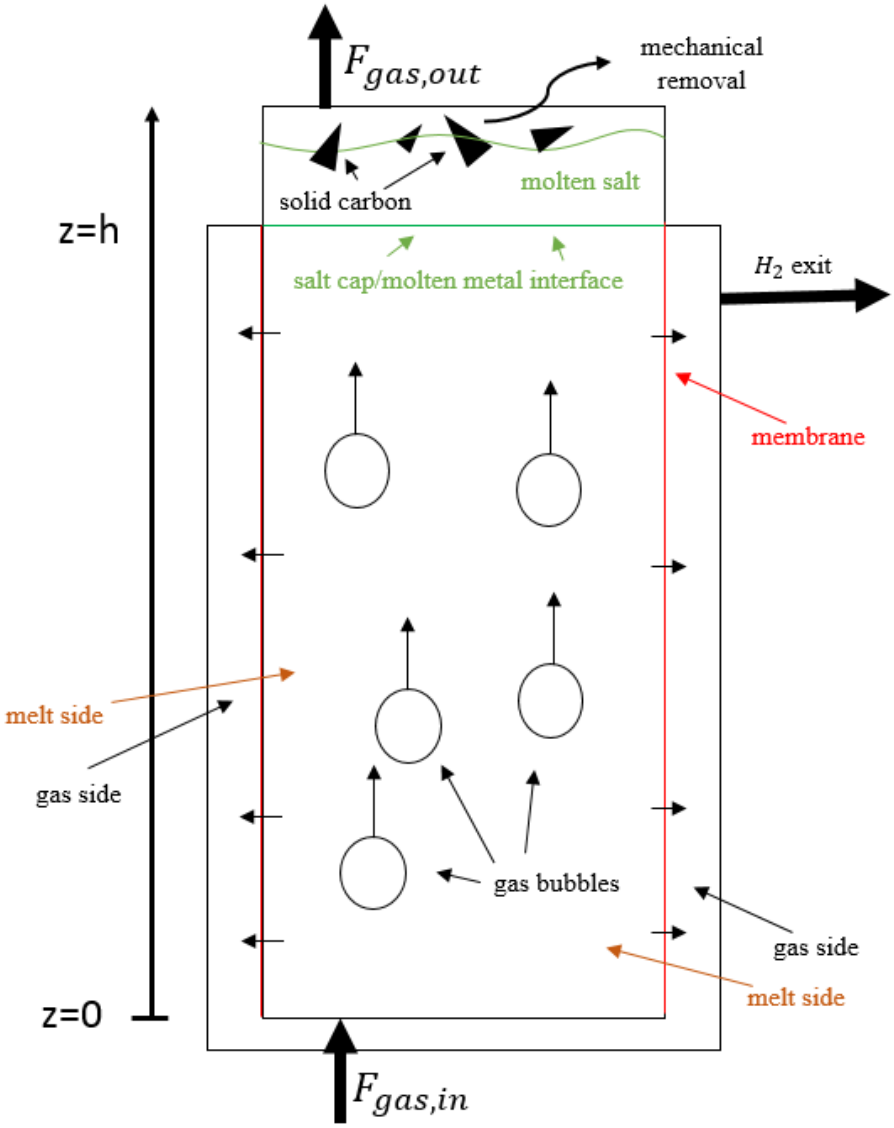

Figure 6.1: Schematic representation of a molten metal membrane/bubble column reactor. The red lines indicate a reactor wall constructed from a membrane material. The black vessel surrounding the bubble column collects the hydrogen as it evacuates the active reactor space across the membrane. As the bubbles rise through the column, hydrogen passively transports from the gas bubbles to the melt phase and then from the melt phase across the membrane walls. In general, some fraction of the gas exits from the top of the reactor, with the balance exiting through the membrane/reactor walls. The model equations presented in this chapter describe how both the fraction of the gas that exits by each of these mechanisms and the gas phase mole fractions in each exit stream vary as functions of design and operation decisions.

hydrogen in the gas bubbles (Sievert's law). [24] This inter-phase flux is named J_{m,H_2}. It is defined in Equation 6.3 such that a positive flux is a flux out of the gas phase and into the melt phase.

$$J_{m,H_2} = k_t\left[P_{H_2}^{1/2} K_H - C_{H_2}\right] \tag{6.3}$$

K_H is the Sievert's law constant that relates the square root of the hydrogen partial pressure in the bubbles to the hydrogen solubility within the melt phase. J_{m,H_2} varies along the length of the reactor in response to changes in the gas phase partial pressure and the melt phase hydrogen concentration. P_{H_2} is the partial pressure of hydrogen in the gas bubbles, and C_{H_2} is the concentration of hydrogen in the melt phase.

In Figure 6.1, the red lines represent a reactor wall constructed of a membrane material that is permeable to hydrogen. If the reactor wall is permeable to hydrogen, then mass transport will occur between the the melt phase on the melt side of the membrane and the gaseous phase on the gas side of the membrane. The same Sievert's law constant describes the equilibrium condition between the melt phase hydrogen concentration and the hydrogen partial pressure across the membrane. The simplest possible constitutive law for describing the relationship between the states of the reactor and the flux across the membrane walls is to assume that the flux is proportional to the thermodynamic driving force as shown in Equation 6.4.

$$J_{mem,H_2} = k_m\left[P_m^{1/2} K_H - C_{H_2}\right] \tag{6.4}$$

P_m represents the partial pressure of hydrogen on the gas side of the membrane. This expression is written such that a positive value of J_{mem,H_2} indicates a flux into the melt phase. For the calculations shown here, the hydrogen permeability (k_m) is assumed to be 9.45×10^{-4} m/s. This permeability estimate is explained in Appendix 6.B.

When the gas phase hydrogen partial pressure is higher inside the gas bubbles than it is on the gas side of the membrane, it is possible for the melt phase to be supersaturated with respect to the hydrogen on the gas side of the membrane while simultaneously being undersaturated with respect to the hydrogen in the bubbles. In this case, hydrogen will passively transport from the gas bubbles into the melt, while simultaneously evacuating the melt across the membrane. This situation is depicted schematically in Figure 6.2. Fluxes into and out of the melt phase generate melt phase hydrogen concentration

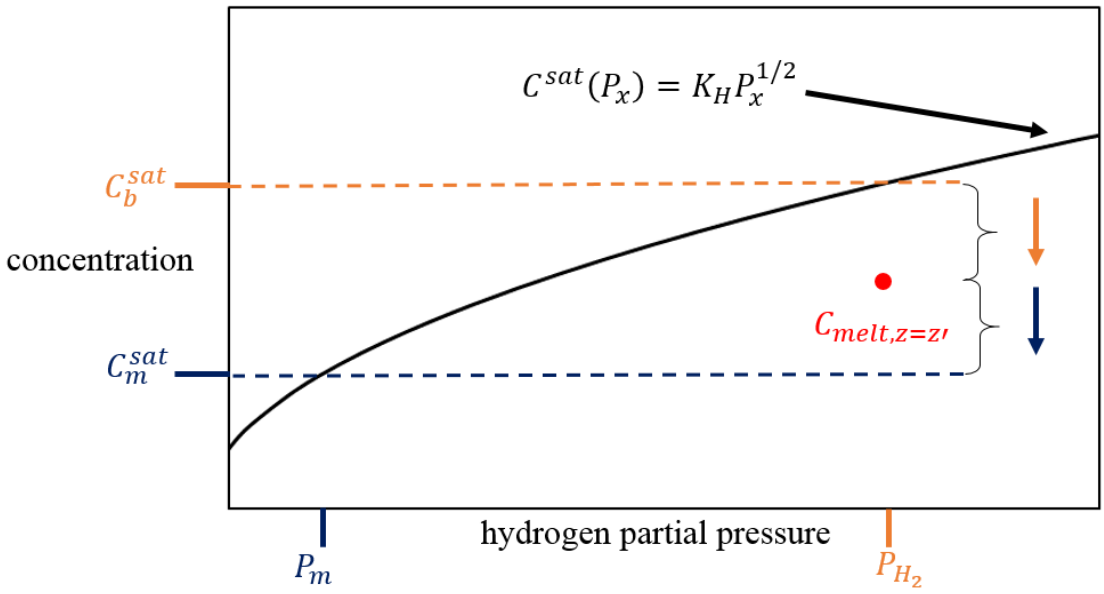

Figure 6.2: A schematic hydrogen solubility diagram. The black curve is the melt hpase solubility of hydrogen implied by a Sievert's law constatn, K_H. P_x represents any hydrogen partial pressure that is contacted by the melt phase. Following the notation in this dissertation, P_{H_2} is the hydrogen partial pressure in the bubble phase and P_m is the hydrogen partial pressure on the gas side of the membrane. The red dot marks a possible melt phase concentration that is simultaneously below the solubility implied by P_{H_2} but above the solubility implied by P_m. This situation generates simultaneous transdport from the bubbles to the melt phase and from the melt phase across the membrane.

gradients along the axial direction that passively dissipate via molecular diffusion (along the z axis in Figure 6.1). The melt phase is dilute enough such that Fick's first law is a suitable description of the melt phase diffusion. Therefore, the diffusive flux (J_{z,H_2}) is

defined in Equation 6.5.

$$J_{z,H_2} = -D\frac{dC_{H_2}}{dz} \tag{6.5}$$

6.2.1 Reaction rate laws

Methane pyrolysis occurs in the gas phase in the absence of catalysis. Extensive literature review suggests that the most trustworthy reaction kinetics are the ones reported in Napier et. al. [7]. This choice is justified and discussed in Appendix 6.B.5

$$r_{gas} = \frac{k_{f,g}}{RT}\left[P_{CH_4} - \frac{1}{K_{eq}}P_{H_2}^2\right] \tag{6.6}$$

The units of $k_{f,g}$ are 1/s, such that r_{gas}/RT has units of moles/pressure/volume/time. The quantity $k_{f,g}$ has an Arrhenius dependence with an activation energy of 391.6 KJ/mole and an exponential prefactor of 3.8 $\times 10^{13}$ s^{-1}. To convert the reaction rate per gas volume to a reaction rate per reactor volume, r_{gas} must be multiplied by the bubble volume fraction, ϕ_g.

$$r_{catalyzed} = \frac{k_{f,m}}{RT}\left[P_{CH_4} - \frac{1}{K_{eq}}P_{H_2}^2\right] \tag{6.7}$$

The melt-phase catalysis mechanism and its relation to the gas phase reaction mechanism are not yet fully understood, but the catalyzed reaction rate is hypothesized to be proportional to the amount of melt/gas interfacial area such that $k_{f,m}$ has units of volume/area/time and $k_{f,m}/RT$ has units of moles/pressure/area/time. Here, the activation energy and kinetic prefactor are estimated to be 207.1 KJ/mole and 7.16$\times 10^6$ mL/cm^2/s based on the data reported in studies of a 27 mole % Ni/Bi melt [22] and the discussion in Section 6.3. To convert the reaction rate per gas/melt interfacial surface area to a reaction rate per reactor volume, $r_{catalyzed}$ must be multiplied by the reactive

surface area per unit reactor volume, a^i. The reverse reaction mechanism and rate law have not yet been well characterized experimentally, but very close to equilibrium, the reverse reaction rate must be proportional to $P_{H_2}^2$ for the overall reaction rate law to be consistent with reaction equilibrium thermodynamics. Since both reaction rate laws have identical partial pressure dependencies, they can be combined into a single rate law with a forward rate constant that depends on the melt/gas interfacial area per unit reactor volume (a_i) and the bubble volume fraction (ϕ_g). Therefore, the total reaction rate on a moles/s/volume of reactor basis can be written as Equation 6.8.

$$R = \left(\frac{k_{f,m}a^i}{RT} + \frac{k_{f,g}\phi_g}{RT}\right)\left[P_{CH_4} - \frac{1}{K_{eq}}P_{H_2}^2\right] \tag{6.8}$$

These reaction rate laws depend on the component partial pressures. The total pressure varies with reactor height due to the hydrostatic head created by the melt phase effective density.

$$\frac{dP_z}{dz} = -\rho g(1-\phi_g) \tag{6.9}$$

$$P_z(z=0) = P_0 \tag{6.10}$$

where P_0 is the total pressure at the reactor entrance, ρ is the molten metal density, ϕ_g is the gas phase volume fraction, and g is the gravitational constant.

6.2.2 Gas phase volumetric and surface area distributions: ϕ_g and a^i

Both the catalyzed reaction rate and the interphase hydrogen transport rate are proportional to the melt/gas phase contact area per unit reactor volume (a^i), and the gas phase reaction rate is proportional to the gas phase volume fraction (ϕ_g). Modeling

this reactor requires quantifying the relationships among the gas/liquid surface area, the total gas volume, and the total reactor volume. The reactor volume (V_r) is assumed to be known. The total gas hold up within a bubble column reactor is the product of the total volumetric flow rate into the reactor (assumed known) and the gas phase residence time. The gas phase residence time depends only on the height of the reactor and the linear speed of the gas bubbles through the reactor. The speed at which gas bubbles rise through molten metals can be estimated from correlations or determined experimentally for a specific reactor/melt system. [25] The amount of gas/melt surface area per unit reactor volume depends on the type of bubble distributor used and the general hydrodynamics within the reactor. It is typically estimated from correlations or measured for a specific distributor/column system. [26, 27]

Regardless of how one estimates these parameters, the model needs to account for how they change along the length of the reactor. There is an implicit relationship among the temperature, pressure, total number of moles, and the total volume the gas bubbles fill. When the total moles goes up due to reaction or down due to interphase transport, the volume needs to expand and contract. Similarly, a tall reactor generates a hydrostatic pressure drop along the height of the reactor. The lower pressures at the top of the column should lead to some volumetric expansion that affects both a^i and ϕ_g.

Here, the methods listed above are utilized to estimate the bubble generation rate, average bubble size, and linear velocity of bubbles entering the reactor ($\dot{B}$, r_b, u_b). Then, it is assumed that the bubble density does not change along the length of the reactor, but that the average bubble radius fluctuates to accommodate the changes in gas volume implied by the changes in state variables in accordance with the ideal gas law. Then, the surface area and volume distributions can be calculated from the known bubble density and the average bubble radius as a function of all the reactor states, which vary along the length of the reactor.

Given a total inlet molar rate ($F_{T,0}$), an inlet pressure (P_0), an inlet temperature (T_0), and an average bubble size at the reactor inlet ($r_{b,0}$), the inlet bubble rate ($\dot{B}$) can be calculated by Equation 6.11

$$\dot{B} = \frac{F_{T,0} R T_0}{P_0(\frac{4}{3}\pi r_{b,0}^3)} \tag{6.11}$$

where the "0" subscript indicates a quantity at the reactor inlet (i.e., $z = 0$). Assuming that gas phase volumetric changes manifest as changes in the average bubble size (i.e., bubble density doesn't change, and the ideal gas law holds), then Equation 6.12 defines the relationship between the average bubble size and the reactor states, where the z subscript denotes a quantity that changes along the length of the reactor.

$$r_{b,z} = \left(\frac{F_{T,z} R T_z}{P_z(\frac{4}{3}\pi)\dot{B}} \right)^{1/3} \tag{6.12}$$

Now that $r_{b,z}$ is defined, the only quantity still required to determine $\phi_{g,z}$ and a_z^i is the number of bubbles per unit volume of reactor (i.e., the bubble suspension density, ρ_b [number of bubbles/reactor volume]). The total number of bubbles within the reactor at a given time depends on the rate at which bubbles enter the reactor ($\dot{B}$), and the average time a bubble spends in the reactor. The average time spent in the reactor is the residence time (τ), which can be determined from the average linear bubble velocity and the reactor height

$$\rho_b = \frac{\dot{B}\tau}{V_r} \tag{6.13}$$

$$\phi_{g,z} = \rho_b \frac{4}{3}\pi r_{b,z}^3 \tag{6.14}$$

$$a_z^i = \rho_b 4\pi r_{b,z}^2 \tag{6.15}$$

where a z subscript indicates a quantity that varies along the reactor height coordinate and τ is calculated from the linear bubble velocity and total reactor height (h) as described above. Now that $\phi_{g,z}$ ans a_z^i have been defined as functions of the states of the model, the combined reaction rate expression can be re-written as Equation 6.16.

$$R = \left(\frac{k_{f,m}}{RT}\frac{\dot{B}\tau}{V_r}4\pi\left(\frac{F_{T,z}RT_z}{P_z(\frac{4}{3}\pi)\dot{B}}\right)^{2/3} + \frac{k_{f,g}}{RT}\frac{\dot{B}\tau}{V_r}\frac{4}{3}\pi\left(\frac{F_{T,z}RT_z}{P_z(\frac{4}{3}\pi)\dot{B}}\right)\right)\left[P_{CH_4} - \frac{1}{K_{eq}}P_{H_2}^2\right] \quad (6.16)$$

where $\dot{B}$, τ, and V_r are known from the reactor design and feed conditions, and everything else is defined as a function of reactor position in the model equations that follow. The rate parameters used here are calculated from [7, 22] and listed in Table 6.1.

	rate prefactor A	E_a
$k_{f,g}$; gas phase from [7]	3.8×10^{13} [s^{-1}]	392 [KJ/mole]
$k_{f,m}$; 27% NiBi molten metal from [22]	7.2×10^{6} [mL/cm^2/s]	207 [KJ/mole]

Table 6.1: The first order kinetic rate constant for the gas phase chemistry was taken from [7]. The melt phase catalyzed reaction rate constant was adapted from [22]. Both rate laws follow the standard Arrhenius form where $k_{f,k} = Ae^{-\frac{E_a}{RT}}$.

6.2.3 Material Balance ODEs

Now that all of the important physicochemical rates have been described, a set of model equations can be constructed. A material balance can be written on each component in each phase, resulting in Equations 6.17-6.19.

$$\text{Gas phase } CH_4 \text{ balance}: \quad \frac{1}{A_c}\frac{dF_{CH_4}}{dz} = -R \quad (6.17)$$

$$\text{Gas phase } H_2 \text{ balance}: \quad \frac{1}{A_c}\frac{dF_{H_2}}{dz} = 2R - J_{m,H_2}a^i \quad (6.18)$$

$$\text{Melt phase } H_2 \text{ balance}: \quad -A_c D_{H_2}\frac{d^2C_{H_2}}{dz^2} = J_{m,H_2}a^i A_c + J_{mem,H_2}\pi d \quad (6.19)$$

where d is the reactor diameter, A_c is the reactor cross sectional area, and F_i denotes the gas bubble phase molar flow rate of component i in the z direction. This set of differential equations requires 4 boundary conditions (one for equation 6.17, one for Equation 6.18, and two for Equation 6.19):

$$F_{CH_4}(z=0) = F_{CH_4,feed} \tag{6.20}$$

$$F_{H_2}(z=0) = F_{H_2,feed} \tag{6.21}$$

$$-D_{H_2}\frac{dC_{H_2}}{dz}\bigg|_{z=0} = 0 \tag{6.22}$$

$$-D_{H_2}\frac{dC_{H_2}}{dz}\bigg|_{z=h} = 0 \tag{6.23}$$

where h signifies the maximum melt height in the reactor and $F_{i,feed}$ is the component i gas flow rate into the reactor at $z = 0$ in moles/time. The feed gas mixture (typically pure methane) enters the reactor at $z = 0$ through some gas distributor, generating gas bubbles within the melt phase. The hydrogen flux out of the reactor melt phase at $z = h$ is zero because $z = h$ is where the melt phase ends and the molten salt cap begins. The hydrogen is assumed to have negligible solubility in the molten salt phase, so the flux across the molten metal/molten salt phase boundary is negligible. If the reactor is not constructed from a membrane, then J_{mem,H_2} is zero for all z.

6.2.4 Nondimensionalization

The following characteristic dimensions are utilized to construct dimensionless equations. The subscript "c" is used to indicate a characteristic quantity whereas the subscript

"0" denotes the parameter value calculated at the reactor inlet.

$$F_c = F_{CH_4,feed} \tag{6.24}$$

$$V_c = V_{reactor} \tag{6.25}$$

$$z_c = h \tag{6.26}$$

$$C_{H_2,c} = K_H P_0^{1/2} \tag{6.27}$$

$$P_c = P_0 \tag{6.28}$$

$$a_c^i = a_0^i = \rho_b 4\pi r_{b,0}^2 = \rho_b 4\pi \left(\frac{F_{T,0} R T_0}{P_0 (\frac{4}{3}\pi) \dot{B}} \right)^{2/3} \tag{6.29}$$

$$\phi_{g,c} = \phi_{g,0} = \rho_b \frac{4}{3}\pi r_{b,0}^3 = \rho_b \frac{4}{3}\pi \left(\frac{F_{T,0} R T_0}{P_0 (\frac{4}{3}\pi) \dot{B}} \right) \tag{6.30}$$

$$\tag{6.31}$$

With these definitions, the dimensionless gas phase surface area per unit volume and gas phase volume fraction can be written as

$$\overline{a}_z^i = \left(\frac{\overline{F}_{T,z}}{\overline{F}_{T,0} \overline{P}_z} \right)^{2/3} \tag{6.32}$$

$$\overline{\phi}_{g,z} = \frac{\overline{F}_{T,z}}{\overline{F}_{T,0} \overline{P}_z} \tag{6.33}$$

where an overbar indicates a dimensionless quantity. Nondimensionalizing Equation 6.9 and combining it with the dimensionless material balance ODEs yields the following set

of dimensionless model equations.

$$\frac{d\overline{P}_z}{d\overline{z}} = -\beta\Big(\frac{1-\phi_{g,c}\overline{\phi}_{g,z}}{1-\phi_{g,c}}\Big) \tag{6.34}$$

$$\frac{d\overline{F}_{CH_4}}{d\overline{z}} = -Da\big(\overline{a}^i+\theta\overline{\phi}_g\big)\overline{P}_z\big[y_{CH_4}-\frac{\overline{P}_z}{\Gamma}y_{H_2}^2\big] \tag{6.35}$$

$$\frac{d\overline{F}_{H_2}}{d\overline{z}} = 2Da\big(\overline{a}^i+\theta\overline{\phi}_g\big)\overline{P}_z\big[y_{CH_4}-\frac{\overline{P}_z}{\Gamma}y_{H_2}^2\big] - Pe^{-1}\overline{a}^i\big[\overline{P}_z^{1/2}y_{H_2}^{1/2}-\overline{C}_{H_2}\big] \tag{6.36}$$

$$\frac{d^2\overline{C}_{H_2}}{d\overline{z}^2} = -\Omega\overline{a}^i\big[\overline{P}_z^{1/2}y_{H_2}^{1/2}-\overline{C}_{H_2}\big] - \xi\big[\overline{P}_m^{1/2}-\overline{C}_{H_2}\big] \tag{6.37}$$

The dimensionless boundary conditions are

$$\overline{P}_z(z=0) = 1 \tag{6.38}$$

$$\overline{F}_{CH_4}(z=0) = 1 \tag{6.39}$$

$$\overline{F}_{H_2}(z=0) = \overline{F}_{H_2,feed} \tag{6.40}$$

$$\frac{d\overline{C}_{H_2}}{dz}\Big|_{z=0} = 0 \tag{6.41}$$

$$\frac{d\overline{C}_{H_2}}{dz}\Big|_{z=1} = 0 \tag{6.42}$$

The non-dimensionalization introduces four dimensionless model parameters and five dimensionless groups/relative rates. First the parameters:

$$\beta = \frac{\rho g h(1-\phi_{g,c})}{P_0} \tag{6.43}$$

$$\Gamma = \frac{K}{P_0} \tag{6.44}$$

$$\overline{P}_m = \frac{P_m}{P_0} \tag{6.45}$$

- β is the dimensionless pressure gradient. It represents the fraction of the pressure at the reactor entrance that would be attributable to the hydrostatic head if the

gas phase volume fraction was a constant ϕ_{gc} along the length of the reactor. The actual pressure drop across the reactor depends on the average gas phase volume fraction instead of the inlet gas phase volume fraction ($\phi_{gc}\frac{\int_0^h \overline{\phi}_{g,z}dz}{h} \neq \phi_{gc}$). In the limit of an infinitely tall reactor, β approaches 1. For real reactors, β varies between 0 and 1.

- Γ is the dimensionless reaction equilibrium constant that appears in the reverse reaction rate expressions.

- $\overline{P}_m$ is the dimensionless partial pressure of hydrogen on the gas side of the membrane.

The dimensionless groups are defined and discussed next:

$$Da = \frac{k_{f,m}a_c^i P_0 V}{F_c} \tag{6.46}$$

$$\theta = \frac{k_{f,g}\phi_{g,c}}{RTk_{f,m}a_c^i} \tag{6.47}$$

$$\Omega = \frac{h^2}{D_{H_2}}k_t a_c^i \tag{6.48}$$

$$\xi = \frac{h^2\pi d k_m}{D_{H_2}A_c} \tag{6.49}$$

$$Pe = \frac{F_c}{k_t K_H P_0^{1/2} a_c^i V} \tag{6.50}$$

- The Damköhler number (Da) is a ratio of the process time to the reaction time. When this number is large, the reaction proceeds quickly relative to the rate of material flows through the device.

- θ is a ratio of the uncatalyzed gas phase reaction rate to the catalyzed reaction rate at the reactor entrance.

- Ω is a ratio of the intra-phase (melt) hydrogen transport time to the inter-phase

hydrogen transport times. When Ω is large, transport from gas to melt is fast and sustained melt phase axial gradients could be sustained.

- ζ is a ratio of the intra-phase (melt) hydrogen transport time to the cross membrane hydrogen transport times. When ζ is large, sustained intraphase (axial) hydrogen gradients will be large relative to the cross membrane gradients at steady state.
- The Pectlet number (Pe) is a measure of the ratio of the inter-phase diffusion time to the process time. When it is small, hydrogen approaches gas/melt phase equilibrium in the reactor.

6.2.5 Compact notation of system of equations

These equations can be re-written in terms of a state vector $\mathbf{u}$, in which $u_1 = \overline{F}_{CH_4}$, $u_2 = \overline{F}_{H_2}, u_3 = \overline{C}_{H_2}$, $u_4 = \frac{d\overline{c}_{H_2}}{d\bar{z}}$, and $u_5 = \overline{P}_z$. After transforming the second order

equation into two first order equations, the equations simplify to:

$$u_1' = -Da\left(\overline{a}^i + \theta\overline{\phi}_g\right)u_5\overline{R} \tag{6.51}$$

$$u_2' = 2Da\left(\overline{a}^i + \theta\overline{\phi}_g\right)u_5\overline{R} - Pe^{-1}\overline{a}^i\overline{J}_{melt} \tag{6.52}$$

$$u_3' = u_4 \tag{6.53}$$

$$u_4' = -\Omega\overline{a}^i\overline{J}_{m,H_2} - \xi\overline{J}_{mem,H_2} \tag{6.54}$$

$$u_5' = -\beta\left(\frac{1-\phi_{gc}\overline{\phi}_{g,z}}{1-\phi_{gc}}\right) \tag{6.55}$$

$$y_{CH_4} = \frac{u_1}{u_1+u_2} \tag{6.56}$$

$$y_{H_2} = 1 - y_{CH_4} \tag{6.57}$$

$$\overline{R} = \left[y_{CH_4} - \frac{u_5}{\Gamma}y_{H_2}^2\right] \tag{6.58}$$

$$\overline{J}_{m,H_2} = \left[u_5^{1/2}y_{H_2}^{1/2} - u_3\right] \tag{6.59}$$

$$\overline{J}_{mem,H_2} = \left[\overline{P}_m^{1/2} - u_3\right] \tag{6.60}$$

$$\tag{6.61}$$

The boundary conditions are:

$$u_1(\overline{z}=0) = 1 \tag{6.62}$$

$$u_2(\overline{z}=0) = \overline{F}_{H_2,feed} \tag{6.63}$$

$$u_4'\big|_{\overline{z}=0} = 0 \tag{6.64}$$

$$u_4'\big|_{\overline{z}=1} = 0 \tag{6.65}$$

$$u_5\big|_{\overline{z}=0} = 1 \tag{6.66}$$

6.3 Comparison to literature data

A recent paper by Upham et. al. [22] reported pyrolysis catalytic activity screening experiments for 18 molten metals and molten metal alloys. The highest activity was observed for a 27 mole % Nickel/Bismuth alloy. Additional experiments in a 150 mm bubble column enabled the estimation of an Arrhenius rate law with an activation energy of 208 KJ/mole, and a prefactor of 7.9×10^6 mL/cm^2/s (defined such that the rate is proportional to the gas/melt surface area). Experiments were also reported on a taller 1.15 m bubble column in which methane was pyrolyzed to 86 % conversion at 1040 °C and 95 % conversion at 1065 °C.[2] Data collected from a series of experiments run at 1040 °C but at varying residence times/reactor heights were then combined with a reactor model to determine the reactive surface area implied by the observed conversion and the previously characterized reaction kinetics. Then, after assuming that industrial distributors would enable a 25 % gas hold up and an average bubble diameter of 1 cm, the reported kinetics and assumed hydrodynamics enabled the authors to estimate that a 200 kta hydrogen plant would require ≈ 600 m^3 of reactor volume for 95 % conversion at 1065 °C and an inlet pressure of 10 atm. These data have been used to test the model developed here.

Several assumptions and physicochemical descriptions vary between the model presented here and the model used to interpret the data by Upham et. al. [22]. First, the new, higher fidelity reaction rate model allows both gas phase and melt catalyzed pyrolysis, whereas the Upham et. al. [22] explicitly assumed that the gas phase reaction was negligible. Assuming that the gas phase chemistry does not occur implicitly credits whatever gas phase chemistry does occur to the catalytic melt, leading to an overestimation

[2]The discussion in the text of the paper, Figure S1c in the SI, and the reported data in Figure 3a each report different column heights. [22] Here, it is assumed that the height reported in Figure 3a is correct.

of the catalytic activity.

The melt activity has been estimated from the reported apparent rate data by assuming a bubble size distribution and backing out the gas phase reaction rate that is implied by a preferred gas phase reaction rate law. The gas phase kinetics prefered here are the ones reported in Napier et. al. [7] and presented in Equation 6.6. See the gas phase kinetics literature review in Appendix 6.B.5 for justification and discussion. An average bubble size is needed to estimate the fraction of the observed reaction that is due to the gas phase kinetics because the gas phase rate is proportional to the gas phase volume, whereas the melt catalyzed reaction rate is proportional to the interfacial surface area. Here, it is estimated that the average bubble diameter is 7 mm.[3] When one uses this bubble size estimate to subtract out the gas phase reaction rate from the reported apparent reaction rate reported in [22], the melt catalyzed activation energy estimate becomes 207.1 KJ/mole and the reaction rate law prefactor becomes 7.16×10^6 mL/cm^2/s.

Another significant difference between the physicochemical description in [22] and in the model presented here is the reverse reaction rate. Upham et. al. [22] assumed that Reaction 6.2 is irreversible. Experimental conversions are substantially below the equilibrium conversions for most of the conditions considered in [22], so the assumption does not significantly alter the interpretation of their reported data. Still, a reverse reaction rate proportional to the hydrogen partial pressure squared is used here to make the total reaction rate consistent with reaction equilibrium thermodynamics.

The hydrodynamic description also varies between the two models. Upham et. al. [22] explicitly assumed that melt/gas surface area is proportional to the height of the reactor, implying that the surface area per unit volume of reactor is independent of pressure and conversion. Assuming a constant (i.e., average) surface area to height relationship tends

[3]This is a value that has been observed recently in separate but similar experiments reported to us through private communications. [23]

to underestimate the necessary reactor size for a given conversion because it overestimates the available reactive surface area at the reactor inlet and underestimates it at the exit.[4] The highest reaction rates per surface area occur at the inlet because the total pressure is highest, the methane gas phase mole fraction is highest, and the hydrogen gas phase mole fraction is lowest. So the lowest reverse rates and the highest forward rates occur at the inlet, where the gas phase surface area is most overestimated.

Finally, comparing the new, higher fidelity model to the observations in [22] requires estimating some additional physical properties that were not required in [22]. The relevant quantities and their estimation methods are discussed in Appendix 6.B. Table 6.2 specifies the dimensionless parameters and groups for our model implied by the property estimates in Appendix 6.B and the following experimental conditions (taken from [22]): 115 cm tall reactor, operated at a uniform temperature of 1040 °C, and a feed gas rate of 10 sccm of a 80/20 mole % mixture of methane/argon at 200 kPa. The average inlet bubble radius was chosen such that the conversion at the outlet was 86 % (5.75 mm), to match a single experimental data point.

These model parameters lead to the conversion/height and reactive surface area/height relationships shown in Figure 6.3 where the red squares are data points taken from [22] and the black line is the model prediction. The conversion/height realtionship matches the data reported in the screening paper within experimental uncertainty. The primary difference between the model predictions of the current model and the model in the SI of [22] is the reactive surface area/height relationship. As discussed above, surface area was assumed to be a linear function of height in [22], but the new model predicts that more surface area exists near the top of the reactor where rates are slower. This leads to

[4] In a non-membrane reactor, the most gas phase moles and the lowest total pressure both occur at the top of the reactor. The top of the reactor has the highest gas bubble volume fraction and surface area for reaction, yet the top of the reactor is also where the reaction rates are slowest due to hydrogen dilution and reduced hydrostatic pressure.

β	0.49
Γ	65.5
$\overline{P}_m$	NA
Da	3.0
θ	0.0466
Ω	3.3×10^4
ζ	0
Pe	0.028

Table 6.2: The model parameters and dimensionless groups for model 6.51-6.66 associated with the calculation shown in Figure 6.3. ζ is zero and $\overline{P}_m$ is not applicable (NA) because these experiments did not include membranes.

$\approx$ 25 % higher reactive surface area requirement for the same conversion ($\approx$ 38 cm^2 here compared to $\approx$ 29.5 cm^2 in [22]) .

Upham et. al [22] report 95 % conversion for a single 1065 °C experiment, presenting an interesting opportunity to test the model presented in this chapter. The calculation shown in Figure 6.3 estimated the reactive surface area by choosing the initial bubble size such that the model best predicted the outlet conversion at 1040 °C. The single reported experiment at 1065 °C provides an opportunity to test the model because one does not expect the bubble size distribution to be a strong function of temperature. For a given inlet flow rate, inlet pressure, reactor, molten metal solvent, gas mixture, and gas distributor, one does not expect large changes in the average bubble size in response to a temperature change of 25 °C. Therefore, the inlet bubble size determined from the 1040 °C experiments provides an opportunity to test the model at 1065 °C. When this test calculation is done with the model presented in this chapter and the inlet bubble size estimated from the calculation in Figure 6.3, the predicted conversion at 1065 °C is 93.5 %. This prediction is within the experimental uncertainty, especially considering the difficulty of the experiments and the general uncertainty of the measurements (e.g.,

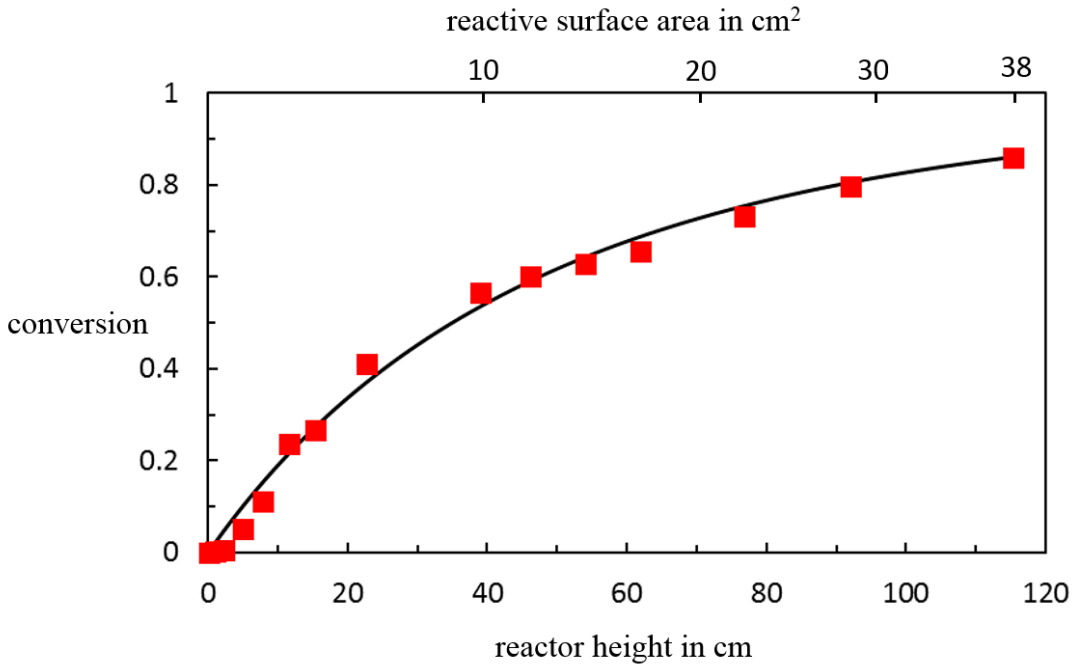

Figure 6.3: Predicted and observed conversion vs reactor height for methane pyrolysis in a 1.15 m molten metal bubble column filled with 27 mole % Ni/Bi at 1040 °C. 10 sccm of a 80/20 mole % methane/argon mixture was fed at 200 kPa. The black line is the conversion predicted by the model presented in this chapter and the red squares are data reported in [22].

How close to isothermal were the experiments? How much reaction occurs in the reactor headspace? What is the uncertainty in the mass spectrometry procedure used to quantify the conversion? etc.).

6.4 Membrane reactor design to avoid metal loss

In this section, a design is presented that potentially avoids the metal loss and reaction equilibrium conversion challenges discussed in the introduction to this chapter by removing the hydrogen from the reactor before the bubbles break through the molten salt cap at the top of the reactor. The estimated membrane properties and other necessary physical properties are estimated and discussed in Appendix 6.B. While the model

presented here can be used for more systematic conceptual design studies in the future, this calculation is intended to illustrate what is possible with a membrane reactor.

Consider a 11.2 m tall, 0.3 m diameter reactor filled with molten 27 mole % Ni/Bi at 1000 °C, similar to the one illustrated schematically in Figure 6.1. The reactor is fed pure methane at 29.7 atm through a gas distributor that creates an average inlet bubble diameter of 1.5 cm and a gas holdup of 25 volume %, implying approximately 100 m^2/m^3 of reactive surface area (at the inlet). The reactor height and melt density implies a 8.4 atm pressure drop across the length of the reactor due to the hydrostatic head, so the outlet pressure is 21.3 atm. The reactor is encased in a vessel that captures the hydrogen as it diffuses through the membrane reactor walls, and the elevated reactor pressure ensures that a membrane transport driving force exists along most of the reactor length. At the stated reactor exit pressure and temperature, the equilibrium conversion is 73.5 %, but the utilization of membranes enables 100 % conversion. The dimensionless parameters and groups associated with this design are listed in Table 6.3.

β	0.269
Γ	4.7
$\overline{P}_m$	0.0337
Da	13.6
θ	0.036
Ω	1.4×10^7
ζ	5.3×10^6
Pe	0.018

Table 6.3: The model parameters and dimensinoless groups associated with the membrane reactor design discussed in this section and in Figures 6.4 and 6.5.

$\beta = 0.269$ indicates that approximately one fourth of of the pressure at the reactor inlet is attributable to the hydrostatic head. Γ=4.7 and an outlet pressure of 21.3 atm

combine to imply an equilibrium conversion of 73.5 % for a pure methane feed without membranes. The relative importance of the melt phase and gas phase reaction rates varies along the length of the reactor as the bubbles expand and contract, but θ=0.036 indicates that 3.6 % of the reaction rate occurring at the reactor inlet is due to the uncatalyzed gas phase chemistry. Both Ω and ζ are greater than a million. Qualitatively, this indicates that transport between the phases and across the membrane is fast relative to molecular diffusion in the melt phase. This is mostly a result of the long diffusion length implied by the tall reactor (See Appendix 6.B for discussion of the estimation of transport and membrane properties.). $Pe = 0.018$ indicates that transport from the bubbles to the melt is also fast relative to the rates of gas phase convective flow through the reactor. Taken altogether, the transport rates can be classified as interphase transport> membrane transport > axial convective transport > axial diffusive transport. These model parameters and dimensionless groups predict 100 % conversion with 100 % hydrogen removal from the reactor through the membranes. Figures 6.4 and 6.5 illustrate how some of the important states vary along the length of the reactor.

The dimensionless hydrogen and methane gas phase molar flow rates ($\overline{F}_{H_2}$ and $\overline{F}_{CH_4}$), the dimensionless gas phase volume fraction ($\overline{\phi}_{g,z}$), and the dimensionless interfacial surface area per reactor volume ($\overline{a}_z^i$) are plotted against the dimensionless reactor height in Figure 6.4. The dimensionless methane molar flow rate decays along the length of the reactor from 1 to 0. The hydrogen molar flow rate is zero at the reactor inlet but increases along the length of the reactor until reaching its maximum value around $\overline{z}$=0.15. Up until that point, more hydrogen is generated by the reaction than is "lost" from the gas phase to the melt phase via interphase diffusion. After $\overline{z}$=0.15, the hydrogen molar flow begins to decay, eventually reaching zero near the top of the reactor ($\overline{z}$=1). When 0.15<$\overline{z}$<1, the rate of hydrogen diffusion across the gas/melt phase boundary is larger than the rate of hydrogen generation from chemical reaction. The bubble volume expands along the

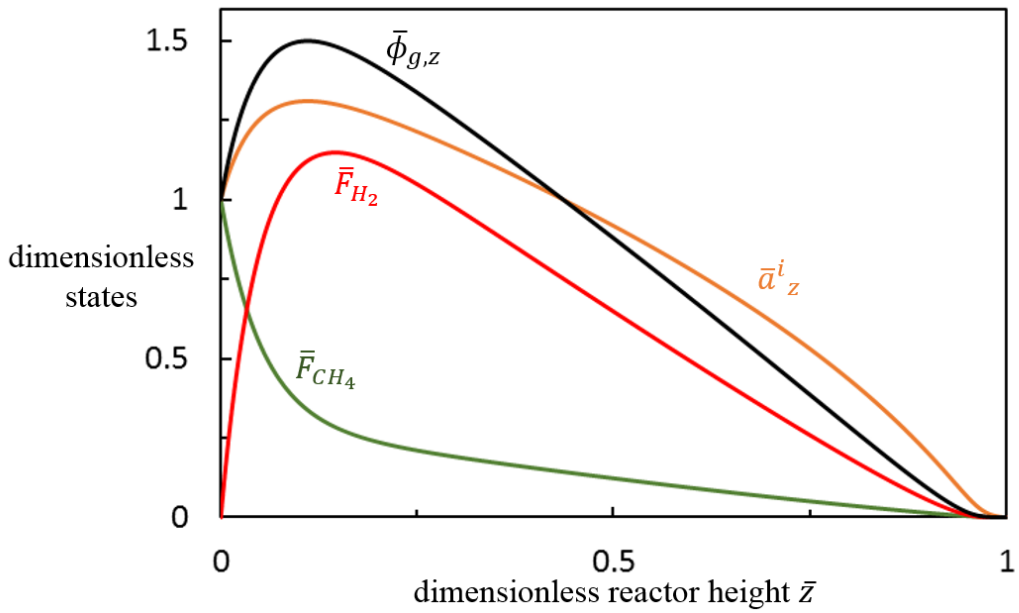

Figure 6.4: Dimensionless gas phase molar flow of methane ($\overline{F}_{CH_4}$), dimensionless gas phase molar flow of hydrogen ($\overline{F}_{H_2}$), dimensionless interface surface area per reactor volume ratio ($\overline{a}^i_z$), and dimensionless gas phase volume fraction ($\overline{\phi}_{g,z}$) as functions of reactor height for the membrane reactor design discussed in this section. The gas phase molar flow of methane decays to zero, indicating 100 % conversion. The hydrogen flow increases at early times due to reaction, but eventually decays to zero, indicating that all of the produced hydrogen has crossed into the melt phase and then further transported across the membrane. The surface area and volume distributions vary along the length of the reactor in response to changes in total pressure and total number of gas phase moles.

length of the reactor due to the hydrostatic pressure drop and the changing total number of moles within the gas phase. This is reflected by the dimensionless volume fraction and surface area reaching maximum values near the same reactor height at which the hydrogen gas phase molar flow maximizes. $\overline{F}_{H_2}$, $\overline{\phi}_{g,z}$, and $\overline{a}^i_z$ do not reach their respective maxima at exactly the same height in the reactor because they do not have identical relationships to the total reactor pressure and total number of gas phase moles.

Figure 6.5 illustrates how several of the important transport related states and fluxes vary along the length of the reactor. $\overline{C}^*_{H_2}$ is the dimensionless hydrogen saturation concentration implied by the reactor pressure and the gas phase hydrogen mole fraction.

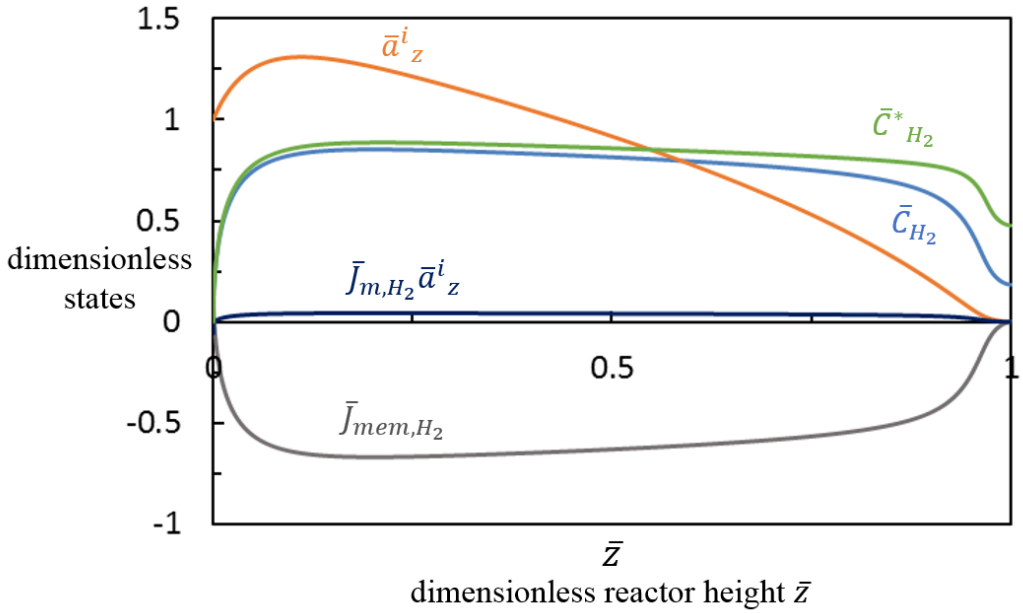

Figure 6.5: Dimensionless interface surface area per unit reactor volume ($\overline{a}_z^i$), dimensionless melt phase hydrogen saturation concentration ($\overline{C}_{H_2}^*$), dimensionless melt phase hydrogen concentration ($\overline{C}_{H_2}$), dimensionless driving force for interphase molar flux of hydrogen ($\overline{J}_{m,H_2}\overline{a}_z^i$), and dimensionless driving force for cross membrane hydrogen transport ($\overline{J}_{mem,H_2}$) as functions of reactor height for the membrane reactor design discussed in this section. The melt phase is supersaturated in hydrogen with respect to the cross membrane gas phase ($\overline{C}_{H_2} > \overline{P}_m^{1/2}$ or $\overline{J}_{mem,H_2} < 0$) and undersaturated with respect to the gas phase ($\overline{C}_{H_2} < \overline{C}_{H_2}^*$ or $\overline{J}_{m,H_2} > 0$) along most of the length of the reactor. This results in simultaneous hydrogen transport out of the gas phase and into the melt and out of the melt phase across the membrane. Near the reactor exit, $\overline{J}_{m,H_2}\overline{a}_z^i$ decreases even though $\overline{J}_{m,H_2}$ is increasing due to the decrease in available surface area for interphase transport as the total number of gas phase moles descreases.

The actual dimensionless concentration in the melt phase is labeled is $\overline{C}_{H_2}$. When the saturation concentration is higher than the actual concentration (as is the case across the entire length of the reactor except directly at the inlet), there is a driving force for hydrogen mass transport from the gas phase into the melt phase. The actual rate of hydrogen transport from the gas to the melt phase is also proportional to the surface area available for transport, so for reference, the dimensionless surface area per unit reactor volume ($\overline{a}_z^i$) is also included in Figure 6.5. The $\overline{J}_{m,H_2}\overline{a}_z^i$ curve is the dimensionless driving

force for interphase hydrogen transport multiplied by the available dimensionless surface area per unit reactor volume. This combination of states is the dimensionless interphase flux rate. As can be observed from the figure, this interphase flux rate decays to zero near the reactor exit even though a thermodynamic driving force for interphase transport remains (i.e., $\left(\overline{C}^{*}_{H_2} - \overline{C}_{H_2}\right) > 0$). This occurs because the available surface area for transport is decaying to zero as the total number of gas phase moles decreases towards zero. As the absolute quantity of available hydrogen in the gas phase decreases, the available surface area for transport also decreases, resulting in slower interphase transport at the top of the column. The last state that is included in Figure 6.5 is $\overline{J}_{mem,H_2}$, which is the dimensionless driving force for transport across the membrane, defined such that a positive flux indicates a flux into the melt phase. This flux is negative along most of the length of the reactor but approaches zero at the reactor outlet. Since the gas phase flow out of the top of the reactor is zero, all of the hydrogen that fluxes into the melt from the gas phase fluxes out across the membrane. Therefore, $\overline{J}_{mem,H_2}$ is negatively correlated to $\overline{J}_{m,H_2}\overline{a}^{i}_{z}$. They would also be identical in magnitude if ζ and Ω were equal. At the reactor outlet (the lowest reactor pressure along the length of the reactor), the melt phase is approaching phase equilibrium with the hydrogen on the gas side of the membrane.

Figure 6.6 illustrates how the dimensionless pressure varies along the reactor height under several possible descriptions of the hydrostatic head. The black curve is the dimensionless pressure described by the complete set of model equations presented in this chapter. The curvature arises because the effective melt density varies as the gas volume fraction varies. At lower reactor heights, the volume fraction increases causing the pressure drop per height to decrease. Eventually, the gas phase volume fraction begins to decrease. At that point, the pressure drop per height starts to increase as described in Equation 6.9. The pressure drop per height is highest at the reactor outlet because

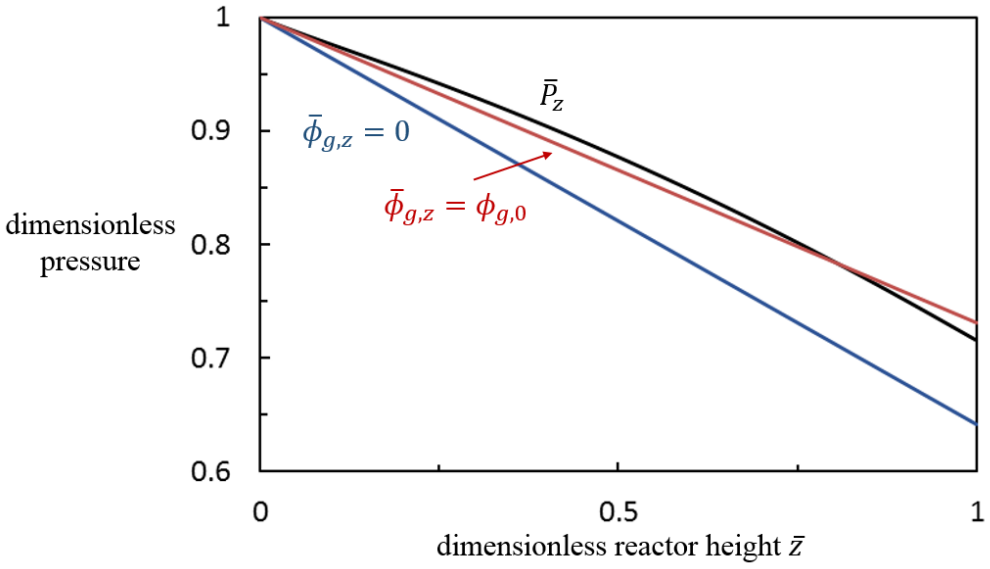

Figure 6.6: Dimensionless pressure versus dimensionless reactor height under 3 different descriptions of the molten solvent density. The black line is the pressure described by the full set of model equations presented here. It explicitly includes the effect of gas phase volumetric expansion and contraction as a function of the model states. The red curve illustrates how the pressure would vary with height if the gas phase volume fraction was assumed to maintain a constant value of $\overline{\phi}_{g,z} = \phi_{g,0}$. The blue curve illustrates how the pressure would vary with reactor height if one assumed that the pressure drop only depended on the melt phase density, thereby implicitly ignoring the impact the lower density gas phase has on reducing the hydrostatic pressure drop (i.e., $\overline{\phi}_{g,z} = 0$ in Equation 6.9).

the gas phase volume fraction is lowest. The red curve is the dimensionless pressure implied by assuming that the effect the gas phase volume fraction has on the hydrostatic head can be approximated by assuming that $\overline{\phi}_{g,z} = \phi_{g,0} = \phi_{g,c}$ in Equation 6.9. Implicitly assuming a constant solvent density causes the pressure to vary linearly with reactor height. This assumption overestimates the pressure gradient at the bottom of the reactor and underestimates the pressure gradient at the top. The blue curve is the pressure that is implied by ignoring the effect the gas phase volume fraction has on the hydrostatic head (i.e., $\phi_{g,z} = 0$ in Equation 6.9) One implicitly makes this assumption if one defines the hydrostatic pressure drop to be proportional to the pure molten solvent density and the reactor height. Such a description overestimates the pressure gradient because the

gas phase density is always lower than the solvent density. Ignoring the gas phase effect on the density and pressure drop leads to a systematic overestimation of the combined density and a systematic overestimation of the pressure drop.

6.5 Conclusions

In conclusion, a new molten metal catalyzed methane pyrolysis reactor model has been developed and described here that accurately recreates the published experimental data in the literature. It also includes a new membrane functionality that allows one to consider reactor designs that have not yet been possible to characterize experimentally. The model presented here can be used as is for conceptual design studies of methane pyrolysis systems that do not intend to control the solid form of carbon produced or that intend to use some secondary post processing step to upgrade the carbon form. This work might be extended to include simultaneous solid form selection and control by coupling the current model equations to a solid carbon population balance model and attempting to analyze the combined methane pyrolysis/solid form selective carbon precipitation model in the spirit of the analysis in chapters 3 and 4). In that way, it may be possible to produce high value, non-metal contaminated, solid forms of carbon while simultaneously producing pure hydrogen through a membrane. Harvesting some value from the solid carbon would likely have a significant impact on the overall process economics, considering it is stoichiometrically required to produce 3 times as much carbon as hydrogen on a mass basis.

Appendices

6.A Notation

Notation

Symbol	Units	Description
k_t	length/time	mass transport coef. for gas bubbles to melt
P_{H_2}	pressure	Hydrogen partial pressure in gas bubbles
K_H	moles/length^3/pressure$^{1/2}$	hydrogen Sievert's Law constant
k_m	length/time	mass transport coef. for gas side of membrane to melt, i.e., $\approx$ membrane permeance
D	length^2/time	hydrogen melt phase diffusivity
$k_{f,g}$	1/time)	uncatalyzed forward rate constant
ϕ_g	volume/volume	bubble volume fraction
K_eq	pressure	equilibrium constant for Reaction 6
$k_{f,m}$	volume/area/time	catalyzed forward rate constant
a^i	area/volume	melt/gas interfacial area per unit reactor volume
P_z	pressure	reactor pressure as function of height
ρ	mass/volume	density of pure molten melt
$\dot{B}$	/time	bubble generation rate at z=0
FT, z	moles/time	total bubble phase molar flow rate
ρ_b	bubbles/reactor volume	bubble number density
$r_{b,z}$	length	average bubble radius
R	moles/volume/time	total rate expression per unit reactor volume
A_c	area	reactor cross sectional area
J_{m,H_2}	moles/area/time	hydrogen flux from gas bubbles to melt
J_{mem,H_2}	moles/area/time	flux from gas side of membrane to melt
h	length	height of molten metal within reactor

6.B Physical property estimates

Several physical properties must be characterized experimentally before one can use the models presented here. Some of these properties are different for different molten metal solvents. Here, the properties are estimated for the Ni/Bi alloy that is discussed

in the main text of the chapter. In several cases, the exact values have not been characterized and reported experimentally, and so correlations and best-estimates have to be utilized. In this Appendix, each of these physical properties are introduced, estimated, and discussed. In many cases, a reasonable estimate for the same property may be a factor of 2-10 higher or lower. The estimates presented here were chosen such that they conservatively represent the properties that are likely to be achievable in a molten melt solvent if research continues on this process.

6.B.1 Melt hydrogen solubility constant

The melt hydrogen solubility is assumed to follow Sievert's law. [24] A Sievert's law description of the solubility requires a Sievert's law constant (K_H) that quantifies the proportionality between the hydrogen melt phase solubility and the square root of the partial pressure of hydrogen in the gas phase. The hydrogen solubility in solid Nickel is known to be ≈ 8 standard cubic centimeters per 100 g of metal when contacted with 1 atm of hydrogen. [28] This implies that K_H=0.1 moles/m^3/Pa$^{1/2}$ or 0.0325 moles/Liter/atm$^{1/2}$. Less data is available on bismuth, and no data was found on the specific Ni/Bi system of interest. For the calculations described in this chapter, it was assumed that K_H=0.025 moles/Liter/atm$^{1/2}$.

6.B.2 Diffusivity

We have not uncovered any reported measurements of hydrogen diffusivities in a molten Ni/Bi alloy, but there is a substantial literature on hydrogen diffusivities and metal self diffusivities in molten metals. Across various systems and temperature ranges, the reported diffusivities tend to fall between 1 $\times 10^{-2}$ and 1 $\times 10^{-5}$ cm^2/s, with higher diffusivities reported at higher temperatures and in metals with higher hydrogen solubil-

ities. [29–32] In the calculations presented here, the hydrogen diffusivity is assumed to be 3 $\times 10^{-3}$ cm^2/s in 27% Ni/Bi at 1000 °C.

6.B.3 Mass transport coefficient, k_t

The mass transport coefficient is estimated using the expression implied by the pentration theory description of a gas/liquid interface for a bubble rising through a fluid of much higher viscosity. [33] This calculation leads to an estimate of the mass transport coefficient of 0.002 m/s for the membrane reactor design preseneted here.

6.B.4 Cross membrane mass transport coefficient, k_m

Most hydrogen membranes reported in the literature are characterized in terms of their permeance and selectivity for gas separations. Typically, the permeance has units of moles/area/time/pressure, such that the pressure gradient across a membrane multiplied by the component's permeance gives the component molar flux through the membrane. The selectivity quantifies the primary component flux through the membrane relative to to the non-primary components. In other words, the selectivity defines the effectiveness of each membrane stage to separate a gas mixture. Both conventional definitions are less useful here because the physical situation is slightly different in a molten metal membrane reactor. In this reactor, the membrane separates a molten metal phase from a gas phase, so no component can traverse the membrane unless it is soluble in both the melt phase and in the gaseous phase. Carbon is not expected to exhibit any appreciable permeance because it is mostly insoluble in the gas phase. Furthermore, the observed membrane selectivity to hydrogen over methane in the molten metal reactor will be significantly higher than it might be for a methane/hydrogen gas separation because methane is unlikely to maintain appreciable melt phase solubility (relative to hydrogen). A future

version of this model could include methane melt solubility, and then it would also require a hydrogen/methane membrane selectivity. It is expected that ignoring these factors at this time generates minimal inaccuracies that do not appreciably affect the rest of the design.

The other important difference between a molten metal/gas membrane and a gas/gas membrane is that the thermodynamic driving force for separation is different. In a gas separation, the flux is proportional to the pressure gradient, but in the molten melt/gas membrane system, the driving force is the difference in the actual melt phase concentration and the saturation melt phase concentration implied by the partial pressure of hydrogen on the gas side of the membrane. This effectively changes the pressure scaling from a linear to a square root relationship. The membrane flux is described in this chapter as a membrane transport coefficient (k_m) multiplied by the difference between the melt phase hydrogen concentration (C_{H_2}) and the melt phase hydrogen saturation concentration implied by the hydrogen partial pressureon the gas side of the membrane and the Sievert's law constant (See Equation 6.4). With this description, the transport coefficient required here has units of length per time. Once a reasonable estimate of the permeance of a typical hydrogen membrane is made, one still requires some method for converting a permeance with units of moles/length^2/time/pressure to length/time. There is not a perfect way to make this adjustment, but a reasonable procedure is outlined as follows: First, multiply the reported permeance by the pressure it is reported for/measured from, giving a molar flux. Then, divide that molar flux by the saturation concentration implied by the same pressure and an appropriate Sievert's law constant for the melt of interest.

$$k_m = \text{Permeance}[\frac{\text{moles}}{\text{m}^2 \text{ s Pa}}] \times P_{\text{exp}}[\text{pa}] \times \frac{1}{K_H P_{\text{exp}}^{1/2}}[\frac{\text{m}^3}{\text{moles}}] \tag{6.67}$$

where P_{exp} is the pressure the membrane was characterized at.

For membranes constructed from precious metals, permances are reported between 1 $\times 10^{-8}$ and 1 $\times 10^{-7}$ moles/m^2/s/Pa for temperatures ranging from ambient to 300 ^{o}C. [34] Permeances ranging from 1×10^{-7} to 1×10^{-5} moles/m^2/s/Pa have been reported at at elevated temperatures (e.g., $400 - 850^{o}$C). [34, 35] Silica based membranes are cheaper to produce, but they tend to, on average, exhibit lower permeances. For example, a 2007 review article reported permeances for silica derived membranes between 0.89 and 200 $\times 10^{-8}$ moles/m^2/s/Pa at various temperatures in the range of $200 - 600$ ^{o}C, with most of the reported permeances closer to the lower end of that range. [34, 36] Studies that explicitly characterize the hydrogen permeance as a function of temperature indicate that the permeance follows an Arrhenius rate law, resulting in significantly higher permeances at higher temperatures. Extrapolating the Arrhenius temperature dependence calculated in reference [37] to the 1000 ^{o}C temperature used for the design discussed in this dissertation results in a predicted membrane permeance of 2.3 $\times 10^{-7}$ moles/m^2/s/Pa.

These studies highlight that membrane properties can vary widely as a function of the materials and methods of construction. Here, the reported Arrhenius law for silica membranes discussed in Araki et. al. [37] will be used. These membranes were characterized with pressure drops of 100 kPa. The permeance (2.3 $\times 10^{-7}$ moles/m^2/s/Pa), P_{exp} (100 kPa), and K_H (0.077 moles/m^3/Pa$^{1/2}$) combine with Equation 6.67 to give an estimated k_m of 9.45 $\times 10^{-4}$ m/s.

6.B.5 Gas phase kinetics literature review

Characterizing the un-catalyzed, gas phase reaction rate of Reaction 6.2 is challenging for several reasons. The first is that the the reactor must be operated at elevated temper-

atures to achieve appreciable equilibrium conversions and chemical rates. The reaction is endothermic which leads to large adiabatic temperature drops even at low conversions. Therefore, designing isothermal reactors for kinetic studies is difficult. Furthermore, the experimental setup is complicated by the heterogeneous nature of the reaction. The solid carbon that is produced by the reaction can serve as a catalyst for further reaction if it is allowed to accumulate. [6] This solid carbon catalytic effect can be mostly avoided by studying the reaction in shock-tube reactors. [6,38] In shock-tube reactors, a shock wave is generated that elevates the pressures and temperatures for a short residence time on the order of miliseconds (See [39] for additional discussion of the differences in shock-tube and non-shock-tube reactor setups).

The shock-tube reactors reduce the solid carbon auto-catalytic and wall effects considerably, but these reactors introduce new challenges. To extract a kinetic rate law from a measurement of reaction conversion in a shock-tube reactor, one must characterize the residence time and temperature distribution within the produced shock-wave. One can calculate different residence time distributions depending on the assumptions one makes about the flow within the shock-tube, and these assumptions are difficult to independently validate or verify. Furthermore, diffusive mixing between the driver gas and the reacting fluid can occur if the shock wave is not carefully constructed. When this effect is not properly considered, investigators overestimate the reactant partial pressures, thereby reducing the "observed" reaction rate constants.

The non-shock-tube ("flow") experiments tend to report higher kinetic rates, presumably due to the auto-catalytic impact of the accumulated solid carbon in these systems. Therefore, there seems to be agreement in the literature that the kinetic expressions based on shock-tube experiments are expected to be more reflective of the real, un-catalyzed, gas phase reaction rates. Still, different investigators have reported very different rate constants based on experiments done in similar shock-tubes. The primary distinction

among these studies is the method chosen for describing the residence time and temperature distributions.

For example, Glick et. al. [4] was one of the first studies to explicitly discuss the challenges associated with characterizing the reaction rates from shock-tube data. They diluted their reactant mixture with a large excess of noble gases to ameliorate the endothermic temperature drop. They were able to achieve an "isothermal" reactor (defined as a temperature drop of approximately 150 °C) and they reported residence times "on the order of a millisecond." They offered an apparent activation energy of 85 kcal/mole (355.6 KJ/mole) between temperatures of 727 and 3227 °C, but this value cannot be taken with much confidence considering the discussion of the uncertainty within the experimental conditions (temperature +/- 150 °C and residence time +/- a factor of 10).

A later study by Kevorkian et. al. described the hydrodynamic challenges in more detail and attempted to correct for them during the data analysis. They also explicitly rejected any data that showed evidence of mixing between the reactant and driver gases. [38] Unfortunately, sufficient detail about the calculation of the residence time distribution within the shock waves is not included in the published paper, so it is difficult to judge the quality of the final reported rate expression. That being said, this paper seems to have been the first study to clearly articulated and attempt to account for all of the challenges detailed above. The study was done over the temperature range of 1383-1767 °CK, generating an Arrhenius plot with an activation energy of 93 kcal/mole (389.1 KJ/mole). This study was also noteworthy for making specific arguments based on the kinetic theory of gases that seem to support the claim that the shock-tube experiments are less likely to be corrupted by wall effects than the flow system studies. This claim about wall effects was further supported by the non-shock-tube experiments and discussion in a later study. [6]

Yet another study was later reported by Napier et. al. [7] that explicitly measured

the temperature distribution within the shock wave using two independent measuring techniques. The two measurement techniques validated each other by agreeing within 20 ^{o}C for all reported measurements. A figure was included in this study that compares the measured temperature distributions as functions of the incident shock velocity to several predictions of the temperature distributions under several sets of assumptions and descriptions. The set of assumptions deemed most likely to be accurate leads to calculated temperature profiles that are systematically lower than the measured temperatures, implying that kinetic rate expressions based on these temperature estimates are likely to overestimate the actual reaction rate constant at a given temperature. This observation is further supported by comparing the Napier kinetics to the Kevorkian kinetics discussed above. Napier estimated the activation energy to be 93.6 kcal/mole (391.6 KJ/mole). This is almost identical to the estimated activation energy of Kevorkian (93 kcal/mole or 390.1 KJ/mole), but when the prefactor is included, the Napier kinetics predict reaction rates that are approximately a factor of 4 smaller than the Kevorkian kinetics. This is consistent with the hypothesis proposed in Napier et. al. about past studies systematically overestimating the temperatures within their reactors. In conclusion, the current author's best estimate of the un-catalyzed gas phase reaction rate is the kinetic rate expression reported by Napier et. al. [7]

$$k_{f,g} = 3.8 \times 10^{13} \exp(-391.6/\mathrm{RT}) \quad [1/s] \tag{6.68}$$

where the activation energy is in KJ/mole and the reaction rate has units of inverse seconds such that $\frac{k_{f,g}}{RT} P_{CH_4}$ is the forward reaction rate with units of moles/volume/time. The Napier kinetics are chosen here because the measured temperature distribution seems more likely to be accurate than the calculated one. However, one should not be surprised if future experiments indicate that the true reaction rate prefactor is 2-5 times higher.

One more kinetic study requires discussion because the rate constant reported in this study was utilized in the molten tin methane pyrolysis papers discussed earlier. [17,19,40] In reference [40], a new kinetic expression was determined by fitting a PFR model to a prediction from a proprietary kinetic model (referred to in [40] as the Dsmoke model) that was reported to include 240 species, 14,000 reactions, and soot formation. The proprietary model (Dsmoke) was reported to have been validated across a "very large set of experimental data for conditions that do not involve transport and diffusion processes, such as stirred reactors, batch reactors and shock tubes, rapid compression machines and motored engines." None of this can be verified because the model cannot be found in the literature. The Dsmoke model is then used to predict methane conversions in a homogeneous gas-phase plug flow reactor. Then, a conventional plug flow reactor model with a single reaction rate expression for Reaction 6.2 is fit to the predictions of the higher fidelity Dsmoke model. A new simple kinetic expression is extracted from this fit, and these kinetics are reported. The reported activation energy is 88.4 kcal/mole (370 KJ/mol) which is significantly lower than the shock-tube reactor literature but only slightly lower than the bulk of the non-shock-tube reactor studies. Perhaps, the Dsmoke model explicitly includes the autocatalytic effect of the solid carbon on the reaction rate, resulting in a lower apparent activation energy and higher reaction rates. Or perhaps, the prediction is higher because the more complicated Dsmoke model was fit to data that included implicit catalysis, generating the same issues and inaccuracies already discussed in the context of the non-shock-tube reactor studies. One cannot distinguish between these possibilities based on the information that is reported. Regardless of the quality and fidelity of the Dsmoke model, the reported, simplified kinetics do not predict the Dsmoke results with sufficient accuracy to be serve as a reasonable replacement. The new, simplified kinetics underpredict the higher fidelity Dsmoke model at higher temperatures (2300 K) and overpredict them at lower temperatures (1500 K), consistent

with underestimating the activation energy. The best agreement seems to be at 2100 K, although even 2100 K shows substantial disagreements between the predicted methane conversions at short residence times. The predictions seem to get progressively worse at lower temperatures such that residence time necessary for full conversion is off by about two orders of magnitude at the lowest temperature considered (1500 K). Furthermore, 17 experiments were reported and compared to predictions from the Dsmoke model, but these experiments were not compared to the new simplified kinetics. These 17 comparisons show errors in predicted methane conversion between 1 % and 60% (defined as the absolute value of (observed conversion-predicted conversion)/observed conversion). These large deviations between experiments and predictions from the Dsmoke model seem to contradict the claims about the Dsmoke model's accuracy and fidelity, thereby further calling into question the decision to fit a simpler, homogeneous kinetic rate expression to the results obtained from the higher fidelity Dsmoke model in the first place.

The current author prefers the Kevorkian and Napier rate models to both rate models in [40]. This paper would not have been discussed here if it had not been utilized to describe the reaction rates in the tin studies referenced earlier. [17,19] Those investigators stated that they tested four different kinetic rate expressions [4,7,38,40] with their reactor model and chose the kinetic model reported in [40] because it best reproduced their experimental observations.

Bibliography

[1] B. Parkinson, M. Tabatabaei, D. C. Upham, B. Ballinger, C. Greig, S. Smart, and E. Mcfarland. Hydrogen production using methane: Techno-economics of decarbonizing fuels and chemicals. *International Journal of Hydrogen Energy*, 2018.

[2] EIA. March 2018 monthly energy review. Technical report, Energy Information Adminsitration, 2018.

[3] M. Steingberg. Fossil fuel decarbonization technology for mitigating global warming. *International Journal of Hydrogen Energy*, 24(8):771–777, 1999.

[4] H. Glick. Shock tube studies of reaction kinetics in alipatic hydrocarbons. *Symposium (International) on Combustion*, 7(1), 1958.

[5] G. B. Skinner and R. A. Ruehrwein. Shock tube studies on the pyrolysis and oxidation of methane. *J. Phys. Chem.*, 63(10):1736–1742, 1959.

[6] H. Palmer, J. Lahaye, and K. Hou. On the kinetics and mechanism of the thermal decomposition of methane in a flow system. *J. Phys. Chem.*, 72(1):348–353, 1967.

[7] D. H. Napier and N. Subrahmanyam. Pyrolysis of methane in a single pulse shock tube. *J. Appl. Chem. Biotechnol.*, 22:303–317, 1972.

[8] R. Aiello, J. E. Fiscus, H. zur Loye, and M. D. Amiridis. Hydrogen production via the direct cracking of methane over ni/sio$_2$: catalyst deactiviation and regeneration. *Applied Catalysis*, 192:227–234, 2000.

[9] T. V. Choudhary, C. Sivadinarayana, C. C. Chusuei, A. Klinghoffer, and D. W. Goodman. Hydrogen production via catalytic decomposition of methane. *J. Catal.*, 199:9–18, 2001.

[10] M. S. Rahman, E. Croiset, and R. R. Hudgins. Catalytic decomposition of methane for hydrogen production. *Top. Catal.*, 37(2-4):137–145, 2006.

[11] M. Serban, M. A. Lewis, C. Marshall, and R. D. Doctor. Hydrogen production by direct contact pyrolysis of natural gas. *Energy Fuels*, 17(3):705–713, 2003.

[12] A. Abanades, E. Ruiz, E. M. Ferruelo, and F. Hernandez. Experimental analysis of direct thermal methane cracking. *International Journal of Hydrogen Energy*, 36(20):12877–12886, 2011.

[13] A. Abanades and C. R. R. Salmieri. Technological challenges for industrial development of hydrogen production based on methane cracking. *Energy*, 46(1):359–363, 2012.

[14] D. Paxman, S. Trottier, M. Nikii, M. Secanell, and G. Ordorica-Garcia. Initial experimental and theoretical investigation of solar molten media methane cracking for hydrogen production. *Energy Procedia*, 49:2027–2036, 2014.

[15] M. Plevan, T. Geiβler, A. Abanades, K. Mehravaran, R. K. Rathnam, C. Rubbia, D. Salmieri, L. S. ad S. Stuckrad, and T. Wetzel. Thermal cracking of methane in a liquid metal bubble column reactor: Experiments and kinetic analysis. *International Journal of Hydrogen Energy*, 40(25):8020–8033, 2015.

[16] I. Schultz and S. Agar. Decarbonisation of fossil energy via methane pyrolysis using two reactor concepts: Fluid wall flow reactor and molten metal capillary reactor. *International Journal of Hydrogen Energy*, 40(35):11422–11427, 2015.

[17] T. Geiβler, M. Plevan, A. Abanades, A. Heinzel, K. Mehravaran, R. Rathnam, C. Rubbia, D. Salmieri, L. S. ad S. Stuckrad, A. Weisenburger, H. Wenninger, and T. Wetzel. Experimental investigation and thermo-chemical modeling of methane pyrolysis in a liquid metal bubble column reactor with a packed bed. *International Journal of Hydrogen Energy*, 40:14134–14146, 2015.

[18] A. Abanades, R. K. Rathnam, T. Geiβler, A. Heinzel, K. Mehravaran, G. Muller, M. Plevan, C. Rubbia, D. Salmieri, and L. S. ad S. Stuckrad. Development of methane decarbonisation based on liquid metal technology for co2-free production of hydrogen. *International Journal of Hydrogen Energy*, 25(41):8159–8167, 2016.

[19] T. Geiβler, M. Plevan, A. Abanades, A. Heinzel, K. Mehravaran, R. Rathnam, C. Rubbia, D. Salmieri, L. S. ad S. Stuckrad, A. Weisenburger, H. Wenninger, and T. Wetzel. Hydrogen production via methane pyrolysis in a liquid metal bubble column reactor with a packed bed. *Chem. Eng. J.*, 299:192–200, 2016.

[20] B. Parkinson, J. W. Matthews, T. B. McConnaughy, D. C. Upham, and E. W. McFarland. Techno-economic analysis of methanepyrolysis in molten metals: Decarbonizing natural gas. *Chemical Engineering & Technology*, 2017.

[21] K. Wang, W. S. Li, and X. P. Zhou. Hydrogen generation by direct decomposition of hydrocarbons over molten magnesium. *Journal of Molecular Catalysis A: Chemical*, 283(1-2):153–157, 2008.

[22] D. C. Upham, V. Agarwal, A. Khechfe, Z. R. Snodgrass, M. J. Gordon, H. Metiu, and E. W. McFarland. Catalytic molten metals for the direct conversion of methane to hydrogen and separable carbon. *Science*, 358:917–921, 2017.

[23] C. Palmer and E. McFarland. Private Communication. 2018.

[24] A. Sieverts. Absorption of gases by metals. *Zeitschrift fur Metallkunde*, 21:37–46, 1929.

[25] R. J. Andreini, J. S. Foster, and R. W. Callen. Characterization of gas bubbles injected into molten metals under laminar flow conditions. *Metallurgical Transactions B*, 8(3):625–631, 1977.

[26] K. Akita and F. Yoshida. Bubble size, interfacial area, and liquid-phase mass transfer coefficient in bubble columns. *Ind. Eng. Chem., Process Des. Develop.*, 13(1):84–91, 1974.

[27] A. A. Kulkarni and J. B. Joshi. Bubble formation and bubble rise velocity in gas-liquid systems: A review. *Ind. Eng. Chem. Res.*, 44:5873–5931, 2005.

[28] R. H. Fowler and C. J. Smithells. A theoretical formula for the solubility of hydrogen in metals. *Proc. R. Soc. Lond.*, 160:37–47, 1937.

[29] J. Zeng, D. Li, Z. Xu, and Y. Wang. Hydrogen diffusion in molten aluminum a206 casting alloy. *Advanced Science Letters*, 4:1740–1744, 2011.

[30] Q. Yang, L. I. U. Yuan, and Y. Li. Hydrogen diffusion coefficient in liquid metals evaluated by solid-gas eutectic unidirectional solidificaiotn. *Transactions of Nonferrous Metals Society of China*, 24:4030–4037, 2014.

[31] P. Depuydt and N. A. D. Parlee. The diffusion of hydrogen in liquid iron alloys. *Metallurgical and Materials Transactions B*, 3:529–236, 1972.

[32] U. Freudenberg and W. Glaser. Hydrogen diffusion in molten metal potassium at 550 degrees C. *Journal of Physics F: Metal Physics*, 15:L253–L255, 1985.

[33] M. L. McCabe, J. C. Smith, and P. Harriott. *Unit Operations of Chemical Engineering*. McGraw Hill, 2005.

[34] G. Q. Lu, J. D. da Costa, M. Duke, S. Giessler, R. Socolow, R. Williams, and T. Kreutz. Inorganic membranes for hydrogen production and purification: A critical review and perspective. *J. Coll. Interf. Sci.*, 314:589–603, 2007.

[35] S. Yun and S. T. Oyama. Correlations in paaldium membranes for hydrogen separation: A review. *Journal of Membrane Science*, 375:28–45, 2011.

[36] J. Dong, Y. S. Lin, M. Kanezashi, and Z. Tang. Microporous inorganic membranes for high temperature hydrogen purification. *J. App. Phys.*, 104(12):13, 2008.

[37] S. Araki, N. Mohri, Y. Yoshimitsu, and Y. Miyake. Synthesis, characterization and gas permeation properties of a silica membrane prepared by high-pressure chemical vapor deposition. *J. Memb. Sci.*, 290:138–145, 2007.

[38] V. Kevorkian, C. E. Heath, and M. Boudart. The decomposition of methane in shock waves. *J. Phys. Chem.*, 64(8):964–968, 1960.

[39] M. S. Khan and B. L. Crynes. Survey of recent methane pyrolysis literature. *Ind. Eng. Chem.*, 62(10):54–59, 1970.

[40] S. Rodat, S. Abanades, J. Coulie, and G. Flamant. Kinetic modelling of methane decomposition in a tubular solar reactor. *Chem. Eng. J.*, 146:120–127, 2008.

Chapter 7

Conclusions and Future Work

Directing crystallization towards a preferred solid form is a fundamental, recurring challenge in solid phase engineering. In both CCUSM and MP processes discussed here, the preferred solid form is neither thermodynamically stable nor naturally abundant. A conventional procedure does not exist for controlling solid form in these systems, and even if it did, it would be unlikely to apply to systems with concurrent concentrated, reactive mass transport. The physicochemical complexity inherent to both the 2-phase (serial approach) and 3-phase (process intensified approach) reactors that these chemical transformations require implies that entirely new approaches and tools are necessary to rationally design these processes. These tools have been developed here, and along the way, procedures and design rules for solid form selective crystallizers and precipitators have been generated that can be applied to many other systems and industries.

7.1 Summary of major conclusions

7.1.1 Chapter 2: Thermodynamic Assessment of sustainable engineering technologies

Chapter 2 assessed the following sustainable energy technologies from the perspective of material balances, thermodynamic minimum energy requirements, and back of the envelope calculations: carbon capture and sequestration from point sources and from air, carbon capture and utilization as structural materials, hydrogen from steam methane reforming with CCS, and molten metal methane pyrolysis. There are two primary takeaways that are relevant to the rest of this dissertation. First, CCUSM has lower energetic costs per carbon emission avoided than CCS *if* the carbonates produced are utilized by the cement industry. This caveat requires solid form selection because the thermodynamcially metastable solid forms make better structural materials. [1,2] Second, the energetic costs of MP are much higher than SMR+CCS and so the co-produced solid carbon must be converted to something of economic value for the hydrogen produced from MP to compete with hydrogen produced from SMR. Again, this implies that MP requires solid form selection.

7.1.2 Chapter 3: Polymorph selection by continuous crystallization

Chapter 3 introduced a new procedure for controlling solid form during continuous crystallization that is applicable to any crystal system for which the dominant solid formation mechanisms are size-independent linear crystal growth and secondary nucleation. The vast majority of small organic molecules as well as some non-negligble fraction of inorganic crystal systems crystallize by these mechanisms. A population balance model

was constructed that described the process dynamics within a continuous crystallizer. The model was transformed from a set of partial and ordinary differential equations to a set of only ordinary differential equations through the method of moments and then nondimensionalized. Finally, analysis of the transformed model yielded design rules for selecting solid form during continuous crystallization. The results are shown to be consistent with the applicable experimental data in the literature. [3–5]

7.1.3 Chapter 4: Polymorph selection by continuous precipitation

Chapter 4 extended the solid form selection design rules presented in Chapter 3 to include systems for which significant agglomeration occurs. Including agglomeration expands the applicability of the design rules from most small organic molecules to essentially all small organic molecules and from some inorganic solids to most inorganic solids. More specifically, the addition of agglomeration allowed the design rules to be applied to the motivating $CaCO_3$ system (CCUSM). Data collected at UCSB by Sina Schiebel (under the author's supervision) corroborated the design rules implied by the agglomeration-enabled model. Pure, thermodynamically metastable vaterite crystals were generated and characterized using XRD, SEM, and solid state ^{43}Ca NMR. It was also demonstrated that the updated design rules are consistent with the previously reported non-agglomerating design rules for the L-glutamic acid experiments discussed in Chapter 3.

7.1.4 Chapter 5: Maxwell-Stefan diffusion during the reactive absorption of CO_2

Chapter 5 introduced the challenges associated with describing mass transport in concentrated, reactive, electrolytic solutions and presented a mass transport model that accurately accounts for the non-idealities, concentration, and electrolytic effects prevalent at gas/liquid interfaces during CO_2 reactive absorption into brine solutions. Results are compared to the conventional enhancement factor methods to illustrate that in some extreme cases, the higher fidelity models diverge from the simpler conventional descriptions.

7.1.5 Chapter 6: Methane Pyrolysis reactor design

Chapter 6 introduced a membrane reactor model for molten metal methane pyrolysis. The model was validated against available molten metal methane pyrolysis data in the literature and used to illustrate that it is possible to use membranes and reactive separation principles to avoid some of the solid processing complexities that are currently holding up the MP process development effort.

7.2 Next steps in the techno-economic assessment of CCUSM and MP

All of the tools necessary for the design and optimization of the serial CCUSM setup (reactive absorption followed by solid form selective reactive precipitation) were developed and described in this dissertation. The membrane/bubble column reactor model introduced in Chapter 6 specifically for the MP process also serves as a reactive absorption model for the CCUSM process after two minor modifications. First, reactive

absorption is unlikely to require membranes, and so the dimensionless group ζ should be set to zero. Second, the interphase flux was described by a constitutive relation based on Sievert's law in Chapter 6, but it should be described by the system of equations described in Chapter 5 for the reactive absorption model. Once these two changes are made, the membrane reactor model presented in Chapter 6 can be utilized for reactive absorption design calculations. The solid form selective reactive precipitator design can then be undertaken with the design rules developed in Chapter 4. Taken together, Chapters 4, 5, and 6 can be utilized to characterize and optimize the process choices for the serial reactive absorption and precipitation CCUSM process.

It may be possible to follow a similar approach in the MP system. The reactor model in Chapter 6 enables the conceptual design of a methane pyrolyzer that produces gaseous hydrogen and solid carbon. If the solid carbon produced is not the preferred solid form (likely result), it may be possible to use the principles and design rules in Chapter 4 to solubilize and re-precipitate the preferred solid form as a post-processing step. The serial process scheme is more challenging for MP than it is for CCUSM because solubilizing the carbon for re-precipitation may be a substantial challenge in and of itself.

7.3 Long term goals for the techno-economic assessment of CCUSM and MP processes

The most exciting future work for the techno-economic assessment of both the CCUSM and MP processes is the generation of an intensified process model that includes reaction, interphase transport, and precipitation inside the same device. The reactor model in Chapter 6 assumes that all of the carbon formed by reaction immediately enters the solid phase, effectively ignoring the carbon distribution among the gas and melt phases.

This assumption predicts the correct amount of solid carbon at steady-state, but it does not consider the dissolved carbon concentration in the melt phase. If carbon is nucleating and growing in the melt, then the concentration of carbon in the melt must be above its solubility. A population balance model like the one developed in Chapters 3 and 4 could be coupled to the reactor model in Chapter 6 to monitor and predict the solid form and population density of carbon solids directly as a function of reactor position and time. Coupling material balance equations and population balance equations for carbon in all phases within the reactor will lead to an intensified process model capable of distinguishing between different solid forms of carbon. If the nucleation, growth, and agglomeration kinetics can be characterized for each solid form of interest, then the relationships between different operation and design choices to the solid forms and particle size distributions produced can be characterized. These relationships might then be utilized to design a process that produces acceptable solid distributions without any post-processing steps at all.

Furthermore, this new intensified reactor model could be used for reactive absorption and precipitation for CCUSM studies in much the same way that the membrane MP model described in Chapter 6 can be used for the conceptual design of a reactive absorber. Combining $CaCO_3$ population balance models to the interphase, reactive transport equations in Chapter 5 and the reactor model equations in Chapter 6 would allow one to characterize the intensification gains during reactive absorption that motivated much of the work presented here. Adding population balance equations that monitor the solid distribution within the liquid phase of a bubble column reactor could lead to very interesting insights for both the MP and the CCUSM processes.

7.4 Future work on solid form selection

7.4.1 Polymorph screening by continuous crystallization

The pharmaceutical industry must attempt to determine and characterize all of the solid forms available to a drug molecule during drug development because different solid forms exhibit unique shelf-lifes, bioavailabilities, and therapeutic effects. The typical approach is combinatorial screening in micro-batch crystallizers over vast ranges of experimental conditions. It is impossible to guarantee that all of the forms have been observed with this type of approach, as evidenced by the periodic drug recalls related to unknown or unexpected solid forms. [6] The work presented here implies that a better way to approach this problem might be with continuous micro-reactors that could be varied over a continuous range of conditions and introduced with a vast variation of possible disturbances to encourage nucleation. This idea should be flushed out and tested against the current best practices. I hypothesize that a well-designed continuous screening procedure could significantly reduce the cost and efficacy of pharmaceutical solid-form screening.

7.4.2 Implications of stochastic, primary nucleation on solid form selection

Primary nucleation is a stochastic, rare event. A recently published set of papers utilized this fact to explain the nondeterministic detection times and polymorphism observed during batch crystallization of paracetamol and isonicotinamide. [7, 8] Both the detection time and the solid form were distributed statistically. Some combinations of stochastic nucleation and deterministic growth will be accurately reproduced by models that assume both processes to be deterministic, but others, especially ones with especially

"rare" nucleation, may not.

The model equations that the solid form selection design rules were produced from assume that the steady-state, secondary nucleation rates within the crystallizer/precipitator are much larger than the steady-state, primary nucleation rates, such that the primary rates can be treated as if they were negligible (i.e., exactly zero). Since the primary rates cannot be exactly zero in a supersaturated solution, and since the steady-state structure changes if an infinitesimal, deterministic, primary nucleation rate is introduced, this treatment requires careful justification. The treatment is defended in Chapter 3.7 and further supported by the absolute conformity of the available experimental data to the design rules, but of course, no quantity of experimental observations conforming to these design rules can *prove* that the model is correct or that the treatment of primary nucleation is justified. The fundamentally stochastic nature of primary nucleation offers a potential path to proving (or at least to further supporting) the validity of this treatment (and thus these design rules) for systems with non-zero, primary nucleation rates. I hypothesize here that introducing a *stochastic*, primary nucleation rate in the model equations will not substantially change the steady-state structure and linear stability features for at least some region of parameter space. I further hypothesize that if a surface in parameter space exists for which the preceding hypothesis is true on only one side, then this surface can serve as a quantitative condition for when the treatment of primary nucleation in Chapters 3 and 4 is strictly valid. I further propose a physical mechanism by which, for relatively "slow," stochastic, primary nucleation rates, non-zero stochastic, primary nucleation may be experimentally indistinguishable from the complete absence of deterministic, primary nucleation; The few nuclei that form per residence time may wash out of the crystallizer before they have grown to an observable size, and thus the *observed* nucleation rate is zero, even though there is some non-zero nucleation probability. In this way, the primary nuclei density fluctuates in time around some small,

unobservable average density.

7.4.3 Geometric interpretation of solid form design rules

The polymorph selection design rules are abstract and difficult to explain to colleagues unfamiliar with population balances and crystallizer design. There may be a geometric presentation of the design rules similar to the Van Heerden diagrams (heat generation/heat removal plots) often used to teach undergraduate chemical engineers about the steady-state multiplicity and dynamic stability of adiabatic CSTRs. [9] If this idea were further developed, it might increase the impact of the design rules by making them less intimidating to a larger class of potential users.

7.4.4 Paracetamol Form II by continuous precipitation

Paracetamol form II is thermodynamically metastable relative to form I, but it is preferred for its superior compression properties. If paracetamol growth and nucleation kinetics were characterized for both forms I and II as functions of temperature and supersaturation, the design rules presented here could be utilized to propose experimental conditions that yield form II. Paracetamol is an ideal system for the design rules to be applied to next because it is a difficult solid form selection problem that has been published on frequently over the last 25 years. [10, 11] Process conditions that yield form II without requiring complicated process control or additives would make an immediate impact on the field, both by offering a simple yet elegant solution to the specific challenge of solid form selection during paracetamol production and by providing further experimental evidence in support of the design rules presented here.

Bibliography

[1] B. R. Constantz, A. Youngs, and T. Holland. Reduced-carbon footprint concrete compositions. u.s. patent 7,815,880, 2010.

[2] B. R. Constantz, K. Farsad, C. Camire, and I. Chen. Methods and compositions using calcium carbonate. u.s. patent 7,922,809, 2011.

[3] T. C. Farmer, C. L. Carpenter, and M. F. Doherty. Polymorph selection by continuous crystallization. *AIChE J.*, 62:3505–3514, 2016.

[4] T. Lai, S. Ferguson, L. Palmer, B. L. Trout, and A. S. Myerson. Continuous crystallization and polymorph dynamics in the l-gltanic acid system. *Org. Process Res. Dev.*, 18:1382–1390, 2014.

[5] T. C. Lai, J. Cornevin, S. Ferguson, N. Li, B. L. Trout, and A. S. Myerson. Control of polymorphism in continuous crystallization via mixed suspension mixed product removal systems cascade design. *Cryst. Growth Des.*, 15.7:3374–3382, 2015.

[6] J. Bauer, S. Spanton, R. Henry, J. Quick, W. Dziki, W. Porter, and J. Morris. Ritonavir: An extraordinary example of conformational polymorphism. *Pharm. Res.*, 18(6):859–866, 2001.

[7] G. M. Maggioni and M. Mazzotti. Modeling the stochastic behavior of primary nucleation. *Faraday Discussions*, 179:359–382, 2015.

[8] G. M. Maggioni, L. Bezinge, and M. Mazzotti. Stochastic nucleation of polymorphs:experimental evidence and matematical modeling. *Cryst. Growth Des.*, 17(12):6703–6711, 2017.

[9] C. van Heerden. The character of the stationary state of exothermic processes. *Chem. Eng. Sci.*, 8:133–145, 1958.

[10] P. D. Martino, A.-M. Guyot-Hermann, P. Conflant, M. Drache, and J.-C. Guyot. A new pure paracetamol for direct compression: the orthorhombic form. *International Journal of Pharmaceuticals*, 128:1–8, 1996.

[11] L. H. Thomas, C. Wales, L. Zhao, and C. C. Wilson. Paracetamol form ii: An elusive polymorph through facile multicomponent crystallization routes. *Cryst. Growth Des.*, 11:1450–1452, 2011.